

Microscopic and Spectroscopic Analysis of Atmospheric Aerosols from Organic and Freshwater Sources

by

Nicole Olson

A dissertation submitted in partial fulfillment
of the requirements for the degree of
Doctor of Philosophy
(Chemistry)
in the University of Michigan
2021

Doctoral Committee:

Assistant Professor Andrew P. Ault, Chair
Professor Zhan Chen
Professor Stephen Maldonado
Professor Allison L. Steiner

Nicole Olson

niolson@umich.edu

ORCID iD: [0000-0003-1600-8050](https://orcid.org/0000-0003-1600-8050)

© Nicole Olson 2021

Dedication

For my parents, and their unwavering support and unconditional love.

“Like branches on a tree, we all grow in different directions, yet our roots remain forever connected.”

Acknowledgements

First, I would like to thank my advisor, Dr. Andrew Ault. I never thought I would have the opportunity to work with you after first crossing paths when I was 10 years old. Your passion for science and dedication to discovery have made me a better scientist, and for that I'll forever be grateful. Thank you to my committee members, Drs. Chen, Maldonado, and Steiner, for advice and feedback throughout the years. I've been fortunate to work with a number of brilliant collaborators that include: Dr. Jason Surratt and the Surratt group, Dr. Kerri Pratt and the Pratt group, Dr. Cassie Gaston and the Gaston group, Dr. Judy Westrick, Dr. Johnna Birbeck, Dr. Stephen Jacquemin, Aaron Parker, Dr. Paul Shepson, and Dr. "Nate" Slade. Thank you to my undergraduate advisor, Dr. Louise Stracener, for encouraging me to apply to graduate schools when I wasn't so sure.

To members of the Ault and Pratt groups, who are talented scientists and even better friends. Your companionship and comradery helped me navigate through graduate school, and I feel privileged to have met life-long friends at Michigan. To Nancy/Jessica, thank you for introducing me to hot pot, boxing, and speaking Chinese, and for being the best aunt to my cat. To Jia, for always checking my math, enabling my bubble tea addiction, and letting me beat you in Uno. To Madeline, for leading lunch-time meditation circles and teaching me that I can enjoy Indian food. To Jamy, for hosting Bachelor/Bachelorette fantasy leagues and being a great friend. To Yao, for bringing positivity and excitement into the lab, which was especially appreciated in my later years of graduate school. To Drs. Becky Craig, Amy Bondy, Nate May, Rachel Kirpes, Kim Daley, and Alison Fankhauser, thank you for being the best mentors I could have imagined.

Lastly, but most important, my family. Thank you to my grandparents for only being a phone call away and for being some of the few people to read this dissertation cover to cover. To my cat, Halle, who will never read this but should be thanked nonetheless. She helped transform our apartment into a home and taught me that sometimes, the best way to deal with stress is to take a long nap in the sun. To the Forbes family for accepting me as one of their own and trusting me to take care of their Jake. To my brother, Jacob “Cobb”, who is currently pursuing a Ph.D. because he can’t let Big Sis have all the fun! You’re not only my brother, you’re my best friend. I cherish our time spent together and having an ally to gripe about graduate school with. You make me a better person and being your Big Sis has been the greatest honor of my life. To my Dad, thank you for instilling in me a love for science and the environment at a young age. I am writing this today because you have always believed in me and encouraged me to chase my dreams, no matter how hard the journey is. You are the most generous person I know, especially as I remember the time that you took 2 weeks off work to live with me in Michigan because I was so scared to do it all alone. I should also thank you for driving 14 hours (or less if you’re behind the wheel) to help me move almost every single year. To my Mom, whose infamous “girls weekends” always gave me something to look forward to. Your ability to telepathically sense when I’m struggling is incredible, and was usually well-timed with a care package containing my favorite foods. Your support and desire to celebrate all my accomplishments, no matter how small, truly helped me get through the hard times. Finally, to my Jake. Your “all in” attitude started the moment I accepted the offer to attend graduate school. Thank you for being the first person I want to tell good news to, for all the times you picked me up and dropped me off at school, for reminding me what’s important in life, and for moving to Michigan to make pursuing my dreams easier for me. I feel

like the luckiest woman in the world to have met you and I cannot wait to see where we go from here. To all my loved ones, thank you – I owe everything to you.

Table of Contents

Dedication	ii
Acknowledgments	iii
List of Figures.....	ix
List of Tables	xiii
List of Equations	xiv
List of Appendices.....	xv
Abstract.....	xvi
Chapter 1. Introduction	1
1.1 Characteristics and Formation of Atmospheric Aerosol Particles	1
1.1.1 Impacts on Climate and Human Health.....	1
1.1.2 Aerosol Mixing State.....	2
1.2 Physicochemical Characterization of Individual Aerosol Particles	3
1.2.1 Electron Microscopy.....	4
1.2.2 Raman Microspectroscopy	5
1.2.3 Atomic Force Microscopy – Infrared Spectroscopy.....	7
1.2.4 Optical Photothermal Infrared (O-PTIR) + Raman Spectroscopy	8
1.3 Research Objectives and Scope of Dissertation	9
Chapter 2. Reactive Uptake of Isoprene Epoxydiols Increases the Viscosity of the Core of Phase-Separated Aerosol Particles.....	10
2.1 Introduction	10
2.2 Methods.....	10
2.2.1 Aerosol Generation.....	13
2.2.2 Microscopy and Spectroscopy Analysis.....	13
2.3 Results and Discussion.....	16
2.4 Conclusions	26
Chapter 3. Lake Spray Aerosol Incorporated into Great Lakes Clouds.....	28

3.1 Introduction	28
3.2 Methods	30
3.2.1 Aircraft Sampling	30
3.2.2 Laboratory Aerosol Generation	30
3.2.3 Microscopy of Ambient and Laboratory-Generated Particles	30
3.3 Results and Discussion.....	31
3.4 Conclusions	42
Chapter 4. Harmful Algal Bloom Toxins in Aerosol Generated from Inland Lake Water..	44
4.1 Introduction	44
4.2 Methods	47
4.2.1 Freshwater Sample Collection and Aerosol Generation.....	47
4.2.2 Bulk Measurement Techniques and Toxin Characterization	48
4.2.3 Single Particle Analysis.....	48
4.2.4 Analysis of Insoluble Residues.....	49
4.3 Results and Discussion.....	50
4.4 Conclusions	62
Chapter 5. Harmful Algal Bloom Toxins in Ambient Freshwater Aerosol.....	65
5.1 Introduction	64
5.2 Materials and Methods	66
5.2.1 Freshwater and Aerosol Collection	66
5.2.2 LC/MS/MS Toxin Characterization	67
5.2.3 Single Particle Analysis.....	67
5.2.4 Analysis of Insoluble Residues.....	67
5.3 Results and Discussion.....	68
5.4 Atmospheric and Health Implications.....	75
Chapter 6. Simultaneous Optical Photothermal Infrared (O-PTIR) and Raman Spectroscopy of Submicrometer Atmospheric Particles	78
6.1 Introduction	77
6.2 Methods.....	80
6.2.1 Laboratory-Generated Aerosol Particle Samples	81

6.2.2 Ambient Particle Sampling.....	82
6.2.3 Optical Photothermal Infrared (O-PTIR) Spectroscopy.....	82
6.2.4 Raman Microspectroscopy	83
6.2.5 O-PTIR Imaging.....	83
6.3 Results and Discussion.....	82
6.4 Conclusions	90
Chapter 7. Conclusions and Future Directions.....	91
7.1 Conclusions	91
7.2 Future Directions.....	93
Appendices.....	96
References	123

List of Figures

Figure 1.1. Radiative forcing estimates and uncertainties for greenhouse gases and aerosols.....	2
Figure 1.2. Representations of particle composition with increasing complexity and detail.	3
Figure 1.3. Example SEM images and EDX maps of lake spray and sea spray aerosol.	5
Figure 1.4. Raman map of an aerosol particle with highlighted regions showing the locations of specific vibrational modes.	6
Figure 1.5. Schematic of AFM-IR operation.	7
Figure 1.6. Schematic of optical photothermal infrared (O-PTIR) + Raman spectroscopy.	8
Figure 2.1. Schematic of experimental design to generate SOA particles.....	17
Figure 2.2. AFM and SEM images of SOA particles.	19
Figure 2.3. 3D AFM height images and height traces of SOA particles.	20
Figure 2.4. Spreading ratios of SOA particles..	22
Figure 2.5. Plots depicting SOA morphology as a function of particle size.....	23
Figure 2.6. SEM images and EDX spectra of SOA particles.	25
Figure 2.7. Raman spectra of SOA particles.....	26
Figure 3.1. Map depicting area of aircraft sampling with wind speed and wave height data.....	34
Figure 3.2. Map depicting cloud coverage and vertical profile measurements during aircraft sampling.....	35
Figure 3.3. SEM images and EDX spectra of ambient and laboratory-generated LSA..	37
Figure 3.4. Elemental mole ratios of LSA, freshwater, and seawater.....	39

Figure 3.5. Comparison of ambient particle types observed during aircraft sampling.....	42
Figure 4.1. Map of sampling locations and microcystin concentrations at each location..	51
Figure 4.2. Chemical structure, chromatogram, and mass spectrum of microcystin-LR.	53
Figure 4.3. Quantification of microcystin congeners present in Mona Lake freshwater and LSA.	56
Figure 4.4. Average size distributions for water samples and aerosol experiments.	58
Figure 4.5. Mass spectra of biological and organic LSA particles from Mona and Muskegon Lakes.	60
Figure 4.6. Microcystin congeners present at all sampling locations with fraction of particle types observed from each location.....	62
Figure 5.1. Total microcystin and phycocyanin (blue-green algae, BGA) concentrations for each freshwater sample.	69
Figure 5.2. Aerosolized toxins at Grand Lake St Marys.....	70
Figure 5.3. O-PTIR (solid trace) and FTIR (dashed trace) spectra of microcystin-LR.	71
Figure 5.4. O-PTIR (left, red trace) and corresponding Raman spectra (middle, green trace) of representative individual particles defined as LSA, SOA, Biomass burning/soot/dust, and biological.....	72
Figure 5.5. Scanning electron microscopy images with corresponding energy dispersive x-ray spectra of representative individual particles defined as LSA, SOA, biomass burning, soot, dust, and biological.....	73
Figure 5.6. Average aerosol and POC number size distributions for each sampling location....	75
Figure 6.1. Schematic of optical photothermal infrared spectroscopy..	83
Figure 6.2. IR and Raman spectra of ammonium sulfate particles on different substrates.	85

Figure 6.3. IR (left, red trace) and Raman (right, green trace) spectra of laboratory-generated standards.	86
Figure 6.4. IR (left, red trace) and Raman (right, green trace) spectra obtained from ambient particles.....	87
Figure 6.5. IR spectra and maps of a phase-separated particle..	89
Figure A.1. Experimental setup to generate SOA particles.	97
Figure A.2. AFM images of SOA particle re-humidified to the RH at which they were generated.	97
Figure A.3. SEM images of ambient particles collected during the Southern Oxidant and Aerosol Study (SOAS) campaign in Centerville, AL, a rural forested location.....	98
Figure A.4. AFM and SEM images of SOA generated at 30% RH.....	99
Figure A.5. SEM images of toluene SOA/sulfate particles generated at 30% RH before and after IEPOX uptake.....	100
Figure A.6. Spreading ratios of SOA particles generated at 30% RH.	100
Figure A.7. SEM-EDX and Raman spectra of seed particles before SOA coating.	101
Figure A.8. SEM images of SOA particles.....	102
Figure B.1. Aircraft flight path map of July 12, 2016 cloud water sampling.....	104
Figure B.2. Inorganic ion concentrations for freshwater collected in Brevort, Michigan during aircraft sampling on July 12, 2016.....	105
Figure B.3. The average number size distributions of laboratory-generated LSA.	106
Figure B.4. SEM images and EDX spectra of particle types identified as dust and SOA/biomass burning during SEM-EDX analysis.....	107

Figure C.1. SEM-EDX and Raman analysis of insoluble residues present in Mona Lake freshwater.....	108
Figure C.2. Chromatograms showing separation of microcystin congeners present in Mona Lake freshwater. Inset shows congeners present at lower concentrations.....	109
Figure C.3. Structures of all microcystin congeners analyzed.	110
Figure C.4. pH of freshwater samples measured using pH paper.....	111
Figure C.5. Representative ATOFMS spectra of Mona Lake LSA classified as A) LSA salt, B) LSA organic, and C) LSA biological particles.	112
Figure C.6. ATOFMS spectra obtained by taking the difference of Mona Lake LSA salt and Muskegon Lake LSA salt clusters.	113
Figure C.7. SEM images and EDX spectra of LSA particle types.	114
Figure D.1. Sampling locations around Grand Lake St. Marys.....	116
Figure E.1. IR (left, red trace) and Raman (right, green trace) spectra of ammonium sulfate crystals, illustrating the crystalline modes observed by Raman	119
Figure E.2. IR (left, red trace) and Raman (right, green trace) spectra obtained from an ammonium sulfate particle on a gold substrate.....	121
Figure E.3. Optical images of each particle analyzed in Figure 6.3.....	122

List of Tables

Table 4.1. Concentrations of microcystin congeners detected in freshwater and aerosol samples.	55
Table A.1. Experimentally determined Raman modes and tentative assignments for α -pinene and toluene SOA/sulfate.	103
Table C.1. Liquid chromatography retention times of the microcystin congeners observed in Mona Lake freshwater.	109
Table E.1. Number of particles analyzed for each substrate or compound.	118
Table E.2. Table of heat capacity, heat conductivity, and refractive index values obtained from literature for all standard compounds tested.	119
Table E.3. Table listing peaks identified by IR and Raman for each substrate tested.	120
Table E.4. Table listing all vibrational modes experimentally determined in IR and Raman spectra.	121

List of Equations

Equation 2.1.	Volume Equivalent Diameter	16
Equation 2.2.	Spreading Ratio.....	16
Equation 6.1	Photothermal Expansion	79
Equation 6.2	Photothermal Response.....	79
Equation C.1	Total Aerosol Volume.....	115
Equation C.2	Aerodynamic Diameter	115
Equation C.3	Mass Concentration.....	115
Equation C.4	Mass Fraction.....	115
Equation C.5	Enrichment Factor	115

List of Appendices

Appendix A. Reactive Uptake of Isoprene Epoxydiols Increases the Viscosity of the Core of Phase-Separated Aerosol Particles Supplemental Information.....	97
Appendix B. Lake Spray Aerosol Incorporated into Great Lakes Clouds Supplemental Information	105
Appendix C. Harmful Algal Bloom Toxins in Aerosol Generated from Inland Lake Water Supplemental Information	109
Appendix D. Harmful Algal Bloom Toxins in Ambient Freshwater Aerosol Supplemental Information	117
Appendix E. Optical Photothermal Infrared (O-PTIR) and Raman Spectroscopy of Submicrometer Atmospheric Particles Supplemental Information	118

Abstract

Atmospheric aerosols impact climate by scattering or absorbing solar radiation and by participating in the formation of clouds and ice crystals. Additionally, the inhalation of aerosol particles contributes significantly to cardiovascular and cardiopulmonary diseases, and is a leading cause of mortality on a global scale. Despite the climate and health implications of aerosol particles, the magnitude of their impacts is still highly uncertain. The physical and chemical (physicochemical) properties of aerosol particles determine their impacts, though these properties are analytically challenging to measure due to their small size, chemical complexity, and continuous evolution in the atmosphere. Single-particle methods are necessary to build upon our understanding of the multiphase aerosol processes occurring in the atmosphere, and to elucidate the impact of these particles on climate and health. In this dissertation, single-particle microscopic and spectroscopic methods were applied to study both ambient and laboratory-generated particles to enable better predictions of the climate and health impacts of aerosol particles.

Secondary organic aerosol (SOA), formed from multiphase reactions between aerosol particles and atmospheric gases, was systematically studied in an indoor atmospheric chamber. Particles were collected at multiple points during the multiphase reaction for physicochemical analysis using electron microscopy, atomic force microscopy, and Raman microspectroscopy. Particles underwent physicochemical transformation after heterogeneous reactions, leading to the formation of isoprene-derived organosulfate compounds in the particle phase that increased particle viscosity and altered the internal structure of particles. This study highlighted the dynamic physicochemical properties of SOA, a major fraction of organic aerosol in the atmosphere.

Particles emitted from freshwater lakes, known as lake spray aerosol (LSA), were studied through laboratory and ambient observations to determine the impacts of this newly identified particle type on climate and health. An aircraft campaign used microscopy to show that cloudwater and ambient LSA over Lake Michigan have very similar physicochemical properties, suggesting the incorporation of LSA into clouds with likely contributions to lake-effect precipitation. In a separate study, freshwater was collected during a severe harmful algal bloom (HAB) and analyzed

for algal toxins using mass spectrometry. Aerosol particles were generated in the laboratory from the freshwater samples, with an observed enrichment of hydrophobic toxins in the aerosol phase. Following this laboratory-based study, a field campaign was performed at a lake experiencing a severe HAB. Freshwater and aerosol samples were analyzed for the presence of algal toxins using mass spectrometry and infrared spectroscopy, and the amount of aerosolized toxins in ambient environments was determined. These projects highlight a new route of exposure to HAB toxins that has implications for people living near or downwind of HABs globally.

Lastly, a new analytical spectroscopy method was developed and applied to characterize vibrational modes present in submicron aerosol particles. This method combined optical photothermal infrared (O-PTIR) and Raman spectroscopy for simultaneous spectroscopic acquisition. This project identified the ideal substrate for analysis, characterized single- and multi-component standards, and showed the first classification of ambient aerosol particles with O-PTIR + Raman. The spectroscopic analysis of submicron particles enabled exploration of samples previously unstudied by vibrational spectroscopy, significantly advancing the fields of atmospheric and analytical chemistry.

The methods and results obtained in this dissertation have resulted in detailed measurements of particle physicochemical properties, providing new insights into the mechanisms of multiphase atmospheric processing and improving understanding of the impacts of aerosols on climate and human health.

Chapter 1. Introduction

1.1 Characteristics and Formation of Atmospheric Aerosol Particles

Atmospheric aerosols are a collection of solid or liquid particles suspended in the air.¹ Aerosol particles can range in size from 1 nm to 100 μm in diameter, with modes referring to nucleation (< 10 nm), Aitken (10 – 100 nm), accumulation (100 – 1000 nm), and coarse (>1 μm) size ranges.² Particles are formed from a plethora of natural and anthropogenic sources, each with complex physical and chemical (physicochemical) properties that vary for each individual particle.^{1,3} Aerosols can be directly emitted into the atmosphere as solid or liquid particles, otherwise known as primary aerosol.¹ One example of primary aerosol is the production of lake spray aerosol (LSA) from wave-breaking and bubble bursting in freshwater environments.^{4,5} Conversely, secondary particles are formed through the oxidation and condensation of atmospheric gases onto pre-existing particulate matter.^{1,6} In addition to secondary aerosol formation, particles can undergo modifications resulting from multiphase physicochemical processing during their atmospheric lifetime.¹ Particulate matter has a range of possible morphologies, from nearly spherical (like secondary aerosol) to amorphous (like LSA) to chain agglomerates (like soot).^{5,7,8} Aerosol particles impact climate and human health, with the extent of these impacts dependent on particle physicochemical properties.^{1,3}

1.1.1 Impacts on Climate and Human Health

Atmospheric aerosol particles affect climate directly by scattering or absorbing solar radiation and indirectly by acting as cloud condensation nuclei (CCN) or ice nucleating particles (INP).^{1,6,9} Atmospheric particles represent the largest source of uncertainty in global radiative forcing (Figure 1.1) due to their complex and dynamic physicochemical properties, combined with high temporal and spatial variability.¹⁰ In addition to impacting climate, increased concentrations of atmospheric particles are linked to negative health effects,¹¹ with over 4 million premature deaths attributed annually to atmospheric pollution.¹² Despite the importance of aerosols,

mechanistic understanding of many key atmospheric processes remains low, in part due to challenges associated with measuring dynamic aerosol physicochemical properties. With aerosol impacts closely tied to the properties of individual particles, understanding the chemical composition and distribution of species within populations is essential to uncovering the extent of their influence.

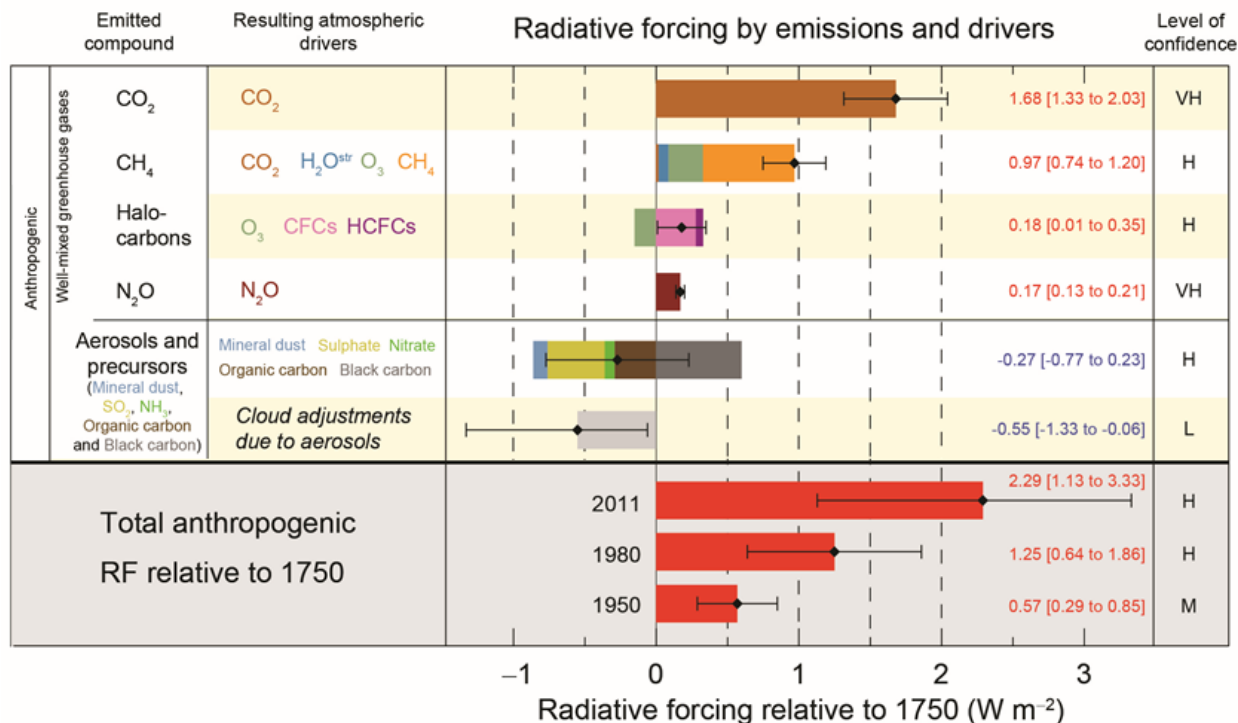


Figure 1.1. Radiative forcing estimates and uncertainties for greenhouse gases and aerosols. Reproduced from Stocker et al.¹⁰

1.1.2 Aerosol Mixing State

Aerosol physicochemical mixing state is an all-encompassing term that refers to the distribution of both chemical and physical features within an aerosol population, and is challenging to measure and quantify.^{3,13,14} The distribution of chemical species within an aerosol population can be described in terms of external and internal mixtures. An external mixture consists of particles that contain only one pure species per particle (e.g. ammonium sulfate or soot), while an internal mixture describes a population where each particle has the same chemical species present in the same abundance (e.g. all particles contain the same amounts of sulfate and soot).¹³ However, internal and external mixtures are idealized cases, and neither are representative of most ambient aerosol populations. As changes in chemical composition affect particle properties such as

reactivity,^{15,16} hygroscopicity,¹⁷ and optical scattering,^{18,19} it is imperative to understand the chemical mixing state of individual particles in a population. Figure 1.2 illustrates the different chemical and physical aspects that can be incorporated into aerosol mixing state.³ Despite the important implications of mixing state for aerosol impacts on climate, few direct measurements of aerosol mixing state exist because this requires the measurement of individual particles which is time intensive and analytically challenging.

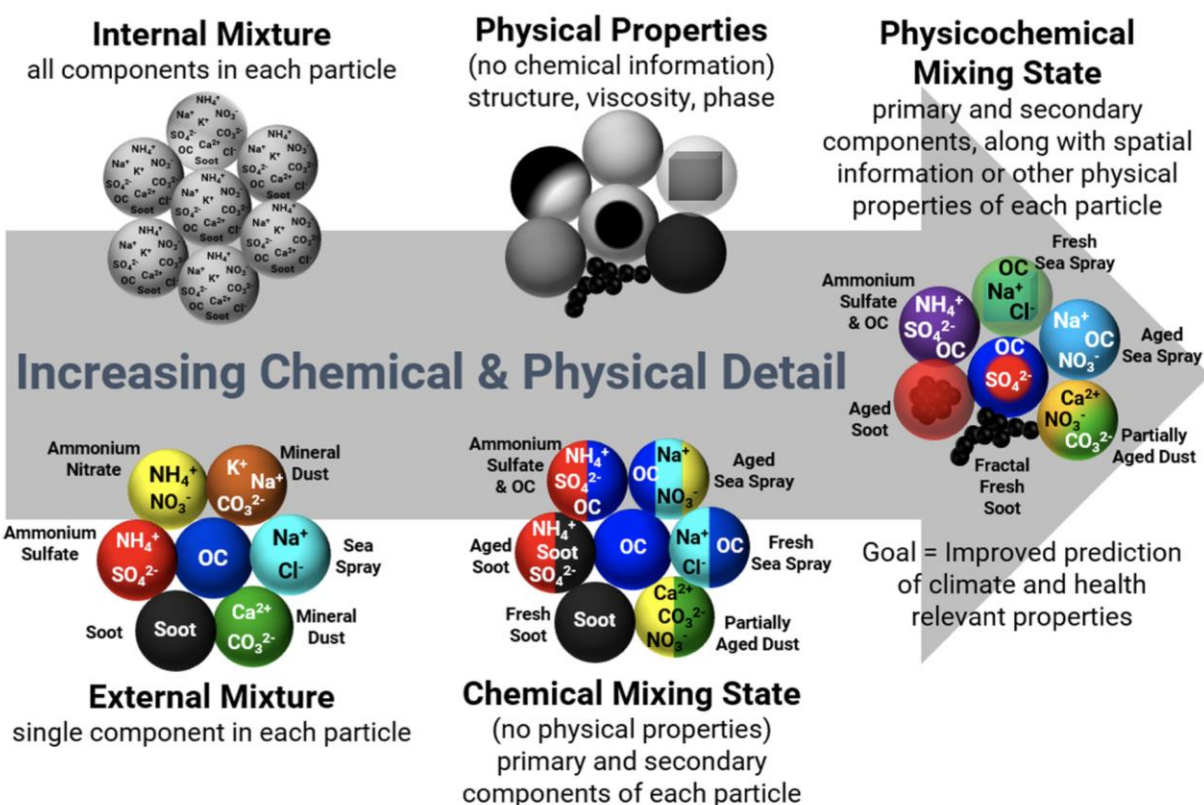


Figure 1.2. Representations of particle composition with increasing complexity and detail. Chemical mixing state provides information on primary versus secondary components, but does not provide spatial information or other physical properties. Physicochemical mixing state provides both chemical detail and spatial information or physical properties. Note that the locations of the colors in the chemical mixing state particles are not meant to convey spatial distribution, only the presence of both primary and secondary components. Reproduced from Ault and Axson.³

1.2 Physicochemical Characterization of Individual Aerosol Particles

Single-particle microscopic and spectroscopic methods can be used to study aerosol physicochemical mixing state.³ Microscopy provides information on particle size and morphology,

while spectroscopic methods yield detailed chemical information regarding elemental composition or functional groups present, depending on the type of spectroscopy utilized. The offline and non-destructive nature of these techniques allows for analysis of the same sample by multiple techniques, providing a multimodal approach to characterizing aerosol mixing state. Typically, an aerosol impactor with size-resolved stages collects particles onto substrates for various offline microscopic and spectroscopic analyses. The single-particle microscopy and spectroscopy methods used in this dissertation are described below.

1.2.1 Electron Microscopy

Scanning electron microscopy with energy dispersive X-ray spectroscopy (SEM-EDX) has been used to characterize the structure and elemental composition of aerosol particles down to 50 nm in diameter.^{3,5,20-24} With SEM, an electron beam is focused on the sample to produce images of particles impacted onto substrates. The ability to detect different electronic transitions provides information on surface structure (if utilizing back-scattered electrons and a thicker substrate) or internal features (if utilizing transmitted electrons and a thin sample),³ depending on the substrate and sample composition. Recently, tilted-SEM has been used to obtain information on three-dimensional particle morphology by imaging particles at separate angles.^{25,26} Electron imaging releases element-specific X-rays that can be collected simultaneously to obtain semi-quantitative elemental spectra with high spatial resolution (<10 nm).³ Rastering the electron beam across the sample, otherwise known as elemental mapping, provides physicochemical mixing state information for individual particles with different elemental composition and structure (Figure 1.3).²⁷ The automation of computer-controlled SEM-EDX (CCSEM-EDX) allows for analysis of thousands of particles per sample to increase throughput and enables analysis of a statistically representative number of particles.^{3,23,28} Clustering algorithms have been developed for analysis of large CCSEM-EDX datasets to mathematically group individual particles based on physicochemical similarity and limit human bias during sorting.²⁹⁻³² The grouping of similar particles enables size-resolved characterization of aerosol sources.

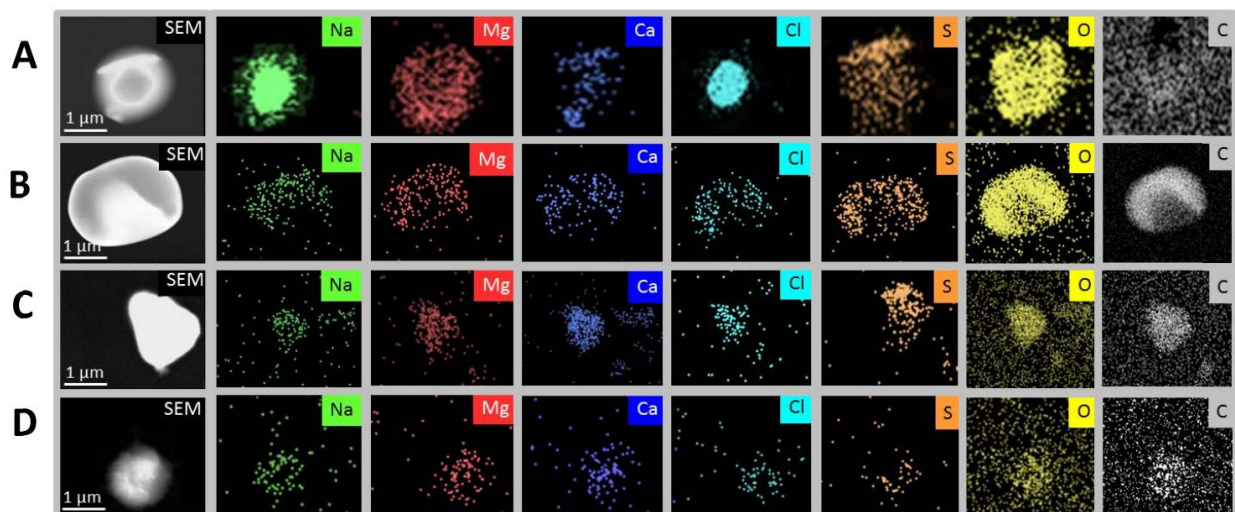


Figure 1.3. Example SEM images and EDX maps of lake spray and sea spray aerosol. SEM images and EDX elemental maps of representative: (A) SSA and (B) LSA particles collected at UMBS on July 16, 68 2014 9:00 – 21:00 EST, as well as LSA generated in the laboratory from (C) Lake Superior and (D) Lake Michigan freshwater sample. Reproduced from May et al.²⁷

1.2.2 Raman Microspectroscopy

Raman microspectroscopy has been used to characterize aerosol physicochemical properties by combining an optical microscope with vibrational spectra that probe functional groups present in individual particles $> 1 \mu\text{m}$.^{3,22,33-37} Raman spectroscopy probes molecular vibrations, rather than the electronic transitions utilized in SEM-EDX, to provide information on covalently bonded organic and inorganic functional groups. Raman spectroscopy has the sensitivity to differentiate species in slightly different bonding environments (i.e. NaNO_3 vs. NO_3^-),³⁸ which can be extremely useful in determining aerosol evolution and aging. Raman has also been used to study the relative abundances of acids and their conjugate bases to calculate the pH of individual aerosol particles.^{33,35} This high sensitivity has allowed for the detection of complex organosulfate species, an indicator of multiphase isoprene epoxydiol uptake,³⁹⁻⁴¹ in individual particles generated in the laboratory³⁴ and observed in the ambient environment.⁴² Similar to SEM-EDX, mapping can be performed to identify the location of specific molecular species within an individual aerosol particle (Figure 1.4),⁴³ enabling analysis of aerosol physicochemical properties. In addition to the detailed chemical information obtained by Raman, another advantage over SEM-EDX is that Raman analysis is performed under ambient pressure and temperature to limit particle distortion and the loss of volatile species. Furthermore, the coupling of relative humidity (RH) cells to Raman analysis has enabled study of the hygroscopic growth of particles,⁴⁴ which is

challenging to do under the vacuum conditions of traditional SEM. Recently, a computer-controlled method (CC-Raman) was developed to enable analysis of hundreds of particles per sample.⁴⁵ Though recent advances of Raman, such as surface enhanced Raman spectroscopy (SERS)^{43,46} and tip enhanced Raman spectroscopy (TERS),⁴⁷ have allowed for analysis of slightly submicron particles, the uneven enhancements observed make it difficult to perform quantitative measurements. Similarly, the ability of biological and mineral dust particles to naturally fluoresce^{48,49} can often overwhelm Raman signal and often requires coupling to other vibrational spectroscopies, such as infrared (IR).

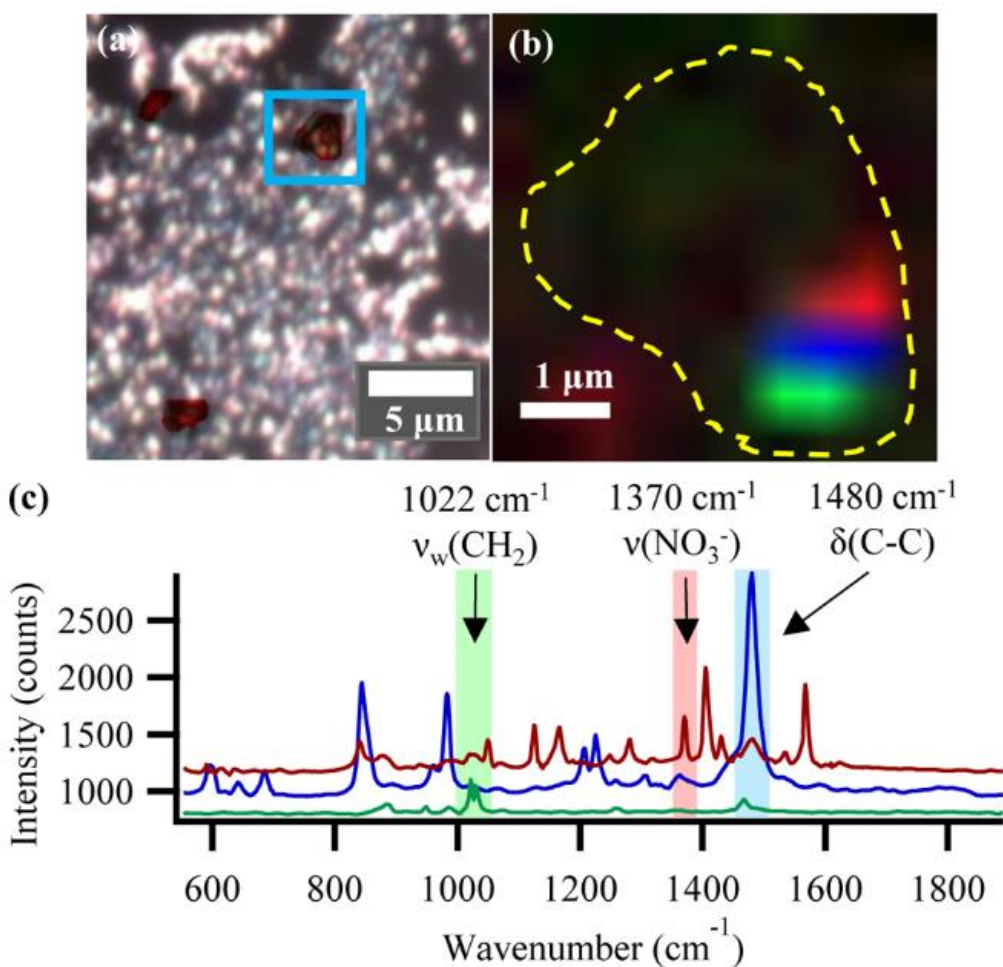


Figure 1.4. Raman map of an aerosol particle with highlighted regions showing the locations of specific vibrational modes. (a) Optical image of aerosol particle, (highlighted in red) against SERS substrates, and mapped area (blue box). (b) Map of the aerosol particle (outlined in yellow dashes) showing the location of three different enhanced chemical species at 1022 cm^{-1} (green), 1370 cm^{-1} (red), and 1480 cm^{-1} (blue). (c) Raman spectra accompanying the mapped intensities. Reproduced from Craig et al.⁴³

1.2.3 Atomic Force Microscopy – Infrared Spectroscopy

Atomic force microscopy coupled to infrared spectroscopy (AFM-IR) has recently been applied to study IR-active vibrational modes in aerosol particles down to 50 nm under ambient conditions.⁵⁰⁻⁵² By detecting the photothermal expansion of an individual particle illuminated by a tunable IR laser with a cantilever, IR absorption-like spectra can be obtained with < 50 nm spatial resolution (Figure 1.5).⁵³⁻⁵⁵ This technique enables analysis of samples under the diffraction-limited resolution of other vibrational spectroscopies, such as Raman and IR. The combination of IR spectra with the high-resolution imaging obtained from traditional AFM has enabled study of particle hygroscopicity,^{44,56} polymer degradation,⁵¹ and particle phase state.^{34,50} The ability to detect vibrational modes in submicron particles that have relevance to the climate and health impacts of particles is a significant breakthrough for both analytical and atmospheric chemistry. However, as with any method, there are limitations. The need for the AFM tip to be in contact with the samples makes analysis of soft or liquid samples difficult. Additionally, obtaining spectra is time intensive, often taking 20+ minutes for a single spectrum and even longer to collect a map. Therefore, a contact-less and rapid method is needed for analysis of vibrational modes present in submicron aerosol particles under ambient conditions.

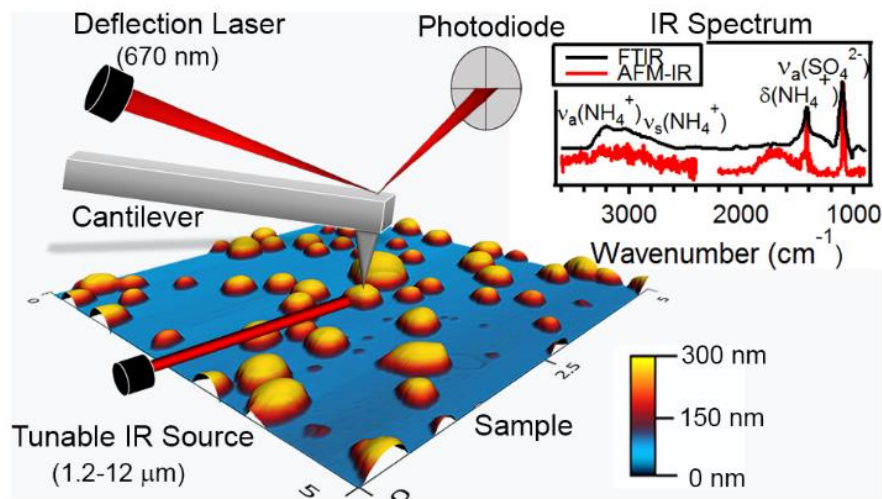


Figure 1.5. Schematic of AFM-IR operation. Local thermal expansion from the IR laser is detected by the cantilever, allowing IR spectra with ~ 50 nm resolution to be collected. IR spectra were collected from individual ammonium sulfate particles using AFM-IR (this study) and micro-FT-IR. Reproduced from Bondy et al.⁵⁰

1.2.4 Optical Photothermal Infrared (O-PTIR) + Raman Spectroscopy

Optical photothermal infrared (O-PTIR) spectroscopy is a new, contact-less analytical method that circumvents the diffraction limitations of traditional IR microscopy by using changes in the scattering intensity of a continuous wave visible laser to detect the photothermal expansion that occurs when a vibrational mode is excited by a tunable IR laser (Figure 1.6).⁵⁷⁻⁶¹ The change in intensity of the elastically (Rayleigh) scattered photons is processed to obtain an IR absorption-like spectrum. As inelastically (Stokes) scattered photons are also generated, they can be simultaneously collected to obtain Raman spectra at the same point and with the same spatial resolution as the O-PTIR spectra. Because the spatial resolution is determined by the visible laser and not the longer-wavelength IR laser, spectra are obtained with a spatial resolution of ~500 nm, orders of magnitude better than previous aerosol analysis using IR microscopy.³ Like all previously mentioned techniques, O-PTIR is able to map the location of specific vibrational modes located within individual particles,⁶²⁻⁶⁴ giving insight into particle physicochemical properties and mixing state. O-PTIR + Raman was applied to study the physicochemical properties of laboratory-generated and ambient particles for the first time as part of this work (Chapter 6). The ability to collect multiple types of vibrational spectra simultaneously with < 1 min acquisition times significantly furthers throughput of complex particle analysis. The contact-less nature of this technique makes it a highly useful method for studying other liquid or heterogeneous samples.

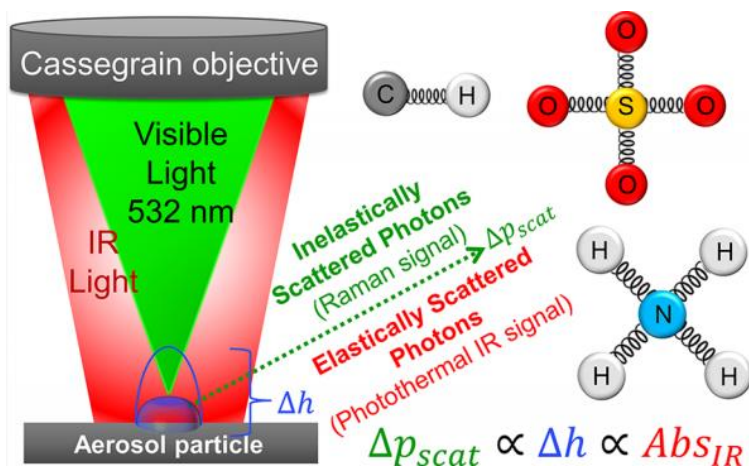


Figure 1.6. Schematic of optical photothermal infrared (O-PTIR) + Raman spectroscopy. Infrared and visible light are focused on the sample through a Cassegrain objective, inducing a photothermal expansion of the particle. Light scattered from the sample (Δp_{scat}) is proportional to the photothermal expansion of the particle (Δh) and absorbance of IR light (Abs_{IR}). Simultaneous IR and Raman spectra are obtained from a single point. Reproduced from Olson et al.⁵⁷

1.3 Research Objectives and Scope of Dissertation

The research presented in this dissertation uses established and novel single-particle microscopy and spectroscopy methods to provide detailed information on the physicochemical mixing state of aerosol particles from freshwater and secondary organic sources. Chapter 2 describes a laboratory chamber study that examines the change in particle composition and viscosity after reaction with atmospheric gases, providing insight into the dynamic physicochemical properties of atmospheric aerosol over the course of their lifetime. This Chapter also discusses implications for further heterogeneous uptake and climate-relevant properties such as water uptake and cloud formation. Chapter 3 investigates the influence of freshwater-derived particles on cloud formation over the Great Lakes, providing evidence that freshwater aerosol can contribute to cloud formation in regions with large bodies of freshwater. This Chapter gives insight into the climate-relevant properties of this specific particle type, which had not been previously studied at the single-particle level. Chapters 4 and 5 explore the aerosolization of harmful algal bloom toxins in freshwater environments, with separate focuses on laboratory-based experiments (Chapter 4) and ambient measurements (Chapter 5). The identification and quantification of algal toxins in aerosol particles highlights potential exposure risks for populations living near algal blooms globally, and suggests the importance of simultaneously measuring bulk phase (water column) and aerosolized toxins. Chapter 6 describes the application of O-PTIR + Raman spectroscopy to characterize vibrational modes present in submicron atmospheric particles for the first time. This Chapter also applied O-PTIR + Raman to study heterogeneous aerosol particles, showing that this new analytical method can be applied to other fields beyond aerosol science. Finally, Chapter 7 summarizes the conclusions of this work and future directions for on-going projects. The results presented herein improve our understanding of the physicochemical properties of organic and freshwater-derived particles and describe a new method to characterize submicron atmospheric particulate matter, ultimately furthering understanding of the climate and health impacts of particulate matter.

Chapter 2. Reactive Uptake of Isoprene Epoxydiols Increases the Viscosity of the Core of Phase-Separated Aerosol Particles

Adapted with permission from Olson, N. E., Lei, Z., Craig, R. L., Zhang, Y., Chen, Y., Lambe, A. T., Zhang, Z., Gold, A., Surratt, J. D., and Ault, A. P.: Reactive Uptake of Isoprene Epoxydiols Increases the Viscosity of the Core of Phase-Separated Aerosol Particles, *ACS Earth Space Chem.*, 3, 8, 1402-1414, 2019.

<https://doi.org/10.1021/acsearthspacechem.9b00138> Copyright 2019 American Chemical Society

2.1 Introduction

Climate-relevant aerosol properties, such as the ability to scatter or absorb solar radiation and alter cloud or precipitation patterns by acting as cloud condensation nuclei (CCN) and ice nuclei (IN),^{6,65,66} are dependent on individual particle physiochemical properties, including chemical composition, aerosol phase, and morphology.^{6,65,67,68} These properties are dynamic as the diurnal cycle of relative humidity (RH) modifies the water content of aerosols and, thus, alters the physical state of particles, including particle phase state and viscosity.⁶⁹⁻⁷² Changes in RH and particle composition can both lead to transitions of particle phase states,⁷⁰⁻⁷⁵ which range from liquid and semi-solid to glassy and crystalline state, and can include the separation of phases within individual aerosol particles.^{76,77} Phase-separated particles typically form when inorganic and organic phases are no longer miscible at higher molar concentrations at lower RH.⁷⁴ Inorganic particles, particularly sulfate-containing particles, can react with gas-phase organic species generated by gas-phase oxidation of biogenic and anthropogenic volatile organic compounds (VOCs).^{65,74,78,79} For instance, isoprene and α -pinene are major VOCs emitted from vegetation,^{80,81} while toluene is a ubiquitous anthropogenic VOC.⁸² Oxidation products of VOCs condensing onto existing inorganic aerosols leads to the formation of secondary organic aerosol (SOA), accounting for more than 50% of the total organic aerosol mass globally.^{83,84}

Isoprene, the most abundant non-methane hydrocarbon emitted into the atmosphere (~ 600 Tg y⁻¹),^{80,85} undergoes oxidation by hydroxyl radicals to form large quantities of gaseous isoprene

epoxydiols (IEPOX) under low-NO_x conditions.^{86,87} The increased molecular functionality and associated decrease in vapor pressure that occurs from the oxidation of isoprene (0.62 atm at 293 K) to IEPOX (3.4 x 10⁻⁶ atm at 293 K) facilitates uptake into the particle phase via multi-phase chemical reactions,^{79,83,88-90} particularly under acidic conditions.^{91,92} IEPOX-derived SOA has been shown to contribute up to 40% of submicron organic aerosol mass in isoprene-rich environments,^{93,94} contributing to changes in aerosol physiochemical properties.^{15,76} However, to date, few studies have analyzed changes in SOA physiochemical properties (particle morphology, viscosity, and phase) after IEPOX uptake. Individual particle measurements are necessary to provide better understanding of the effect of IEPOX uptake on particle morphology and phase, which impact how particles participate in light scattering and climate-altering processes.^{95,96}

Phase separation within atmospheric aerosol particles has a wide range of atmospheric implications, including altering SOA formation by modifying the partitioning of organic species from the gas to particle phase.⁹⁷⁻⁹⁹ This includes either inhibition^{15,70-75,98,100} or enhancement of reactive uptake to particles containing more than one phase¹⁰¹ typically an organic outer layer and an aqueous-inorganic core.¹⁰² Given that these results have primarily been based on thermodynamic models, further experimental data is needed on the uptake of key oxidation products for phase separated particles. Phase separations have also been shown to increase solar radiation scattering and absorption.¹⁰³ Therefore, determining aerosol phase, phase separations, and morphology (e.g. core-shell) is necessary to accurately predict atmospheric SOA formation and aerosol impacts on air quality and radiative forcing.

SOA species can exist in glassy, highly viscous states that alter aerosol reactivity.^{81,104-106} Multiphase chemistry of IEPOX in the ambient environment leads to the formation of organosulfates,^{40,42,107,108} polyols,^{83,108-110} and oligomers^{90,109,111,112} in the condensed phase, thereby increasing particle viscosity. Viscosity alters mixing timescales and diffusion throughout the particle, with potential to change the particle phase from homogeneously mixed to phase-separated.¹¹³ Highly viscous organic phases can kinetically inhibit the transfer of mass and, thus, inhibit phase transitions and gas-particle partitioning.^{81,104-106,114-116} More viscous particles have lower gaseous uptake,^{15,81} reactivity,^{81,106} and limited particle growth,⁸¹ impacting particle evolution in the atmosphere.⁷⁰ However, the relationship between reactive uptake, particle viscosity, and phase separation is not well characterized for mixed SOA-inorganic particles, the dominant particle type, by number, in the Southeastern United States.⁷⁸

To date, laboratory studies investigating phase separation have primarily been conducted using inorganic particles coated with organic acids (pimelic,^{73,117} succinic,^{73,75,117} glutaric^{72,75}), sucrose,⁷⁵ and decane.⁸ Additional laboratory studies have investigated phase separation of more chemically complex, atmospherically-relevant biogenically-derived SOA, such as α -pinene SOA.^{77,100,118} However, investigations of α -pinene SOA using imaging methods as direct evidence of phase separation^{77,118} focused on 8.5 – 30 μm particles, a size range that is significantly larger than the number and mass modes of atmospheric particulate matter (PM),⁶ and therefore might not be an accurate representation of particle phase at smaller sizes due to the size-dependent kinetic effects observed in Veghte et al.¹¹⁷ Virtanen et al.¹⁰⁵ found laboratory-generated 100 nm α -pinene SOA particles exhibited semi-solid behavior based on particle bounce measurements. However, this study was performed at 30% RH, which is much lower than the 50-90% ambient RH reported by field studies in the Southeast United States where IEPOX-derived SOA is prevalent,¹¹⁹ and therefore might influence the particle phase state observed.⁷⁷ Studies examining α -pinene SOA at higher RH found particles to have semi-solid behavior up to 90% RH,¹²⁰ but particle morphology (homogeneous versus phase-separated) was not investigated across the different RH conditions. Bertram et al.¹²¹ and Ciobanu et al.¹²² systematically studied phase separation as a function of RH for laboratory-generated SOA and inorganic sulfate mixtures using optical microscopy, though they used 20–30 μm particles that are much larger than atmospheric SOA particles. Additional studies have analyzed the phase separation of laboratory-generated SOA from 0–100% RH.^{100,123} However, most used SOA in the absence of seed particles so the results are not directly comparable to the phase states presented herein. Particle coatings in boreal forest regions, where α -pinene SOA is dominant,¹²⁴ can behave differently than particle coatings in regions where isoprene and α -pinene emissions are both abundant, as shown recently by Slade et al.⁷⁶ Additional insights into atmospherically relevant sizes of α -pinene and isoprene SOA infer phase separation based on indirect methods such as an aerosol mass spectrometer (AMS),¹²⁵ scanning mobility particle sizer (SMPS),^{125,126} tandem differential mobility analyzer,^{127,128} and single particle ablation time-of-flight mass spectrometer (SPLAT),^{98,126} providing information on particle size and phase state at different RH. Smith et al. found lower efflorescence and deliquescence RHs of isoprene-derived SOA¹²⁷ and α -pinene SOA¹²⁸ coated onto sulfate particles compared to pure ammonium sulfate particles, indicating changes in aerosol hygroscopic phase transitions with addition of SOA material. You et al.⁷⁷ showed aerosols can undergo phase separation after extraction of bulk

particle organic material from filters. While informative, bulk measurements are unable to determine the number and composition of individual phase-separated atmospheric particles, but rather show that in 30 μm particles that the bulk SOA phase separates from an aqueous, inorganic phase. Song et al.¹²⁹ measured the phase state of toluene-derived anthropogenic SOA, obtaining results demonstrating that pure toluene-derived SOA particles become more viscous at lower RH. While these studies made important contributions to understanding biogenic and anthropogenic organic aerosol phases, we lack characterization of the changes in particle phase state after the reactive uptake of additional gaseous species, particularly for mixed organic-inorganic systems. Microscopic studies that directly investigate aerosol phase using single particles of atmospherically relevant size, composition, and RH are necessary to determine the factors influencing phase separation in particles, and particle phase changes following reaction with gaseous species.

In this study, we analyzed changes in particle phase state and viscosity after uptake of gas-phase IEPOX onto phase-separated α -pinene and toluene SOA-coated inorganic particles. Particles were characterized using atomic force microscopy (AFM), scanning electron microscopy coupled with energy dispersive x-ray spectroscopy (SEM-EDX), and Raman microspectroscopy to study the particle phase, morphology, and composition before and after IEPOX reactive uptake. Phase separation was influenced by particle size, with most small SOA particles (< 100 nm) remaining homogeneous and particles > 100 nm showing distinct phase-separated core-shell morphology, as confirmed by microscopic images and compositional differences between particle core and shell. Significant changes to particle core phase and morphology were observed after IEPOX reactive uptake, suggesting IEPOX diffusion through the outer organic shell to react with the inorganic core and modification of its physiochemical properties. Overall particle viscosity increased after IEPOX uptake, as shown by measurements of particle heights and spreading ratios, likely driven by a more viscous core. These changes to phase and morphology have important implications for further multi-phase chemical reactions and SOA formation.

2.2 Methods

2.2.1 Aerosol Generation

The system for generating SOA-coated sulfate particles was previously described in detail in Zhang et al.¹⁵ and shown in Figure A.1. Briefly, acidic ammonium sulfate particles ($\text{pH} = 1.4 \pm$

0.2) were generated by atomizing a solution of 0.06 M ammonium sulfate ((NH₄)₂SO₄, Sigma Aldrich, ≥99% purity) and 0.06 M sulfuric acid (H₂SO₄, Sigma Aldrich, ≥98% purity) using a constant output atomizer (TSI Inc., Model 3076) to simulate the pH of ambient aerosol particles in the southeastern United States.¹¹⁹ Initial particle pH was confirmed using the pH indicator method described in Craig et al.¹³⁰ Aerosols passed through a diffusion drier to remove excess water resulting in particle RH of 26 ±3%, remaining near the efflorescence point of 34% RH.¹³¹ A differential mobility analyzer (DMA, TSI Inc., Model 3080) was used to size select seed particles with 100 nm electrical mobility diameter. The DMA operated at a 12:3 sheath:sample flow ratio over the mobility size range of 10 – 600 nm, resulting in a number size distribution with a mode at 100 nm and a geometric standard deviation of 1.5 for acidic seed particles.¹⁵

A Potential Aerosol Mass (PAM) oxidation flow reactor (OFR; Aerodyne Research Inc.)¹³² was used to generate SOA coatings on sulfate seed particles via ozonolysis of 200 ppb α-pinene or photooxidation of 800 ppb toluene. The OFR was operated in continuous flow mode with a mean residence time of 2 min. To establish ozonolysis conditions, 40 ppm O₃ was added at the inlet of the OFR using an external O₃ chamber. To establish photooxidation conditions, the O₃ was photolyzed at λ of 254 nm inside the OFR to generate O(¹D) radicals, which reacted with H₂O to continuously produce hydroxyl (OH) radicals ([OH] ~10¹⁰ cm⁻³). Recent studies suggest that SOA particles generated in OFRs have compositions similar to SOA generated in environmental chambers^{116,133-136} and in the atmosphere.¹³⁷⁻¹⁴²

The aerosol-laden flow exiting the OFR was passed through two Nafion tubes (Perma Pure, Model PD-200T-12) to control and vary the RH prior to performing IEPOX uptake in a glass flow tube (1 m length, 8 cm ID, 40 s residence time) coated with halocarbon wax (Halocarbon Products Corporation) to minimize wall loss. IEPOX uptake was conducted using authentic *trans*-β-IEPOX, which is the predominant IEPOX isomer in the atmosphere,⁸⁶ and was synthesized following published procedures.¹⁴³ At the inlet and outlet of the glass flow tube, aerosols were collected for microscopy and spectroscopy analysis (details below). Aerosol size distributions were measured by a SMPS consisting of a DMA and a condensation particle counter (CPC, TSI Inc., Model 3022A) at the end of the flow tube.

2.2.2 Microscopy and Spectroscopy Analysis

Aerosol particles were collected for microscopy and spectroscopy analysis before and after IEPOX reactive uptake using a 3-stage microanalysis particle sampler (MPS-3, California Measurements Inc.). Particles were impacted onto carbon-type-b Formvar coated copper transmission electron microscopy (TEM) grids (Ted Pella Inc.), silicon wafers (Ted Pella Inc.), and quartz slides (Ted Pella Inc.) for SEM, AFM, and Raman analysis, respectively. Samples from stage 3 (aerodynamic diameter (d_a) < 400 nm) were selected for analysis. Particle morphology was classified as homogeneous or phase-separated based on the criteria defined in Veghte et al,¹¹⁷ where non-phase-separated particles were visually homogeneous and phase-separated particles contained two or more immiscible substances. AFM and Raman measurements were performed at ambient pressure and RH (30-40%), while SEM was performed under vacuum conditions (10^{-5} - 10^{-6} Torr). Because the ambient RH at which particles were imaged using AFM (30-40% RH) was lower than RH when samples were generated (50% RH), samples were re-humidified to 50% RH and imaged with AFM to investigate possible morphology changes resulting from humidity changes to the sample. As shown in Figure A.2, re-humidified samples did not show significant differences in morphology compared to samples imaged at ambient RH. Therefore, AFM images and data in this text were collected at the ambient RH values of 30-40%.

SEM analysis was performed on an FEI Helios 650 Nanolab Dualbeam electron microscope that operated at an accelerating voltage of 10.0 kV and a current of 0.40 nA. The Helios microscope was equipped with a high angle annular dark field (HAADF) detector that provided contrast between areas of different elemental composition.¹⁴⁴ EDX spectra were acquired for 20 seconds using an EDAX detector and GENESIS EDX software version 5.10 (EDAX Inc., Mahwah, NJ). To investigate trends between particle size and phase separation, SEM images were analyzed with image processing software (ImageJ, version 1.50i, National Institutes of Health, USA) to determine individual particle projected area diameters (diameter of particles after impaction onto substrate). Projected area diameters were then converted to volume equivalent diameters (d_{ve}) to simulate particle diameter before impaction and spreading onto substrate.¹⁴⁵ Volume equivalent diameters were calculated using particle volume (v) data obtained from AFM analysis (described below) and the following equation, assuming particles were initially spheres before impaction:¹⁴⁵

Equation 2.1. Volume Equivalent Diameter (d_{ve}) = $\sqrt[3]{\frac{6v}{\pi}}$

AFM was performed with a PicoPlus 5500 AFM (Agilent, Santa Clara, CA) that operated using 300 kHz resonant frequency and 40 N/m spring constant. Tapping mode was performed utilizing Aspire CT300R probes (NanoScience, AZ) to obtain phase and height images. Samples were scanned in 5 μm x 5 μm areas with 0.75 Hz scan rates to obtain 512 pixels per line. Raw data was processed using SPIP 6.2.6 software (Image Metrology, Hørsholm, Denmark) to measure particle height, radius, and d_{ve} . Spreading ratios of individual particles were then calculated using the following equation which divides the particle radius (r) by particle height (h):⁵⁰

Equation 2.2. Spreading Ratio = $\frac{(r)}{(h)}$

T-tests were performed by comparing the mean spreading ratio of each sample to the mean spreading ratio of the sulfate seed aerosol. SOA-coated particles exposed to IEPOX were also statistically analyzed with respect to SOA-coated particles. Spreading ratios were considered to be statistically different for p values < 0.05.

Raman microspectroscopy was conducted using a Horiba LabRAM HR Evolution Raman Spectrometer (Horiba Scientific) equipped with a 50mW 532 nm Nd:YAG laser source, CCD detector and coupled to a confocal optical microscope (Olympus, 100x objective). Raman spectra were collected in the range 500-4000 cm^{-1} for 3 accumulations at 10 second acquisition times for each particle. A diffraction grating of 600 grove/mm with spectral resolution of 1.7 cm^{-1} was used.

2.3 Results and Discussion

Single particles were analyzed for phase and composition at three experimental points: 1) initial acidic ammonium sulfate seed particles with no SOA coating, 2) seed particles coated with α -pinene or toluene SOA, and 3) seed particles coated with SOA and exposed to IEPOX. Figure 2.1 is a schematic representing the changes in particle phase and morphology of single particles obtained at each step in the experiment. Acidic seed particles were expected to be homogeneous, characterized by a single aqueous phase with spherical morphology. Following the coating stage of each experiment by either α -pinene or toluene SOA, the particles are expected to experience phase separation resulting in a core-shell morphology consisting of a viscous organic coating and aqueous inorganic core. Modeling the properties of the α -pinene or toluene SOA organic layers predicts viscosities of 10^3 - 10^9 Pa s for α -pinene SOA^{70,146} and 10^2 - 10^7 Pa s for toluene SOA at

50% RH based on O:C measurements from an aerosol chemical speciation monitor (ACSM).^{129,146} This range of viscosities corresponds to semi-solid material^{147,148} with mixing times of 2.8 h for α -pinene coated SOA and < 1 h for toluene coated SOA at 50% RH for particles < 1 μm diameter.¹²⁹ Uptake of IEPOX vapor is expected to induce particle phase processing that changes the phase state of the inorganic core from aqueous to semi-solid following the diffusion of IEPOX through the SOA coating.¹⁵ The SOA coating inhibited some uptake into the particle, in comparison to an uncoated acidic aqueous particle.¹⁵ Predicted IEPOX diffusion times through the organic coating ranged from 10^1 - 10^4 seconds with a reduction in the reactive uptake coefficient (γ) of ~50% for α -pinene SOA compared to an uncoated acidic particle.¹⁵ Though IEPOX uptake was reduced, uptake was sufficient for significant acid-catalyzed particle-phase chemistry to occur. The continuing chemistry changed the core of the particles from aqueous to a viscous or semi-solid core. The phase transitions of the particle core are shown below using a combination of AFM, SEM-EDX, and Raman microscopy.

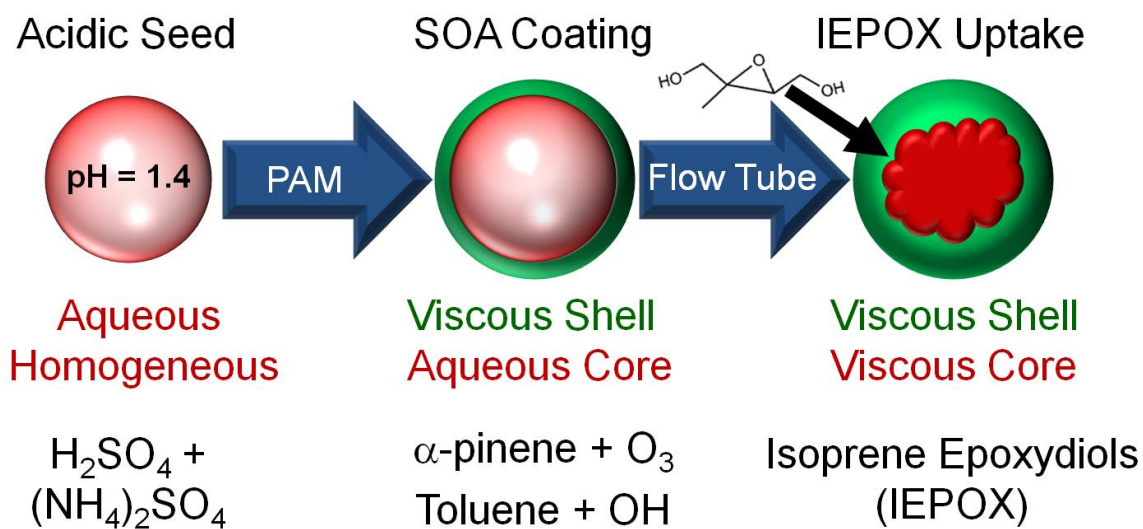


Figure 2.1. Schematic of experimental design to generate SOA particles. First, homogeneous seed particles were generated with an atomizer using solutions of ammonium sulfate and sulfuric acid to achieve an initial pH of 1.4. Next, seed particles were coated with α -pinene or toluene SOA in a Potential Aerosol Mass (PAM) reactor to achieve a coating thickness of ~10 nm before impaction onto substrates and spreading. SOA-coated seed particles were then exposed to gaseous isoprene epoxydiol (IEPOX) in a flow tube.

To demonstrate the changes in particle phase after coating and IEPOX uptake, AFM and SEM images of the three particle types are shown in Figure 2.2. Acidic ammonium sulfate seed particles were homogeneous in phase and composition with a circular morphology, indicative of a

spherical shape when suspended, before addition of SOA coatings (Figure 2.2a). The circular morphology indicates the particles were still liquid and above the efflorescence point,¹³¹ per the experimental design.¹⁵ After coating with SOA, the mixed sulfate-SOA particles exhibited core-shell morphology¹¹⁷ with a circular sulfate core and SOA shell (Figure 2.2b and 2.2d). These coated SOA particles were similar to ambient particles observed during the Southern Oxidant and Aerosol Study (SOAS) in the Southeastern United States during a period of high SOA production (Figure A.3).⁷⁸ Following IEPOX uptake, particles still exhibited phase separation, but changes to the core morphology were observed for both α -pinene SOA/sulfate particles and toluene SOA/sulfate particles (Figure 2.2c and 2.2e). Particle cores became non-circular with a variety of irregular shapes. The less viscous organic coating filled in along the irregular surface created by the viscous core to leave the overall particle morphology spherical, consistent with the outer spherical morphology observed before IEPOX uptake. These core morphology changes suggest IEPOX diffused through the organic shell and reacted with the inorganic core to form viscous IEPOX-derived organosulfates.^{40,42,107,108} AFM showed phase separation after SOA coating and core morphology changes after IEPOX uptake at ambient temperature and RH. SEM corroborated the phase and morphology observed by AFM. The images in Figure 2.2 show α -pinene and toluene SOA-coated inorganic sulfate particles generated at 50% RH. Additional samples generated at 30% RH show similar trends with respect to phase and morphology (Figures A.4 and A.5).

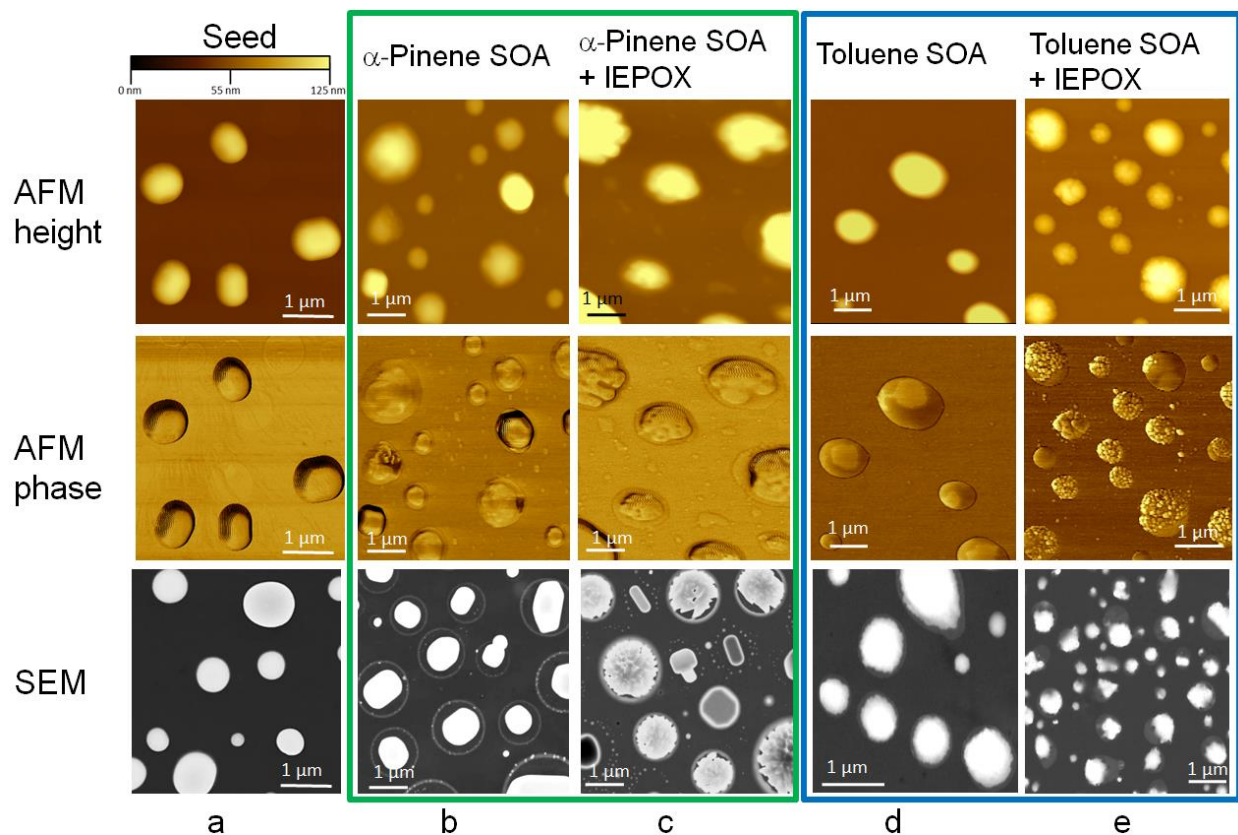


Figure 2.2. AFM and SEM images of SOA particles. Representative AFM height images (top row), AFM phase images (middle row), and SEM images (bottom row) of seed particles (a), α -pinene SOA/sulfate particles (b), α -pinene SOA/sulfate after IEPOX uptake (c), toluene SOA/sulfate (d), and toluene SOA/sulfate after IEPOX uptake (e). All particles were generated at 50% RH.

To quantify the observed changes in particle morphology and phase state shown in Figure 2.2, AFM height traces from 10 seed particles, SOA-coated particles, and SOA particles exposed to IEPOX were averaged (Figure 2.3c and 2.3d). Acidic ammonium sulfate seed particles had average heights of 70 ± 10 nm, which is in the range of spreading values observed for liquid particles impacted on silicon previously.⁵⁰ After coating with α -pinene- or toluene-derived SOA, particle heights increased, indicating particles spread less upon impact, as depicted in the cartoon in Figure 2.4a. α -Pinene coated core-shell particles were taller (150 ± 10 nm), on average, than toluene coated core-shell particles (110 ± 10 nm). The increase in particle height after impactation onto substrates is related to particle viscosity because more viscous particles will spread less and will therefore remain taller.^{50,149} The particle heights observed here are in agreement with predicted viscosities of the α -pinene (9.3×10^7 Pa s)^{70,146} and toluene (7.8×10^4 Pa s)^{129,146,147} SOA

at 50% RH in previous work.^{15,113,129,146,150} The results presented here are only applicable at 50% RH, as toluene SOA has higher viscosity than α -pinene SOA at lower RH.¹⁴⁶ After IEPOX uptake, both types of mixed sulfate-SOA particles were taller and larger in diameter than SOA coated particles. Average particle height of α -pinene SOA + acidic seed particles exposed to IEPOX were 170 ± 10 nm (20 nm taller than α -pinene SOA + acidic seed) and toluene SOA + acidic seed particles exposed to IEPOX were 130 ± 10 nm (20 nm taller than toluene SOA + acidic seed). Representative 3-dimensional AFM images show particle morphology at the three steps in the experiment (Figure 2.3a and 2.3b). With the high volume fraction of organic present, the core would not be expected to effloresce at the 30-40% RH values at which the particles were imaged.^{121,127} 3D images show particles coated with SOA become taller on the substrate than seed particles. Particle cores become taller after IEPOX uptake while the particle shell appeared flat on the substrate, suggesting the cores are becoming more viscous through IEPOX uptake and core chemistry modification.

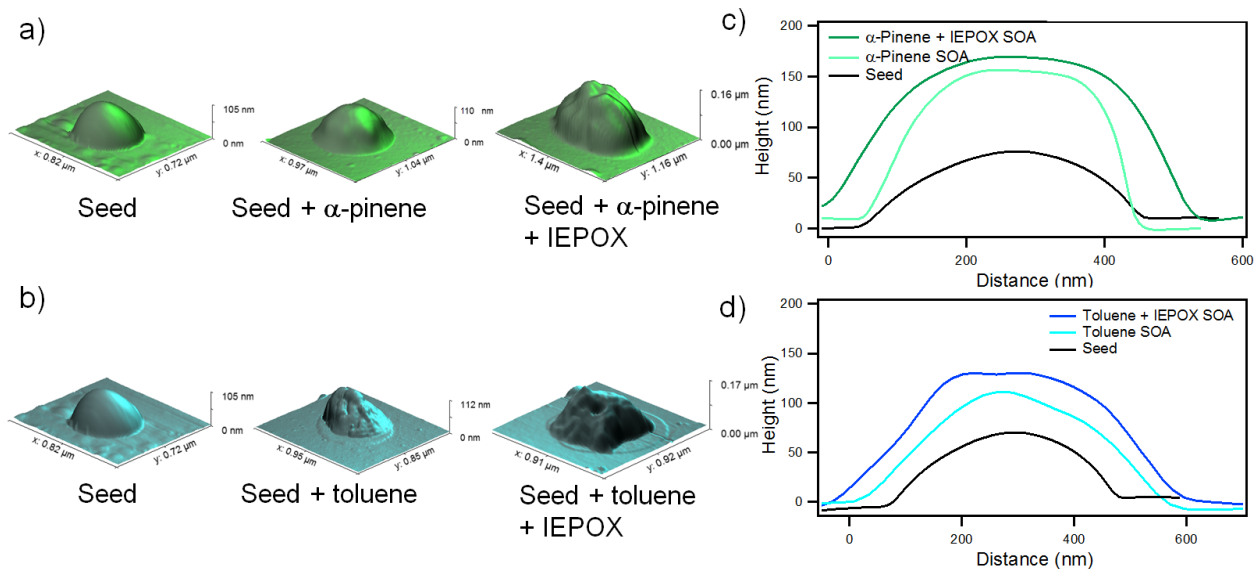


Figure 2.3. 3D AFM height images and height traces of SOA particles. Representative 3D AFM images of a) α -pinene SOA/sulfate and b) toluene SOA/sulfate particles before and after IEPOX uptake. 3D images show flat shells for phase-separated SOA and viscous, tall cores. Average height traces of 10 particles composed of c) α -pinene SOA/sulfate and d) toluene SOA/sulfate before and after IEPOX uptake.

To further investigate changes in particle viscosity and account for differences in particle diameter, spreading ratios were calculated for individual SOA + acidic seed particles using Eq. 2,

which compares particle radius to particle height. Particle spreading is used as an indirect measurement of particle viscosity, as more viscous particles will remain taller on the substrate by spreading less and will thus have a lower spreading ratio compared to more liquid-like particles of lower viscosity.⁵⁰ Average spreading ratios for ~30 particles per sample measured at 50% RH are shown in Figure 2.4. Seed particles had an average spreading ratio of 6.6 ± 0.7 . After coating with α -pinene or toluene SOA, the average spreading ratio decreased to 3.4 ± 0.2 for α -pinene SOA + acidic seed and 3.9 ± 0.4 for toluene SOA + acidic seed particles, and were thus more viscous, in agreement with predictions by Zhang et al.¹⁵ This shift to less spreading upon impaction for phase-separated particles agrees with qualitative observations in Bondy et al.⁵⁰ for liquid-liquid phase-separated polyethylene glycol and ammonium sulfate particles. After reactive uptake of IEPOX leading to altered core morphology, average spreading ratio further decreased to 2.6 ± 0.2 for α -pinene SOA and 3.4 ± 0.7 for toluene SOA particles. Spreading ratios of α -pinene SOA and seed particles generated at 30% RH are shown in Figure A.6 and follow similar trends of decreased spreading after coating with α -pinene oxidation products and further decrease in spreading following IEPOX uptake.

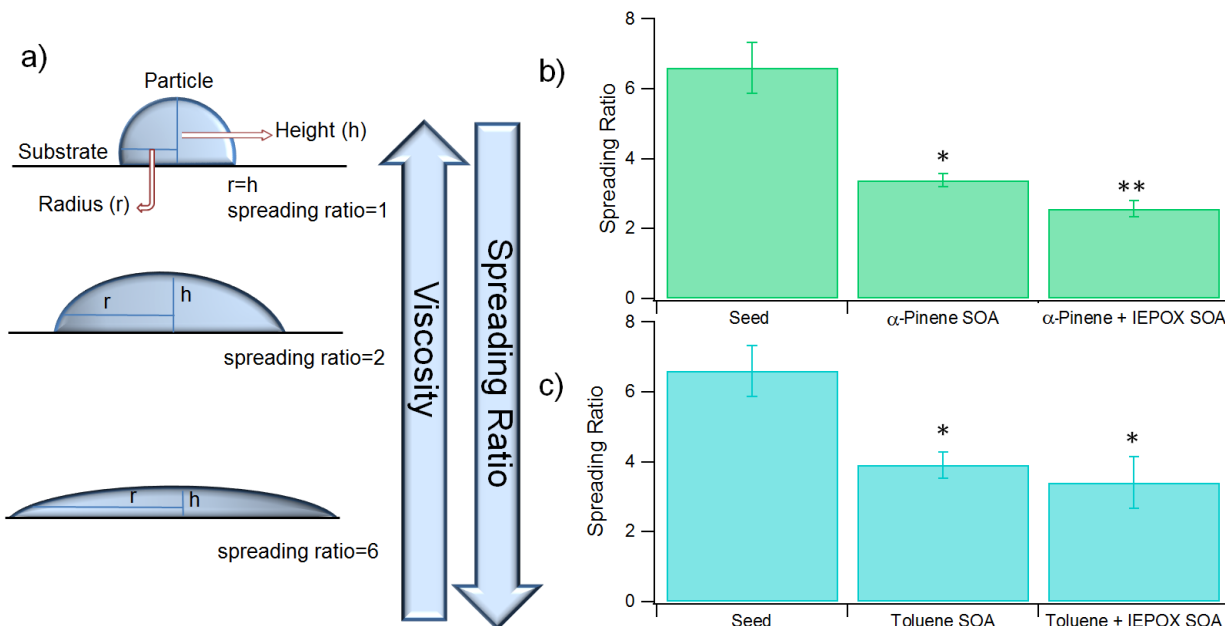


Figure 2.4. Spreading ratios of SOA particles. a) Diagrams depicting particle spreading onto substrates. Particle spreading is inversely related to particle viscosity. Bar charts show average spreading ratio of ~ 30 particles/sample for b) α -pinene SOA/sulfate particles before and after IEPOX uptake and c) toluene SOA/sulfate particles before and after IEPOX uptake. Error bars represent standard error. Single asterisks denote spreading ratios that are statistically different than seed aerosol ($p < 0.05$). The double asterisk denotes spreading ratio that are statistically different than spreading ratio before IEPOX uptake.

To examine the relationship between particle size, composition, and phase separation, particle phase state and d_{ve} of ~ 500 particles per sample were measured and plotted as histograms (Figure 2.5). We observed particles under 80 nm (d_{ve}) to have homogeneous composition for all SOA samples, similar to previously published work.^{73,117} Before IEPOX uptake, the smallest phase-separated particles were 160 ± 10 nm (d_{ve}) for α -pinene SOA + acidic seed (mode 570 ± 20 nm) and 127 ± 5 nm (d_{ve}) for toluene SOA + acidic seed (mode 342 ± 5 nm), and most often resulted in a core-shell morphology. This agrees with Fard et al.¹⁵¹ who stated the most likely morphology for phase-separated atmospheric particles greater than 100 nm was core-shell due to kinetically fast inorganic diffusion, preventing further nucleation after the first inclusion. After IEPOX uptake, the size of the smallest phase-separated particles decreased to 83 ± 3 nm (d_{ve}) for α -pinene SOA (mode 239 ± 3 nm) and 80 ± 3 nm (d_{ve}) for toluene SOA (mode 259 ± 3 nm). When the particle core contains less water and is a more viscous semi-solid, the organic layer becomes less miscible and can initiate a separate phase at smaller particle sizes.⁷¹ The transition regime, the size range where phase-separated and homogeneous particles both exist,⁷³ became wider for both

SOA types after IEPOX uptake, expanding from 150 – 230 nm to 80 – 180 nm after uptake of IEPOX onto α -pinene SOA + acidic seed and from 130 – 280 nm to 80 – 270 nm for toluene SOA + acidic seed after IEPOX uptake. The widening of the transition region, due to greater variability in core composition based on differences in reactive uptake of IEPOX,¹⁵ introduces increased difficulty for predicting phase for particles within these size ranges. Pie chart insets in Figure 2.5 show the percent of particles that were phase-separated versus homogeneous. After IEPOX uptake, the percent of phase-separated particles decreased from $67.9 \pm 0.6\%$ to $58.8 \pm 0.2\%$ for α -pinene SOA and from $68.2 \pm 0.2\%$ to $61.6 \pm 0.1\%$ for toluene SOA.

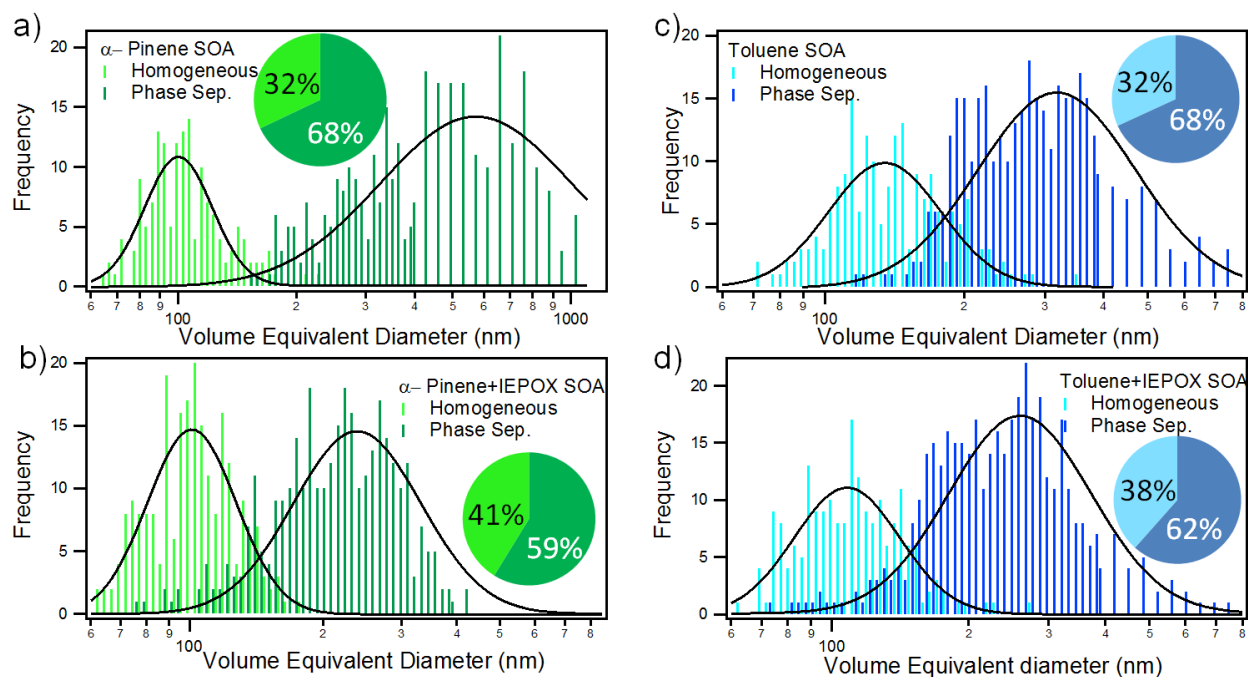


Figure 2.5. Plots depicting SOA morphology as a function of particle size. Histograms depicting size-dependent morphology behavior of a) α -pinene SOA/sulfate, b) α -pinene + IEPOX SOA/sulfate, c) toluene SOA/sulfate, and d) toluene + IEPOX SOA/sulfate particles. Lognormal fits show modes at 570 ± 20 nm for phase-separated α -pinene SOA/sulfate, 239 ± 3 nm for phase-separated α -pinene + IEPOX SOA/sulfate, 342 ± 5 nm for phase-separated toluene SOA/sulfate, and 259 ± 3 nm for phase-separated toluene SOA/sulfate. After determining modes, sticks representing phase-separated particles were offset by 25 nm to visualize differences between homogeneous and phase-separated traces. Pie charts represent the percent of particles that were phase-separated versus homogeneous.

Chemical composition plays a key role in determining viscosity, so both α -pinene and toluene SOA-containing particles were analyzed using SEM-EDX for elemental composition and Raman microspectroscopy for functional group composition. Raman spectra of acidic ammonium

sulfate seed particles do not show evidence for the presence of organic species (Figure A.7), as shown previously.^{33,35} Once seed particles were coated with α -pinene or toluene SOA, separate EDX and Raman spectra were taken for the particle core and shell. EDX showed particle cores contained sulfur and oxygen, indicative of sulfate, while particle shells contained primarily carbon and oxygen, indicative of α -pinene or toluene SOA (Figure 2.6). Sulfur is clearly discernable and located primarily in the core of particles. Raman spectra show the broad $\nu(\text{N-H})$ region around 3200 cm^{-1} indicating ammonium and a mode for $\nu_s(\text{SO}_4^{2-})$ was observed at 976 cm^{-1} in the particle core before IEPOX uptake (Figure 2.7).^{36,45,152-155} Peaks in the $\nu(\text{C-H})$ region between $2800\text{-}3000\text{ cm}^{-1}$ indicate organic materials in the shell of α -pinene and toluene SOA-coated acidic seed particles. Specifically, methyl $\nu(\text{CH}_3)$ and methylene $\nu(\text{CH}_2)$ symmetric and anti-symmetric stretches were detected, along with modes in the organic fingerprint region which are listed in the Supporting Information (Table S1). Differences in composition between particle core and shell for both SOA types shows that the coating of α -pinene or toluene SOA creates chemically distinct phases with a primarily inorganic core and organic shell, instead of homogeneously mixed particles. After IEPOX uptake, EDX spectra show particle cores contained carbon for both types of SOA, suggesting IEPOX reaction forming organic species, possibly organosulfur compounds (i.e., organosulfates and oligomers thereof), within the particle core. After IEPOX uptake, SOA cores contained methyl $\nu(\text{CH}_3)$ and methylene $\nu(\text{CH}_2)$ symmetric and anti-symmetric stretches in the Raman spectra. Particle cores also showed signs of organosulfate formation with peaks around 1060 cm^{-1} in the Raman spectra, indicative of $\nu_s(\text{RO-SO}_3)$.⁴² Peaks indicative of organosulfates were not observed in the shell for either α -pinene and toluene SOA after IEPOX uptake indicating that the shells did not mix with the core as it solidified. Future work will investigate conditions for organosulfate formation in various types of SOA across a range of RH conditions.^{39,40,98,107,110,156,157}

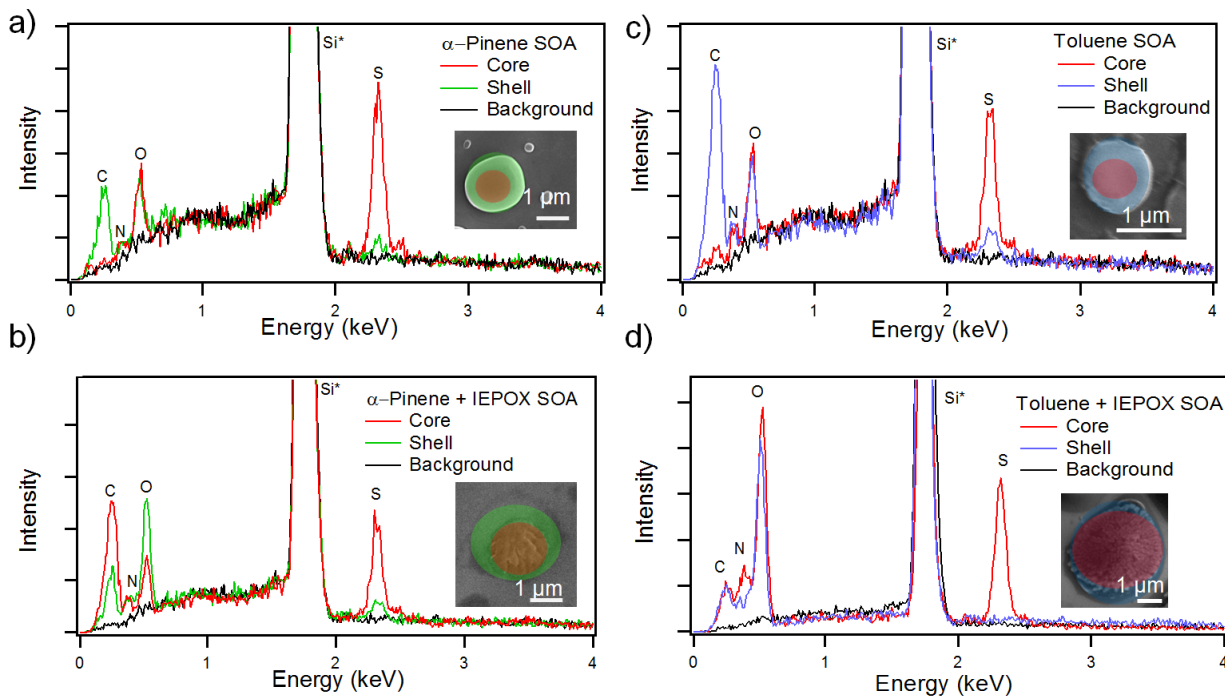


Figure 2.6. SEM images and EDX spectra of SOA particles. Representative SEM images and EDX spectra of a) α -pinene SOA/sulfate particles, b) α -pinene SOA/sulfate + IEPOX particles, c) toluene SOA/sulfate particles, and d) toluene SOA/sulfate + IEPOX particles showing differences between core and shell composition. Elements with asterisk denote contribution from substrate. Images were colored to easily identify phase-separated morphology. Unedited images are shown in Figure A.8.

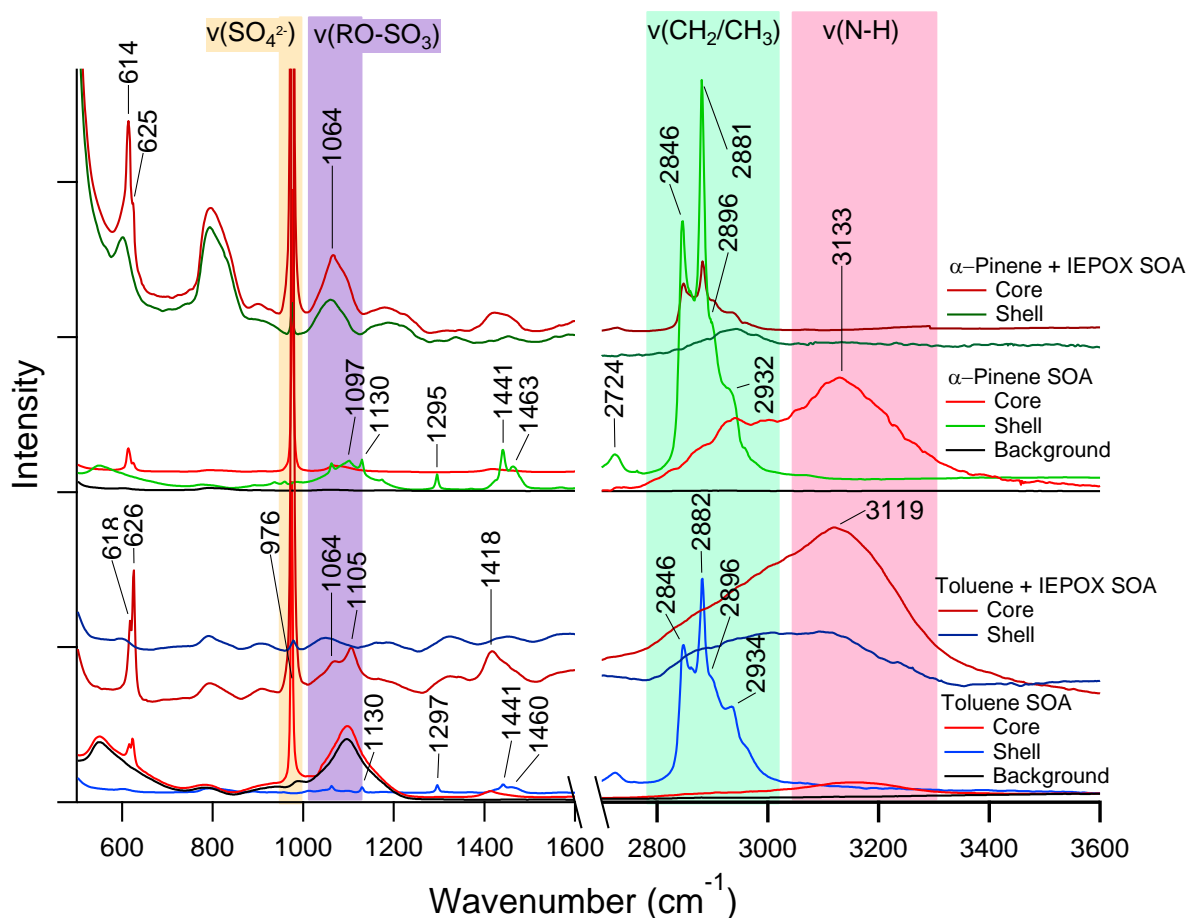


Figure 2.7. Raman spectra of SOA particles. Representative Raman spectra of α -pinene SOA/sulfate particles before and after IEPOX reactive uptake (top) and toluene SOA/sulfate particles before and after IEPOX reactive uptake (bottom) showing differences between core and shell composition.

2.4 Conclusions

The existence of liquid-liquid phase-separated particles in the ambient atmosphere and their role in modifying reactive uptake has important consequences for SOA formation and PM concentrations. Recent flow tube studies have shown that IEPOX uptake can be reduced by liquid-liquid phase separations involving coatings of α -pinene SOA around an acidic aqueous core rich in sulfate.¹⁵ This is true even with a pH of 1.5 for the core, typical of pH values for the southeast United States (0-2).^{119,158} Chamber studies have shown that inorganic sulfate can rapidly be converted into organosulfates after reaction with IEPOX,¹⁵⁹ which are quite viscous. The atmospheric implications of the results from this study are that the core of phase-separated submicron particles can be converted from aqueous-inorganic to viscous organics, such as IEPOX-

derived organosulfates, which can further inhibit SOA formation. This viscous core formation occurs within acidic inorganic particles coated with both α -pinene (biogenic) and toluene (anthropogenic) SOA. That the increased core viscosity occurs on the timescale of flowtube experiments (< 1 min) indicates that the α -pinene and toluene coatings were not sufficiently viscous at 50% RH to fully inhibit IEPOX uptake and the subsequent rapid formation of viscous organosulfates in the core. The increase in core viscosity and thus diffusion and mixing timescales likely limits additional reactive uptake of IEPOX, since acidic particles ($\text{pH} = 1.5$) have been shown to form organosulfates that almost completely shut off IEPOX uptake within 40 hours of simulated atmospheric aging.¹⁵⁹ The prevalence of phase separated and viscous particles may impact atmospheric model predictions of IEPOX-derived SOA, as many of these models do not consider the kinetic limitations of phase-separated particles on multiphase chemical processes yielding SOA.¹⁶⁰ Recent modeling has shown that α -pinene SOA coatings around acidic cores can decrease SOA formation by 33%, even at 55-80% RH,¹⁶¹ but the impact of transforming an aqueous acidic core to a diffusion limited viscous core could have an even larger effect, but has not yet been evaluated. The increased viscosity and morphologies observed could also impact the CCN and INP properties of these aerosols.^{66,68,162} Therefore, further studies are needed to improve understanding of phase separation and viscosity in flowtube, chamber, and ambient particles of different and more complex compositions and at different atmospheric conditions.

Chapter 3. Lake Spray Aerosol Incorporated into Great Lakes Clouds

Adapted with permission from Olson, N. E., May, N. W., Kirpes, R. M., Watson, A. E., Hajny, K. D., Slade, J. H., Shepson, P. B., Stirm, B. H., Pratt, K. A., and Ault, A. P.: Lake Spray Aerosol Incorporated into Great Lakes Clouds, *ACS Earth Space Chem.*, 3, 12, 2765-2774, 2019. <https://doi.org/10.1021/acsearthspacechem.9b00258> Copyright 2019 American Chemical Society.

3.1 Introduction

In aquatic environments, breaking waves entrain air beneath the water's surface and form bubbles that then burst at the surface to eject droplets into the atmosphere. Sea spray aerosol (SSA) produced by bubble bursting in marine environments has been more extensively studied than lake spray aerosol (LSA) production in freshwater environments.^{5,163,164} SSA production is generally modeled as a function of wind speed, with speeds greater than 4 m s^{-1} inducing wave-breaking particle production.¹⁶³ Similarly, airborne lake-derived particles have been observed during aircraft measurements over the Laurentian Great Lakes during the presence of whitecaps at wind speeds above 3.5 m s^{-1} .⁴ The Laurentian Great Lakes, have annual mean wind speeds $> 6.6 \text{ m s}^{-1}$ (other than Lake Ontario)¹⁶⁵, indicating the frequent presence of wind speeds necessary to produce breaking waves and white caps.^{166,167} LSA observed from Lake Michigan has been chemically characterized for samples collected at the shore in a ground based study⁵ and after transport inland ($> 25 \text{ km}$).²⁷ LSA is composed primarily of calcium carbonate, other inorganic ions, organic species, and biological material.^{5,27,168} A regional modeling study suggested that particles produced from wave breaking over the Great Lakes could increase surface level aerosol number concentrations by $\sim 20\%$ over the remote northern Great Lakes and by $\sim 5\%$ over other parts of the Great Lakes region.¹⁶⁷ However, the model utilized a parameterization for SSA production and only considered ultrafine ($< 100 \text{ nm}$) particle production due to limited knowledge, at the time, of LSA production.¹⁶⁷ More recent laboratory¹⁶⁴ and field work⁴ has identified both ultrafine (80 nm) and accumulation (200 nm) modes for nascent LSA, indicating contributions to aerosol concentrations at diameters important for cloud formation.⁹ However, models have not yet evaluated the impact of LSA on regional cloud formation and climate due to a lack of observations.

Moisture and heat released from the Great Lakes impact clouds and precipitation regionally via the lake effect.¹⁶⁹ The lake effect is a meteorological phenomenon resulting from the upward flux of water vapor and subsequent precipitation when air masses transition from water to land, forming clouds and leading to precipitation regionally.¹⁶⁹ It is important to determine sources of aerosols that may act as cloud condensation nuclei (CCN) and ice nucleating particles (INPs) over the Great Lakes where the upward flux is adding extra moisture, particularly as many areas in the Great Lakes region are relatively pristine with low concentrations of particles ($\sim 100 \text{ cm}^{-3}$).¹⁶⁷ Further, decreased winter ice extent¹⁷⁰ and increased annual wind speeds¹⁷¹ associated with warming of the Great Lakes are predicted to increase emissions of LSA in the future. Thus, given the importance of lake-effect meteorology regionally,¹⁶⁹ it is essential to quantify the extent that LSA are lofted to and entrained in clouds.

Both CCN and INP activation are dependent on individual particle size and composition.^{9,172-184} Previous studies in marine environments have shown that SSA can act as both CCN or INPs,^{9,175,185-192} with efficiencies varying with seawater composition.^{186,193,194} Laboratory studies suggest increased INP efficiency from freshwater samples containing biological material.¹⁹⁵⁻¹⁹⁷ Borduas-Dedekind et al.¹⁹⁸ discovered increased CCN activity for freshwater containing organic matter, suggesting the incorporation of organics into LSA¹⁶⁸ likely increases the CCN ability of these particles. Notably, recent laboratory studies have shown freshwater INP concentrations that are orders of magnitude greater than INPs produced from seawater.^{197,199} However, to our knowledge, the CCN and INP efficiency of LSA have not been characterized. The identification of droplets in Great Lakes regional clouds^{200,201} containing primarily calcium, the highest concentration cation in Great Lakes freshwater,²⁰² suggests that LSA likely participates in cloud formation though the source wasn't identified at the time. Laboratory studies have shown that particles composed of CaCO_3 , the primary inorganic component of LSA,⁵ undergo multiphase reactions with HNO_3 and N_2O_5 , thereby increasing the hygroscopicity and CCN efficiencies of these particles.^{203,204} LSA particles transported inland have been shown to undergo heterogeneous processing leading to the formation of $\text{Ca}(\text{NO}_3)_2$,²⁷ analogous to aging of SSA.²⁰⁵⁻²⁰⁷ It has also been shown that clouds over the Great Lakes contain freshwater bacteria.²⁰⁸ Therefore, the incorporation of biological material into LSA^{168,209} may increase the CCN and INP efficiencies of LSA. Taken together, the composition of individual particles emitted from the Great Lakes and

their modification after emission is critical to understanding the overall aerosol mixing state in the region, a key attribute connected to CCN and INP concentrations and impacts.^{13,67,210}

In this study, ambient particles and cloud water samples were collected by aircraft over northern Lake Michigan during high wind and wave activity on July 12, 2016. In addition, surface freshwater samples collected from Lake Michigan at the time of aircraft sampling were used to generate LSA in the laboratory. Individual ambient and laboratory-generated LSA particles were analyzed by scanning electron microscopy with energy dispersive X-ray spectroscopy (SEM-EDX) to determine size-resolved chemical composition and morphology. Residual particles from aerosolized cloud water were also analyzed by SEM-EDX to compare with ambient and laboratory-generated LSA particle composition. Particle size, morphology, and inorganic elemental mole ratios provide evidence that LSA emitted from the Great Lakes are incorporated into clouds, indicating that LSA is a potential source of CCN and INPs in regions with large bodies of freshwater.

3.2 Methods

3.2.1 Aircraft Sampling

Atmospheric aerosol and cloudwater samples were collected during a flight occurring on July 12, 2016 using a Beechcraft Duchess twin-engine aircraft (Purdue University Airborne Laboratory for Atmospheric Research).^{4,201,211} Wind speed and atmospheric pressure were measured during aircraft sampling using a Best Air Turbulence (BAT) probe to characterize the atmospheric boundary layer.²¹² Potential temperature was calculated following previously established methods.^{213,214} A flight-modified Picarro cavity ring-down spectrometer (model number G2301-f) measured real-time concentrations of water vapor and CH₄.²¹⁵⁻²¹⁷ Size-resolved aerosol particle number concentrations were measured using an optical particle counter (model 1.109, Grimm Aerosol Technik GmbH) that quantified particles from 0.20 – 32 μm.²¹⁸ Grimm particle size data was corrected for inlet transmission efficiency following the method described in Peterson et al.²¹⁸

Atmospheric particles were collected using a three stage modified Davis Rotating Uniform Size-Cut Monitor (DRUM) impactor (model DA400, DRUMAir, LLC). Particle samples in three size ranges (stage A: $d_a = 1.2\text{--}2.5$ μm, stage B: $d_a = 0.34\text{--}1.2$ μm, and stage C: $d_a = 0.07\text{--}0.34$ μm) were collected onto aluminum foil. Aerosol particle samples were stored in the dark at room

temperature.²¹⁹ A modified Mohnen slotted rod cloud water collector extended out of the top of the aircraft for cloud water collection.²²⁰ Cloud droplets were impacted onto slotted Teflon rods, which are characterized by a 50% cutoff d_a of $\sim 5.5 \mu\text{m}$,²⁰¹ and collected into glass vials (sample volume ranging from 5 – 15 mL each). Cloudwater samples were frozen upon collection and stored at $-20 \text{ }^\circ\text{C}$ until analysis. Prior work has shown that freezing aquatic samples creates minimal changes to the size and composition of aerosol particles generated from or insoluble residues within a thawed sample.^{21,168}

Atmospheric particle sampling was conducted from 14:51 – 15:51 EDT on July 12, 2016 at 600 m above ground level (AGL) over northern Lake Michigan in the area of Manistique Bay between Thompson, MI (45.866, -86.406) and Seul Choix Point, MI (45.921, -85.912, Figure 3.1). The cloud layer present on July 12 was near the surface (cloud height at 300 m AGL with thickness of approximately 70 m) such that the aircraft could not safely fly below, and as a result the particles sampled that day were collected above the cloud layer. After particle sampling, two cloud water samples (16:20 – 16:50 EDT and 17:00 – 17:30 EDT) were collected over the northern portion of Lake Michigan at 300 m AGL (Figure 3.1, Figure B.1). Convective available potential energy (CAPE) was obtained from the National Weather Service station 72634 in Gaylord, Michigan, a location 100 km southeast from sampling and under cloud coverage at the time of measurement (Figure 3.2). CAPE was measured from a sounding (<http://weather.uwyo.edu/upperair/sounding.html>) recorded at 12:00 UTC (08:00 EDT). The CAPE value was 556.8 J/kg, indicating a slightly unstable atmosphere (CAPE range 500 – 1000 J/kg), where the sampled particles and clouds were likely influenced by the atmospheric boundary layer.^{221,222} Wind speed and wave height data were obtained from National Oceanic and Atmospheric Administration Great Lakes Environmental Research Laboratory (NOAA GLERL) buoy 45022 (45.405, -85.086) located approximately 40 km southeast from sampling.

3.2.2 Laboratory Aerosol Generation

Surface freshwater was collected from Lake Michigan at Brevort, Michigan (46.018, -85.041) on July 12, 2016. The freshwater sampling location corresponds to the area of Lake Michigan over which aircraft sampling was conducted. After collection, the freshwater samples were frozen ($-20 \text{ }^\circ\text{C}$) and thawed prior to aerosol generation and analysis by ion chromatography. Freshwater samples were filtered with a $0.22 \mu\text{m}$ filter (Celltreat Scientific Products) prior to

triplicate measurements of sodium, potassium, magnesium, calcium, chloride, and sulfate concentrations using Thermo Dionex ICS-1100 (cation) and ICS-2100 (anion) ion chromatography columns (Thermo Fisher Scientific, Figure B.2). Freshwater samples were then used to generate aerosols in a laboratory LSA generator, described in detail by May et al.¹⁶⁴ Briefly, the LSA generator circulates 4 L of freshwater sample at 2 L min⁻¹ via a diaphragm pump into four plunging jets, which create bubbles that burst at the freshwater sample surface to generate aerosol particles. During all experiments the LSA generator was kept at room temperature (23 ± 1 °C) with a relative humidity (RH) of 85%. Prior to particle generation, particle-free air (HEPA capsule filter, Pall) was cycled through the LSA generator to ensure background particle concentrations were minimal (< 20 particles cm⁻³), in comparison to the average total particle concentration generated from the freshwater samples (~ 500 particles cm⁻³), as measured by a condensation particle counter (CPC; TSI Inc., model 3775). Generated LSA passed through two silica gel diffusion dryers to achieve an RH of ~ 15% before measurement, a standard established for SSA.¹⁶³ The aerosol number size distributions (20 – 800 nm, Figure B.3) were measured by a scanning mobility particle sizer (SMPS), consisting of a differential mobility analyzer (DMA; TSI Inc., model 3082) and a CPC (TSI Inc., model 3775). Particle diameters were converted to aerodynamic diameter (d_a)^{145,223} after analysis using a spherical shape factor based on SEM image analysis and a particle density of 2.71 g cm⁻³ representing CaCO₃.²⁷ Laboratory-generated LSA were collected for microscopy analysis using a three stage microanalysis particle sampler (MPS-3, California Measurements Inc.). Cloud water was nebulized using a glass nebulizer (Meinhard, Type A, operated at 1 mL/min) before impaction of insoluble residue particles using the MPS-3.²²⁴ Particles were impacted onto carbon-type-b Formvar coated copper transmission electron microscopy (TEM) grids (Ted Pella Inc.) for electron microscopy analysis. Samples impacted onto MPS-3 stages 2 and 3 (d_a of 400 – 2800 nm and 70 – 400 nm, respectively) were analyzed.

3.2.3 Microscopy of Ambient and Laboratory-Generated Particles

Particles collected on stages A, B, and C (0.07 – 2.5 µm) of the DRUM impactor during ambient sampling and on stages 2 and 3 (0.07 – 2.8 µm) of the MPS-3 during laboratory experiments were analyzed by manual SEM-EDX and computer controlled SEM-EDX (CCSEM-EDX). SEM analysis was conducted using a FEI Helios 650 Nanolab Dualbeam electron microscope operating at an accelerating voltage of 20.0 kV and a current of 0.40 nA. EDX spectra

were acquired for 20 seconds using GENESIS EDAX software version 5.10 (EDAX Inc., Mahwah, NJ). The elements detected by EDX were C, N, O, Na, Mg, Si, P, S, Cl, K, Ca, and Fe. Due to the overwhelming signal from the Al foil substrate used for ambient sampling, Al was excluded from the CCSEM-EDX measurements. A total of 3264 ambient particles and 1993 nebulized cloud water residual particles were chemically analyzed by CCSEM-EDX. K-means clustering was applied in MATLAB (Mathworks, Inc., version R2015a) to sort particles into 10 clusters based on the relative atomic percentages of elements from the CCSEM-EDX spectra.^{29,225} Particle clusters present in each sample were determined by mathematical similarity of spectra to limit human bias during sorting. In K-means clustering, the fraction of total error, defined as total distance of particle spectra to their cluster centroid divided by the distance of all particles to the centroid of one cluster, is used to determine the optimal number of clusters to characterize the data set.^{30-32,226,227} Particle types were identified based on the similarity of elemental composition to EDX spectra reported in single particle measurements from previous studies,^{5,21,27,78,154,168,228,229} and clusters representing the same particle types were combined.

3.3 Results and Discussion

On July 12, 2016, elevated wave heights resulting from high wind speeds were observed on Lake Michigan. During the aircraft particle sampling period, wave heights peaked at 1.4 m, and wind speeds peaked at 9.4 m s^{-1} over northern Lake Michigan (Figure 3.1a). Wave height mapping indicated wave heights over 1 m were present over a large area of northern Lake Michigan (Figure 3.1b), and white capped waves were observed visually on the surface of Lake Michigan during aircraft sampling. NOAA HYSPLIT 48 h backward air mass trajectories (Figure 3.1c) and heights (Figure 3.1d) show that the air mass measured on July 12 traveled across Lake Michigan from the southeast prior to reaching the aircraft sampling area, passing over areas with significant sources of anthropogenic pollutants near Chicago, Illinois and Gary, Indiana.^{230,231}

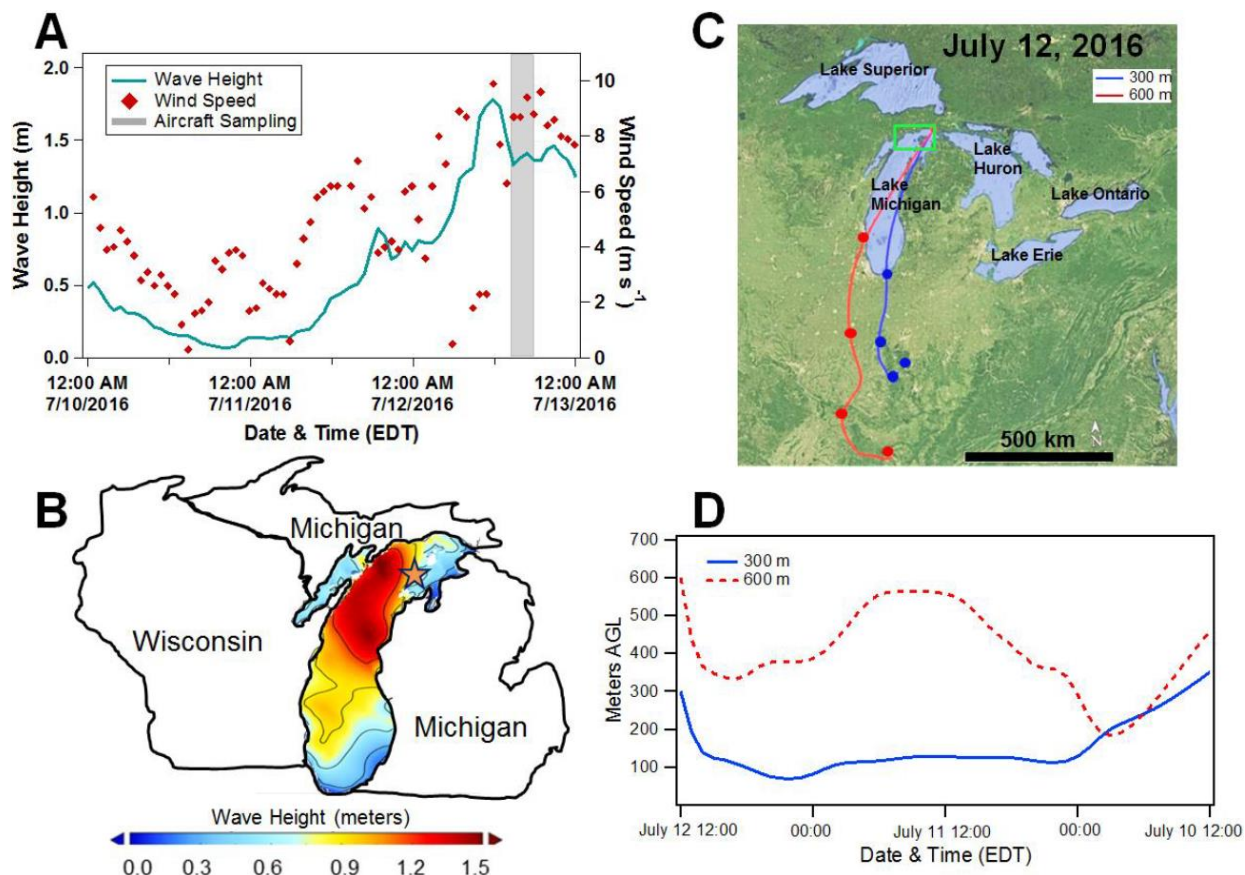


Figure 3.1. Map depicting area of aircraft sampling with wind speed and wave height data. (A) Wave height and wind speed during ambient sampling. Data were obtained from NOAA GLERL buoy 45022, represented by a star in part B. Grey shaded areas show periods of aircraft sampling. (B) Wave height maps for July 12, 2016 12:00 EDT during aircraft sampling over Lake Michigan. (C) 48 Hour HYSPLIT back trajectory July 12, 2016 13:00 EDT at starting heights of 300 and 600 m AGL that correspond to heights of cloud water and aerosol sampling, respectively. Circles on traces mark the location of air masses every 12 hours. The area of aircraft sampling is displayed in a green box on the map. Map data adapted from Google. Copyright 2016. (D) 48 hour height profiles of air masses sampled during aircraft sampling.

A NASA MODIS image shows stratocumulus clouds present over much of northern Lake Michigan on July 12 (Figure 3.2a). Boundary layer height and depth were determined from vertical profile measurements of potential temperature, water vapor, and CH_4 during aircraft ascent (Figure 3.2b). The top of the boundary layer, occurring at 1050 m, is indicated by the largest rate of change in water vapor.^{213,214} This confirms aircraft particle (600 m) and cloud water (300 m) sampling occurred within the boundary layer.

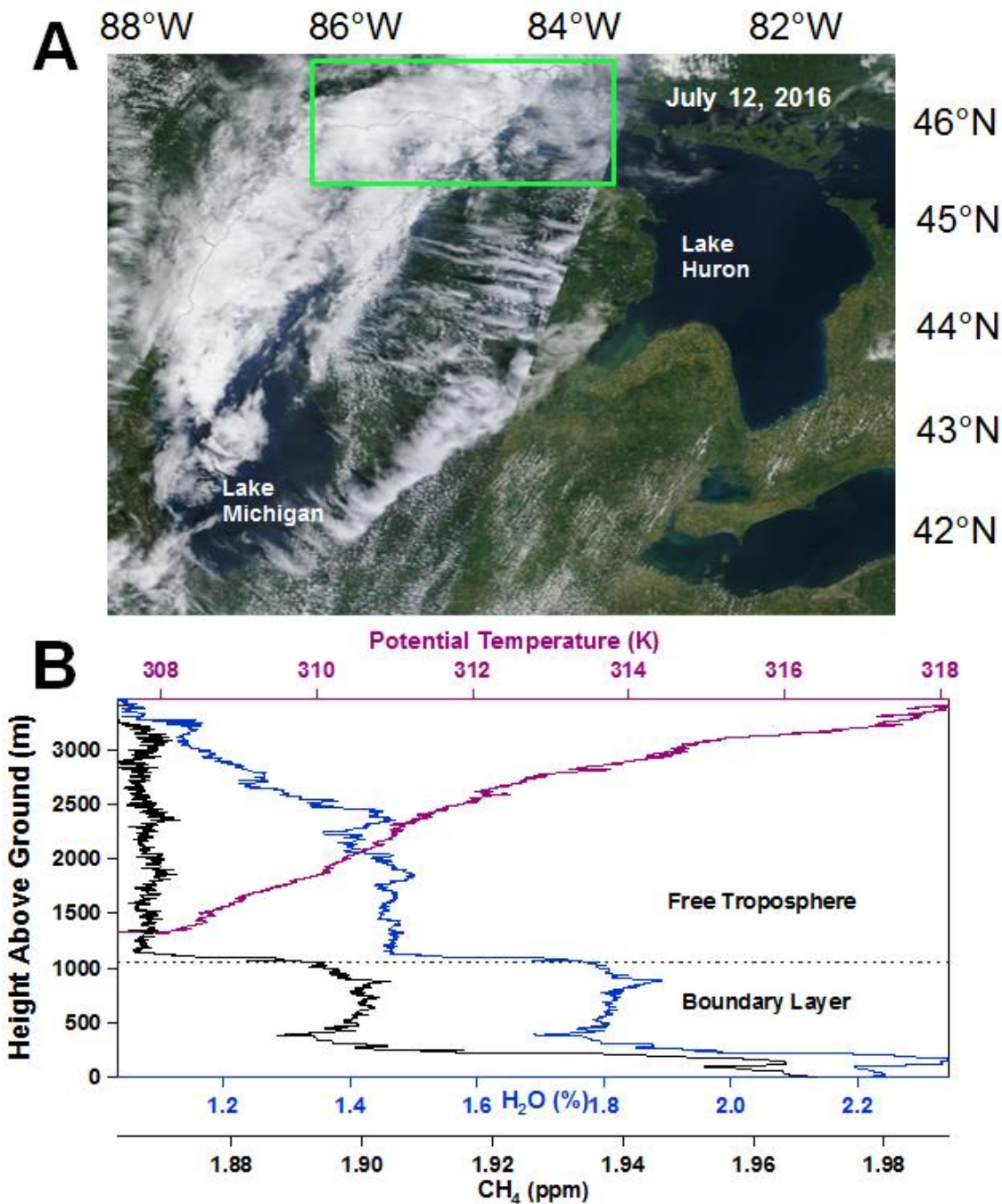


Figure 3.2. Map depicting cloud coverage and vertical profile measurements during aircraft sampling. (A) NASA MODIS image shows cloud coverage over Lake Michigan on July 12, 2016. Green box indicates the area of aircraft sampling. (B) Vertical profiles of potential temperature and water vapor obtained from 16:36-17:05 during July 12 sampling.

Ambient and laboratory-generated particles were examined using SEM-EDX to identify LSA particles based on elemental composition and morphology.^{5,27} Representative images and EDX spectra for both ambient and laboratory-generated LSA particles show strong Ca, C, and O

peaks (indicative of CaCO_3 and organics), minor Na and Mg peaks, and an amorphous solid morphology after drying on the substrate (Figure 3.3).⁵ This Ca-dominant elemental composition is consistent with Great Lakes freshwater composition²⁰² (Figure B.2) and previous measurements of Lake Michigan LSA chemical composition and morphology, both in the ambient atmosphere^{5,27} and laboratory.^{164,168} The ambient LSA is not believed to be CaCO_3 mineral dust, as soil from this region is rich in Fe and Al and regional sand is composed primarily of quartz or amorphous silica (Si, O).^{5,232} SEM images and EDX spectra of residual particles generated from ambient cloud water also show similar morphology and composition to ambient and laboratory-generated LSA (Figure 3.3c), suggesting that LSA particles emitted from Lake Michigan become incorporated into clouds above Lake Michigan.

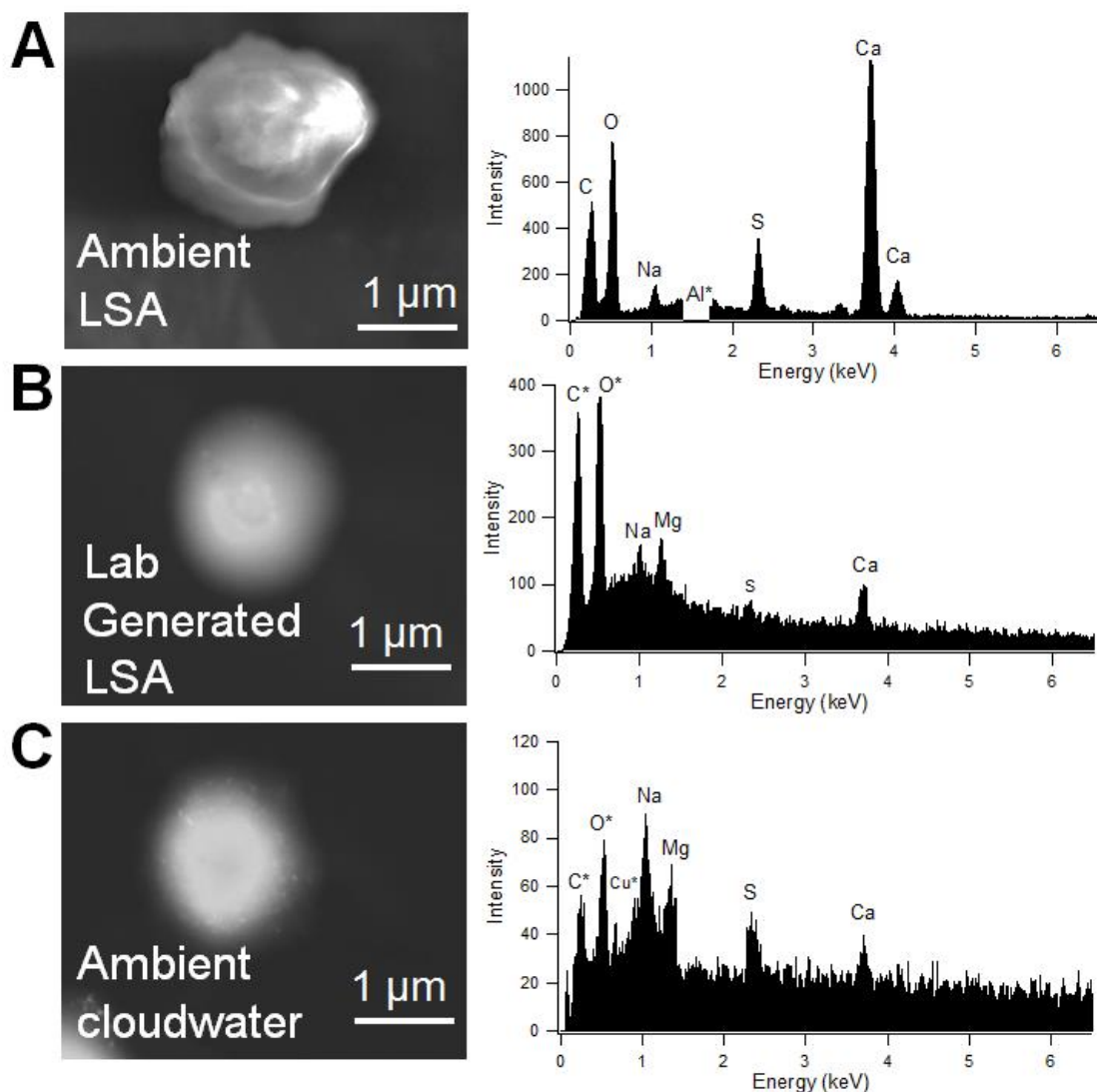


Figure 3.3. SEM images and EDX spectra of ambient and laboratory-generated LSA. Representative SEM images (left) and EDX spectra (right) of individual particles, with asterisks denoting elemental contribution from substrate. (A) Ambient LSA particle collected on aluminum foil during aircraft sampling on July 12, 2016. Aluminum background was removed from the spectrum and is noted by an asterisk. (B) LSA particle generated in the laboratory from the Lake Michigan freshwater sample and collected on a TEM grid. (C) Cloud water residual particle collected on a TEM grid.

Elemental mole ratios were calculated for ambient LSA, laboratory-generated LSA, and cloud water residual particles using atomic weight percentages of each element measured by CCSEM-EDX (Figure 3.4). Elemental mole ratios for Lake Michigan freshwater were obtained from ion concentrations reported by Chapra et al.²⁰² The Ca/Na mole ratios of the cloud water

residual particles classified as LSA (3.5 ± 0.8) and ambient LSA (3.1 ± 0.1) resembled those of the laboratory-generated LSA (3.8 ± 0.3), Lake Michigan freshwater (3.3), and ambient LSA previously reported by May et al (3 ± 3).²⁷ Similarly, the Mg/Na mole ratios of the cloud water residual particles (2.2 ± 0.2) and ambient LSA (1.9 ± 0.3) were also consistent with those of laboratory-generated LSA (1.4 ± 0.2), Lake Michigan freshwater (1.7), and ambient LSA previously reported by May et al (1.8 ± 0.5).²⁷ Both Ca/Na and Mg/Na ratios are significantly different from seawater (0.02 and 0.1 for Ca/Na and Mg/Na, respectively),^{206,233,234} emphasizing the freshwater origin of these particles. The variability measured for the cloud water residual particles is larger than for other particle classes due to potential influence from multiple particle types present in the cloud water prior to and during the nebulization process.^{224,235} Ambient LSA collected above the cloud layer and residual particles generated from the collected cloud water featured higher S/Ca mole ratios (1.0 ± 0.2 and 0.7 ± 0.2 , respectively) compared to laboratory-generated LSA (0.4 ± 0.1) and Lake Michigan freshwater (0.28). These observations suggest the collected LSA had likely undergone either cloud processing, with sulfate formation following partitioning of gaseous SO₂ into cloud drops and oxidation, or heterogeneous reactions prior to droplet formation.²³⁶

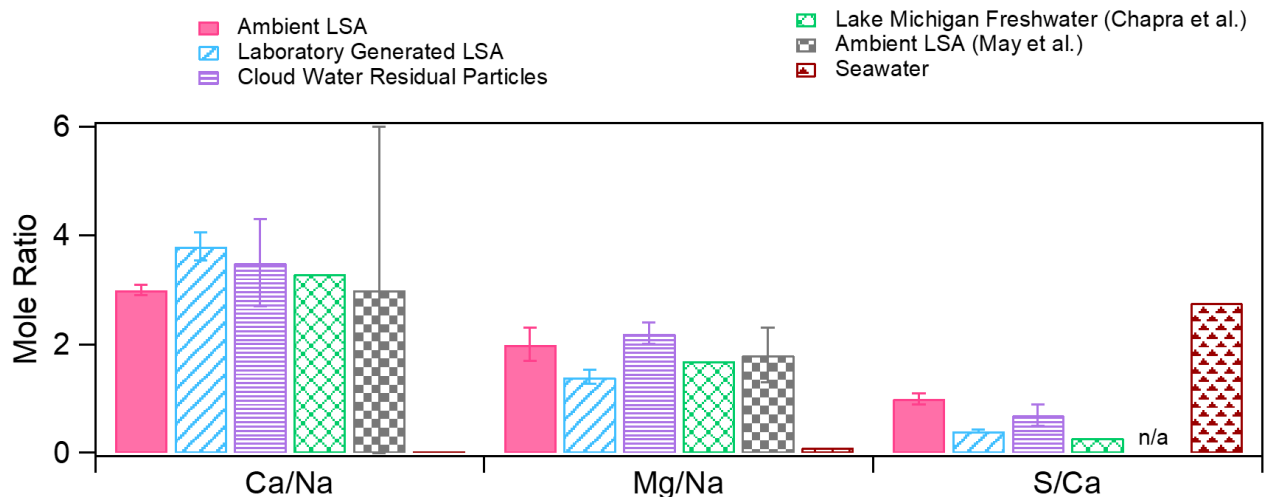


Figure 3.4. Elemental mole ratios of LSA, freshwater, and seawater. Comparison of ambient LSA, laboratory-generated LSA, cloud water residual LSA particles, Lake Michigan freshwater, and seawater elemental mole ratios. Ambient LSA, cloudwater residual particles, and laboratory-generated LSA mole ratios were calculated from the atomic weight percentages of each element measured by CCSEM-EDX. Error bars represent 95% confidence intervals. Only cloud water residual particles that contained the elements Ca, Na, and Mg were classified as LSA and included here. Seawater and Lake Michigan freshwater mole ratios were calculated from ion concentrations reported by Pilson et al.²³³ and Chapra et al.,²⁰² respectively. Comparison to ambient LSA mole ratios provided by May et al.²⁷ are included.

In addition to LSA, CCSEM-EDX identified two additional ambient particle types: secondary organic aerosol (SOA)/biomass burning and dust. Example SEM images and EDX spectra of these particles are shown in Figure B.4. LSA was differentiated from SOA and biomass burning particles (defined by combinations of C, O, N, and S)⁷⁸ by the presence of Ca. Both SOA and biomass burning are abundant in this region^{43,76,237} and differentiating them using only SEM-EDX is challenging because both particle types contain the elements C, O, N, and S and have similar morphology.⁷⁸ Biomass burning is commonly differentiated from SOA by the presence of K, which is often not clearly detected by EDX for biomass burning particles with significant SOA coatings.^{78,230} Organics from SOA or biomass burning can be particularly challenging to distinguish in resuspended rain, snow, and cloud water samples.^{224,235,238-240} Therefore, since their distinction was not central to the findings of this study, the SOA and biomass burning particle types are combined here.

The CCSEM-EDX data enabled determination of the size-resolved contributions of the observed particle types. Ambient LSA particles were primarily observed in the submicron size range (Figure 3.5a). LSA particles were the most abundant particle type at the smallest sizes

measured (0.17 – 0.23 μm), where they composed 65% of the observed particles, by number, in this size range. This is supported by the number mode of laboratory-generated LSA occurring at 0.20 μm (measured by SMPS operating in the 0.020 – 0.80 μm range), similar to the mode observed in ambient particles over Lake Michigan (0.20 μm), as measured by the optical particle counter (0.20 – 4 μm , Figure 3.5 and B.3). This analysis shows LSA to exist in a size range²⁴¹ and with composition (CaCO_3 + organics) that suggests LSA can act as CCN^{198,242,243} or INPs.^{198,244,245} These size distributions are similar to the previously observed accumulation mode peaks for laboratory-generated (0.2 μm)^{5,164,168} and ambient LSA (0.2 – 0.3 μm).^{4,5,27} LSA particles likely also contributed at smaller diameters, as previous studies have observed a second, ultrafine mode (0.02 – 0.08 μm) for LSA particles^{4,164} (Figure B.3); however, particles at that size were unable to be chemically analyzed in this study. In comparison, dust particles primarily contributed to the 0.75 – 1.4 μm size range, where they accounted for 10–15% of all particles analyzed, by number, in this size range. SOA/biomass burning particles accounted for 30–40% of all particles < 0.30 μm , ~70% of all particles from 0.30 – 1.0 μm , and 70–90% of particles > 1.0 μm . The contribution of SOA/biomass burning particles is consistent with the observations by Gunsch et al.,²³⁷ who identified highly aged biomass burning particles comprising ~80% of 1 – 2.5 micron summertime aerosol, by number, at a field site located 75 km from the flight sampling area. Similarly, Sheesley et al.²⁴⁶ observed organic aerosol contributing up to 90% of the aerosol population, by mass, in this geographic region.

Similar to the ambient particle analysis, CCSEM-EDX also identified cloud water residual particles corresponding to SOA/biomass burning (63%) and dust (11%), in addition to LSA (26%) (Figure 3.5b). As cloud water residual particles were resuspended from solution during the nebulization process, particle size could not reliably be related to the ambient diameter and, thus, was not used as a parameter during classification.^{224,235,247} Therefore, percentages listed are number fractions of the total particles analyzed. The abundance of each particle type identified from ambient aerosol particles for SOA/biomass burning (68%), dust (6%) and LSA (26%) were similar to the amounts observed in cloud water residual particles (63%, 11%, and 26%, respectively). Similar to the ambient particles, the LSA particle type contained Ca, C, and O, with additional Na and Mg. SOA/biomass burning particles were characterized by a circular morphology and contained elements C, O, and S (Figure B.4), as in the ambient particles. Dust particles were characterized by irregular shapes and the elements C, O, Si, and Fe.^{21,239} Similar to

this work, Twohy and Anderson²⁰⁰ previously conducted a flight study that characterized ambient particles and cloud water residual particles collected downwind of the Great Lakes. They classified 8% of the aerosol particles and 6% of the cloud water residual particles as salts containing calcium.²⁰⁰ Though the source was not identified at the time, the common Ca elemental signature^{5,27,168} indicates it is likely to have been LSA. Similarly, they identified 3% and 58%, by number, as dust and sulfate-containing (SOA or biomass burning) particles, respectively.²⁰⁰ That study suggested that the majority of particles $> 0.2 \mu\text{m}$ were activated as CCN because they did not find significant changes in the number fractions of each particle type when comparing ambient particles to cloud water residues.²⁰⁰ The study by Twohy and Anderson²⁰⁰ occurred over the Great Lakes region in wintertime while the current study took place in July. While the two studies were performed in different seasons, both found similar atmospheric particle and cloud water composition.

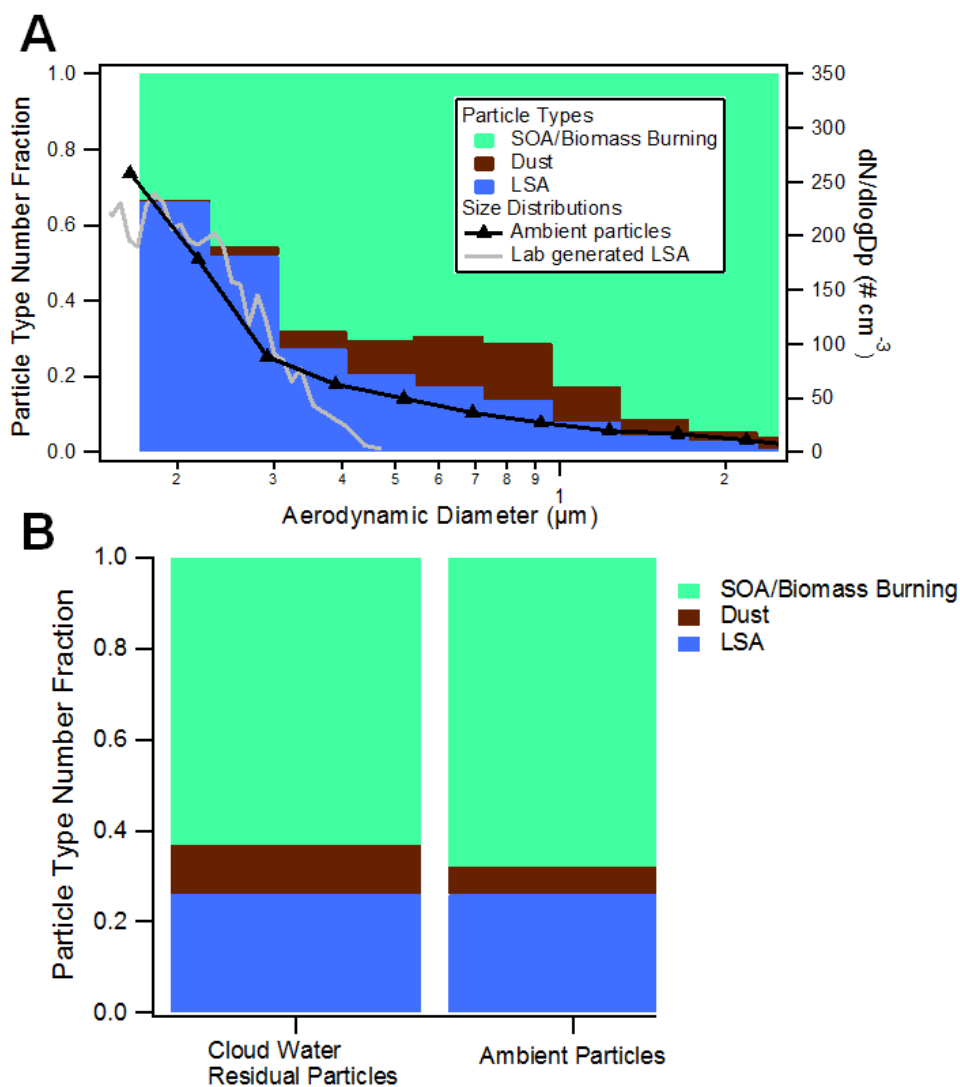


Figure 3.5. Comparison of ambient particle types observed during aircraft sampling. (A) CCSEM-EDX size-resolved number fractions of ambient particles collected during aircraft sampling on July 12, 2016. Black trace shows the size distribution of ambient particles measured by an optical particle counter ($0.20 - 4 \mu\text{m}$) during aircraft sampling. Grey trace shows the average size distribution of laboratory-generated LSA measured by SMPS ($0.020 - 0.80 \mu\text{m}$) for comparison. (B) Number fractions of particle types identified by CCSEM-EDX for cloud water residual particles ($n = 1993$ particles) and ambient particles ($n = 3264$ particles). Example SEM images and EDX spectra of each particle type are shown in Figures 3.3 and B.4.

3.4 Conclusions

In this study, a recently identified source of particles, lake spray aerosol (LSA)^{4,5,27} was shown to be lofted to cloud heights and incorporated into clouds over Lake Michigan. This was shown through single particle microscopy and chemical analysis comparing laboratory-generated LSA to ambient LSA and cloud water. The size, morphology, and elemental composition of

laboratory-generated LSA resembled that of ambient particles collected via aircraft over Lake Michigan during a wave breaking event. Additionally, 26% of 1993 residual particles generated from cloud water collected above Lake Michigan in July 2016 were identified as LSA, identifying a new potential source of CCN in regions with large bodies of freshwater.

The potential for LSA to act as CCN and/or INPs are particularly important in the Great Lakes region as air masses transition from water to land with excess water vapor, which condenses, forming lake effect clouds, fog, and precipitation, regionally. With the chemical characterization in the present study, we suggest that the previously measured calcium-rich droplets in Great Lakes clouds²⁰⁰ were LSA from the freshwater lakes. This provides further evidence that freshwater-generated aerosols can form cloud droplets, likely impacting cloud properties both over and downwind of the Great Lakes. Previous studies have identified LSA over 25 km inland from the nearest Great Lake,²⁷ suggesting LSA acting as CCN can impact a spatially broad region surrounding the Great Lakes. Measurements of the CCN and INP efficiencies of LSA with organic and biological components are needed to fully assess their meteorological and climate importance. In addition, detailed characterization of LSA production as a function of wind speed, wave height, and water composition is necessary for further parametrization in models to assess LSA impacts. Further ambient measurements of LSA physicochemical properties are needed to improve modeling of the potential wide-ranging climate^{197,199} and health^{168,209} impacts of LSA. In addition to the Great Lakes region, LSA could potentially impact many other regions containing large bodies of freshwater, such as the African Great Lakes, Lake Winnipeg and Great Bear Lake in Canada, and Lakes Baikal, Ladoga, and Onega in Russia.

Chapter 4. Harmful Algal Bloom Toxins in Aerosol Generated from Inland Lake Water

Adapted with permission from Olson, N. E., Cooke, M. E., Shi, J. H., Birbeck, J. A., Westrick, J. A., and Ault, A. P.: Harmful Algal Bloom Toxins in Aerosol Generated from Inland Lake Water, *Environ. Sci. Technol.*, 2020, 54, 8, 4769-4780. <https://doi.org/10.1021/acs.est.9b07727> Copyright 2020 American Chemical Society.

4.1 Introduction

The frequency and intensity of harmful algal blooms (HABs) from cyanobacteria in freshwater are increasing globally due to increased anthropogenic nutrient loading.²⁴⁸⁻²⁵¹ Warmer global temperatures are also expected to increase HAB frequency and intensity due to longer growing seasons and amplified algal growth rates.²⁵²⁻²⁶¹ Intracellular and extracellular algal toxins from cyanobacteria pose a threat to human and animal health.^{209,262} In 2014, a HAB with high concentrations of microcystin in Lake Erie infiltrated the public drinking water treatment facility for the city of Toledo, Ohio, causing a do not drink posting for > 400,000 people due to toxin levels unsafe for ingestion.^{263,264} The immediate impact of HAB toxins on human health necessitates a deeper scientific understanding of their chemical structure and mechanisms of transport. Variations in HAB toxin concentrations and the relative amounts of different toxin congeners (i.e. chemical structures) have been observed that are independent of overall HAB biomass concentrations.²⁶⁵⁻²⁶⁸ The physical size of a HAB does not correlate with the concentration of toxins produced, which creates difficulty in predicting and mitigating HAB-related health impacts.

Many genera of cyanobacteria, commonly known as blue-green algae (BGA, e.g. *Microcystis*), and associated cyanotoxins (e.g. microcystin) have been identified within freshwater HABs, but there is limited understanding of their impacts on human health.^{269,270} Microcystin is a class of cyclic heptapeptides named by the combination of amino acids in their structure,²⁷¹ with over 200 microcystin congeners identified to date.²⁷²⁻²⁷⁶ However, despite differences in the acute toxicities of different congeners, there is minimal overall understanding of HAB toxicity.^{277,278} Laboratory studies examining the toxicity of microcystin-containing aerosols administered to mice have shown ten times higher sensitivity to inhaled microcystin compared to orally ingested

microcystin.^{279,280} Therefore, toxic effects from exposure to aerosolized microcystin likely occur at lower doses than for microcystin ingestion,²⁸¹ on which the Environmental Protection Agency (EPA) recommendations are based. This raises concerns regarding unexpected exposure that could occur for populations living near or downwind of HABs, for occupations that interact with HABs, or for recreational users on HAB-impacted water. Studies have observed microscopic lesions in both the nasal cavity²⁸¹ and liver²⁸⁰ after microcystin inhalation. It is believed that microscopic lesions observed in the nasal cavity from microcystin inhalation enhanced absorption into the bloodstream leading to systemic impacts.²⁸¹ The diversity of cyanobacteria and associated toxins, as well as our limited knowledge of exposure routes and acute toxicities, necessitate further study as this has the potential to negatively impact populations living and working near HABs globally.²⁸²

Lake spray aerosol (LSA) is produced by freshwater wave breaking and bubble bursting,¹⁶⁴ similar to the production of sea spray aerosol (SSA) from wave breaking in marine environments.^{163,234,283,284} LSA from freshwater lakes have been observed along lakeshores on the ground,⁵ after transport inland,²⁷ lofted to cloud heights,^{4,285} and incorporated into cloud water.²⁸⁵ Modeling of LSA concentrations shows that freshwater aerosol production contributes significantly to particle number concentrations over the Great Lakes region.¹⁶⁷ LSA are generated in a size range important for inhalation exposure with modes in the ultrafine (30-80 nm) and accumulation (200-300 nm) size ranges.^{4,164} LSA have a distinct chemical composition in comparison to SSA,^{234,286} and are composed primarily of calcium carbonate and organic carbon.^{5,164} Recently May et al.¹⁶⁸ showed that LSA generated from HABs contained greater organic and biological material than LSA generated during non-HAB conditions, demonstrating the incorporation of biological material from HABs into LSA. However, little is known regarding the incorporation of toxins from freshwater HABs into LSA in the Great Lakes region.

The few studies of aerosolized HAB toxins in freshwater environments include Backer et al., which observed microcystin in ambient LSA emitted from small, inland lakes in Michigan^{287,288} and California.²⁸⁹ Wood et al.²⁹⁰ detected microcystin-containing aerosols at a freshwater site 20 m from the shore and 30 m high, demonstrating freshwater aerosol can be transported aloft and inland. Cheng et al.²⁹¹ identified microcystin-containing droplets produced from freshwater bubble bursting in the laboratory. These studies confirmed that freshwater toxins can become aerosolized, however they all used enzyme-linked immunosorbent assays (ELISA)

that are unable to distinguish between the congeners of aerosolized microcystin.^{292,293} Additional questions remain about the relationship between freshwater and aerosolized toxin concentrations. Further studies are needed to assess aerosolized toxin congeners with respect to toxin concentrations found in bulk water. Toxin incorporation into aerosol is not expected to be uniform at the particle-to-particle level, which makes understanding its presence as a function of size and at the single particle level (i.e. toxins as a function of aerosol mixing state)^{3,13,294} important for distinguishing the health implications in the Great Lakes region or other regions with HABs (e.g. Florida).^{27,43,230,237,285,295} Characterizing the aerosolization of HAB toxins in freshwater environments is crucial for understanding the impacts of toxin inhalation on public health.

Given the limited information on freshwater HAB toxin aerosolization, it is useful to consider what is known about aerosolization of toxins in oceanic environments from red tides and other marine blooms. Studies examining toxin aerosolization in oceanic blooms by wave breaking²⁹⁶⁻³⁰¹ and recreational activities^{302,303} show adverse respiratory effects after as little as 1 hour exposure.^{300,303} Exposure to toxin-containing aerosols particularly impacts people with pre-existing breathing diseases, such as asthma.^{301,304,305} Gambaro et al.³⁰⁶ detected microcystin in SSA particles generated from seawater artificially spiked with microcystin, showing algal toxin transfer from seawater to aerosol particles. Similarly, organic material increases in SSA during blooms,^{36,234,286} impacting water uptake,¹⁹⁴ incorporating metals,³⁰⁷ and even emitting whole, intact bacterial cells.²⁴ Blanchard et al.³⁰⁸ discovered elevated bacterial cells in aerosol particles compared to bulk water concentrations due to aerosolization of the surface-active organics present in the sea surface microlayer.³⁰⁹ Brevetoxins produced from red tides contain hydrophobic functional groups³¹⁰ that impact toxin type and potency,³¹¹ but further information is needed regarding the impact of hydrophobic structures on the aerosolization efficiency of HAB toxins. Pierce et al.²⁹⁹ observed marine toxin aerosolization up to one mile inland, suggesting inland transport of aerosolized toxins in addition to previously reported inland transport of SSA.^{27,206} Toxins in atmospheric particles were transported many kilometers inland without degradation,²⁹⁰ consistent with the stability of microcystin under a range of chemical and physical conditions.^{312,313} The well-established aerosolization, transport, and health consequences of toxins from marine blooms highlight the need to study these properties in freshwater environments.

In this study, freshwater was collected in Michigan from Mona Lake during a HAB and high microcystin concentrations and Muskegon Lake in which the microcystin concentrations were

below EPA recommended levels. Freshwater samples were analyzed for the presence of BGA and microcystin toxins, after which LSA was generated using established methods in the laboratory¹⁶⁴ to gain understanding of fundamental emission processes of nascent LSA in a controlled setting.²⁸⁴ Microcystin present in the freshwater samples was also detected in aerosol samples. However, microcystin congeners were not transferred from freshwater to the aerosol phase uniformly, leading to greater enrichment of hydrophobic microcystin congeners in aerosol particle samples. Freshwater samples were also analyzed for insoluble organic particles using nanoparticle tracking analysis (NTA).²³⁸ A relationship between increasing freshwater organic particle concentrations and higher aerosol number concentrations was observed. Overall, this study demonstrates the emissions of microcystin within particles and suggests that the relative amounts of toxins present in the aerosol phase are distinctly different than those present in the water column. These key findings improve the currently limited understanding of freshwater HABs toxins in size-resolved aerosols, which will ultimately lead to a better understanding of this potential route of exposure for HABs toxins and their health impacts.

4.2 Methods

4.2.1 Freshwater Sample Collection and Aerosol Generation

Freshwater samples were collected from the surface of Mona Lake (43.1856, -86.2360) on July 11, 2018 and September 4, 2018 and from Muskegon Lake (43.2325, -86.2677) on June 11, 2015 and October 25, 2015 (Figure 4.1A). Freshwater samples were stored in 8 L carboy LDPE containers (United States Plastic Corp) and frozen (-20°C) prior to analysis. After thawing, freshwater samples were then used to generate aerosol particles using the method described by May et al.¹⁶⁴ Briefly, 4 L aliquots of freshwater were cycled through four plunging jets at 2 L/min, creating bubbles that burst at the air-water interface to generate aerosol particles. Particles were sampled from the headspace of the tank after passing through two silica gel diffusion driers to achieve a relative humidity (RH) of $\sim 15\%$, a standard established for SSA.¹⁶³ The tank was kept at room temperature ($23 \pm 1^{\circ}\text{C}$) for all experiments. Particle-free air (Pall, HEPA Capsule Filter) was cycled through the LSA generator to test for leaks before LSA generation. Background particle concentrations were minimal (< 20 particles/ cm^3) compared to the particle concentrations generated from freshwater samples ($\sim 500 - 1500$ particles/ cm^3). The aerosol number size distributions for each LSA sample were measured by a scanning mobility particle sizer (SMPS)

consisting of a differential mobility analyzer (DMA, TSI Inc., model 3082) and a condensation particle counter (CPC, TSI Inc., model 3755) for particles ranging from 14.1 – 736.5 nm diameter. Particles with diameters from 0.52 – 19.8 μm were measured by an aerodynamic particle sizer (APS, TSI Inc., model 3321).

4.2.2 Bulk Measurement Techniques and Toxin Characterization

A spectrophotometer (AquaFluor 8000, Turner Designs) measured phycoerythrin fluorescence of freshwater samples, serving as an indicator of BGA.³¹⁴ ELISA kits (Thermo Fischer Scientific) measured total microcystin concentrations in freshwater samples. For comparison, 12 microcystin congeners were also measured using the liquid chromatography triple quadrupole mass spectrometry (LC-MS/MS) method developed by Birbeck et al.³¹⁵ Laboratory-generated LSA were impacted onto glass fiber filters (Whatman, grade GF/c, 47 mm) using a cyclone (URG Corp., model 2000-30ED) and single stage impactor (URG Corp., model 2000-30FV) that operated at 3 L/min and impacted particles < 2.5 μm aerodynamic diameter (d_a). Impacted particles were extracted following the method described by Wood et al.²⁹⁰ Filters and 5 mL of 100% methanol were placed into 50 mL beakers covered by ParafilmTM. Samples were sonicated for 30 minutes, after which the supernatant of each sample was placed into a glass vial. The extraction procedure was repeated for a total of three times. The supernatants from each filter were combined, dried under nitrogen, and solubilized in LC/MS grade water before LC-MS/MS analysis using a Thermo TSQ Quantiva triple quadrupole MS (Thermo Scientific) equipped with an online concentrating column (Thermo Scientific Hypersil GOLD aQ 2.1 x 20 mm, 12 μm).³¹⁵ Extract from three filters, each representing sixty minute LSA experiments, were analyzed by LC-MS/MS, as well as aliquots from each corresponding freshwater sample. The mobile phases consisting of 0.1% formic acid in water and 0.1% formic acid in acetonitrile separated the microcystin congeners present using gradient analysis with a C18 column (Thermo Accucore aQ, 50 x 2.1 mm, 2.6 μm) then detected using selective reaction monitoring (SRM) in positive electrospray ionization (ESI) mode. Retention times and concentrations of each measured microcystin congener were determined by calibration using commercially available standards.

4.2.3 Single Particle Analysis

An aerosol time-of-flight mass spectrometer (ATOFMS) measured the size and chemical composition of individual LSA particles ranging from 0.1 – 1.5 μm .³¹⁶ Briefly, particles entered

the instrument and were focused into a narrow particle beam by passing through an aerodynamic focusing lens. Particle sizes were determined by measuring the time it takes an individual particle to pass through two continuous wave lasers (wavelengths of 405 and 488 nm, respectively) separated by 6 cm. Particle d_a was determined after calibration using polystyrene latex spheres of known diameters ranging from 0.1 – 1.5 μm . Individual particles were desorbed and ionized by a 266 nm Nd:YAG laser upon entering the mass spectrometer source region, generating positive and negative ions for individual particles. Ions were detected using a dual polarity time-of-flight mass spectrometer. A total of 5277 particles were chemically analyzed by ATOFMS from the Mona Lake – July sample, 2332 particles from the Mona Lake – September sample, 1616 particles from the Muskegon Lake – June sample, and 1007 particles from the Muskegon Lake – October sample. Single-particle mass spectra were analyzed using the MATLAB toolkit FATES (Flexible Analysis Toolkit for the Exploration of Single-particle mass spectrometry data).³¹⁷ Mass spectral peak assignments correspond to ions identified from previous studies.^{5,27,168,224,235,239,247,284,294,307,318-320}

A three-stage microanalysis particle sampler (MPS-3, California Measurements, Inc.) impacted LSA particles onto Formvar coated copper microscopy grids (Ted Pella Inc.) for scanning electron microscopy coupled to energy dispersive x-ray spectroscopy (SEM-EDX) analysis. The MPS-3 operated at 2 L min^{-1} and impacted particles with diameters 2.5 – 5.0 μm , 0.7 – 2.5 μm , and < 0.7 μm onto stages 1, 2, and 3, respectively. SEM analysis was performed using a FEI Helios 650 Nanolab Dualbeam electron microscope that operated at an accelerating voltage of 20.0 kV and a current of 0.40 nA. The Helios microscope utilized a high angle annular dark field (HAADF) detector to provide contrast between areas of differing chemical composition.¹⁴⁴ EDX spectra were acquired for 20 seconds using an EDAX detector and GENESIS EDX software version 5.10 (EDAX Inc.). Raman microspectroscopy was performed on a Horiba LabRAM HR Evolution Raman Spectrometer (Horiba Scientific) to analyze droplets of freshwater placed onto quartz substrates (Ted Pella Inc.). The Raman spectrometer contained a 50 mW 532 nm Nd:YAG laser, CCD detector, 600 gr/mm grating, and a 100x objective confocal microscope (Olympus Life Science). Raman spectra were collected using 3 accumulations at 15 second acquisition times for the range 500 – 4000 cm^{-1} .

4.2.4 Analysis of Insoluble Residues

Concentrations and number size distributions of the insoluble residues present in each freshwater sample were analyzed by NTA using a NanoSight LM10 (NanoSight Ltd.) traditionally

applied to nanoparticle analysis,^{3,321,322} following the method for environmental insoluble residues described in Axson et al.²³⁸ NTA determines the size-resolved number concentration (i.e. size distribution) of individual particles in a liquid medium by illuminating them with a laser and monitoring the Brownian motion of particles to determine their 2-D displacement. The Stokes-Einstein equation is then used to determine the individual particle hydrodynamic diameter.^{323,324} Aliquots of each freshwater sample were filtered prior to analysis using a 2 μm glass syringe filter before 500 μL was loaded into the LM10 cell housing a 405 nm laser. Freshwater sample flowed through the instrument using a syringe pump that operated at 60 rpm. Light scattering was measured using a sCMOS camera (Hamamatsu, Orca) coupled to a 20x objective microscope. Ten 60 second videos of each freshwater sample were analyzed using the NTA 3.2 (Build 60) software. The average of the ten videos generated an average size distribution in the range 10 nm – 1 μm for each freshwater sample. Droplets of Mona Lake – September freshwater were placed on Raman and SEM substrates following previously established methods,³²⁵ and the insoluble residues were analyzed by SEM-EDX and Raman microspectroscopy after the droplet dried.^{36,234} The insoluble residues were composed of particulate organic carbon (POC, Figure C.1)^{326,327} and will be referred to as POC.

4.3 Results and Discussion

BGA and microcystin concentrations present in freshwater samples were analyzed prior to aerosol generation. Mona Lake – September had the highest phycocyanin/BGA (1166 $\mu\text{g/L}$) and microcystin concentrations (280 and 230 $\mu\text{g/L}$ for ELISA and LC-MS/MS methods, respectively) of all samples (Figure 4.1B). For this reason, we focused on this sample for aerosol generation in subsequent laboratory experiments. Mona Lake – July had the second highest concentrations of phycocyanin/BGA (192 $\mu\text{g/L}$) and microcystin (21 and 8 $\mu\text{g/L}$ for ELISA and LC-MS/MS methods, respectively). Both Muskegon Lake samples had lower phycocyanin/BGA concentrations (93 and 86 $\mu\text{g/L}$ for the June and October samples, respectively). Muskegon Lake also had lower microcystin concentrations of 0.3 and 0.8 $\mu\text{g/L}$ (using ELISA) and 0.03 and 0.08 $\mu\text{g/L}$ (using LC-MS/MS) for the June and October samples, respectively. The microcystin concentrations present in Muskegon Lake were below the EPA swimming advisory (8 $\mu\text{g/L}$ total microcystin)³²⁸ and drinking advisory (1.6 $\mu\text{g/L}$ total microcystin) recommendations,³²⁹ while Mona Lake samples were above for both guidelines. For all samples, ELISA kits predicted slightly higher amounts of algal toxins more than likely due to the simultaneous detection of toxins and

their degradation products and differing responses of each congener to ELISA.^{293,315,330} ELISA is not able to differentiate between microcystin congeners like the LC-MS/MS method used.³¹⁵

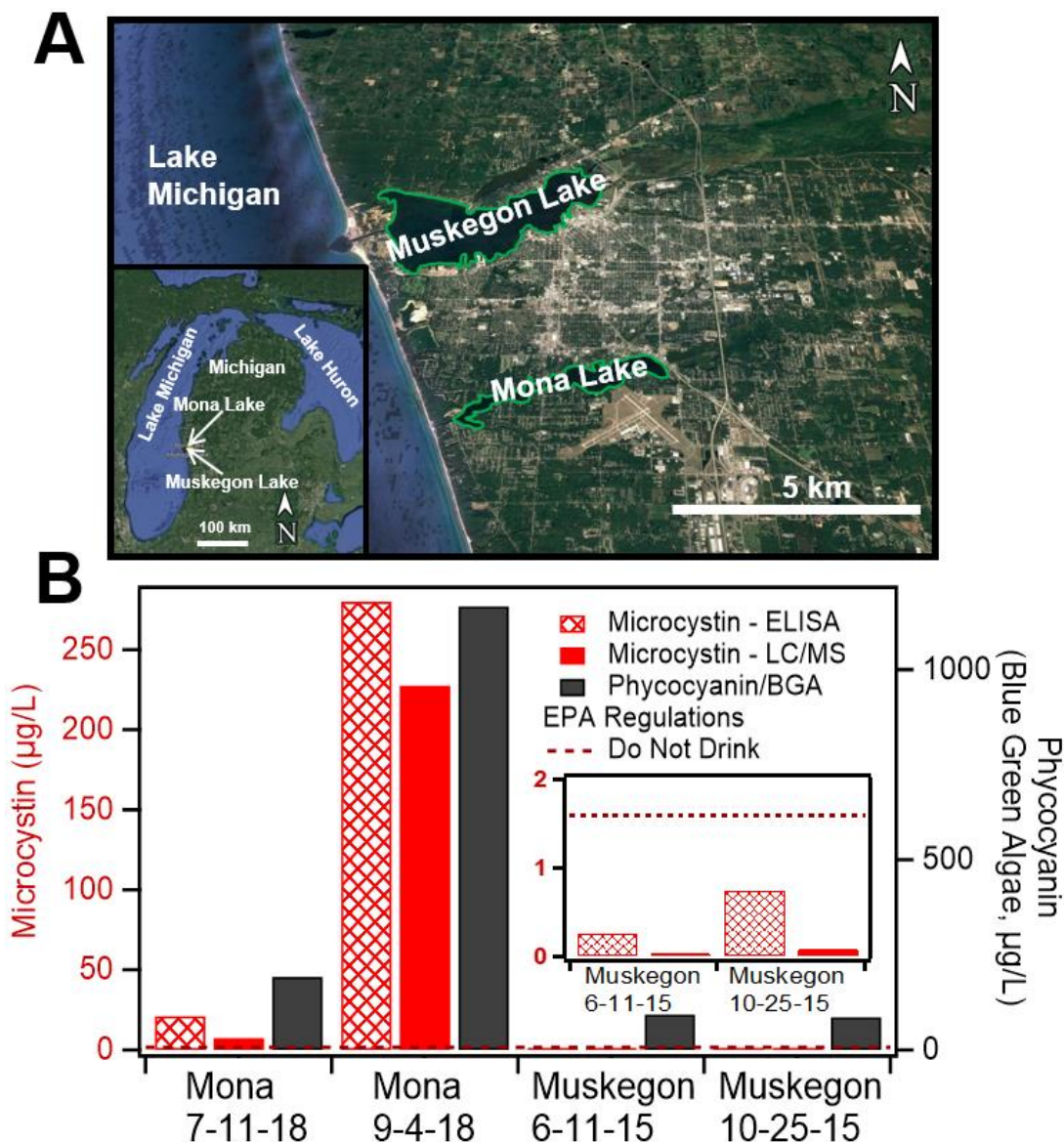


Figure 4.1. Map of sampling locations and microcystin concentrations at each location. A) Map of Mona and Muskegon Lakes located in Western Michigan, with inset showing location of inland lakes relative to the surrounding Great Lakes. B) Total microcystin and phycocyanin (blue green algae, BGA) concentrations for each freshwater sample. Inset shows microcystin for Muskegon Lake samples. Dashed line shows EPA drinking water advisory of 1.6 µg/L total microcystin.

Aerosolized microcystin congeners from Mona Lake LSA were quantified with LC-MS/MS, described in Birbeck et al.³¹⁵ Figure 4.2A shows the molecular structure of microcystin-LR (MC-LR), the congener with the highest concentration in the aerosol generated from Mona Lake (Figure 4.2B). Chromatograms of the retention times of each microcystin congener measured

in Mona Lake LSA are shown in Figure 4.2B, with the chromatogram of microcystin congeners detected in Mona Lake freshwater shown in Figure C.2. Retention times and structures for each congener are listed in Table C.1³¹⁵ and illustrated in Figure C.3. The commercially available microcystin congeners were previously optimized for select quantitative and qualitative ion transitions using known fragmentation patterns from the literature.³³¹⁻³³⁴ The microcystin congeners were separated by gradient analysis HPLC and detected using SRM analysis on the triple quadrupole MS system. Figure 4.2C shows the mass spectral fragments detected for MC-LR, with fragmentation patterns illustrated in Figure 4.2A. Quantitative and qualitative fragment ions were observed at m/z +135.07 [Ph-CH₂-CH(OCH₃)]⁺, +155.08 [H+Mdha-Ala]⁺, +163.08 [C₁₁H₁₄O+H]⁺, and +212.97 [H+Glu-Mdha]⁺, and are known fragments of that microcystin molecule.³³¹⁻³³⁴

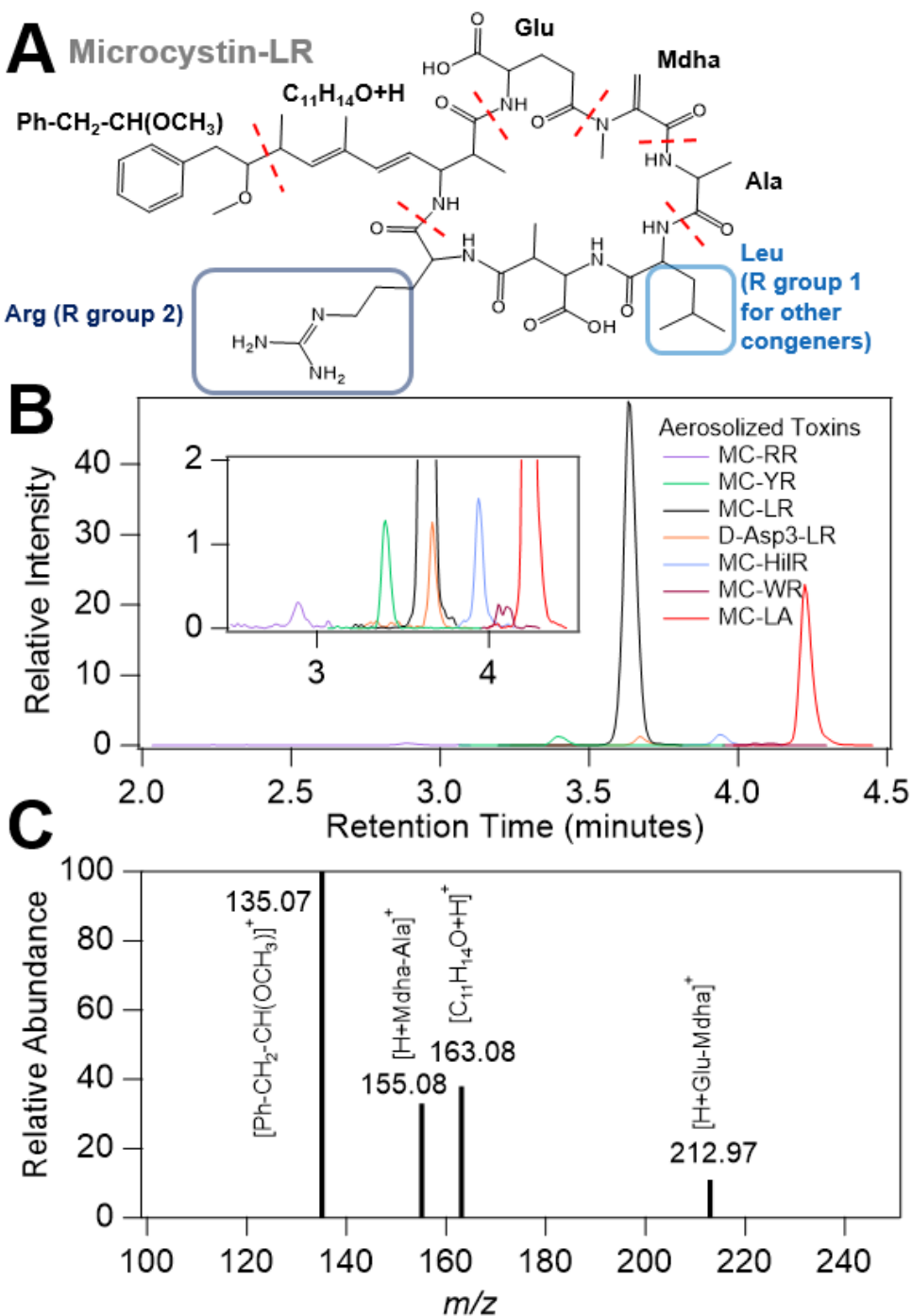


Figure 4.2. Chemical structure, chromatogram, and mass spectrum of microcystin-LR. A) Structure and fragmentation of microcystin-LR, the microcystin congener with the highest concentration in Mona Lake LSA. B) Chromatogram showing microcystin congeners present in Mona Lake LSA. Inset shows congeners present at lower concentrations. C) Mass spectrum of microcystin-LR identified from Mona Lake LSA. All congener structures, retention times, and their abundance in the Mona Lake freshwater sample are provided in the supporting information.

The LC-MS/MS method allows for the quantification of each microcystin congener based on calibration with microcystin standards. The congeners detected and quantified in Mona Lake – September freshwater are shown in Figure 4.3A and listed in Table 4.1. Microcystin concentrations in LSA were determined by extracting LSA impacted onto filters and analyzing the extract with LC-MS/MS. Average aerosolized microcystin concentrations from three experiments are shown in Figure 4.3B and listed in Table 4.1. Of the eight toxins detected in freshwater, seven were also detected in aerosol particles. However, the relative concentrations of specific toxins in the water and aerosol phase differed substantially. In our experiments, MC–LR and MC–LA, were more concentrated than other congeners in aerosol particles (Figure 4.3B). Enrichment calculations (details in the supporting information) show enrichment factors of 830 and 2000 for MC–LR and MC–LA, respectively, in the aerosol phase relative to the bulk freshwater (Table 4.1). MC–LR and MC–LA contain the amino acid leucine (Figures 4.2A and C.3), a hydrophobic amino acid.³³⁵⁻³³⁸ Conversely, the amino acid arginine is significantly more hydrophilic,³³⁶⁻³³⁸ and the congener with this structure, MC–RR, was significantly less enriched in the aerosol relative to freshwater (enrichment factor of 10). Hydrophobic molecules have been shown to be enhanced in SSA particles relative to bulk seawater,^{17,284,309,339-343} which is believed to be due to hydrophobic and low solubility species partitioning to the air-water interface of bubbles as they rise through the water column. Octanol-water partitioning coefficients $\log(K_{ow})$ for MC–LR (1.67) and MC–RR (-0.71)³⁴⁴ support preferential transfer of MC–LR to the aerosol phase, while MC–RR remains primarily in the bulk freshwater. De Maagd et al.³⁴⁵ suggested the hydrophobicity of MC-LR changes as a function of pH, with higher pH values leading to lower $\log(K_{ow})$ values. Freshwater sample pH ranged from 6.9-7.1 (Figure C.4) though it is unclear what the role of pH is with respect to toxin emissions into the particle phase and future work is needed in this area. Though extracellular microcystin excreted from algal cells generally accounts for 20% of total toxins,²⁷⁰ this percentage can increase drastically during bloom senescence, algaecide treatment, and lysis.²⁶³ The aerosolized microcystin detected was likely extracellular because the bubble-bursting process lyses cells, as noted by the observation of aerosolized bacterial cell components from marine algal blooms.²⁴ Additionally, the freshwater samples used within this manuscript were collected near bloom senescence and intact cells are unlikely to be aerosolized as the cell size of *Microcystis* ($> 4 \mu\text{m}$)³⁴⁶ is larger than the mass and number modes of the generated aerosol. Therefore, extracellular microcystin likely dominated the measurements.

Microcystin Congeners	Microcystin in Water ($\mu\text{g/L}$)	Microcystin in Aerosol (ng/m^3)	Enrichment (Aerosol/Water)	Octanol-water partitioning coefficients $\log(K_{ow})$
D-Asp ³ -RR	1.2	Not detected	N/A	N/A
MC-RR	114.8	0.7 ± 0.4	10	-0.71 ± 0.05
MC-YR	22.2	1.8 ± 0.5	140	N/A
MC-LR	76.4	40 ± 20	830	1.67 ± 0.09
D-Asp ³ -LR	1.6	0.8 ± 0.3	800	N/A
MC-HilR	2.0	1.4 ± 0.2	1200	N/A
MC-WR	3.8	0.8 ± 0.1	400	N/A
MC-LA	5.6	7 ± 3	2000	1.30 ± 0.06

Table 4.1. Concentrations of microcystin congeners detected in freshwater and aerosol samples. Error bars refer to the standard deviation of triplicate aerosol experiments. MC-HtyR, MC-LY, and MC-LW were below the limit of detection ($5 \times 10^{-3} \mu\text{g/L}$). MC-LF and nodularin were not detected in the freshwater samples. Enrichment factors were calculated by dividing the toxin concentration in aerosol by the toxin concentration in freshwater (details are provided in the supporting information). Octanol-water partitioning coefficients $\log(K_{ow})$ are provided by McCord et al.³⁴⁴

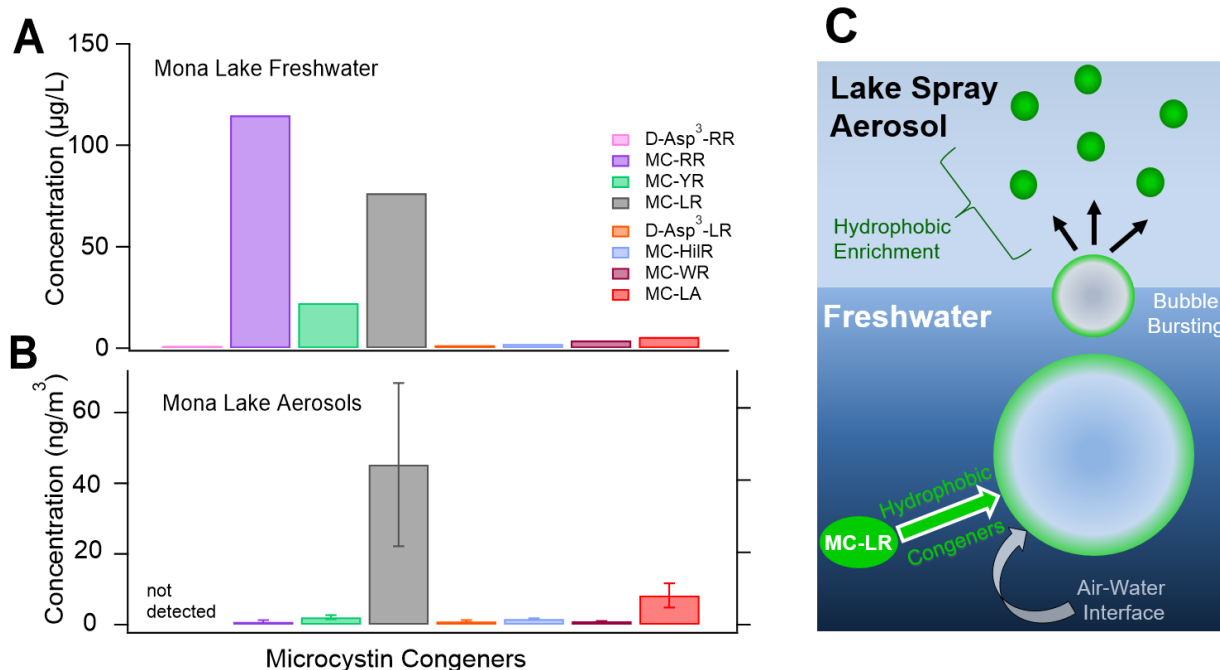


Figure 4.3. Quantification of microcystin congeners present in Mona Lake freshwater and LSA (parts A and B, respectively). Concentrations reported in µg/L refer to the mass of toxin per mass of water. Concentrations reported in ng/m³ refer to the mass of toxin per meter cubed of air measured. C) Schematic showing the aerosolization of hydrophobic microcystin congeners.

Toxin concentrations present in the aerosol samples were converted to ng/m³ for comparison to previously reported measurements, as mass per volume of air is the standard unit for particulate matter and specific particle-phase toxins. We detected 50 ± 20 ng/m³ of total aerosolized microcystin (Table 4.1). Backer et al.²⁸⁸ detected aerosolized microcystin concentrations up to 23 ng/m³ during ambient sampling on the shore of a small lake in Michigan. However, the freshwater microcystin concentrations in that study were significantly lower than those observed herein (5 µg/L²⁸⁸ and 230 µg/L, respectively), which likely accounts for the difference in aerosolized toxin concentrations observed.

The size and concentration of LSA and insoluble residues in freshwater were analyzed to investigate trends between the properties of organic material of the water and aerosol phases. Mona and Muskegon Lake LSA had a mode at 46 nm in the number size distribution (Figures 4.4A and 4.4B), similar to the Aitken mode observed for LSA generated from Lake Michigan freshwater (30 – 80 nm).^{4,5,164} A larger LSA mode at 270 nm was also observed, corresponding to the accumulation mode previously identified in laboratory^{164,168} and field studies (200 – 300 nm).^{4,5,27,285} POC present in Mona Lake – September freshwater as insoluble residues had a number

size distribution mode at 155 nm and an average concentration of $1.15 (\pm 0.04) \times 10^9$ POC/mL (Figures 4.4A and 4.4C, respectively). Similar concentrations of $1.22 (\pm 0.03) \times 10^9$ POC/mL were observed for Mona Lake – July freshwater, with a slightly larger mode at 240 nm. POC concentrations for the Muskegon samples were much lower ($3.62 \pm 0.08 \times 10^8$ and $3.32 \pm 0.07 \times 10^8$ POC/mL for June and October samples, respectively). These POC distributions correspond to mass concentrations of 68, 38, 6, and 7 $\mu\text{g}/\text{cm}^3$ for Mona Lake – July, Mona Lake – September, Muskegon Lake – June, and Muskegon Lake – October samples, respectively. Average LSA number concentrations for Mona Lake – September were 1400 ± 200 particles/ cm^3 (Figure 4.4C). LSA number concentrations were lower for Mona Lake – July and both Muskegon Lake samples (260 ± 20 particles/ cm^3 , 270 ± 15 particles/ cm^3 , and 110 ± 6 particles/ cm^3 , respectively). The increase in POC and microcystin for Mona Lake – September corresponded to an increase in overall aerosol production, particularly with enhanced aerosol production in the ultrafine size range (< 100 nm) resembling the size of observed POC. Incorporation of insoluble residues into SSA has been observed³⁴⁷ with aerosol size shifting to that of the insoluble residues,³⁴⁸ similar to the results presented herein. A positive relationship between organic content in water and increased algal growth has been observed,³⁴⁹⁻³⁵¹ demonstrating the importance of simultaneously measuring POC and microcystin in freshwater environments. This analysis is the first use of NTA to investigate the insoluble residues of freshwater in relationship to aerosol generation, and shows that insoluble residues present in freshwater play a role in higher atmospheric aerosol concentrations, as well as impacting the size of particles that form.

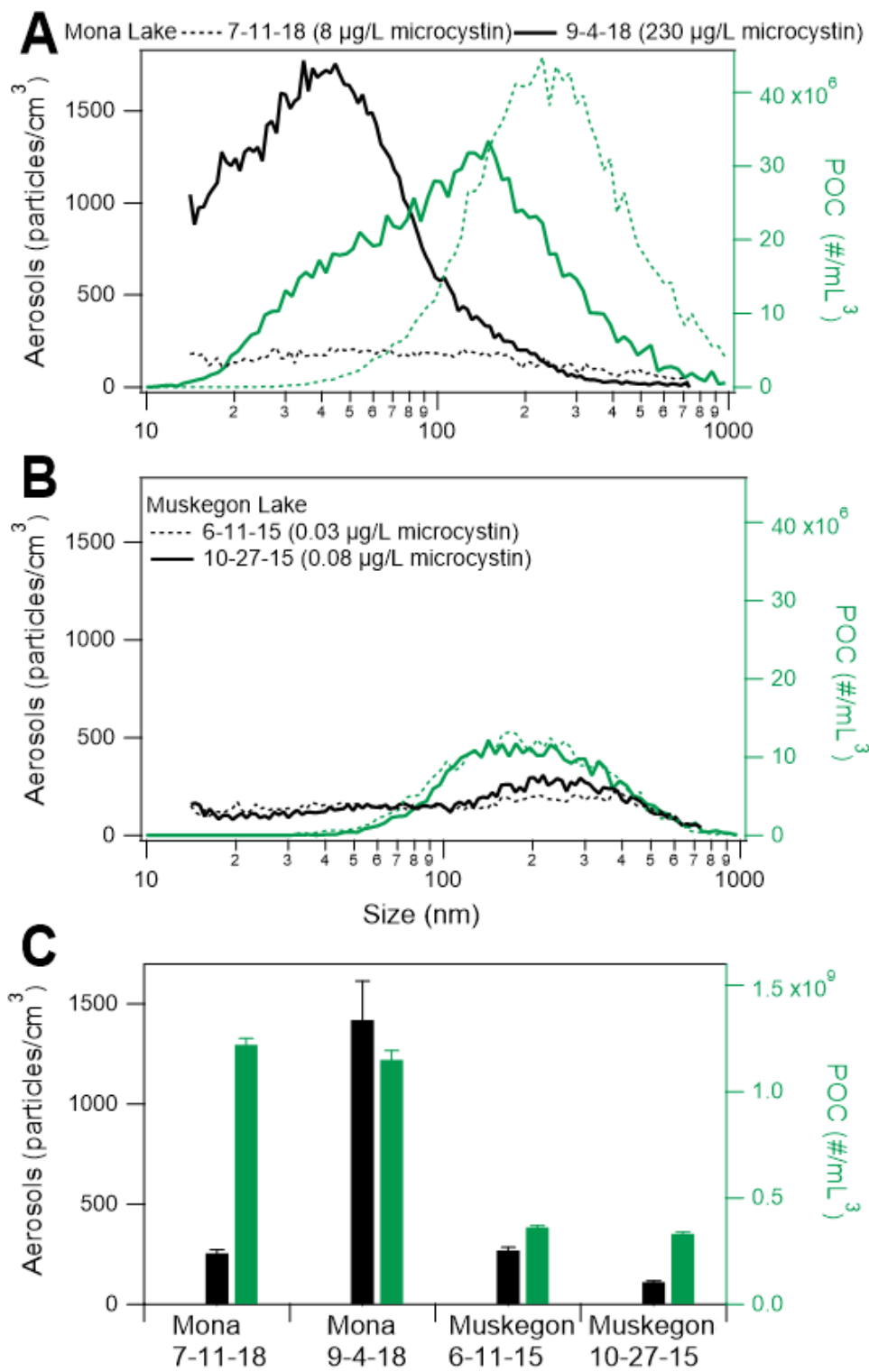


Figure 4.4. Average size distributions for water samples and aerosol experiments. Average aerosol and POC number size distributions for A) Monka and B) Muskegon Lake samples. Microcystin concentrations for each sample are listed in parentheses. C) Quantification of aerosol and POC number concentrations for each freshwater sample.

LSA analyzed by single particle mass spectrometry (ATOFMS) were classified into three particle types following the criteria used in May et al:¹⁶⁸ LSA composed primarily of salt (LSA salt), LSA with organic content (LSA organic), and LSA with enhanced biological material (LSA biological). Average dual polarity mass spectra of all three particle types are shown in Figure C.5 with the major ions labeled. Salt particles contained primarily inorganic ions, with the major ions present being m/z +40 [Ca^+], +23 [Na^+], and +24 [Mg^+] (Figure C.5).^{5,27,168} LSA organic particles were classified by the presence of m/z +66 [CaCN^+] and +82 [CaCNO^+]¹⁶⁸ (Figure C.5), peaks consistent with the presence of organic nitrogen.³⁰⁷ Additional organic ions observed were m/z +74 [$\text{N}(\text{CH}_3)_4^+$], -45 [CHOO^-], -59 [$\text{CH}_3\text{COO}/\text{HCNO}_2^-$], and -71 [$\text{C}_3\text{H}_3\text{O}_2^-$].³¹⁸ LSA biological particles were classified by the presence of m/z -79 [PO_3^-]^{168,307,319,320} and +89, the amino acid aspartic acid [$\text{Asp}-\text{CO}_2^+$].³⁵²

Difference mass spectra, calculated by subtracting the average mass spectra of particles in Muskegon Lake from the average spectra of particles in Mona Lake, highlight the compositional differences between particles generated from each lake (Figures 4.5A, 4.5B, and C.6). Both biological markers were observed in higher concentration in Mona Lake biological LSA (Figure 4.5B), while organic markers were observed in both Mona and Muskegon Lake LSA organic particle types (Figure 4.5A). The identification of salt, organic, and biological particles was verified by SEM-EDX analysis (Figure C.7). Salt particles were identified with SEM-EDX by containing the elements Na, Mg, Ca, and Cl,¹⁶⁸ along with an amorphous morphology similar to previous analysis of ambient LSA collected on the shore⁵ and via aircraft²⁸⁵ over Lake Michigan. Organic particles were identified by SEM-EDX by containing only the elements C and O, and a circular morphology.¹⁶⁸ Biological particles were classified by the presence of elemental P and an amorphous morphology similar to previously observed ambient biological particles.^{20,168}

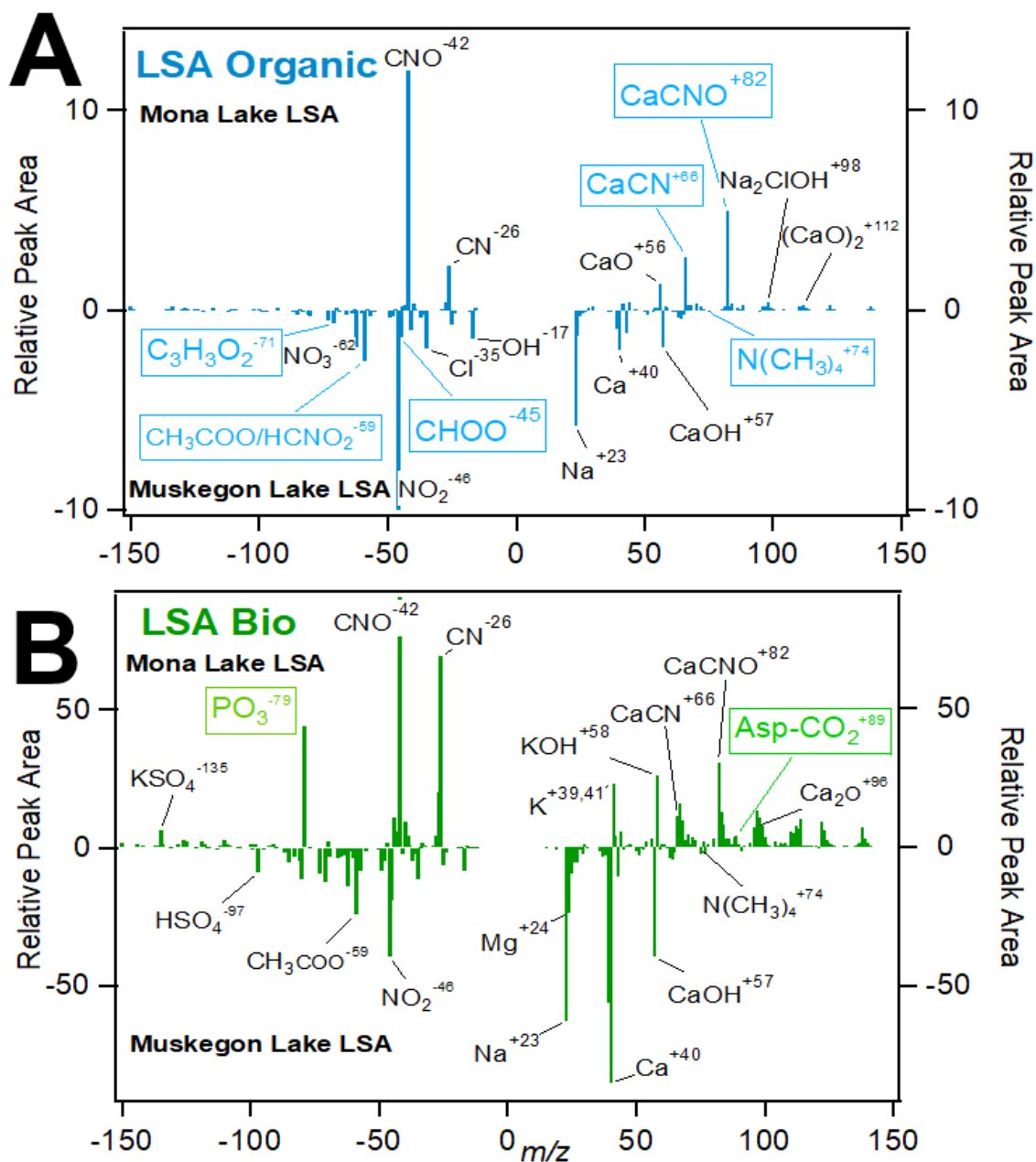


Figure 4.5. Mass spectra of biological and organic LSA particles from Mona and Muskegon Lakes. Difference spectra calculated by subtracting Muskegon Lake mass spectra from Mona Lake spectra of A) LSA organic particles and B) LSA biological particles.

Freshwater toxin concentrations and aerosol particle types were investigated for each freshwater sample. Percentages of microcystin congeners for each freshwater sample were calculated using the concentrations obtained by LC-MS/MS to compare relative toxin abundance for each lake. MC-RR was the toxin of highest concentration in all samples, accounting for 48% (Mona Lake – July), 50% (Mona Lake – September and Muskegon Lake – October), and 67%

(Muskegon Lake – June) of microcystin congeners observed (Figure 4.6A). MC–LR was the second highest for each sample at 34% (Mona Lake – July and Mona Lake – September), 33% (Muskegon Lake – June) and 25% (Muskegon Lake – October). The remaining toxins detected were: D–Asp³–RR (1% for both Mona Lake samples, 0% for both Muskegon Lake samples), MC–YR (8 and 9 % of Mona Lake – July and – September samples, 0 and 12% of Muskegon Lake – June and –October), D–Asp³–LR (1% for both Mona Lake samples, 0% for both Muskegon Lake samples), MC–HilR (1% for both Mona Lake samples, 0% for both Muskegon Lake samples), MC–WR (2% for both Mona Lake samples, 0% for both Muskegon Lake samples), and MC–LA (5% for both Mona Lake – July, 2% for Mona Lake –September, 0% for Muskegon Lake – July, and 13% for Muskegon Lake – October.). Particle types observed by ATOFMS were combined for each freshwater sample. The percentage of particles identified as LSA biological from Mona Lake were 10% and 14% for the July and September samples, respectively (Figure 4.6B). Biological particles generated from Muskegon Lake freshwater comprised 10% and 6% of all particles analyzed from the June and October samples, respectively. Organic particle types were also at higher percentages for Mona Lake LSA (80% and 75% for July and September, respectively) than Muskegon Lake (67% and 60% for June and October, respectively). Salt particles comprised the smallest percentage of LSA generated from Mona Lake freshwater at 10% and 11% for July and September samples, respectively. Conversely, salt particles were 23% and 34% of all particles observed from Muskegon June and October samples, respectively. Mona Lake – September had the highest microcystin (230 µg/L) and phycocyanin/BGA (1166 µg/L) concentrations, corresponding to an increase in the amount of biological and organic particles detected, similar to previous observations.¹⁶⁸ The significantly lower contribution of salt particles to Mona Lake LSA demonstrate the incorporation of biological and organic material from HABs into aerosols.

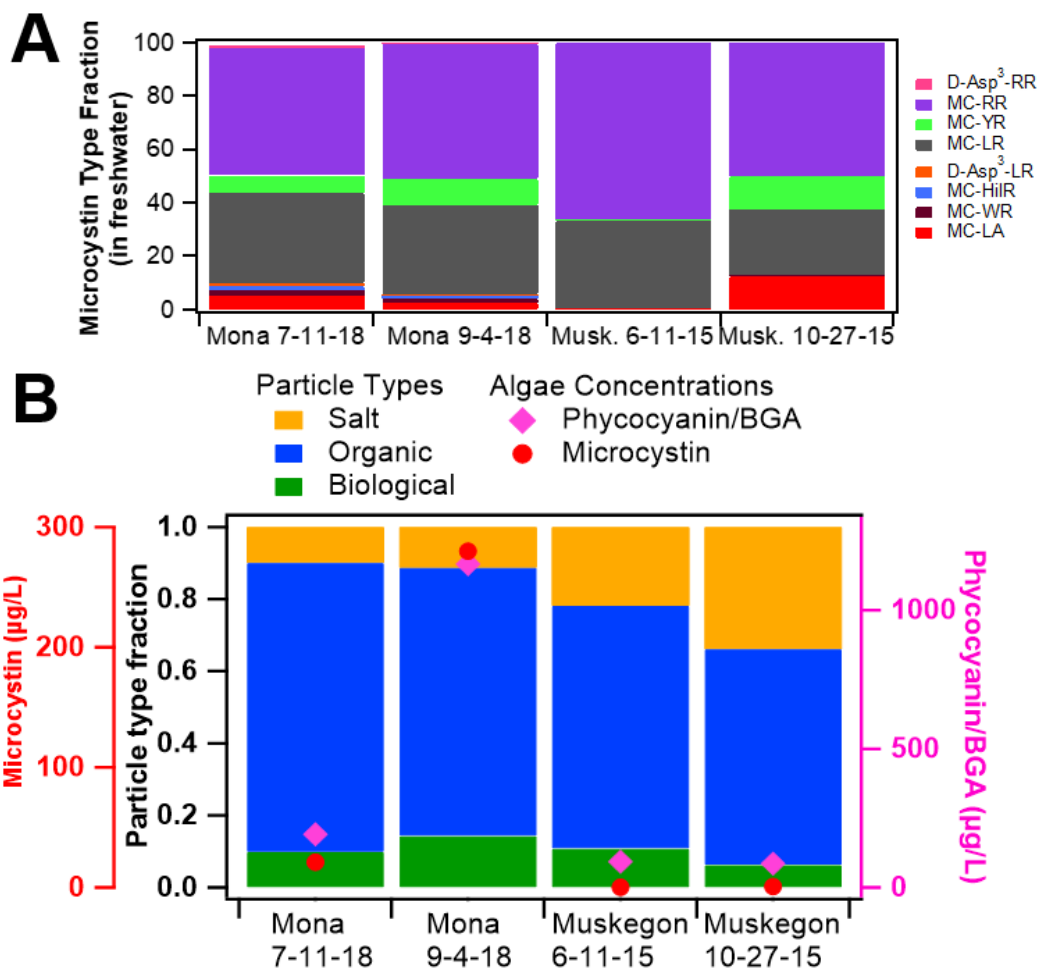


Figure 4.6. Microcystin congeners present at all sampling locations with fraction of particle types observed from each location. A) Fraction of microcystin congeners present in all freshwater samples. B) Number fractions of ATOFMS particle types generated from Mona and Muskegon Lake freshwater. Average phycoerythrin/blue green algae (BGA) and microcystin freshwater concentrations are shown for each sample.

4.4 Conclusions

This study identified HAB toxins, specifically microcystin, in laboratory-generated freshwater particles < 2.5 µm, a key size range impacting human health.¹ Microcystin congeners were quantified in freshwater from a HAB in Mona Lake in Michigan using two microcystin measurement methods (ELISA and LC-MS/MS). Aerosol particles were then generated in the laboratory and analyzed for the presence of toxins relative to the toxins identified in the freshwater samples. Of the eight microcystin congeners detected in the freshwater, seven were also detected in LSA particles, demonstrating that toxins are emitted through the aerosolization process in freshwater environments.

For the first time, we show that hydrophobic microcystin congeners were preferentially aerosolized versus hydrophilic microcystin congeners, which suggests that the relative amounts of toxins present in the aerosol phase are distinctly different than those present in the water column. This is analogous to previous observations of preferentially aerosolized hydrophobic material in SSA from marine environments.^{50,63,84-88} The alignment between aerosol-phase enhancement and octanol-water partitioning coefficients $\log(K_{ow})$'s for different microcystin congeners³⁴⁴ supports the finding that hydrophobic congeners partition to the air-water interface of bubbles passing through the HAB and are then transferred to the aerosol phase after bubble bursting. The fact that aerosol phase concentrations of microcystin cannot be predicted solely based on water concentrations, combined with the differing toxicities of microcystin congeners, demonstrates the need for further aerosolization studies aimed at predicting concentrations of toxins emitted to the atmosphere.

To improve understanding of the linkages between organic material in freshwater and emitted in the aerosol phase, the size and amount of insoluble organic material in freshwater was tracked and related to aerosol size. Increased POC number concentrations corresponded to increased aerosol number concentrations and a shift in the aerosol size distribution to resemble that of the POC size distribution, leading to aerosol production at smaller sizes that are more readily inhaled.³⁴⁹⁻³⁵¹ Our results demonstrate an enhancement in ultrafine aerosol particles with an increase in HAB concentration.

Overall this work highlights the potential exposure risks for populations near or downwind of HABS. Understanding these exposures is challenging since we show that the hydrophobicity of microcystin congeners improves their aerosolization efficiency, leading to different relative amounts of congeners in the aerosol phase compared to the freshwater bloom itself. Ambient measurements are needed to quantify HAB toxin aerosolization, while accounting for different atmospheric (wind speed, turbulence, temperature, RH) and biological (freshwater nutrient levels, type and amount of cyanobacteria, cyanobacteria buoyancy and distribution throughout the water column) conditions. Additional questions remain regarding the diel patterns of freshwater toxin production and associated aerosol emission. Future work is needed to determine relative toxicities of each congener and relate these to the atmospheric concentrations and bloom dynamics to fully assess the health impacts of toxin-containing LSA.

Chapter 5. Harmful Algal Bloom Toxins in Ambient Freshwater Aerosol

Nicole E. Olson,¹ Jia H. Shi,¹ Madeline E. Cooke,¹ Johnna A. Birbeck,² Judy A. Westrick,² Andrew P. Ault^{1*}

¹*Department of Chemistry, University of Michigan, Ann Arbor, MI, USA 48109*

²*Department of Chemistry, Wayne State University, Detroit, MI, USA 48202*

5.1 Introduction

Increased anthropogenic nutrient loadings in freshwater environments combined with rising temperatures have led to a global increase in harmful algal blooms (HABs).^{248,250-252,255,256,258,261} HABs, typically caused by cyanobacteria (blue-green algae, BGA),^{250,270} release toxins (e.g. microcystin) that are a threat to both human health and wildlife.^{209,262-264} With over 200 microcystin congeners identified thus far,^{272-274,276} many questions remain regarding their impact on human health. Drinking water regulations require the monitoring of HAB toxins to ensure the amounts present are safe for ingestion.^{263,264,328,329} However, recent laboratory studies have suggested that inhalation of microcystins results in 10 times higher sensitivity compared to oral ingestion of these toxins.^{279-281,353} Therefore, it is crucial to determine the amounts of aerosolized HABs toxins in order to predict exposure for populations living near or downwind of HABs globally.^{302,354}

The physicochemical properties of lake spray aerosol (LSA), produced from wave breaking and subsequent bubble bursting in freshwater environments,¹⁶⁴ have been extensively studied through laboratory studies^{164,168,355} and in the ambient environment.^{4,5,27,285} LSA is composed primarily of CaCO₃,^{5,168,285} and can be chemically differentiated from the sodium-rich sea spray aerosol (SSA) that is produced in marine environments.^{27,163,234,283,286} The submicron size of LSA suggests it can be important for inhalation exposure.^{4,5,285,355} In a laboratory-based study, May et al.¹⁶⁸ observed the incorporation of biological material from HABs into aerosol particles, showing that both the organic and inorganic content of freshwater impacts aerosol composition. However, questions remain regarding the transfer of algal toxins into aerosol particles and their abundance in ambient freshwater environments.

Recent laboratory studies have observed microcystin in aerosol particles generated from both freshwater²⁹¹ and seawater,³⁰⁶ highlighting that aerosol particles can contain HAB toxins. However, these studies used enzyme-linked immunosorbent assays (ELISA) for microcystin measurements, a technique that is unable to distinguish between microcystin congeners.^{292,293} Recently, a liquid chromatography tandem mass spectrometry (LC/MS/MS) method was developed to separate and quantify microcystin congeners.³¹⁵ Olson et al.³⁵⁵ used this method and observed an enrichment of hydrophobic microcystins in laboratory-generated aerosol particles relative to toxins present in the water column. These results highlight the need for simultaneous water and aerosolized toxin measurements in ambient environments.

Aerosolized algal toxins has been reported in ambient studies taking place in Michigan,^{287,288} California,²⁸⁹ and Florida,^{301,303,356-358} with long-term effects reported after as little as one exposure to aerosolized HAB toxins.³⁵⁶ Toxin-containing particles have been observed up to 1 mile from shore,^{290,299} similar to previous observations of LSA lofted to cloud heights^{4,285} and after inland transport.^{27,206} The stability of microcystin^{312,313,359} and other cyanobacteria^{330,360} suggests minimal degradation after inland transport, thus necessitating measurements of aerosolized toxins at several sites around a HAB-infested lake. With toxin incorporation into particles not expected to be uniform for every particle, single-particle techniques are needed to assess the physicochemical properties of individual toxin-containing particles, and how prevalent these particles are in relation to other particle types in the region.

In this study, freshwater and aerosol samples were collected from five locations around Grand Lake St. Marys (GLSM) in Celina, Ohio, United States. This site was chosen due to severe annual algal blooms resulting from excessive phosphorus loading from crops and livestock operations in a shallow, hypereutrophic environment.^{361,362} GLSM routinely has *Microcystis*, the bacteria that produces microcystin,³⁶³ with microcystin concentrations often exceeding 2000 µg/L.³⁶³ These concentrations are orders of magnitude larger than what the Environmental Protection Agency (EPA)³²⁹ and World Health Organization (WHO) regulates for drinking water.³⁶³ Ambient freshwater and aerosol samples were analyzed with LC/MS/MS for microcystin speciation and quantification. A transfer of microcystins from the bulk water into aerosol particles was observed. In addition, microcystin was characterized with spectroscopic methods which were also used to study the aerosol population as a whole in this region. Finally, the size and concentration of insoluble residues in the freshwater samples was correlated to the size and

concentration of aerosol particles, with increased insoluble residues leading to an increase in aerosol particles observed. Overall, this study identified microcystin in aerosol particles in a size range critical for inhalation exposure. These findings improve our understanding of microcystin-containing aerosols in the ambient environment, and have important implications for populations living near or downwind of HABs globally.

5.2 Methods

5.2.1 Freshwater and Aerosol Collection

Five freshwater samples were collected from the surface of GLSM (40.5439, -84.5033) on August 6, 2019 (Figure D.1) and stored in 8 L carboy LDPE containers (United States Plastic Corp) at room temperature ($\sim 23^{\circ}\text{C}$) until analysis. A spectrophotometer (AquaFluor 8000, Turner Designs) measured phycocyanin fluorescence, serving as an indicator of blue-green algae (BGA) and microcystin.³¹⁴ Microcystin congeners were quantified using a previously established LC/MS/MS method.³¹⁵

A three-stage microanalysis particle sampler (MPS-3, California Measurements, Inc.) impacted aerosol particles onto Formvar coated copper microscopy grids and silicon wafers (Ted Pella Inc.) for scanning electron microscopy coupled to energy dispersive x-ray spectroscopy (SEM-EDX) and optical photothermal infrared (O-PTIR) + Raman analysis, respectively. The MPS-3 operated at 2 L min^{-1} to impact particles with diameters $2.5 - 5.0\ \mu\text{m}$, $0.7 - 2.5\ \mu\text{m}$, and $< 0.7\ \mu\text{m}$ onto stages 1, 2, and 3, respectively. Aerosols were impacted onto glass fiber filters (Whatman, grade GF/c, 47 mm) for LC/MS/MS analysis using a cyclone (URG Corp., model 2000-30ED) and single stage impactor (URG Corp., model 2000-30FV) that operated at 3 L min^{-1} to collect particles $< 2.5\ \mu\text{m}$ in diameter. For comparison, aerosols were also impacted onto baked quartz fiber filters (Sigma Aldrich, 47 mm) using a five-stage impactor (TSI Inc., model 130A) that impacted particles with diameters $1.4 - 2.5\ \mu\text{m}$, $0.7 - 1.4\ \mu\text{m}$, $0.4 - 0.7\ \mu\text{m}$, $0.25 - 0.4\ \mu\text{m}$, and $< 0.25\ \mu\text{m}$ onto stages 1, 2, 3, 4, and 5, respectively. Ambient aerosol number size distributions in the range $0.52 - 19.8\ \mu\text{m}$ were measured by an aerodynamic particle sizer (APS, TSI Inc., model 3321) and averaged every 30 min.

5.2.2 LC/MS/MS Toxin Characterization

Particles impacted onto glass and quartz fiber filters were extracted following the method described by Wood et al.²⁹⁰ Filters were mixed with 5 mL of 70% methanol and sonicated for 15 minutes, after which the supernatant was poured into a glass vial. The extraction procedure was repeated for a total of three times. The supernatant of each filter were combined, filtered through a nylon syringe filter to remove particulates, dried under nitrogen, and solubilized in LC/MS grade water before LC/MS/MS analysis using a Thermo TSQ Quantiva triple quadrupole MS (Thermo Scientific).³¹⁵ Microcystin congeners were separated using gradient analysis (mobile phases of 0.1% formic acid in water and 0.1% formic acid in acetonitrile) and a C18 column (Thermo Accucore aQ, 50 x 2.1 mm, 2.6 μm) before detection using positive electrospray ionization mode. Concentrations of each microcystin congener were determined by calibration using commercially available standards (Enzo Life Sciences). Extract from the filters and aliquots from each corresponding freshwater sample were analyzed by LC/MS/MS to compare toxin concentrations present in the water column and aerosol phase.

5.2.3 Single Particle Analysis

SEM-EDX was performed using a FEI Helios 650 Nanolab Dualbeam electron microscope that operated at an accelerating voltage of 20.0 kV and a current of 0.40 nA. The Helios microscope utilized a high angle annular dark field (HAADF) detector to provide contrast between areas of differing chemical composition.¹⁴⁴ EDX spectra were acquired for 20 seconds using an EDAX detector and GENESIS EDX software version 5.10 (EDAX Inc.). O-PTIR + Raman spectroscopy was performed on a mIRage infrared + Raman microscope (Photothermal Spectroscopy Corp.). The mIRage contained a 40x Cassegrain reflective objective (0.78 numerical aperture, 8.3 mm working distance), continuous wave visible laser (532 nm, 200 mW), and two, pulsed tunable IR lasers (a quantum cascade laser, QCL, covers 880-1950 cm^{-1} at 100 kHz, 40-500 ns pulses, and 2 cm^{-1} spectral resolution; an optical parametric oscillator, OPO, covers 2700-3600 cm^{-1} at 150 kHz, <10 ns pulses, and 4 cm^{-1} spectral resolution). Raman spectra were obtained using a Horiba iHR320 module (Horiba Scientific) that contained a CCD detector and used a 600 gr/mm grating for 4 cm^{-1} spectral resolution. Raman spectra were collected using 3 accumulations at 5 second acquisition times for the range 500 – 4000 cm^{-1} .

5.2.4 Analysis of Insoluble Residues

Concentrations and size distributions of the insoluble residues present in each freshwater sample were analyzed by nanoparticle tracking analysis (NTA) using a NanoSight LM10 (NanoSight Ltd.) and the method for environmental samples described by Axson et al.²³⁸ NTA determines the size of individual particles in water by illuminating the sample with a 405 nm laser and monitoring the Brownian motion of particles, which is then used to determine the individual particle hydrodynamic diameter with the Stokes-Einstein equation.^{323,324} Light scattering was measured using a sCMOS camera (Hamamatsu, Orca) coupled to a 20x objective microscope as freshwater sample was flowed through the instrument using a syringe pump at 60 rpm. Ten 60 second videos of each freshwater sample were analyzed using the NTA 3.2 (Build 60) software to generate an average size distribution in the range 10 nm – 1 µm for each freshwater sample.

5.3 Results and Discussion

Microcystin and phycocyanin concentrations in each freshwater sample were measured immediately following sample collection. The Beach sample had the highest toxin concentrations: 194,000 ppt D-Asp³-MC-RR, 32,000 ppt MC-YR, 5400 ppt D-Asp³-MC-LR, and 370 ppt MC-LR (Figure 5.1). The Dock, Spillway, Central, and Prairie Creek samples all had similar toxin concentrations of: 14,000, 15,000, 23,000, and 19,000 ppt of D-Asp³-MC-RR, respectively; 0, 3500, 3500, and 3100 ppt of MC-YR, respectively; 430, 530, 630, and 580 ppt of D-Asp³-MC-LR, respectively; and 320, 0, 0, and 350 ppt of MC-LR, respectively. Phycocyanin concentrations averaged after triplicate measurements were as follows: 9500 ± 160 µg/L for the Dock sample, 6400 ± 190 µg/L for the Spillway sample, 9400 ± 670 µg/L for the Beach sample, 9700 ± 220 µg/L for the Central sample, and 2400 ± 60 µg/L for the Prairie Creek sample. The diversity in toxin and phycocyanin concentrations at each freshwater sampling location highlight the need for aerosolized toxin measurements at several points around the lake for thorough exposure assessments.

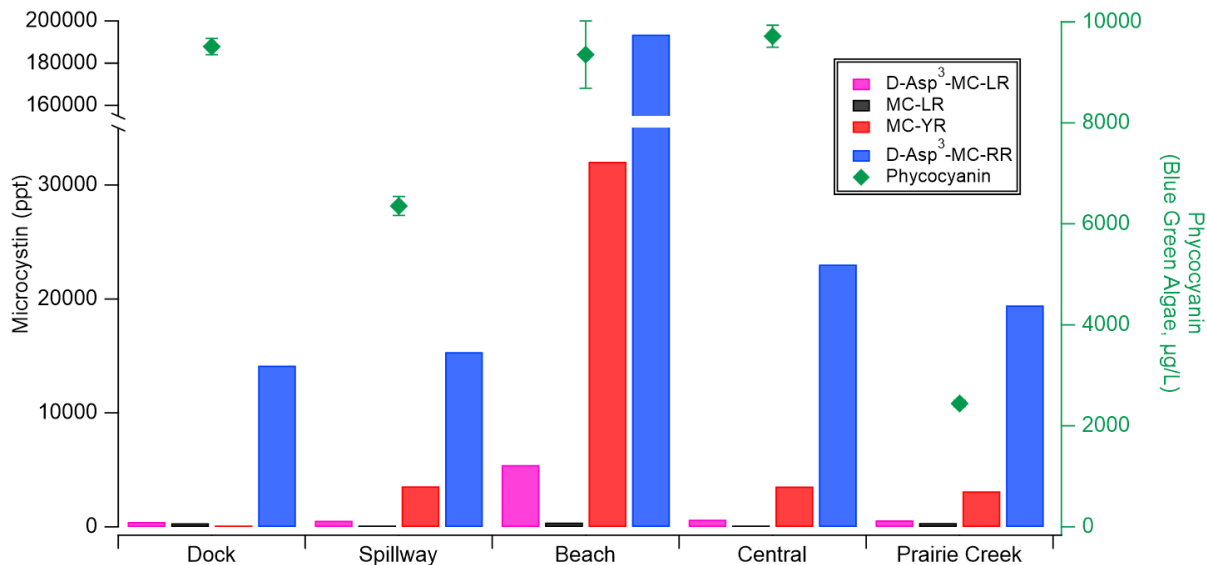


Figure 5.1. Total microcystin and phycocyanin (blue-green algae, BGA) concentrations for each freshwater sample.

Aerosol particles extracted from filters were analyzed with LC-MS/MS to compare the amounts of toxins present in the aerosol phase to those identified in the water column. Of the aerosol samples analyzed thus far, the only toxin detected was D-Asp³-MC-RR at 22 pg/m³ at the Central sampling location (Figure 5.2). These results are consistent with Backer et al. who observed ambient aerosolized microcystin concentrations up to 52 pg/m³ at a site in California.²⁸⁹ The aerosol sample collected at the Beach was below the limit of detection for this method (5 ppt). Analysis of additional aerosol samples collected at the Dock, Spillway, and Prairie Creek are planned and will give insight into the spatial distribution of toxin-containing particles in this region.

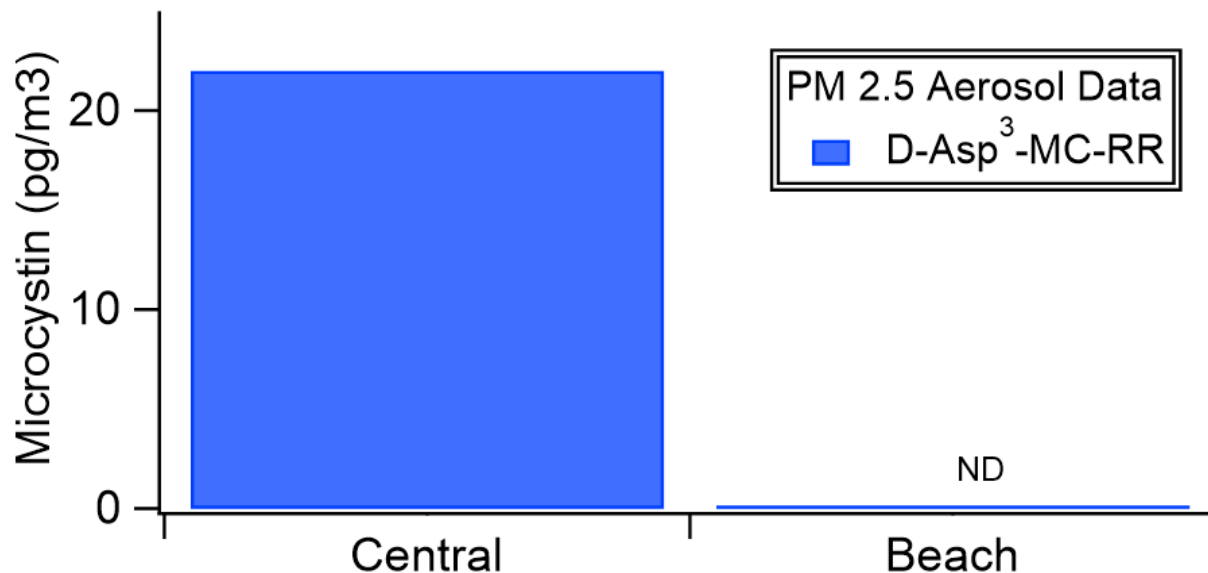


Figure 5.2. Aerosolized toxins at Grand Lake St Marys.

To identify individual toxin-containing aerosols with single-particle spectroscopy, a spectral signature of each toxin is necessary. Halvorson et al. characterized the Raman-active vibrational modes for microcystin-LR³²⁵ and other microcystin congeners.³⁶⁴ However, to our knowledge, no characterization of microcystin with infrared spectroscopy has been performed. Microcystin-LR was characterized both at the bulk (droplet) level with conventional Fourier-transform infrared spectroscopy (FTIR) and as a single particle with O-PTIR (Figure 5.3). Both spectra had similar modes, with peaks at 1100 cm^{-1} representing $\nu_{\text{as}}(\text{C-O})$, $\sim 1415\text{ cm}^{-1}$ representing $\nu_{\text{as}}(\text{O-H})$, 1530 cm^{-1} representing $\nu_{\text{as}}(\text{N-H})$, $\sim 1655\text{ cm}^{-1}$ representing $\nu_{\text{as}}(\text{C=C})$, $\sim 1720\text{ cm}^{-1}$ representing $\nu_{\text{as}}(\text{C=O})$. The spectral agreement suggests IR techniques can identify algal toxins in individual particles. Future work will aim to identify these markers in ambient particles and characterize the vibrational modes for other microcystin congeners.

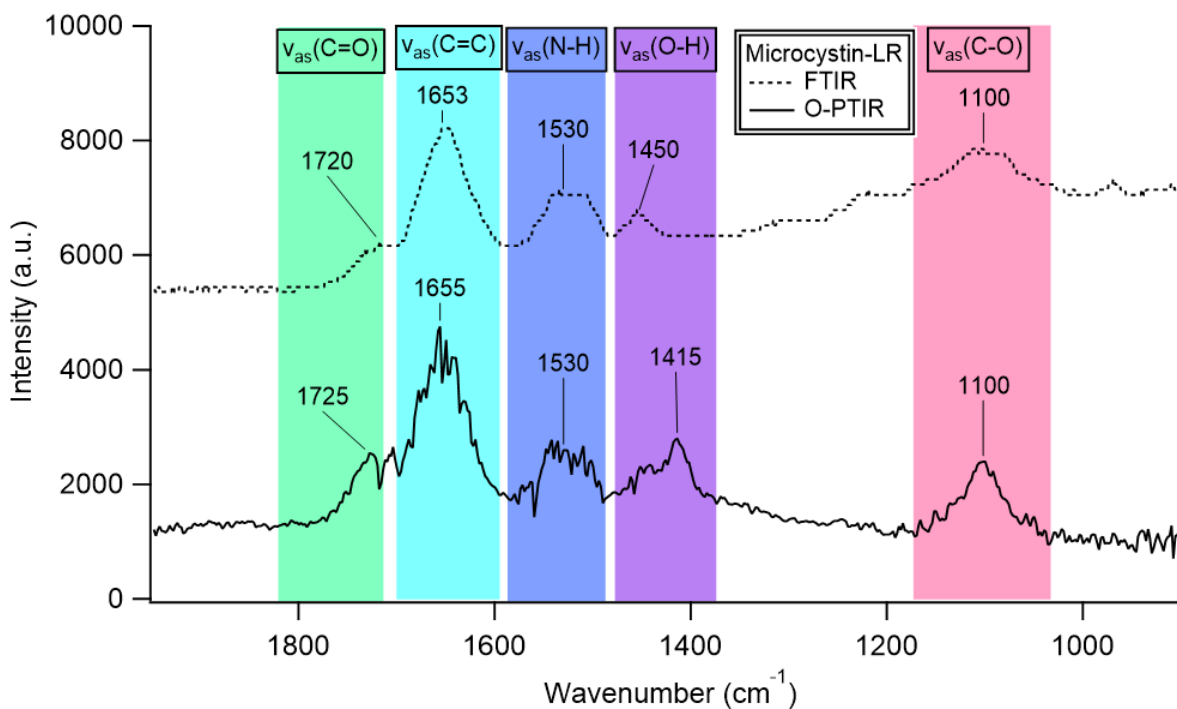


Figure 5.3. O-PTIR (solid trace) and FTIR (dashed trace) spectra of microcystin-LR.

Following toxin characterization, O-PTIR + Raman was used to identify ambient particle types. LSA particles were classified by $\nu(\text{O-H})$ at 1350 cm^{-1} , $\nu_{\text{as}}(\text{C-O})$ at 1414 cm^{-1} , and $\nu(\text{C=O})$ at 1610 cm^{-1} in the O-PTIR spectra³⁶⁵⁻³⁶⁸ and $\nu(\text{C-O})$ at 1087 cm^{-1} , $\delta(\text{C-H})$ at 1490 cm^{-1} , and $\nu(\text{C-H})$ at 2960 cm^{-1} in the Raman spectra (Figure 5.4).^{207,234,369-373} Secondary organic aerosol (SOA) particles were identified by $\nu_{\text{as}}(\text{SO}_4^{2-})$ at 1100 cm^{-1} and $\nu(\text{C-C})$ at 1625 cm^{-1} in the O-PTIR spectra^{50,52,57,374,375} and by $\nu_{\text{s}}(\text{SO}_4^{2-})$ at 1000 cm^{-1} and $\nu(\text{C-H})$ at 2470 and 2924 cm^{-1} in the Raman spectra.^{22,34,35,45,152,153} Organic particles containing $\nu(\text{C-H})$ at 1460 cm^{-1} and $\nu(\text{C-C})$ at 1610 cm^{-1} in the O-PTIR spectra^{57,365-367} also contained Raman modes representing $\nu(\text{C-O-C})$ at 1064 cm^{-1} , $\nu(\text{C=C})$ at 1340 cm^{-1} , $\nu(\text{C=C})$ at 1580 cm^{-1} , and $\nu(\text{C-H})$ at 2960 cm^{-1} .^{57,207,371-373} These modes commonly appear in biomass burning,^{285,376} dust,^{22,374,377-379} and soot aerosol,^{374,380,381} which are all present in this region.^{225,382-384} Additional analysis using elemental spectroscopy was necessary to separate SOA, biomass burning, and soot particles, and is discussed below. Lastly, biological particles were identified by containing $\nu(\text{C-N})$ at 1330 cm^{-1} , $\nu_{\text{a}}(\text{NO}_3^-)$ at 1351 cm^{-1} , $\nu(\text{C-H})$ at 1450 cm^{-1} , and $\nu(\text{C=N})$ at 1630 cm^{-1} in the O-PTIR spectra.^{50,52,57,385} The same particle contained $\nu(\text{NO}_3^-)$ at 1068 cm^{-1} , $\nu(\text{C=N})$ at 1569 cm^{-1} , and $\nu(\text{C-H})$ at 2960 cm^{-1} in the Raman spectra.^{33,43,153,386} The identification of biological particles generated from HAB-containing water aligns with the findings

of prior mass spectrometry analysis,^{168,355} and provides further evidence that material from HABs can become incorporated into aerosol particles.

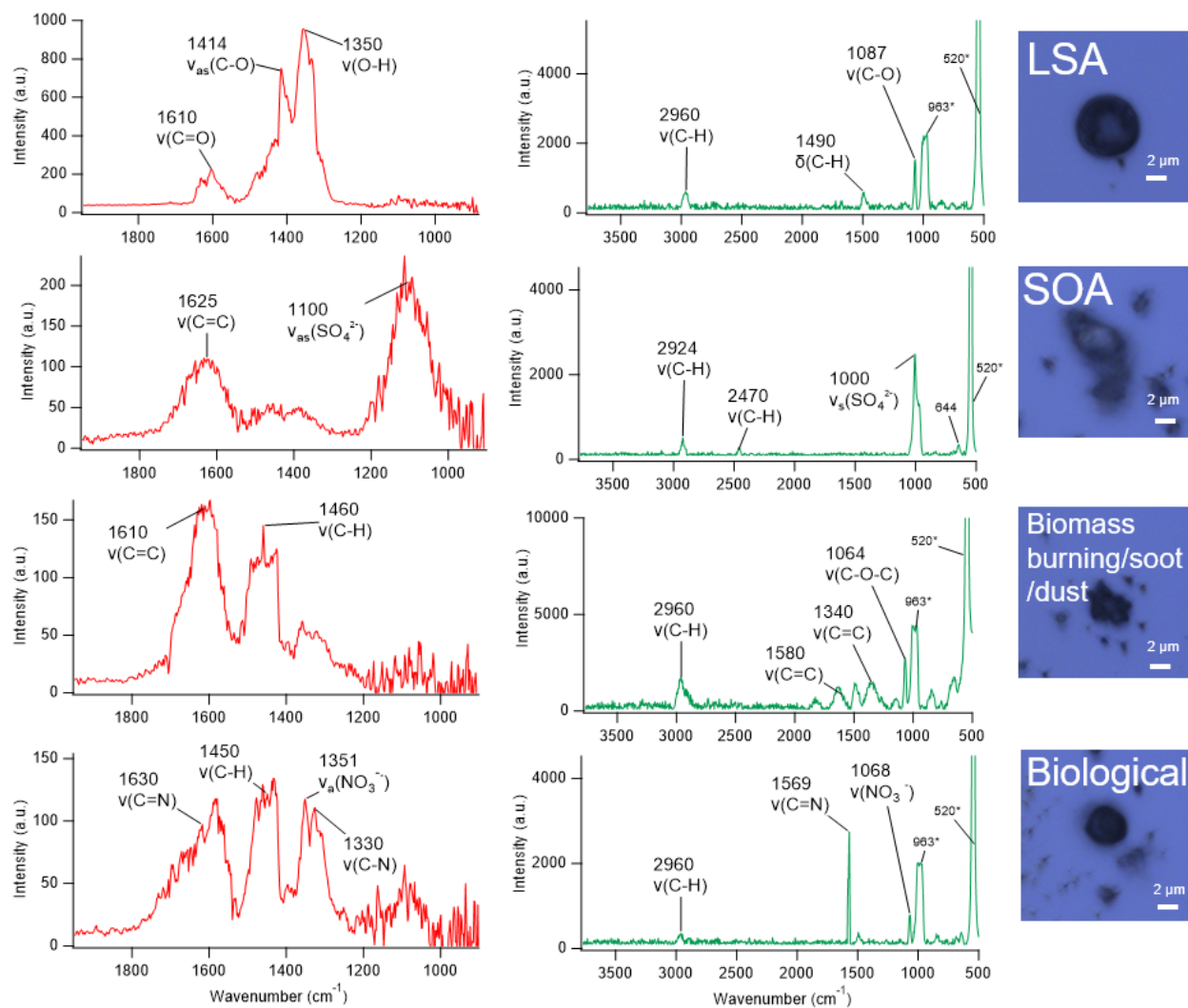


Figure 5.4. O-PTIR (left, red trace) and corresponding Raman spectra (middle, green trace) of representative individual particles defined as LSA, SOA, Biomass burning/soot/dust, and biological. Optical images of each particle analyzed are shown on the right. Peaks labeled with * in the Raman spectra indicate contribution from the substrate on which the particles were collected.

In addition to O-PTIR + Raman, ambient particles were also analyzed with SEM-EDX for complimentary, elemental spectra. SEM-EDX identified LSA particles by the presence of Ca, C, and O in the elemental spectra (indicative of CaCO_3) and an amorphous particle structure (Figure 5.5).^{5,27,168,285,355} SOA particles had a circular morphology and the elements C, O, and S.^{20,22,34,76,387} Biomass burning particles were differentiated from SOA by the presence of K.^{20,22,387} Soot particles were classified by an agglomerate structure and an elemental spectrum dominated by

C.^{20,22,387} Dust particles were identified by the presence of Fe and their supermicron size.^{5,20,238,285,387} Lastly, biological particles were identified by their unique structure and the presence of P.^{20,168,355} The particle types observed with SEM-EDX corroborate the O-PTIR + Raman analysis, and give us insight into the particle sources in this region.

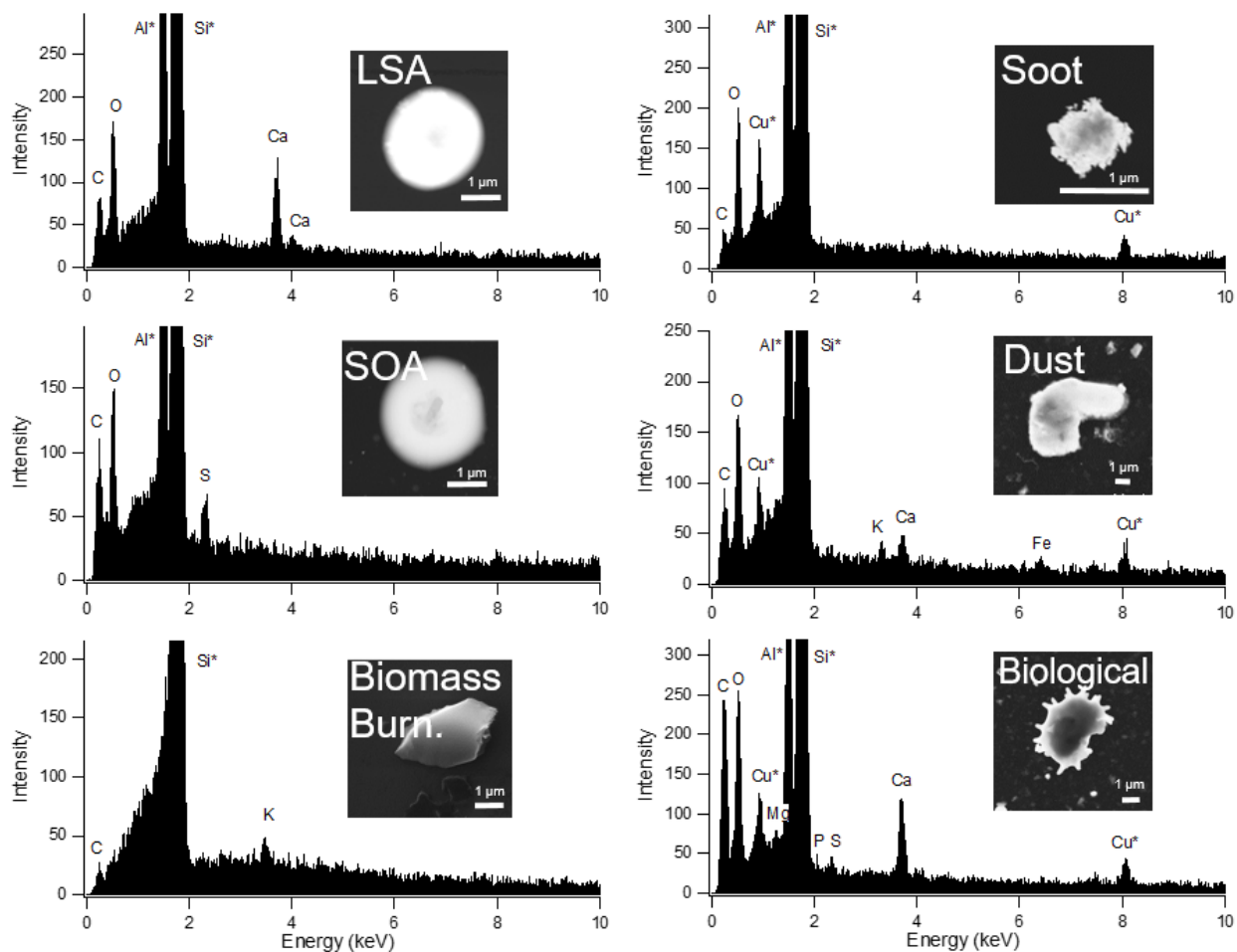


Figure 5.5. Scanning electron microscopy images with corresponding energy dispersive x-ray spectra of representative individual particles defined as LSA, SOA, biomass burning, soot, dust, and biological. Spectral peaks labeled with * indicate contribution from the substrate on which the particles were collected.

The size and number concentrations of ambient particles were compared to the size and concentration of insoluble residues present in the freshwater samples to investigate trends between water properties and aerosol formation. Aerosols collected near the Spillway had a size mode of 790 nm and insoluble residues of 150 nm (Figure 5.6), similar to previous analysis of insoluble residues in freshwater environments.³⁵⁵ Aerosol particles collected from the Central and Dock locations had slightly larger modes (840 nm and 1000 nm, respectively), but similar modes for

insoluble residues (150 nm each). The insoluble residues present in the Prairie Creek freshwater sample were the largest (220 nm) and corresponded to an increase in average aerosol size (940 nm). The Beach location had the largest size of aerosols (1100 nm), and 190 nm sized insoluble residues. Quantification of each aerosol and insoluble residue size distribution revealed that the concentration of insoluble residues impacted aerosol concentration. The Dock had the highest insoluble residue concentration ($1.82 \pm 0.06 \times 10^9$ insoluble residues/mL³) and average aerosol concentrations of 22.4 ± 0.5 particles/cm³. The Spillway and Central locations had similar insoluble residue ($1.64 \pm 0.03 \times 10^9$ and $1.51 \pm 0.06 \times 10^9$ insoluble residues/mL³, respectively) and aerosol (30.9 ± 0.6 and 32.5 ± 0.7 particles/cm³, respectively) concentrations. The Prairie Creek and Beach locations had the lowest amount of insoluble residues ($7.66 \pm 0.02 \times 10^8$ and $1.24 \pm 0.01 \times 10^9$ insoluble residues/mL³, respectively) and correspondingly lower aerosol concentrations were observed in these regions (18.1 ± 0.3 and 23.2 ± 0.4 particles/cm³, respectively). Generally, with the exception of the Dock sample, increased insoluble residue concentrations in the water column corresponded to increased aerosol production, similar to previous observations during late-bloom conditions.³⁵⁵

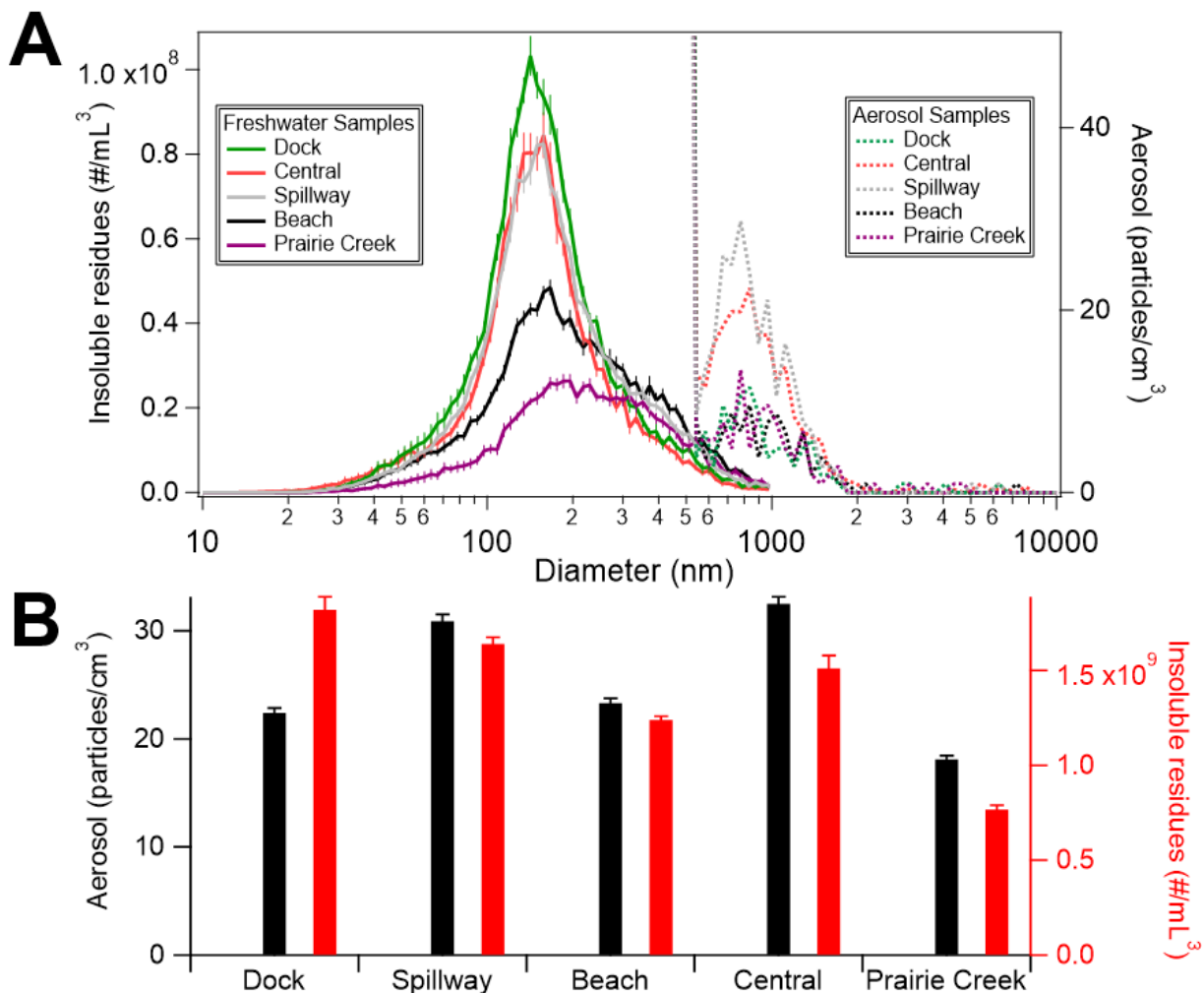


Figure 5.6. A) Average aerosol and POC number size distributions for each sampling location. B) Quantification of aerosol and POC number concentrations for each sample.

5.4 Atmospheric and Health Implications

The identification of the HAB toxin microcystin in ambient aerosols $< 2.5 \mu\text{m}$ in diameter poses a potentially significant human health risk via inhalation. The authors characterized microcystin-LR with O-PTIR + Raman for the first time, providing a detailed spectral signature of the toxin. This information will be valuable as future measurements will focus on identifying microcystin-LR spectroscopically in individual particles. In addition to microcystin characterization, ambient particles were characterized with O-PTIR + Raman and electron microscopy with elemental spectroscopy. LSA particles represented a significant fraction of the ambient particles observed in this region, suggesting that aerosols containing HAB toxins are abundant in regions experiencing severe HABs. The size and concentration of aerosol particles

was measured at several sites around the lake, with an increase in aerosol concentration generally correlated with an increase in insoluble residues in the water column. These observations align with previous laboratory measurements³⁵⁵ that reported enhanced ultrafine aerosol production with the presence of insoluble organics in the freshwater. Overall, the results obtained from this study highlight the potential health impacts of HAB toxin aerosolization in ambient environments.

Chapter 6. Simultaneous Optical Photothermal Infrared (O-PTIR) and Raman Spectroscopy of Submicrometer Atmospheric Particles

Adapted with permission from Olson, N. E., Xiao, Y., Lei, Z., and Ault, A. P.: Simultaneous Optical Photothermal Infrared (O-PTIR) and Raman Spectroscopy of Submicrometer Atmospheric Particles, *Anal. Chem.*, 92, 14, 9932-9939, 2020.

<https://doi.org/10.1021/acs.analchem.0c01495> Copyright 2020 American Chemical Society.

6.1 Introduction

Atmospheric aerosols impact climate by scattering or absorbing solar radiation, nucleating cloud droplets and ice crystals, and undergoing heterogeneous reactions with atmospheric gases.² Atmospheric particles represent the largest uncertainty in the evolving radiative balance of our changing climate² due to their complex and evolving physicochemical properties^{26,295,388} and the analytical challenge of measuring them.^{3,13} Particles with diameters $<1\ \mu\text{m}$ almost always account for $>99\%$ of particles by number in the atmosphere.^{2,294} Submicrometer particles are the most important contributors to the uncertain impacts of aerosols on radiative balance, and thus climate, due to their optical and cloud droplet forming properties.² Submicrometer particles also contribute a large fraction of fine particulate matter mass ($\text{PM}_{2.5}$, PM with aerodynamic diameters $<2.5\ \mu\text{m}$), the most important size range for impacts on human health.^{11,389} Inhaled submicrometer atmospheric particles deposit deep in the alveoli of the lungs, contributing significantly to pulmonary and cardiovascular diseases, and $\sim 8\%$ of global deaths annually from air pollution.³⁹⁰ Determining the size, chemical composition, phase state (liquid, semi-solid, or solid), and structure (e.g., core-shell) of individual particles is crucial for estimating their impacts on climate and health.^{14,74,105,391}

Spectroscopic methods providing both chemical and physical characterization of individual particles $<1\ \mu\text{m}$ under ambient conditions are limited.³ The most common microspectroscopic methods applied to atmospheric particles have traditionally been under vacuum, such as electron microscopy with energy dispersive X-ray spectroscopy (EDX) which provides elemental information,^{20,29,206,234,392} but limited information about organic species.

Scanning transmission x-ray microscopy coupled with near edge x-ray absorption fine structure spectroscopy (STXM/NEXAFS) provides greater spectroscopic detail on carbon-containing species,^{37,234,393} but focuses on electronic transitions and is often under vacuum, which can modify particle morphology. In contrast, vibrational spectroscopy methods (i.e., infrared (IR) and Raman) provide information on key inorganic species (e.g., sulfate, nitrate, and ammonium) and organic functional groups present in atmospheric particles under ambient conditions.^{3,45} Fourier Transform IR (FTIR) performed on bulk samples has shown the ability of vibrational spectroscopy to complement the widespread use of mass spectrometry in aerosol analysis.³⁹⁴

Raman spectroscopy has been used to study vibrational modes in individual atmospheric and laboratory-generated particles $\sim 1 \mu\text{m}$ or larger.^{22,33,36,37,45,48,49,286} To illustrate the benefits of vibrational spectroscopy for analysis of chemical species in atmospheric particles, inorganic sulfate ions (SO_4^{2-}) and organosulfates (ROSO_3^-) can be difficult to distinguish via aerosol mass spectrometry and other mass spectrometers using hard ionization methods,³⁹⁵ but Raman clearly differentiates modes for sulfate (973 cm^{-1}), bisulfate (1040 cm^{-1}), and organosulfates (1065 cm^{-1}) in model systems,⁴² particles generated in atmospheric chambers,³⁴ and the ambient atmosphere.⁴² Recent advances to push Raman $< 1 \mu\text{m}$ include surface enhanced Raman spectroscopy (SERS)^{43,46,396,397} and tip enhanced Raman spectroscopy (TERS),⁴⁷ but both are challenging due to inconsistent enhancements between substrates and for different vibrational modes.⁴⁶ Fluorescence emission after excitation by visible lasers provides additional challenges for the broad use of Raman spectroscopy for atmospheric particles, and is particularly challenging for primary biological, mineral dust, and soot particles, which can all fluoresce.^{37,48,239}

Atomic force microscopy coupled to photothermal infrared spectroscopy (AFM-PTIR)⁵³ has recently been applied to study particles and their chemical properties^{50-52,374,398} by providing information on vibrational modes in particles down to 100 nm diameter.^{50,52} The basic principle of AFM-PTIR is that a tunable IR laser, such as an optical parametric oscillator (OPO), scans across the mid-IR (i.e., $800\text{-}3600 \text{ cm}^{-1}$), while an AFM tip is in contact with a particle or surface.^{53,55,399,400} When the laser wavenumber excites a vibrational mode of a molecular species in the sample, the sample heats and slightly expands.^{50,55,401} This photothermal expansion is detected by the AFM tip at each frequency as the laser source is scanned across the spectral range to produce an IR spectrum. The relationship between IR absorption and photothermal expansion detected by the AFM-PTIR tip is shown in Equation 6.1:

Equation 6.1
$$u(t) = aG\alpha_T\Delta T(t)$$

where $u(t)$ is the photothermal expansion of the sample in m^2 , a is the area of the heated region in m^2 (e.g., sphere = circle = radius, cube = square = edge length), G is a geometric constant based on the shape of the sample (e.g., sphere or cube), α_T is the thermal expansion coefficient of the sample in K^{-1} , and $\Delta T(t)$ is the time-dependent temperature increase of the sample in K .⁵⁵ The thermal expansion of the sample (u) is proportional to the temperature change of the sample after absorption of incident IR radiation (ΔT), the power absorbed by the sample (P_{abs}), and the optical absorption from the Beer-Lambert Law.⁵⁵ Thus, IR absorption-like spectra are obtained by measuring the photothermal expansion of the sample as a function of wavenumber. See Dazzi and Prater for further details.⁵⁵ AFM-PTIR analysis has been time intensive; often taking 20-30 minutes to collect a high quality spectrum. Additionally, tip interactions, particularly during the analysis of soft or liquid samples, have been challenging.⁴⁰²

Optical photothermal infrared (O-PTIR) spectroscopy has recently been developed and overcomes both the issues of the AFM tip and slow collection time of earlier AFM-PTIR instruments.⁴⁰³ With O-PTIR, localized IR absorption is obtained after co-aligning a continuous wave (CW) visible laser (532 nm) and a pulsed, tunable IR laser on the sample and measuring the photothermal expansion that occurs when the incident frequency of the IR laser matches an IR absorption mode of the sample.^{401,404,405} The resulting modulated photothermal expansion causes a change in the intensity of the elastically (Rayleigh) scattered light from the visible laser,⁴⁰⁶ which can be processed to generate an IR spectrum. The photothermal response is shown in equation 6.2:

Equation 6.2
$$\Delta P_{PR} \propto \frac{\sigma N}{K C_p} \frac{\partial n}{\partial T} P_{pr} P_{IR}$$

where P_{PR} refers to the probe (visible laser) power, σ is the absorption cross section of the sample, N is the number density of absorbing molecules in the sample, K is the heat conductivity of the sample, C_p is the heat capacity of the sample, n is the refractive index of the illuminated volume of the sample, T is the temperature, and P_{IR} refers to the power of the IR laser.⁶² The generated O-PTIR spectra resemble FTIR absorbance spectra.⁶² Unlike traditional FTIR microscopy, O-PTIR can achieve submicron spatial resolution^{67,68} because the spatial resolution is determined by the visible laser, not the longer wavelength IR laser. The potential of this new analytical technique has

been shown during recent applications where O-PTIR imaged live cells,^{60,62} tissues,⁴⁰⁶ polymers,^{407,408} and plasmonic nanostructures.⁴⁰⁹

Herein, we report simultaneous collection of O-PTIR and Raman spectra to characterize submicron atmospheric particles. As the 532 nm probe laser used for O-PTIR also generates Stokes and anti-Stokes shifted photons from inelastic scattering, these can be detected simultaneously to generate both O-PTIR and Raman spectra. The capability of O-PTIR+Raman to analyze submicron particles with <1 minute acquisition times are shown below. Microscopy substrates were tested for optimal sample signal and to minimize interferences within OPTIR+Raman spectra. Organic and inorganic functional groups were characterized for both laboratory-generated standards and ambient aerosol particles. Mapping was performed on two-component, liquid-liquid phase-separated particles to determine the spatial distribution of chemical species. These results highlight the capability of O-PTIR to analyze particles well below the diffraction limited spatial resolution of traditional IR microscopy and show the power of the combined O-PTIR+Raman analytical method to study physicochemical properties of atmospheric aerosol particles.

6.2 Methods

6.2.1 Laboratory-Generated Aerosol Particle Samples

Standard solutions were prepared using 18.2 M Ω Milli-Q water and the following chemicals: ammonium sulfate ((NH₄)₂SO₄, Honeywell Fluka), ammonium nitrate (NH₄NO₃, Acros Organics), ammonium oxalate ((NH₄)₂C₂O₄, Sigma-Aldrich), sodium acetate (CH₃COONa, Sigma-Aldrich), sucrose (C₁₂H₂₂O₁₁, Fisher Scientific), polyethylene glycol (PEG 400, C_{2n}H_{4n+2}O_{n+1}, Honeywell Fluka), and sodium dodecyl sulfate (SDS, NaC₁₂H₂₅SO₄, Research Products International). All chemicals were >98% purity and used without further purification. Particles were generated by atomizing 50 mM solutions with a Collison nebulizer using HEPA-filtered air. Samples were inertially impacted onto silicon (Ted Pella Inc., product number 16013), quartz (Ted Pella Inc.), germanium (Wafer World Inc.), aluminum foil (Ted Pella Inc.), silver foil (ESPI Metals), and gold deposited onto silicon (Platypus Technologies) substrates using a microanalysis particle sampler (MPS, California Measurements Inc.). Samples impacted onto stage 3 of the MPS (<400 nm aerodynamic diameter before spreading after inertial impaction onto the substrates^{50,410}) were analyzed. To provide context with respect to mass of material detected, a 400 nm particle with a 50 mM concentration of ammonium sulfate contains 160 attograms of

sulfate per particle and 60 attograms of ammonium. Liquid liquid phase separated particles were generated by atomizing a mixed solution of PEG and ammonium nitrate at a 1:1 mass ratio using 1% by weight of each compound. All samples were stored in the dark at room temperature following established protocols²¹⁹ and analyzed within 24 hours at room temperature (23 °C) and RH (30%). At minimum, ten particles per sample were analyzed to ensure representative and reproducible spectra, with details on the number of particles analyzed for each sample available in the Supporting Information (Table E.1). All spectra were obtained at a single point (laser spot size ~450 nm) in the center of particles unless otherwise stated.

6.2.2 Ambient Particle Sampling

Atmospheric particles were collected onto silicon substrates in Ann Arbor, MI on February 4, 2020 from 13:04 – 14:15 EST using an MPS. Stages 1, 2, and 3 (aerodynamic diameters of 2.8 – 5.0 μm , 0.4 – 2.8 μm , and <0.4 μm , respectively) were analyzed.

6.2.3 Optical Photothermal Infrared (O-PTIR) Spectroscopy

This study used a mIRage infrared + Raman microscope (Photothermal Spectroscopy Corp.) based on the O-PTIR concept of Zhang et al.,⁶² which was recently utilized for polymers and fibers.^{58,59,411} The mIRage contains a custom microscope frame with two motorized objectives: a visible objective (4 \times , 0.13 numerical aperture, 17.3 mm working distance, Nikon Plan Fluor) and a Cassegrain reflective objective for simultaneous use of IR and visible lasers (40 \times , 0.78 numerical aperture, 8.3 mm working distance, 55 μm x 42 μm field of view). The mIRage uses a CW laser source (532 nm, 200 mW, ~20% reaches sample) as the probe (detected by a photodetector, range 0-1 mV) and two pulsed, tunable infrared lasers to generate photothermal enhancement. A quantum cascade laser (QCL) covers 880-1950 cm^{-1} with tunable repetition rate of 100 kHz, 40-500 ns pulses, up to 1 W power per pulse (much lower in practical use, see below), and 4 chips with spectral resolution of 2 cm^{-1} . An OPO covers the range 2700-3600 cm^{-1} with tunable repetition rate up to 150 kHz, <10 ns pulses, >250 mW power per pulse, and spectral resolution of 4 cm^{-1} .

Focusing was optimized for each QCL chip at 1726, 1575, 1270, and 1026 cm^{-1} using the IR signal from a polyethylene terephthalate standard within the instrument. IR spectra were collected at a scan rate of 100 cm^{-1}/s for 15 s acquisitions and averaged after 3 accumulations. The

IR laser repetition rate was set at 100 kHz and 300 ns per pulse. The powers of the IR and visible lasers were set to approximately 4-10 mW each (details in Appendix E and Table E.2). Prior to collecting sample spectra, a background profile of the laser was collected from an AFM cantilever that absorbs uniformly at all wavenumbers. The sample spectra were then divided by the background profile to produce photometrically accurate background compensated spectra across the full spectral range.

6.2.4 Raman Microspectroscopy

Raman scattering was detected after photons passed back through the Cassegrain objective into a Horiba iHR320 module (focal length = 320 mm) with three gratings (600, 1200, and 1800 groove/mm), spectral dispersion at 500 nm of 2.31 nm/mm, scan speed of 160 nm/sec, and step size of 0.002 nm. Spectra were collected across the spectral range of 200–4000 cm^{-1} using the 600 groove/mm grating to yield spectral resolution of 4 cm^{-1} . Raman spectra were collected using 5 s acquisitions with 3 accumulations and calibrated against the known Raman peaks of silicon and acetaminophen.

6.2.5 O-PTIR Imaging

PTIR Studio software (version 4.0, Photothermal Spectroscopy Corp.) was used to process spectra and IR images. Spectra were not smoothed and raw data is shown. IR images were generated by inputting the wavenumber of interest and scanning the field of view with 100 nm steps.⁵⁰ IR absorbance images were generated to show the intensity of IR signal on a color scale from 0 – 1 mV.

6.3 Results and Discussion

A diagram illustrating the operating principle of O-PTIR+Raman is shown in Figure 6.1a. A pulsed IR laser and CW laser of 532 nm are co-aligned and focused through a Cassegrain objective onto the sample. If the vibrational energy levels of the sample match the incident frequency of IR light, IR light is absorbed by the sample (Abs_{IR}) leading to photothermal expansion (Δh) and change in refractive index based on the heat capacity (C_p), heat conductivity (K), and absorption cross section of the sample (σ).^{49,52,62} Table E.2 includes available values for the compounds used. The change in scattering (Δp_{scat}) due to changes in refractive index with temperature and photothermal expansion is detected and extracted to give an IR spectrum of the

sample.^{62,406,412} The inelastically scattered photons from the sample pass back through the Cassegrain objective to a Raman spectrometer. With O-PTIR+Raman, we are able to observe molecular vibrations associated with changes in the dipole moment (IR) and polarizability (Raman) of the species analyzed. The ability to detect both IR active and Raman active vibrational modes simultaneously from the same spot and with the same submicron spatial resolution allows for far more comprehensive sample characterization. As an example, we show the symmetric and anti-symmetric stretching modes of sulfate molecules (Figure 6.1b) with the corresponding spectra generated from an ammonium sulfate particle (Figure 6.1c). For example, $\nu_s(\text{SO}_4^{2-})$ is not IR active as the dipole moment of this symmetric molecule does not change during this molecular vibration, however, the polarizability does, making it Raman active. There is a substantial dipole moment change for $\nu_{as}(\text{SO}_4^{2-})$ that corresponds to intense signal in the IR spectrum, but the Raman activity of $\nu_{as}(\text{SO}_4^{2-})$ is weaker. Thus, by obtaining both IR and Raman spectra at the same point simultaneously, greater molecular detail can be obtained for a wide range of samples

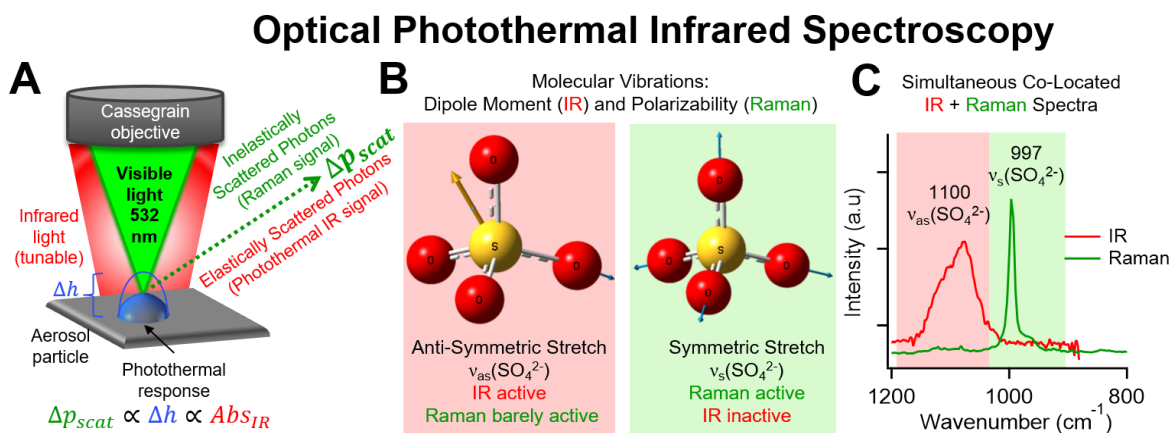


Figure 6.1. Schematic of optical photothermal infrared spectroscopy. A) Infrared and visible light are focused on the sample through a Cassegrain objective, inducing a photothermal expansion of the particle. Light scattered from the sample (Δp_{scat}) is proportional to the photothermal expansion of the particle (Δh) and absorbance of IR light (Abs_{IR}). Simultaneous IR and Raman spectra are obtained from a single point. B) Molecular vibrations are shown corresponding to anti-symmetric (red) and symmetric (green) stretching modes of sulfate. C) IR and Raman spectra obtained from a sulfate-containing particle. The peak width of $\nu_{as}(\text{SO}_4^{2-})$ is broader than $\nu_s(\text{SO}_4^{2-})$ as 3-fold degeneracy of T_d symmetry breaks down in non-ideal aerosol environment.

Optimal substrates for both spectroscopies need to be determined as IR and Raman spectra have seldom been collected simultaneously, particularly not from the same spot and with the same spatial resolution. Interferences for different substrates were explored by impacting ammonium sulfate particles onto common microscopy substrates including silicon, quartz, germanium,

aluminum foil, silver foil, and Platypus flat gold. IR vibrational modes observed include $\nu_{\text{as}}(\text{SO}_4^{2-})$ at 1100 cm^{-1} , $\delta(\text{NH}_4^+)$ at 1422 cm^{-1} , $\nu(\text{N-H})$ at $\sim 3040\text{ cm}^{-1}$, with $\delta(\text{O-H})$ at 1766 cm^{-1} and $\nu(\text{O-H})$ at $\sim 3220\text{ cm}^{-1}$ from water (Figure 6.2A). Ammonium sulfate modes are comparable to FTIR spectra of ammonium sulfate (Figure E.1).^{50,52,375} Raman spectra contained peaks at 977 cm^{-1} representing $\nu_{\text{s}}(\text{SO}_4^{2-})$, 634 cm^{-1} for an umbrella bend $\delta(\text{SO}_4^{2-})$, 471 cm^{-1} representing a scissoring motion for SO_4^{2-} , and $\sim 3168\text{ cm}^{-1}$ representing $\nu(\text{N-H})$ (Figure 6.2B).^{22,34,35,45} Optical images of each particle are shown in Figure 6.2C, with images of blank substrates and peaks from substrates listed in Table E.3. Fluorescence was generated with flat gold substrates, which overwhelmed the Raman signal of the sample (Figure E.2). Al foil provided weak IR signal, possibly due to the rough surface. Quartz showed interference peaks in the IR spectra at 1056 and 1223 cm^{-1} and an uneven baseline in the Raman spectra. While germanium and Ag foil had minimal spectral interferences, the IR signal generated from particles on these substrates was lower than with silicon. Silicon was determined to be the best substrate and was used hereafter due to minimal interference in the Raman spectra (520 and 963 cm^{-1}), no interference in the IR spectra, and intense sample signal compared to other substrates tested.

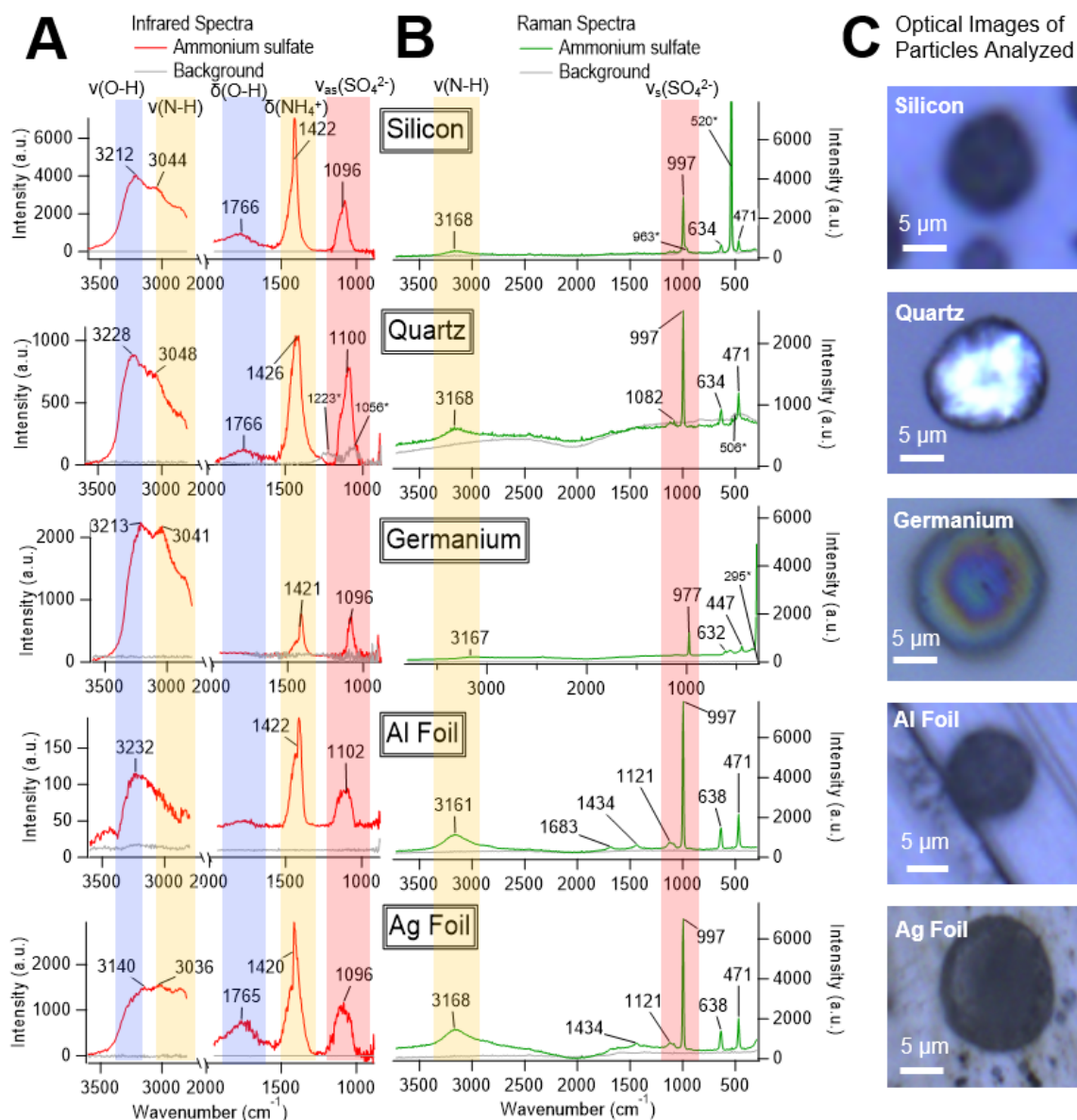


Figure 6.2. IR and Raman spectra of ammonium sulfate particles on different substrates. Background spectra were taken adjacent to the particle on a clear location of the substrate. Peaks labeled with asterisks denote contribution from the substrate and are listed in Table E.2. Optical images of the particles analyzed are shown in panel C. All particles had aerodynamic diameters <400 nm before spreading after inertial impaction onto the substrates, with spreading ratios typically between 4:1 to 10:1.^{39,57} Intensities on IR and Raman spectra are in arbitrary units, but are not related, which is also true for subsequent figures.

Aerosols from single-component solutions were used to evaluate the ability of O-PTIR to study a range of species commonly observed in atmospheric particles. Representative IR and Raman spectra of laboratory-generated particles (ammonium nitrate, sodium acetate, sucrose, SDS, and ammonium oxalate) on silicon substrates are shown in Figure 6.3, with spectral

assignments and corresponding references reported in Table E.4. Optical images of all particles analyzed are shown in Figure E.3. The combined O-PTIR+Raman spectra clearly distinguish organic and inorganic vibrational modes commonly found in atmospheric particles.

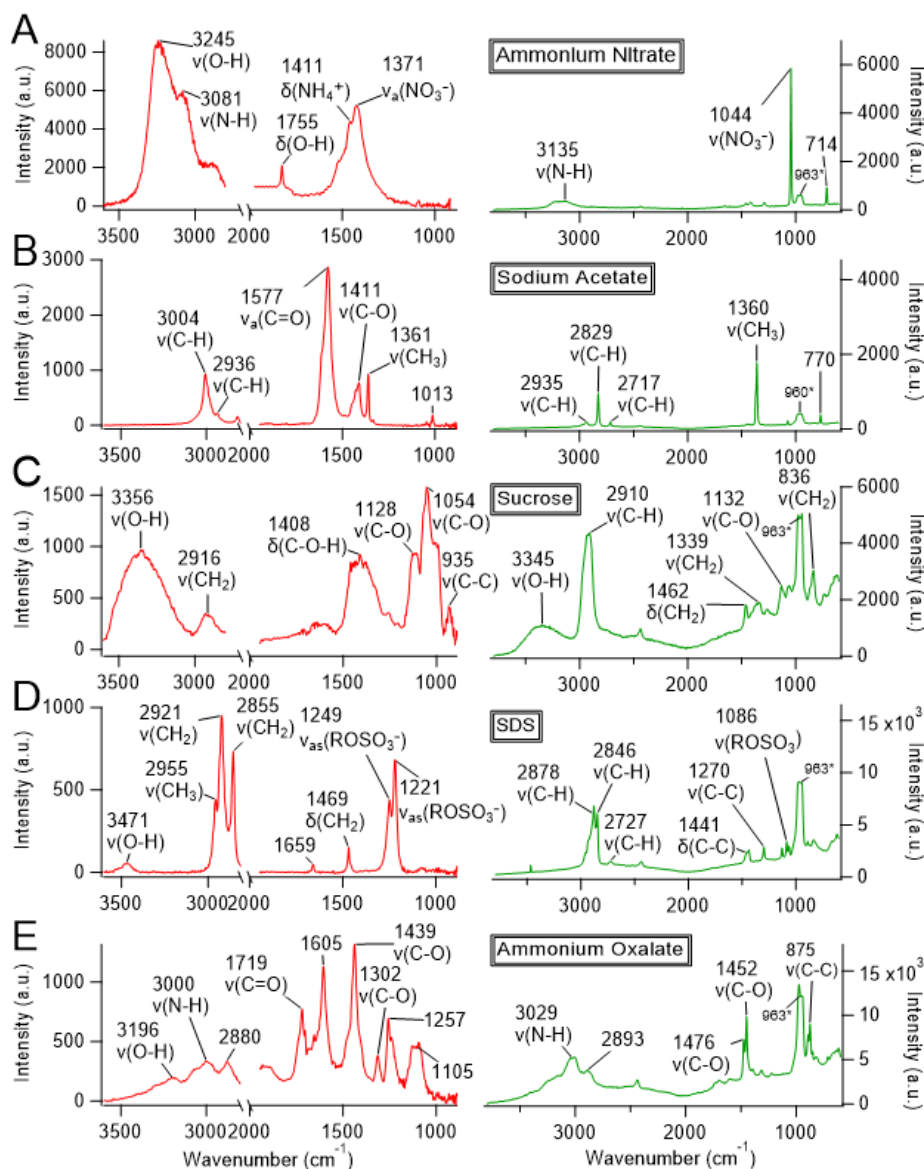


Figure 6.3. IR (left, red trace) and Raman (right, green trace) spectra of laboratory-generated standards. A) ammonium nitrate, B) sodium acetate, C) sucrose, D) SDS, and E) ammonium oxalate particles. Peaks labeled with * in the Raman spectra indicate contribution from the silicon substrate. All particles had an aerodynamic diameter <400 nm before spreading after inertial impaction onto the silicon substrates.

Ambient particles were analyzed with O-PTIR+Raman for the first time. Particles containing ammonium nitrate were identified by IR modes at 1351 and 1411 cm^{-1} , indicative of $\nu_a(\text{NO}_3^-)$ and $\delta(\text{NH}_4^+)$, respectively (Figure 6.4A).^{50,385} The same particle contained Raman modes

at 1068 and 3026 cm^{-1} , representing $\nu(\text{NO}_3^-)$ and $\nu(\text{N-H})$, respectively.^{33,43,45} The agreement between IR and Raman provide robust evidence for the presence of ammonium nitrate, much stronger than either IR or Raman would provide independently due to common peaks in similar regions (e.g., organosulfates $\sim 1065 \text{ cm}^{-1}$ in Raman).^{34,42} Similarly, ambient sulfate-containing particles were identified by $\nu_{\text{as}}(\text{SO}_4^{2-})$ at 1107 cm^{-1} in the IR spectrum^{50,375} and $\nu_{\text{s}}(\text{SO}_4^{2-})$ at 990 cm^{-1} in the Raman spectrum (Figure 6.4C).^{34,35,45} This particle also contained organic modes identified as $\delta(\text{C-H})$ in the IR spectrum⁴¹³ and $\nu(\text{C-H})$, $\nu(\text{CH}_2)$, and $\delta(\text{CH}_2)$ in the Raman spectrum,^{370,372} similar to mixtures of sulfate and organic material identified in ambient particles with AFM-PTIR^{50,76,374} and Raman.^{22,37,43} Additional organic vibrational modes were identified in both IR and Raman spectra of ambient particles (Figure 6.4B), resembling modes detected in oxalate,³⁶⁸ sucrose,³⁷⁰ and SDS^{36,413} (Figure 6.3). OPTIR+Raman spectra show that significant chemical detail can be obtained from atmospheric particles containing complex mixtures of chemical species.¹³

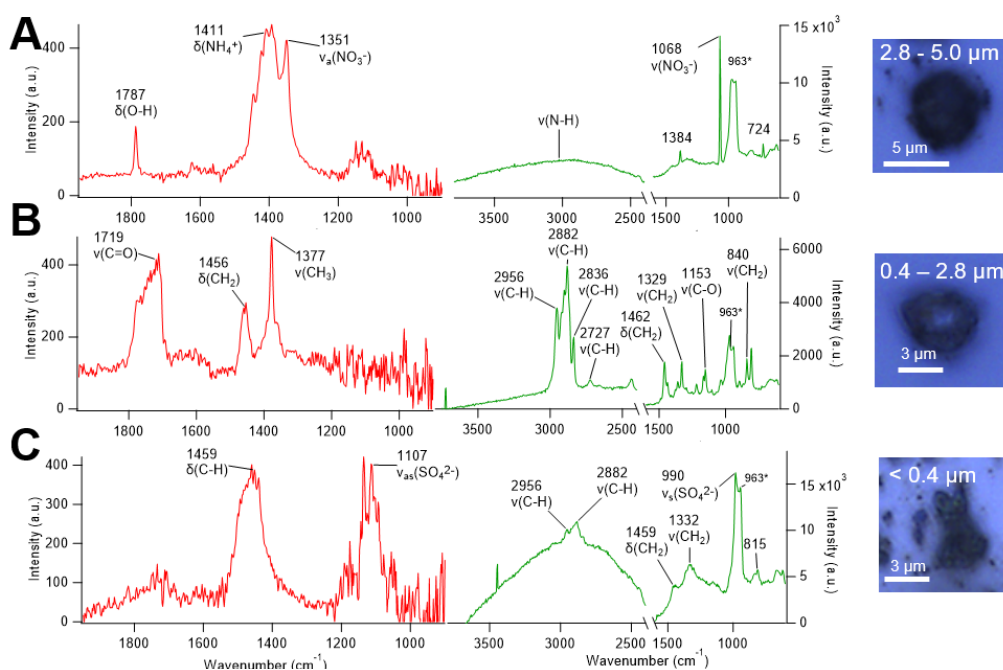


Figure 6.4. IR (left, red trace) and Raman (right, green trace) spectra obtained from ambient particles. Spectra represent A) ammonium nitrate-containing, B) organic, and C) organic- and sulfate-containing particles. Peaks corresponding to vibrational modes identified from laboratory-generated standards are labeled. Peaks labeled with * in the Raman spectra indicate contribution from the silicon substrate. Optical images of each particle analyzed are shown on the right and are labeled with the size range of the impactor stage on which the particle was collected. Uneven baselines in the Raman spectra are likely from fluorescence.

Atmospheric particles are frequently not homogeneous, but rather adopt core-shell and other complicated morphologies.^{74,76,117} To demonstrate the spatial distribution of chemical species within an individual particle, IR spectra and maps were collected from liquid-liquid phase-separated particles containing PEG and ammonium nitrate with aerodynamic diameters <400 nm, which spread upon impaction. A line scan (Figure 6.5A) collected spectra every 2.0 μm across a two-component, phase-separated particle. IR spectra collected from the core and shell of the particle confirm the presence of nitrate primarily in the particle core and PEG primarily in the particle shell (Figure 6.5A). The IR peak intensity ratio of 1105 and 1371 cm^{-1} , corresponding to $\nu(\text{C-O})^{50}$ and $\nu_{\text{a}}(\text{NO}_3^-)^{50}$ respectively, was calculated at each point in the line scan to show the enhancement of PEG on the edge of the particle with minimal PEG in the particle core (Figure 6.5B). Two IR modes representing $\nu(\text{C-O})^{50}$ and $\nu_{\text{a}}(\text{NO}_3^-)^{50}$ (1105 and 1371 cm^{-1} , respectively) were observed with differing spatial distributions in spectral maps with 100 nm step sizes (Figure 6.5C). Inorganic components (nitrate) were located primarily in the core of the particle, while the outer layer of the particle was primarily organic (PEG), similar to previously observed phase-separated particles studied in the laboratory^{34,52,117} and in ambient environments.⁷⁶ These results show that O-PTIR can determine the distribution of chemical species within individual particles related to particle morphology, which can be used to study aerosol physicochemical mixing state.¹³

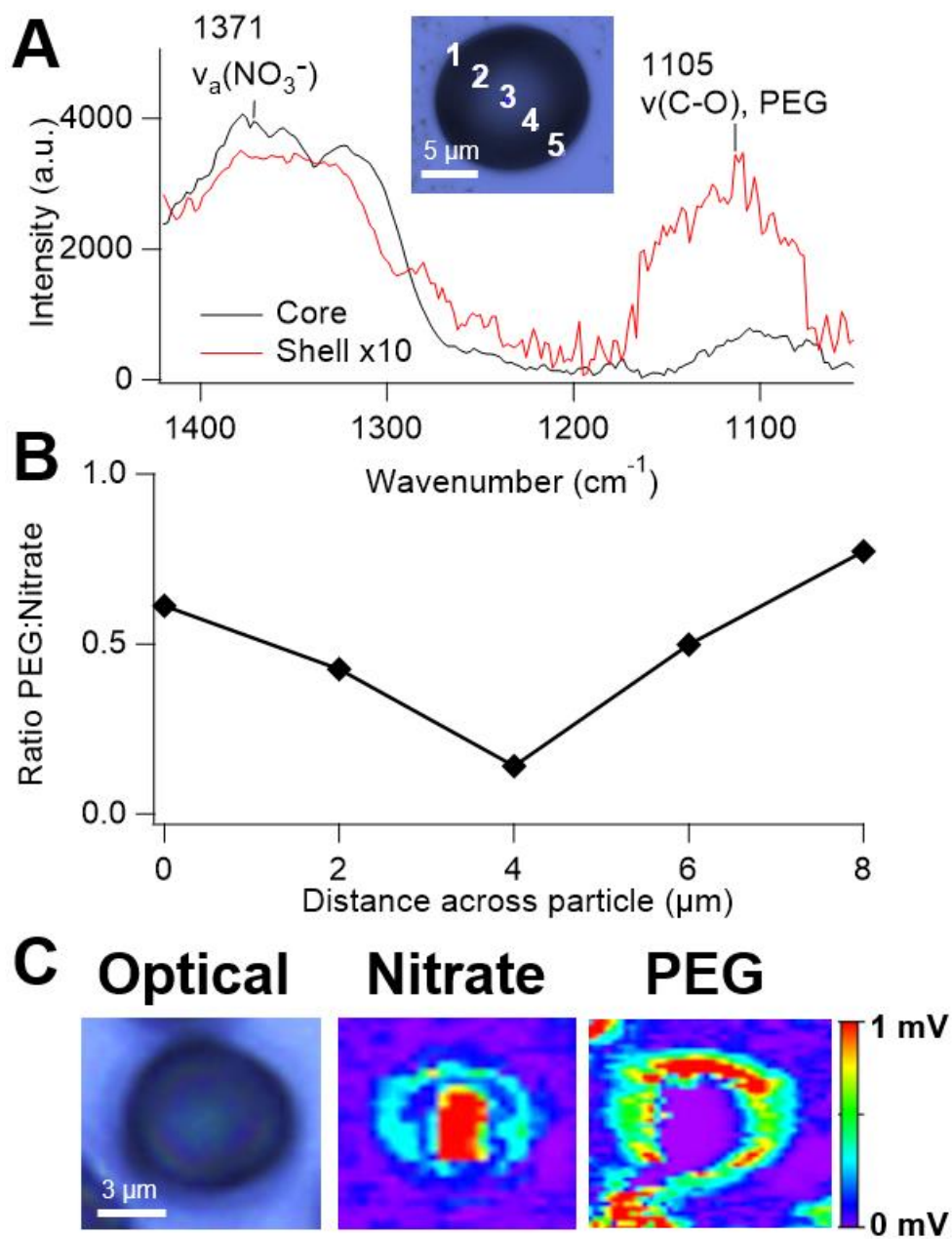


Figure 6.5. IR spectra and maps of a phase-separated particle. A) IR spectra collected from the core (point 3 on the line scan) and shell (point 1) of phase-separated PEG + ammonium nitrate particle. Shell spectra was multiplied x10 for clarity. The optical image of the particle analyzed includes numbers denoting the location of the five spectra acquired during the line scan. B) Ratio of the intensity of PEG and nitrate IR peaks obtained during the line scan, confirming the presence of PEG primarily in the outer shell of the particle with nitrate in the core. C) Optical image of phase-separated PEG + ammonium nitrate particle, with maps showing the location of nitrate (1371 cm^{-1}) in the core of the particle and PEG (1105 cm^{-1}) in the outer shell using 100 nm step size. It should be noted that repeating scans (2 or more) across the sample resulted in minor beam damage to organic compounds and is visible through the slightly irregularly-shaped shell.

6.4 Conclusions

The simultaneous spectroscopic and physicochemical analysis of submicron aerosol particles is analytically challenging because traditional vibrational spectroscopy techniques, such as FTIR, struggle to investigate particles in the size range reported herein (<400 nm aerodynamic diameter before spreading after impaction onto the substrates) as the diffraction limit of IR light traditionally limits spatial resolution. O-PTIR+Raman was applied to simultaneously collect vibrational IR and Raman spectra from individual particles <400 nm aerodynamic diameter under ambient conditions, allowing for faster analysis times and complementary chemical information. We show the potential of O-PTIR+Raman for single-component model systems, two-component phase-separated particles, and ambient aerosol particles. The contactless nature of O-PTIR enables analysis of different phase states (liquid, semi-solid or solid).^{16,34,76} High spatial resolution maps of vibrational modes presented within particles demonstrate the ability of this analytical technique to determine intra-particle chemical differences, which impact aerosol reactivity in the atmosphere.¹⁶ Future work will push the analytical capabilities of O-PTIR to even smaller particles, with a focus on viscous particles that spread less upon impaction and ambient particles whose viscosity changes as a function of relative humidity and temperature. Spectral information obtained will enable key insights regarding physicochemical properties of atmospheric particles in a critical size range for climate and human health. The power of O-PTIR+Raman, shown above for laboratory-generated and atmospheric particles, has applications for a wide range of scientific disciplines from materials science to the biosciences.

Chapter 7. Conclusions and Future Directions

7.1 Conclusions

The impacts of atmospheric aerosol particles on climate and human health are dependent on the physical structure and chemical composition of individual particles. However, aerosol physicochemical properties are seldom measured in detail due to the analytical challenges associated with determining species present in minute concentrations and the time-intensive manner of characterizing the structure of individual particles. This dissertation focuses on the development and use of microspectroscopic techniques to characterize the physicochemical properties of model and ambient particles in the mid-latitude regions. The multimodal approach applied within each chapter gives insight into the complex chemical compositions observed while also monitoring the evolving physical structure of particles during their atmospheric lifetime. The information discovered helps discern the climate and health impacts of particles and provides motivation for future studies.

Chapter 2 discussed the physicochemical changes to secondary organic aerosol (SOA) particles after reactions with gas-phase IEPOX, an isoprene oxidation product. Particles initially had two distinct phases: an inorganic core followed by a coating with organic SOA material. After exposure to gas-phase organics, the morphology and composition of the particle core changed. Organics were present in the particle core (as determined by SEM-EDX) due to the formation of organosulfate species (as determined by Raman spectroscopy). The formation of viscous organosulfates changed the internal structure of the core and increased the viscosity of the particles (as determined by spreading ratios calculated from AFM data). The increase in particle viscosity likely inhibits further heterogeneous reactions and climate-relevant properties, such as water uptake. This chapter suggests the importance of not only monitoring chemical composition but also physical morphology over the atmospheric lifetime of SOA particles.

Chapter 3 investigated the climate impacts of freshwater-derived lake spray aerosol (LSA) particles. An aircraft-based campaign was performed over Lake Michigan to collect ambient

particles and cloudwater. SEM-EDX discerned similar structures and compositions for ambient and laboratory-generated LSA and the insoluble residues present in ambient cloudwater, suggesting the incorporation of LSA into clouds above Lake Michigan. Computer controlled SEM-EDX was applied to thousands of particles for quantitative measurements of the elements present in individual particles as well as the amount of LSA related to other particle types observed. The elemental ratios calculated from the insoluble cloudwater residues were similar to those present in LSA and Lake Michigan freshwater, providing further evidence of the source of these cloudwater residues. Additionally, the amounts of LSA, dust, and SOA observed were similar to previously reported measurements in the Great Lakes region. This study suggested the incorporation of LSA into clouds above the Great Lakes, a phenomenon that likely occurs in other regions around the globe with large bodies of freshwater. The results obtained give insight into the composition and formation of lake-effect precipitation in this region.

Chapters 4 and 5 explored the health impacts of LSA by studying the incorporation of algal toxins into aerosol particles. Harmful algal blooms (HABs) are known to release toxins into freshwater lakes, but little is known about the transfer of these toxins into the aerosol phase. Chapter 4 was a laboratory-based study in which ambient freshwater was collected from a HAB-infested lake and brought to the lab for analysis. Eight toxins were identified in the freshwater sample before aerosols were generated in a controlled laboratory setting, with seven toxins detected in the aerosol phase. These results suggest the transfer of toxins from water into the atmosphere, with likely impacts on human health through inhalation of HAB toxins. An enrichment of the most hydrophobic toxins was discovered in the aerosol particles relative to the freshwater samples, suggesting the importance of simultaneous measurement of freshwater and aerosolized toxins to fully discern the impacts of HABs on human health. Chapter 5 explored this phenomenon through an ambient study performed on Grand Lake St. Mary in Ohio. Similarly to Chapter 4, HAB toxins were identified in freshwater and aerosol samples, with an enrichment of hydrophobic toxins in the aerosol phase. Together, these chapters explore the health impacts of freshwater-derived particles formed during HAB conditions on lakes.

Chapter 6 applied a new multimodal microspectroscopic method, optical photothermal infrared (O-PTIR) + Raman spectroscopy, to study atmospheric particles for the first time. First, the ideal substrate was determined based on minimal interferences within both types of spectra and intense sample signal. Next, this method was validated by analyzing a variety of standard

compounds commonly identified in aerosol particles and comparing the spectra obtained to those reported in the literature. Ambient particles were collected in Ann Arbor and analyzed according to the vibrational modes identified in the standard particles, providing the first analysis of O-PTIR + Raman to ambient atmospheric particles. Lastly, phase-separated particles were chemically analyzed and mapped to show the distribution of chemical species within a single aerosol particle. This method significantly enhanced the resolution of IR spectroscopy to allow for analysis of submicron particles. Additionally, the ability of this technique to study heterogeneous samples advances the fields of both atmospheric and analytical chemistry.

7.2 Future Directions

The research described within this dissertation addresses the challenge of physicochemical measurements of aerosol particles relevant to the mid-latitude regions, with specific chapters focusing on the climate and health impacts of these particles. These five research chapters have contributed new insights into aerosol physicochemical characterization using both novel and established single-particle microspectroscopic methods. However, further work can be performed to understand more about the properties of model systems and ambient aerosol particles.

In Chapter 2, the effects of heterogeneous reactions on aerosol physicochemical properties were studied using model aerosols generated in a laboratory chamber. Though multiple types of organic coatings were investigated, these experiments used one type of gas-phase organic species (IEPOX), one seed particle (ammonium sulfate), and one relative humidity condition (50%). Further studies are warranted that study reactions between different gaseous species (limonene, for example), different starting materials (ammonium nitrate, for example), a wider range of relative humidity conditions, temperature, size of seed particles, and pH of seed particles. Furthermore, the analysis of ambient phase-separated particles from different regions around the globe would be useful to fully classify the changing physicochemical properties of aerosol particles after reaction with organic gases. Lastly, quantitative particle viscosity measurements are needed to assess the effect of viscosity on climate-relevant properties such as water uptake, for example.

Chapter 3 involved an ambient aircraft campaign that investigated the incorporation of freshwater aerosol into clouds above Lake Michigan. This campaign was a case study performed in July 2016, warranting additional measurements of particle and cloudwater composition during different seasons and in different global regions. Additional measurements of the cloud-forming

efficiencies of particles with organic and biological components are needed to fully understand the climate-relevance of freshwater particles. Analysis of LSA using a cloud condensation nuclei counter would provide quantitative measurements on the cloud forming efficiencies of individual particles. Lastly, characterization of freshwater aerosol formation during different atmospheric conditions (as a function of wind speed or temperature, for example) are needed to better constrain model predictions in the Great Lakes region, as well as other regions around the globe with large bodies of freshwater.

In Chapter 4, the aerosolization of toxins emitted from harmful algal blooms in freshwater lakes was investigated through laboratory experiments and bulk analysis of freshwater and aerosol samples. Ambient measurements around the globe are needed to fully quantify the amount of toxins incorporated into aerosol particles to better estimate the potential health effects associated with inhalation of toxins. Single-particle measurements of particles containing algal toxins would be useful, though thorough characterization of algal toxins is needed first (using single-particle mass spectrometry, for example). Additionally, these experiments focused on one class of algal toxins (microcystins), though others are known (such as nodularins, cylindrospermopsins, and anatoxins). Further investigation is also needed to assess the relative toxicities of each microcystin congener, particularly for inhalation as a route of exposure as most work to date has been done with ingestion as the primary mode of exposure.

In Chapter 5, ambient particles were analyzed to identify the concentration of aerosolized harmful algal bloom toxins, as well as the prevalence of freshwater aerosol compared to other particle types in the region (soot and dust, for example). Future work should investigate the lifetime of toxin-containing particles, particularly how long they can stay aloft and how far they can travel inland. To connect these results with those of Chapter 3, identifying if/how much toxins are incorporated into clouds and the subsequent precipitation are critical to monitor how far toxins are transported. Additional questions remain regarding the stability of aerosolized toxins, particularly if they undergo photochemical degradation, for example. All of these future steps will aid in estimating exposure to harmful algal bloom toxins.

In Chapter 6, optical photothermal infrared (O-PTIR) + Raman spectroscopy was applied to classify the vibrational modes present in 400 nm laboratory-generated and ambient particles. Further work is needed to push the analytical capabilities of O-PTIR to even smaller particles and to analyze particles with complex compositions and morphologies (aged soot with an organic

coating, for example). Additional ambient particle characterization is needed to study particles from different regions and sources. Furthermore, the fabrication of an environmental chamber compatible with the O-PTIR + Raman system that can control and monitor temperature and relative humidity would enable detailed study of how the physicochemical properties of particles change during different environmental conditions. This chamber could also be used to measure the dynamic physicochemical properties of particles as they react with different atmospheric gases in situ, providing detailed analysis of the reaction products as they are formed.

This body of work improves current understanding of the physicochemical properties of aerosol particles created from organic and freshwater sources. These results highlight the need for additional laboratory studies and ambient particle measurement at diverse locations to fully understand the dynamic properties of aerosol particles. The future directions outlined above will help improve model measurements of aerosol impacts on a global scale.

Appendix A. Reactive Uptake of Isoprene Epoxydiols Increases the Viscosity of the Core of Phase-Separated Aerosol Particles Supplemental Information¹

A.1 Experimental Details

Experiments were performed using a constant output atomizer (TSI Inc., model 3076) to create acidic ammonium sulfate particles generated from a solution of 0.60M ammonium sulfate (Sigma Aldrich, $\geq 99\%$ purity) and 0.60M sulfuric acid (Sigma Aldrich, $\geq 98\%$ purity). Solution pH was 1.37 ± 0.22 measured using a pH meter (Denver instruments, model UB-10). Particle flow passed through a differential mobility analyzer (DMA, TSI Inc., model 3080) to size select for 100 nm electrical mobility diameter before entering a potential aerosol mass (PAM, Aerodyne Research, Inc.) reactor. The PAM was used to create organic coatings of α -pinene or toluene oxidation products onto sulfate seed aerosol. Charcoal denuders were used to remove excess gases while Nafion tubes (Perma Pure, Model FC100-80-6-MSS-01) maintained the humidity of particles at 30% or 50% relative humidity. A glass flow reactor (1 m length x 8 cm inner diameter) was used for IEPOX reactive uptake before particle collection using a microanalysis particle sampler (MPS, 3 stages, California Measurements, Inc.). Additional details of experimental setup are described in Zhang et al.¹⁵

¹ Appendix A details supplemental information corresponding to Chapter 2

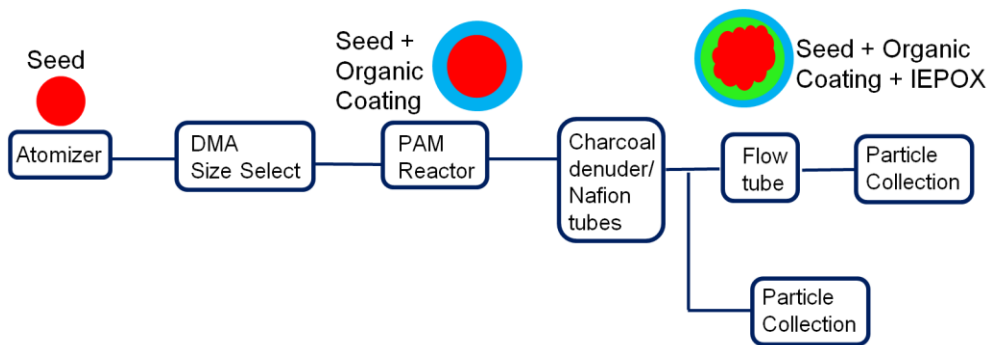


Figure A.1. Experimental setup to generate SOA particles. Cartoons of particles describe particle phase after each addition of chemical species.

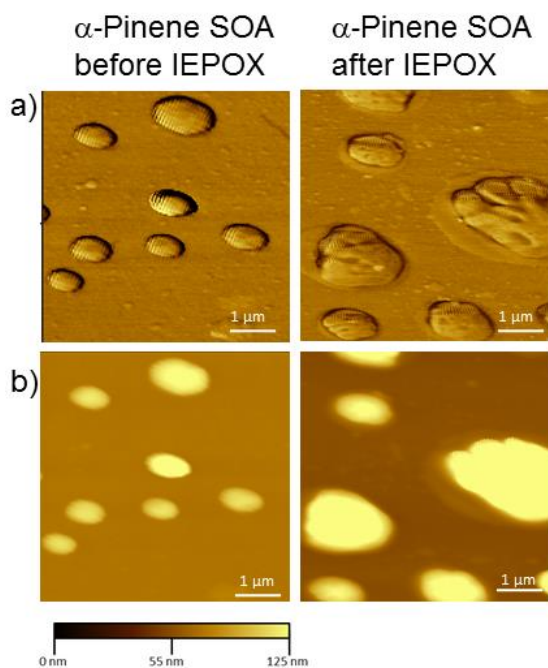


Figure A.2. AFM images of SOA particle re-humidified to the RH at which they were generated. AFM a) phase and b) height images of re-humidified 200 ppb α -pinene SOA/sulfate particles created at 50% RH before and after IEPOX uptake. Samples undergo drying between impaction onto substrates and analysis; therefore these samples were re-humidified to 50% RH during imaging to simulate initial RH. Minimal morphological changes were observed between particles analyzed at ambient RH and re-humidified particles analyzed at 50% RH.

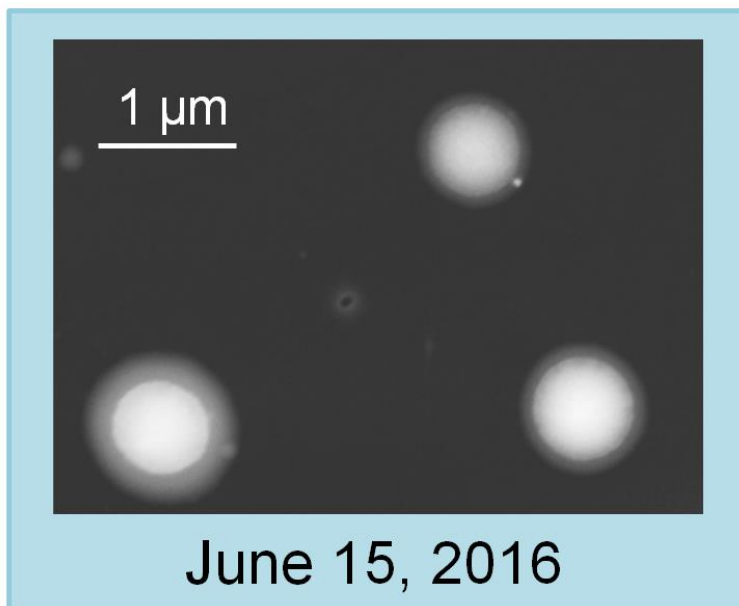


Figure A.3. SEM images of ambient particles collected during the Southern Oxidant and Aerosol Study (SOAS) campaign in Centerville, AL, a rural forested location. These particles were collected on June 15, 2016 during a period of high SOA concentration.⁷⁸

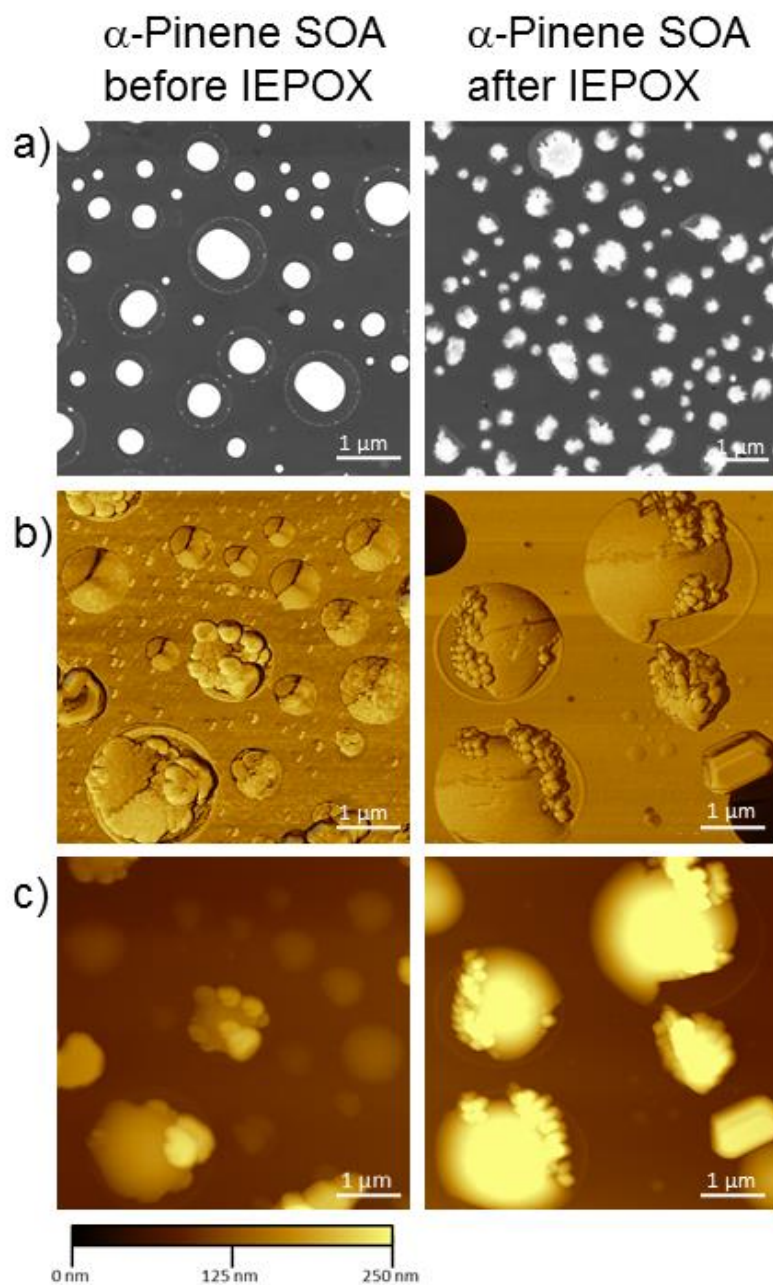


Figure A.4. AFM and SEM images of SOA generated at 30% RH. a) SEM images, b) AFM phase images, and c) AFM height images of α -pinene SOA/sulfate particles generated at 30% RH before and after IEPOX uptake. Particles show similar morphology trends to α -pinene SOA/sulfate particles created at 50% RH. Before IEPOX uptake, particles show core shell morphology. After IEPOX uptake, particle shell remains circular while particle core undergoes morphology changes.

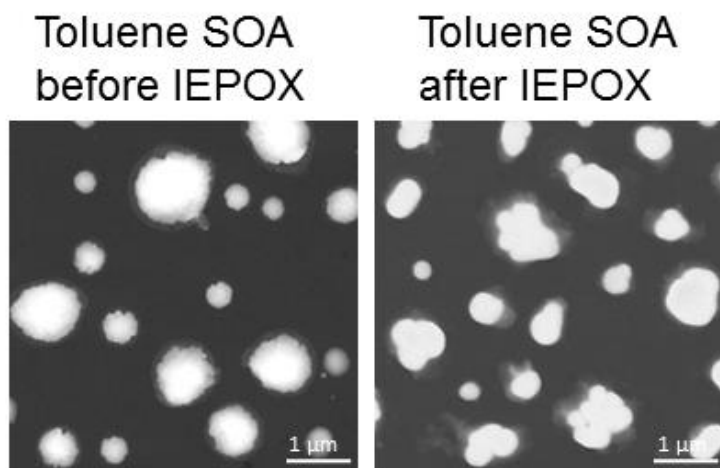


Figure A.5. SEM images of toluene SOA/sulfate particles generated at 30% RH before and after IEPOX uptake. Samples were not available on AFM substrates. Particles show similar morphology trends to toluene SOA/sulfate particles generated at 50% RH. Before IEPOX uptake, particles show core shell morphology. After IEPOX uptake, particle shell remains circular while particle core undergoes morphology changes.

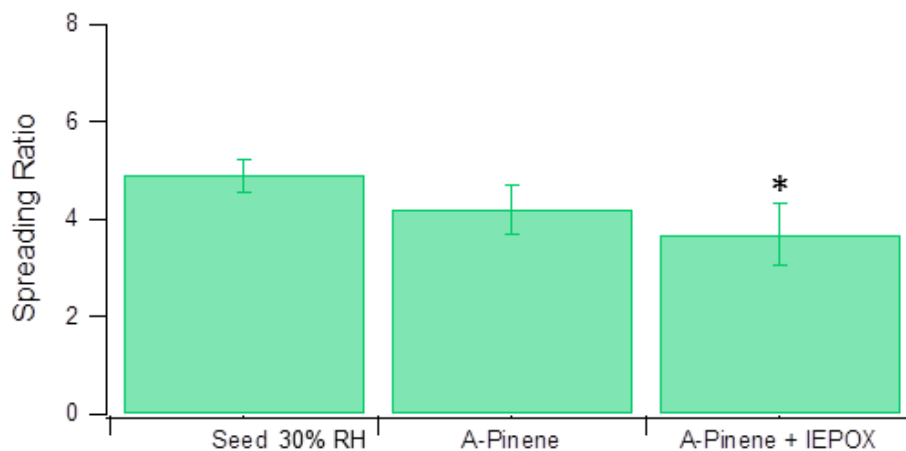


Figure A.6. Spreading ratios of SOA particles generated at 30% RH. Average spreading ratio (30 particles/sample) of α -pinene SOA/sulfate particles generated at 30% RH before and after IEPOX uptake. Error bars show standard error. Asterisks denote spreading ratios that are statistically different than seed aerosol spreading ratio, as determined by t-tests at 95% confidence interval. Toluene samples at 30% RH were not available on AFM substrates.

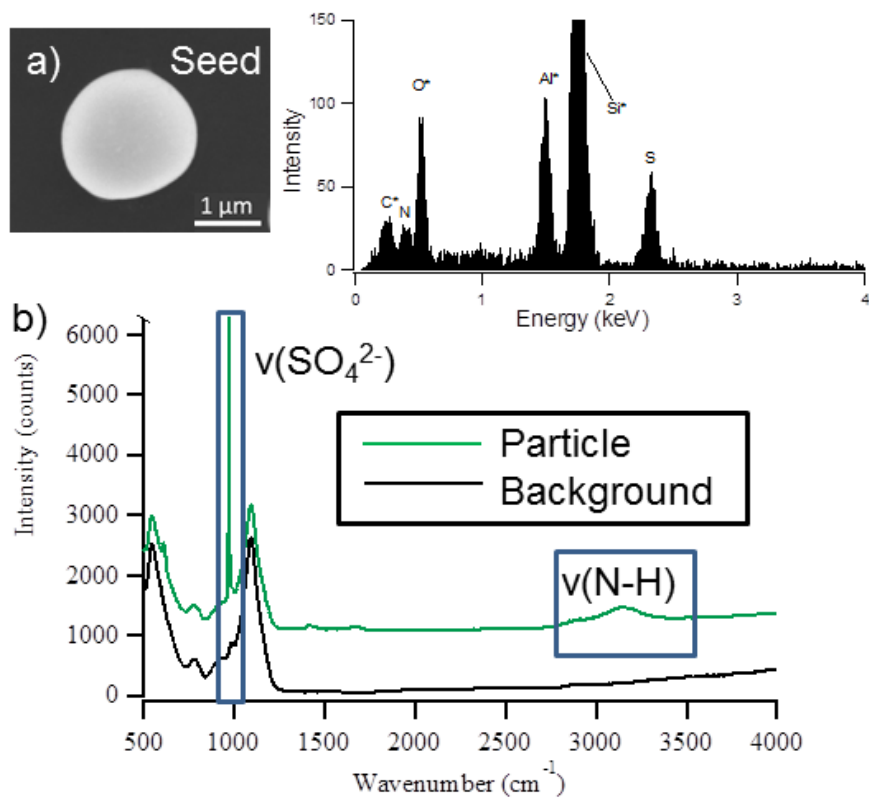


Figure A.7. SEM-EDX and Raman spectra of seed particles before SOA coating. a) SEM image and EDX spectrum and b) Raman spectrum of ammonium sulfate seed aerosol. Elements with asterisks in EDX spectrum denote partial contribution from substrate, sample holder, or detector. Seed aerosols were homogeneous and did not become phase separated until coated with organic species.

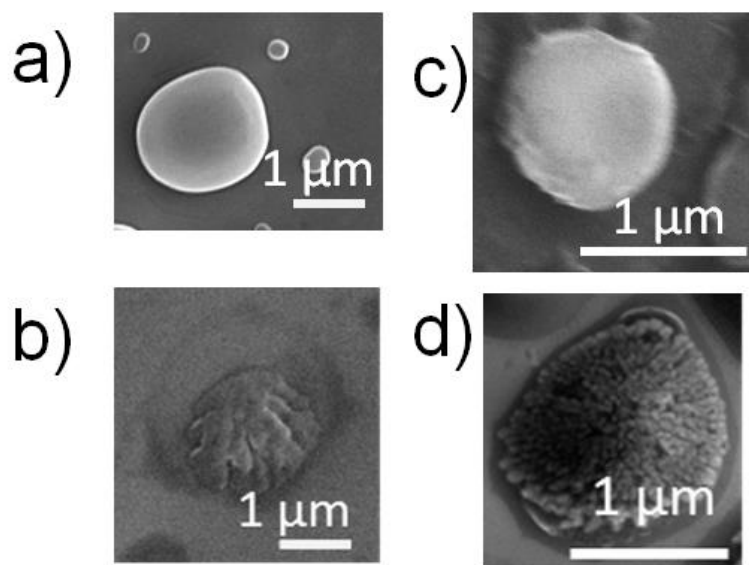


Figure A.8. SEM images of SOA particles. Unedited SEM images of a) α -pinene SOA, b) α -pinene + IEPOX SOA, c) toluene SOA, and d) toluene + IEPOX SOA coated onto ammonium sulfate seed particles. SEM images are shown in color in Figure 2.6 to emphasize phase separation.

Table A.1. Experimentally determined Raman modes and tentative assignments for α -pinene and toluene SOA/sulfate, based on assignments described in Bondy et al.⁴² Modes were classified as vs (very strong), s (strong), m (medium), and w (weak).

Experimental Raman modes (cm ⁻¹)	Assignments
614, 625 (s)	$\nu(\text{C-OH})$
976 (vs)	$\nu_s(\text{SO}_4^{2-})$
1064 (m)	$\nu_s(\text{SO}_3)$
1097, 1105, 1130 (w)	$\nu(\text{C-OH})$
1295 (m)	$\nu_s(\text{CH}_2)$
1418 (w)	$\nu(\text{CH}_2)$
1460, 1463 (w)	$\delta(\text{CH}_2 \& \text{CH}_3)$
2724 (m)	$\nu(\text{C-H})$
2846 (s)	$\nu_s(\text{CH}_2)$
2881 (s)	$\nu_s(\text{CH}_3)$
2896 (s)	$\nu_a(\text{CH}_2)$
2932 (s)	$\nu_a(\text{CH}_3)$
3119, 3133 (m)	$\nu(\text{N-H})$

Appendix B. Lake Spray Aerosol Incorporated into Great Lakes Clouds Supplemental Information²

July 12, 2016
Cloud Water Sampling Flight Path

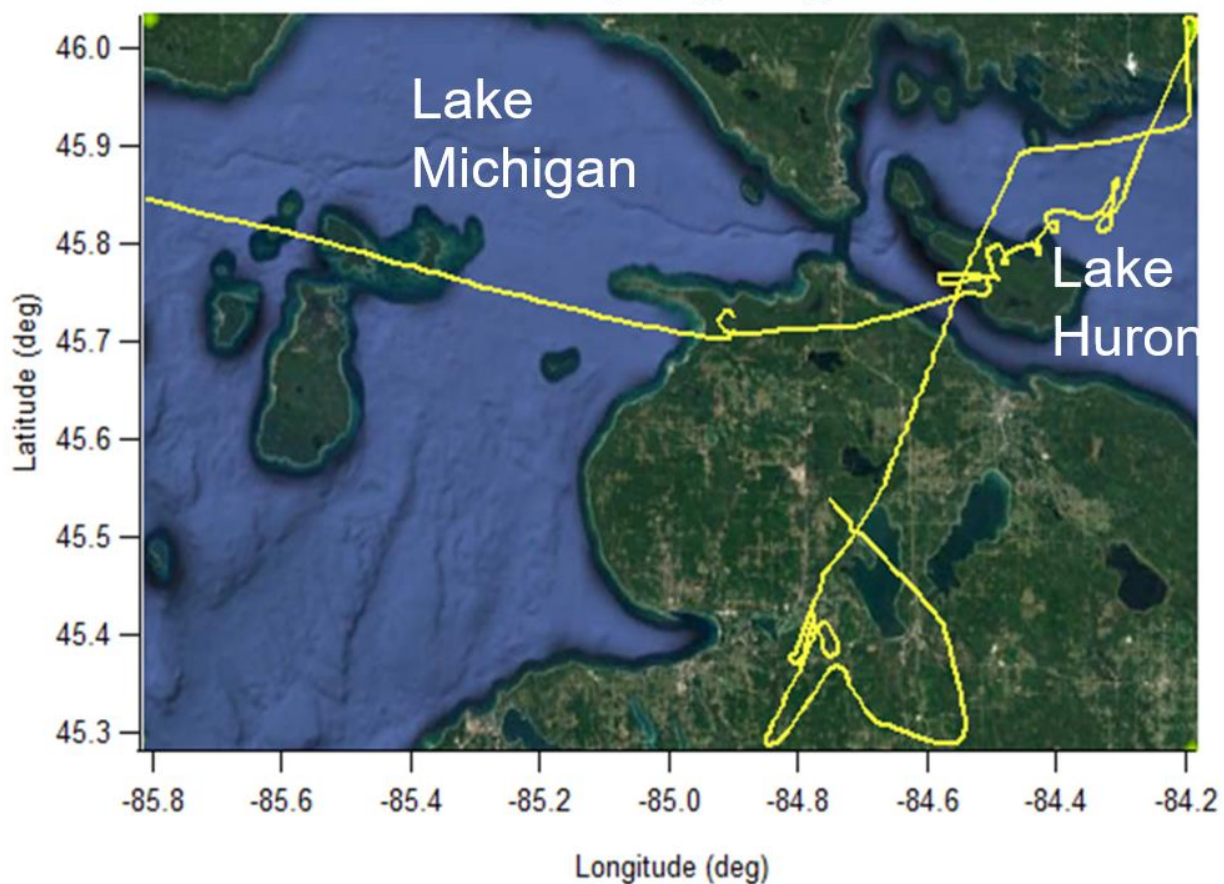


Figure B.1. Aircraft flight path map of July 12, 2016 cloud water sampling. Flight path data are not available for July 12, 2016 aerosol sampling.

² Appendix B details supplemental information corresponding to Chapter 3

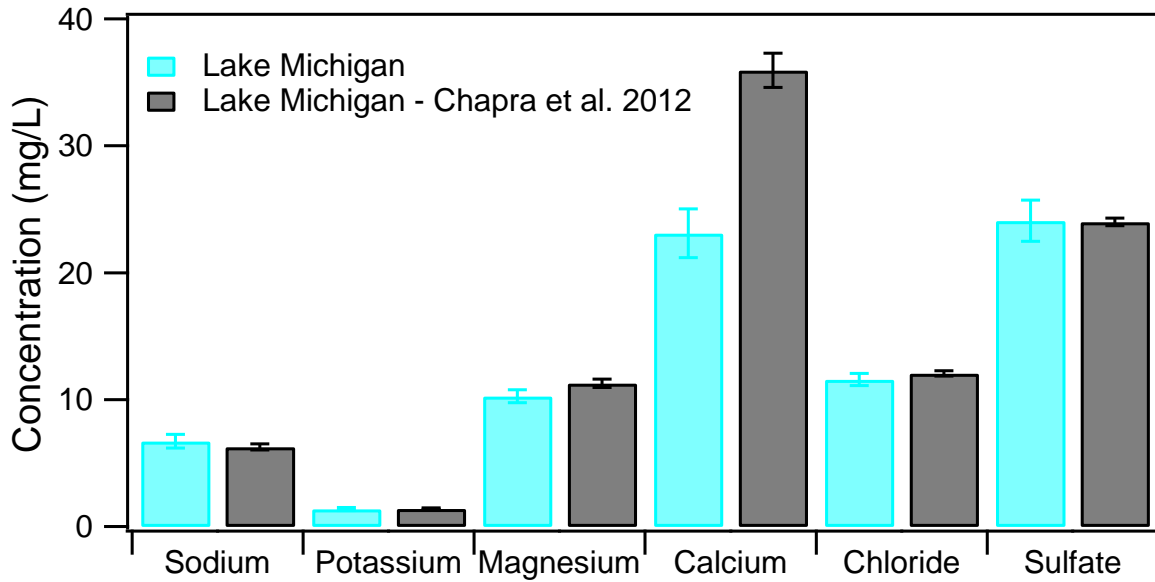


Figure B.2. Inorganic ion concentrations for freshwater collected in Brevort, Michigan during aircraft sampling on July 12, 2016. Bars represent average concentration of triplicate measurements; error bars show corresponding standard deviations. Values are compared to previous Lake Michigan measurements by Chapra et al.²⁰² Calcium values obtained are slightly lower than Chapra et al. due to insoluble CaCO_3 residues that are not measured by the IC method utilized here.

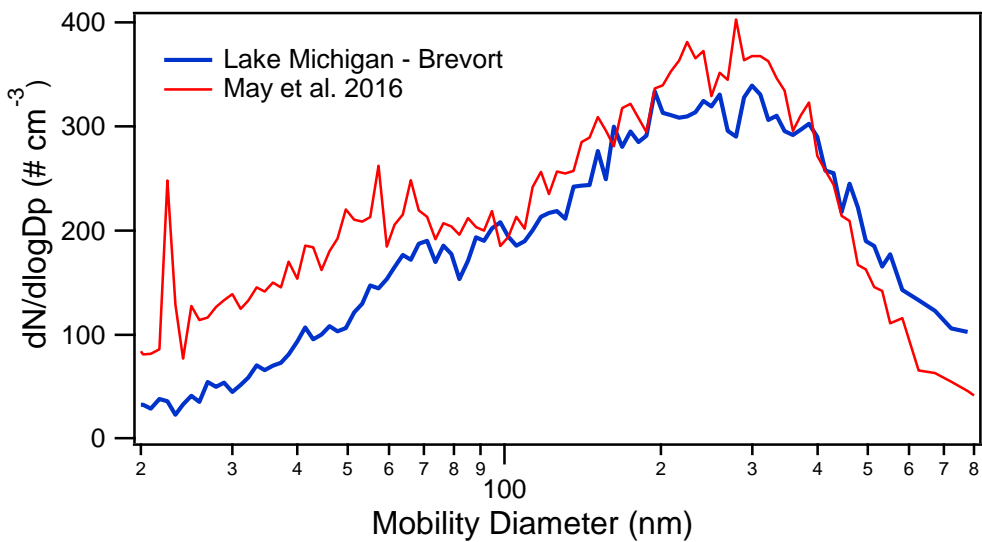


Figure B.3. The average number size distributions of laboratory-generated LSA. Traces represent freshwater collected in Brevort, Michigan at the time of aircraft sample collection (July 12, 2016) and freshwater collected at Michigan City, Michigan courtesy of May et al.¹⁶⁴

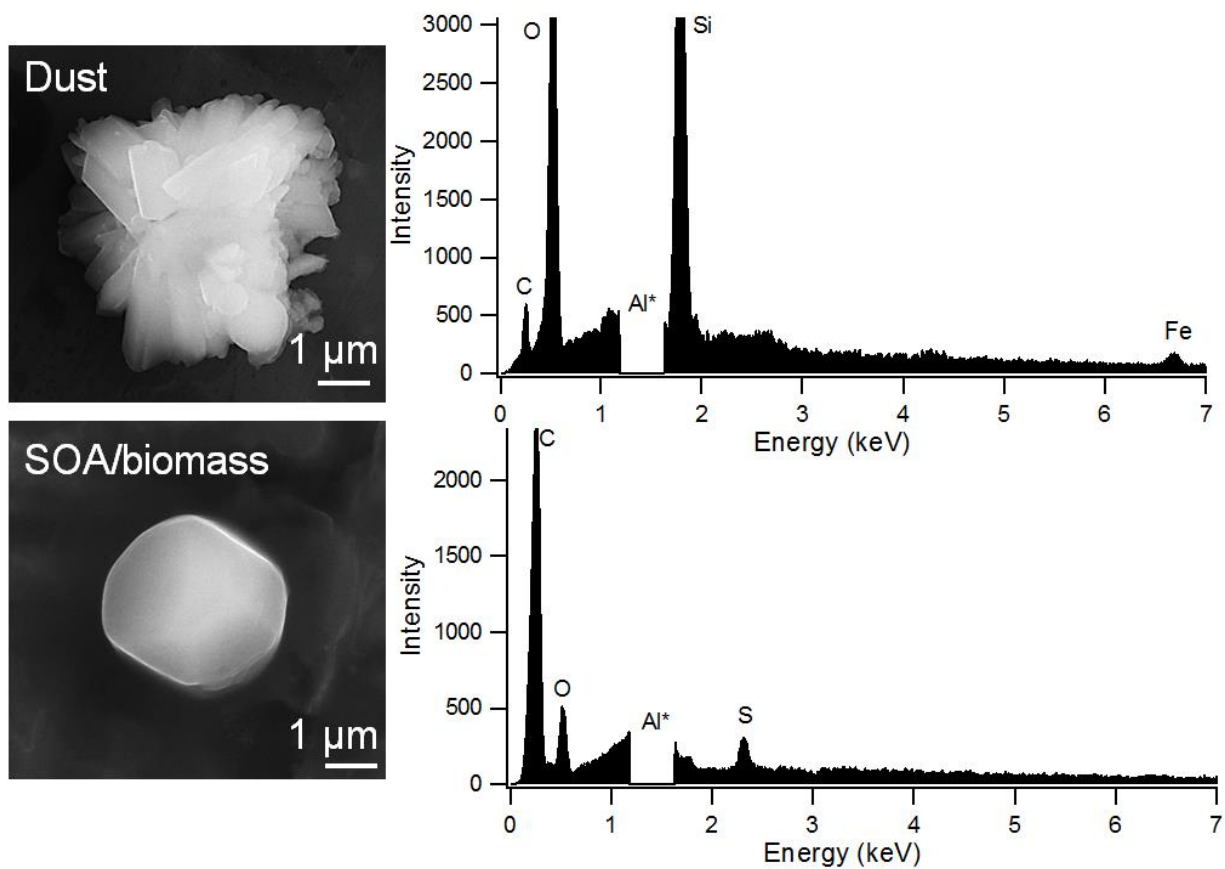


Figure B.4. SEM images and EDX spectra of particle types identified as dust and SOA/biomass burning during SEM-EDX analysis. Aluminum peaks were removed from the spectra and are denoted by asterisks to show contribution from aluminum foil substrate.

Appendix C. Harmful Algal Bloom Toxins in Aerosol Generated from Inland Lake Water
Supplemental Information³

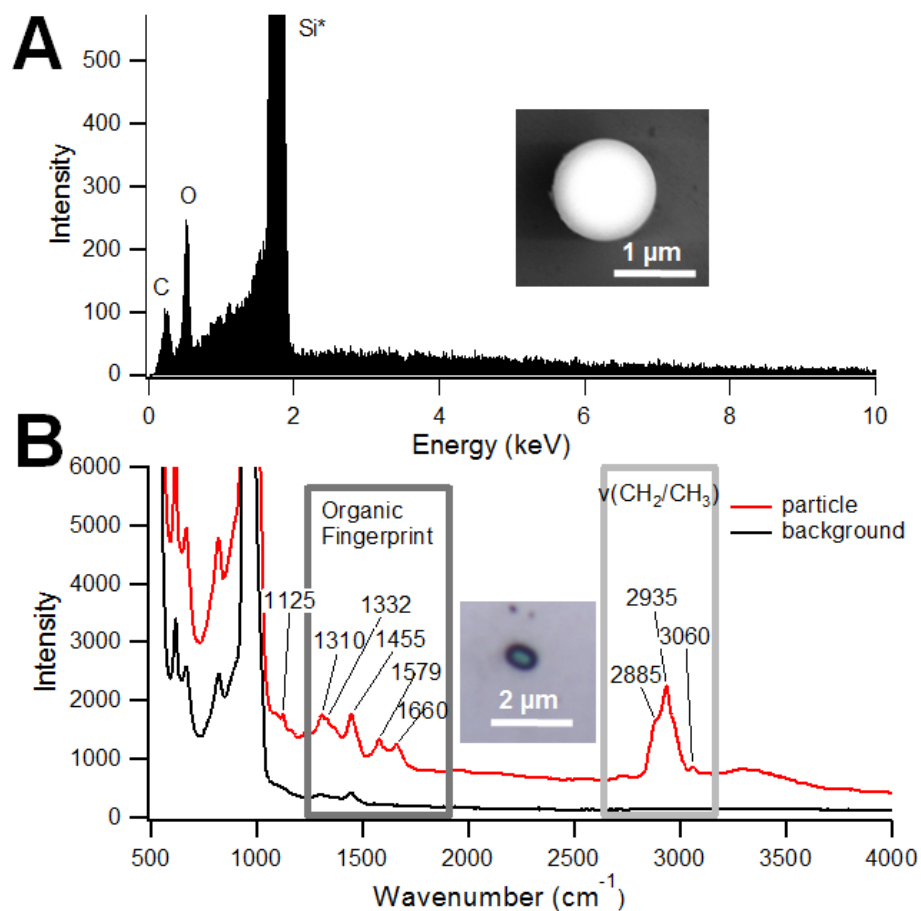


Figure C.1. SEM-EDX and Raman analysis of insoluble residues present in Mona Lake freshwater. Mona Lake freshwater samples were drop coated and dried onto substrates for chemical analysis of insoluble residues using A) SEM-EDX and B) Raman spectroscopy. Silicon was labeled with an asterisk in part A to denote contribution from the silicon wafer substrate. Insoluble residues contained peaks representative of organic material^{43,45,46,168} in both analysis methods and resembled particulate organic carbon (POC).^{326,327}

³ Appendix C details supplemental information corresponding to Chapter 4

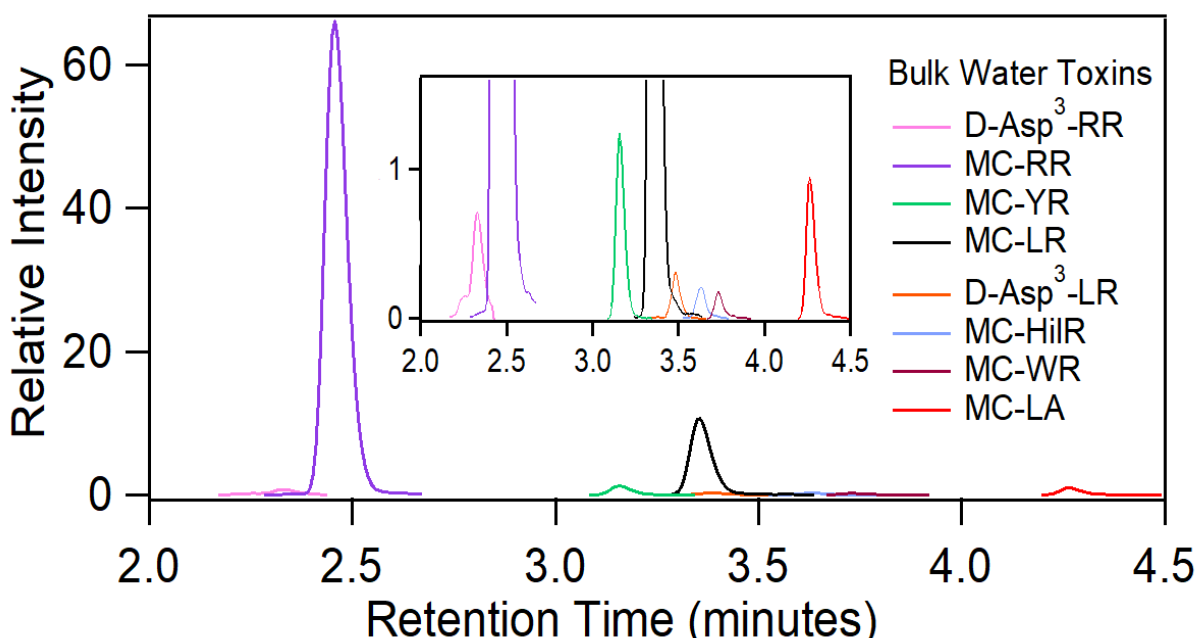


Figure C.2. Chromatograms showing separation of microcystin congeners present in Mona Lake freshwater. Inset shows congeners present at lower concentrations.

Table C.1. Liquid chromatography retention times of the microcystin congeners observed in Mona Lake freshwater. R groups are listed for each congener. Congeners starting with D signify a demethylation between the two R groups. Liquid chromatography was performed following the method in Birbeck et al.³¹⁵

Microcystin	Retention time (min)	R group 1	R group 2	Position between R groups
D-Asp ³ -RR	2.33	Arg	Arg	Demethylated
MC-RR	2.46	Arg	Arg	Methylated
MC-YR	3.16	Tyr	Arg	Methylated
MC-LR	3.36	Leu	Arg	Methylated
D-Asp ³ -LR	3.38	Leu	Arg	Demethylated
MC-HilR	3.64	Hil	Arg	Methylated
MC-WR	3.82	Trp	Arg	Methylated
MC-LA	4.26	Leu	Ala	Methylated

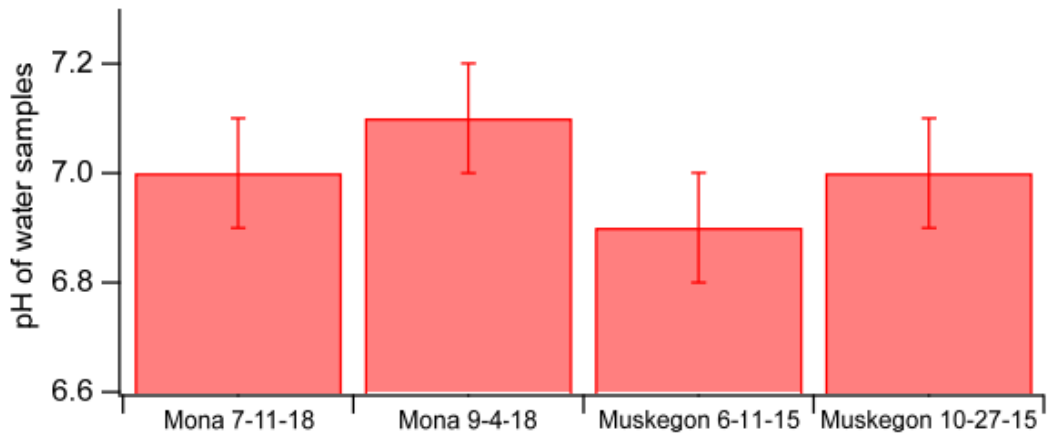


Figure C.4. pH of freshwater samples measured using pH paper. Mona Lake freshwater had pH values of 7.0 ± 0.1 and 7.1 ± 0.1 for the July and September samples, respectively. Muskegon Lake freshwater had pH values of 6.9 ± 0.1 and 7.0 ± 0.1 for the June and October samples, respectively.

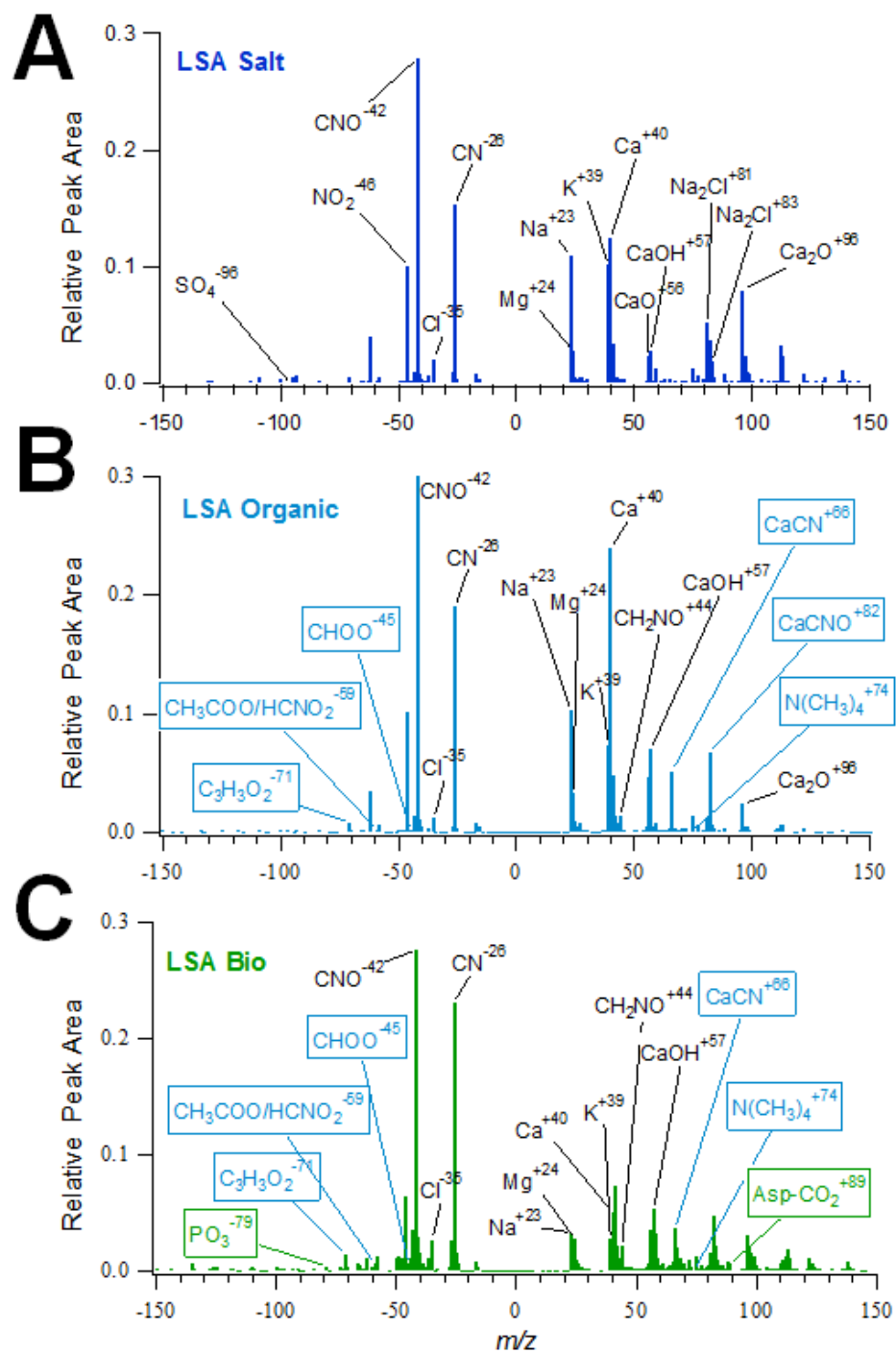


Figure C.5. Representative ATOFMS spectra of Mona Lake LSA classified as A) LSA salt, B) LSA organic, and C) LSA biological particles. Spectra were clustered using the markers identified by May et al.¹⁶⁸

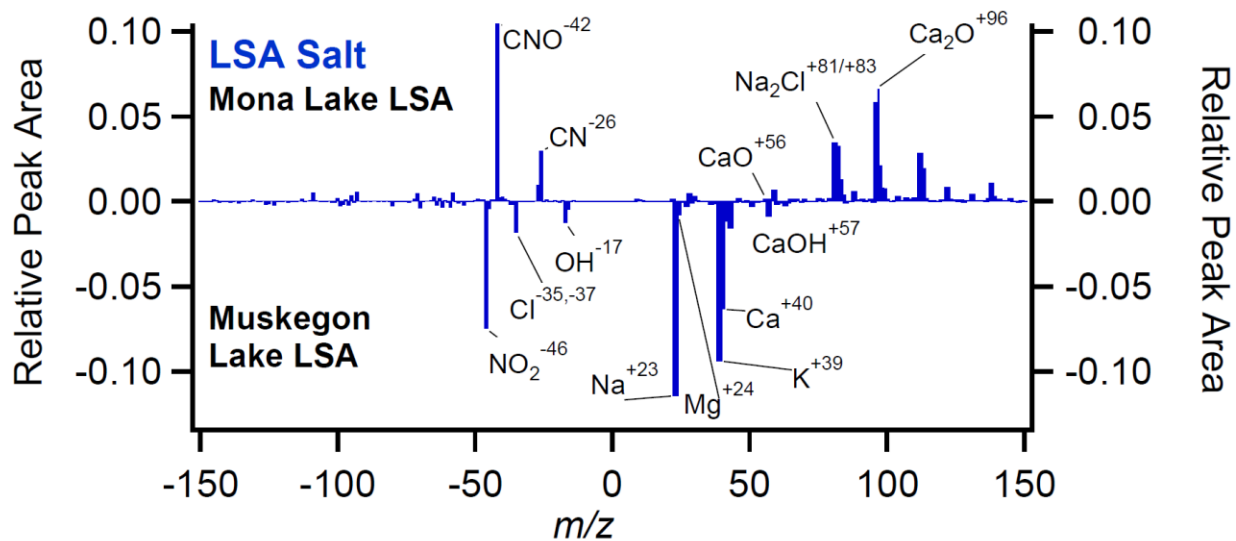


Figure C.6. ATOFMS spectra obtained by taking the difference of Mona Lake LSA salt and Muskegon Lake LSA salt clusters.

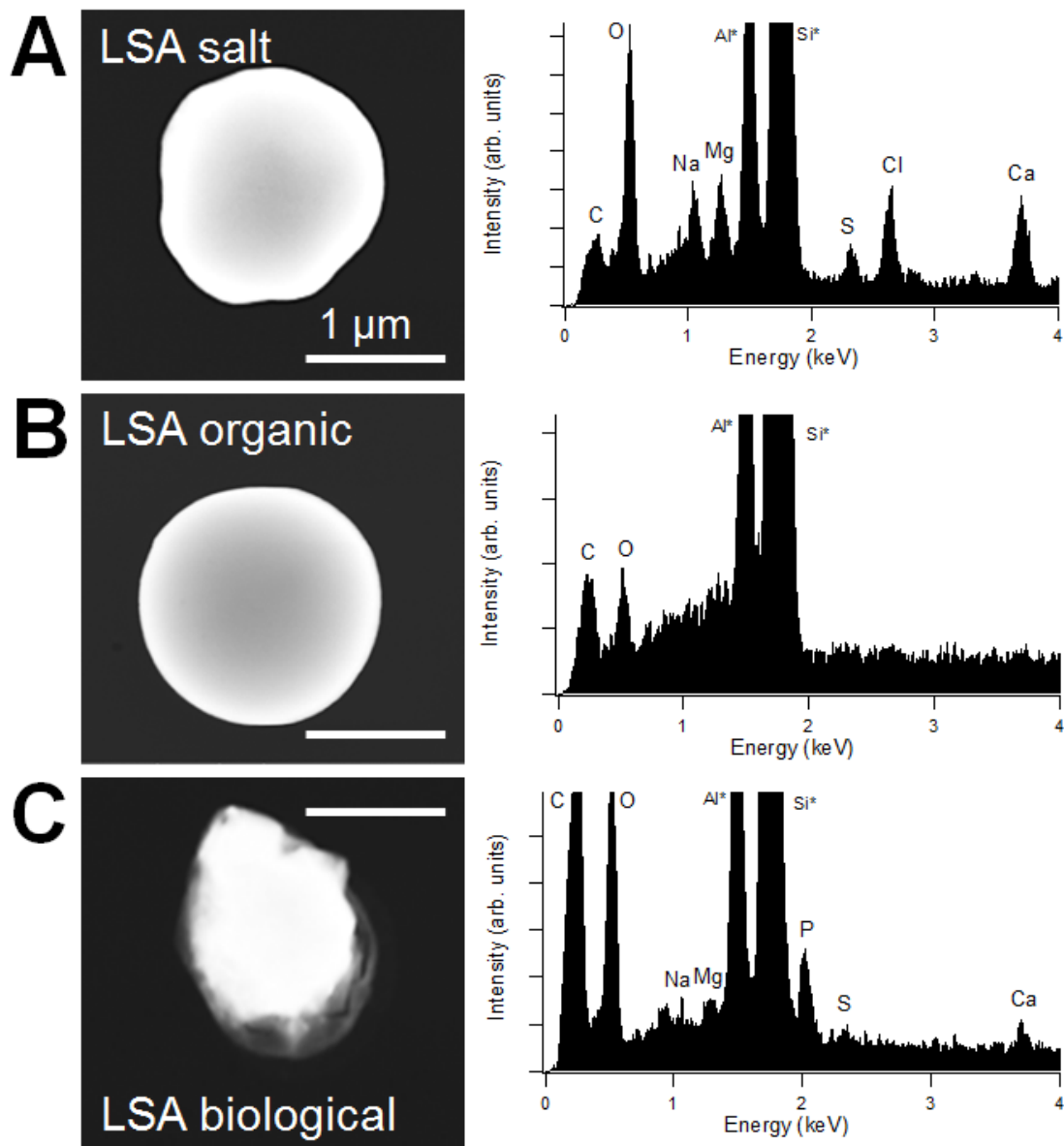


Figure C.7. SEM images and EDX spectra of LSA particle types. Representative SEM images (left) and EDX spectra (right) of A) LSA salt, B) LSA organic, and C) LSA biological particles generated from Mona Lake freshwater sample. Scale bars all represent 1 μm . Particles are similar to those previously observed by May et al.¹⁶⁸

C.1 Enrichment calculations of microcystin in laboratory-generated aerosol

The enrichments of different microcystins in aerosol samples were calculated as a ratio between the concentration of microcystins in all particulate matter (PM) with an aerodynamic diameter (d_a) < 2.55 μm and the concentration of microcystin in the freshwater. The aerosol number concentrations during the laboratory experiments were calculated from size distributions collected with an aerodynamic particle sizer (APS) and a scanning mobility particle sizer (SMPS) distributions, which are shown in the main text. Using the aerodynamic diameter midpoint of each bin, the volume of the average particle in each bin was determined. The concentration of aerosol in the air was determined by multiplying the volume of each individual particle and the number concentration of aerosol determined by the APS (d_a 698.0 nm - 2.55 μm) and SMPS (d_a 23.6 - 694.4 nm) shown below in equation C.1:

$$\text{Equation C.1} \quad \frac{\text{Volume}_{\text{Particle}}}{\text{Particle}} * \frac{\text{Particles}(\#)}{\text{Volume}_{\text{air}}} = \text{Total aerosol volume}$$

The electrical mobility diameter (d_{em}) reported by the SMPS was converted to aerodynamic diameter (d_a) using equation C.2, where χ is a spherical shape factor of 1 based on SEM image analysis and ρ is the density of freshwater aerosol (1.5 g/cm^3):^{27,145,223,414}

$$\text{Equation C.2} \quad d_a = d_{em} * \frac{\chi}{\rho}$$

The mass concentration of aerosol was then determined using equation C.3, in which aerosol mass was calculated by multiplying the aerosol volume by ρ :

$$\text{Equation C.3} \quad \frac{\text{Volume}_{\text{aerosol}}}{\text{Volume}_{\text{air}}} * \rho = \frac{\text{Mass}_{\text{aerosol}}}{\text{Volume}_{\text{air}}}$$

Utilizing the amount of microcystin detected in the air sampled, the fraction of microcystin in the total aerosol mass was determined using equation C.4:

$$\text{Equation C.4} \quad \frac{\text{Mass}_{\text{microcystin}} / \text{Volume}_{\text{air}}}{\text{Mass}_{\text{aerosol}} / \text{Volume}_{\text{air}}} = \frac{\text{Mass}_{\text{microcystin}}}{\text{Mass}_{\text{aerosol}}}$$

Enrichment was calculated using the ratio of each microcystin detected in the aerosol from equation 4 and their respective concentrations in the water, shown below in equation C.5:

$$\text{Equation C.5} \quad \text{Enrichment Factor} = \frac{\text{Mass}_{\text{microcystin}} / \text{Mass}_{\text{aerosol}}}{\text{Mass}_{\text{microcystin}} / \text{Mass}_{\text{waster}}}$$

Appendix D. Harmful Algal Bloom Toxins in Ambient Freshwater Aerosol Supplemental Information⁴

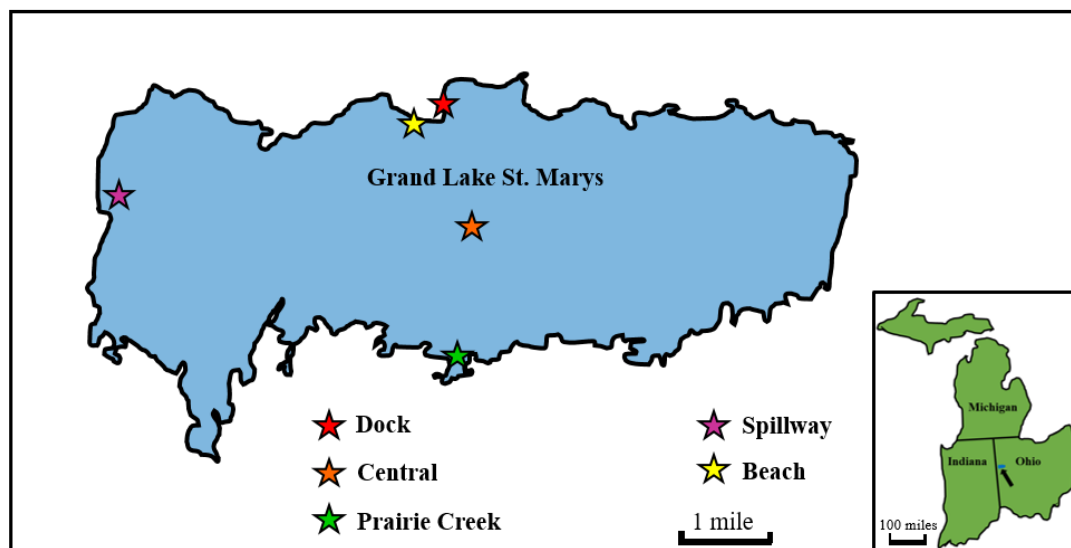


Figure D.1. Sampling locations around Grand Lake St. Marys.

⁴ Appendix D details supplemental information corresponding to Chapter 5

Appendix E. Optical Photothermal Infrared (O-PTIR) and Raman Spectroscopy of Submicrometer Atmospheric Particles Supplemental Information⁵

Because O-PTIR signal is dependent on the heat capacity, heat conductivity, and refractive index of the sample,⁶² the authors gathered these values reported in literature for all standards tested. Probe and IR power differed during data collection depending on the sample characteristics and sensitivity to the laser beams. Probe and IR power was varied to maximize signal intensity without oversaturating the detector. The authors list the probe and IR power used for each sample on silicon substrates. The 4 chips for the QCL laser are as follows: 880–1160 cm^{-1} , 1160.1–1420 cm^{-1} , 1420.1–1700 cm^{-1} , and 1700.1–1950 cm^{-1} .

The LOD in terms of raw signal is 0.12 mA from the photodiode. Particles used in the manuscript were generated from 50 mM solutions. To estimate the LOD based on the initial solution concentration, if the volume of a 400 nm volume equivalent diameter (d_{ve}) particle is $3.35 \times 10^7 \text{ nm}^3$ ($3.35 \times 10^{-20} \text{ m}^3$), then there are $\sim 1.01 \times 10^6$ molecules of analyte in that particle before impaction. After impaction the particle spreads to 1 μm projected area diameter (d_{pa}) on the substrate. The spot size of the green laser ($\lambda = 532 \text{ nm}$) should be similar to the 450 nm spot size at $\lambda = 550 \text{ nm}$ based on manufacturer specs for the Cassegrain objective (40 \times , 0.78 N.A. Schwarzschild Objective, IR Reflective, Pike Technologies Inc.). This means would mean we can detect $\sim 4.5 \times 10^5$ molecules within the illuminated volume that is determined by the spot size of the green laser.

Table E.1. Number of particles analyzed for each substrate or compound.

Figure	Substrate/Compound	Particles Analyzed
Figure 2	Silicon	20
	Quartz	24
	Germanium	16
	Al Foil	31
	Ag Foil	24
Figure 3	Ammonium Nitrate	18
	Sodium Acetate	10
	Sucrose	12
	Sodium Dodecyl Sulfate (SDS)	10
	Ammonium Oxalate	12

Table E.2. Table of heat capacity,⁴¹⁵⁻⁴²² heat conductivity,^{423,424} and refractive index values⁴²⁵⁻⁴³¹ obtained from literature for all standard compounds tested. On the right, the probe and IR power used to obtain O-PTIR spectra from each standard on silicon substrates is listed.

Compound	Heat capacity (J/g°C)	Heat conductivity (W/m·K)	Real refractive index	Probe power (mW)	IR power (mW)
Water	4.18	0.60	1.33	n/a	n/a
Ammonium sulfate	1.42	n/a	1.85	10	10
Ammonium nitrate	1.38	n/a	1.41	10	4
Sodium acetate	0.97	n/a	1.32	4	10
Sucrose	1.04	n/a </tr			

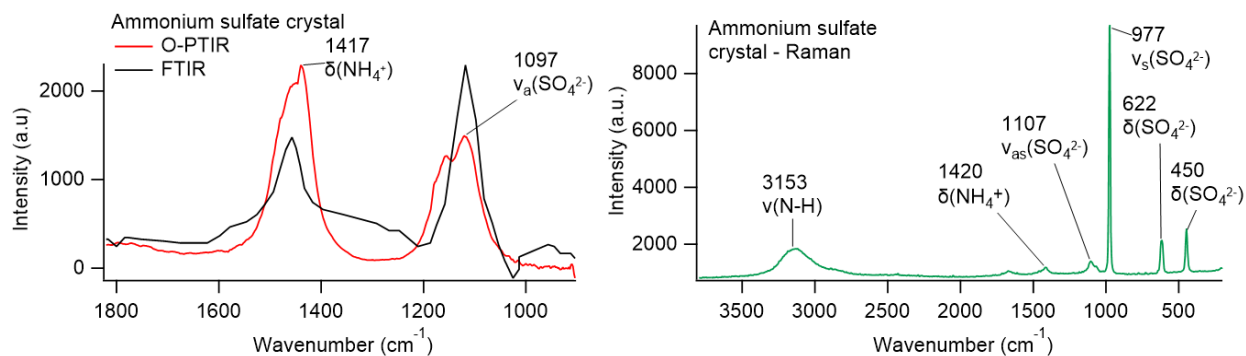



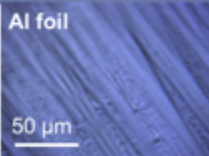




Figure E.1. IR (left, red trace) and Raman (right, green trace) spectra of ammonium sulfate crystals, illustrating the crystalline modes observed by Raman.¹⁵² O-PTIR and FTIR spectra of ammonium sulfate aligns well, similar to previous comparison of photothermal IR and FTIR.⁵⁰

Table E.3. Table listing peaks identified by IR and Raman for each substrate tested. Optical images of blank substrates (with no particles) are included on the right.

Material	IR background peaks (cm⁻¹)	Raman background peaks (cm⁻¹)	Optical Images of Substrates
Silicon	n/a	520, 963	
Quartz	1056, 1223	506	
Germanium	n/a	295	
Al foil	n/a	n/a	
Ag foil	n/a	247	
Gold	1413	1343, 2703	

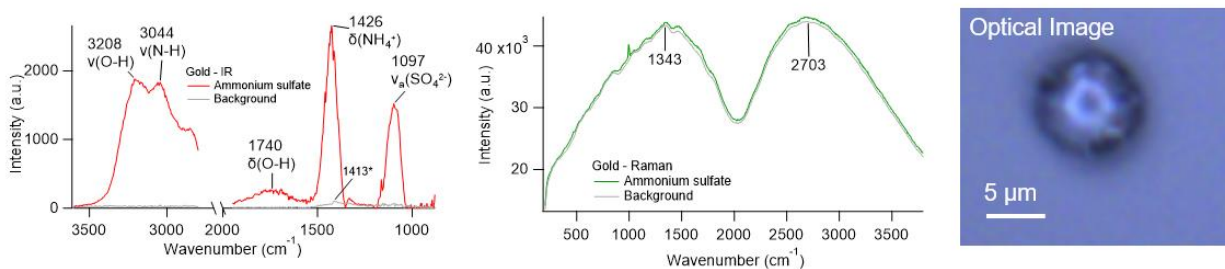
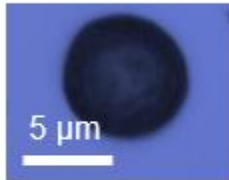


Figure E.2. IR (left, red trace) and Raman (right, green trace) spectra obtained from an ammonium sulfate particle on a gold substrate. Raman spectra were dominated from fluorescence due to the substrate. An optical image of the particle is included on the right.

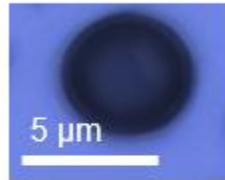
Table E.4. Table listing all vibrational modes experimentally determined in IR and Raman spectra. Literature is referenced to corroborate the spectral assignments.^{22,33,35,36,43,45,50,52,152,153,365-373,375,385,386,413,432}

Compound	Experimental IR modes	IR References	Experimental Raman modes	Raman References
Ammonium sulfate	$\nu_{as}(\text{SO}_4^{2-})$ at 1100 cm^{-1} $\delta(\text{NH}_4^+)$ at 1422 $\nu(\text{N-H})$ at ~ 3040 cm^{-1}	Onasch et al. 1999 Bondy et al. 2017 Or et al. 2018	$\nu_s(\text{SO}_4^{2-})$ at 977 cm^{-1} $\delta(\text{SO}_4^{2-})$ at 634 and 471 cm^{-1} $\nu(\text{N-H})$ at ~ 3168 cm^{-1}	Venkateswarlu et al. 1975 Jentzsch et al. 2013 Rindelaub et al. 2016 Kirpes et al. 2018
Ammonium nitrate	$\nu_s(\text{NO}_3^-)$ at 1371 cm^{-1} $\delta(\text{NH}_4^+)$ at 1411 cm^{-1} $\nu(\text{N-H})$ at 3081 cm^{-1}	Theoret et al. 1964 Bondy et al. 2017 Or et al. 2018	$\nu(\text{NO}_3^-)$ at 1044 cm^{-1} $\nu(\text{N-H})$ at 3135 cm^{-1}	Rousseau et al. 1968 Jentzsch et al. 2013 Craig et al. 2015 Craig et al. 2017
Sodium acetate	$\nu(\text{CH}_3)$ at 1361 cm^{-1} $\nu(\text{C-O})$ at 1411 cm^{-1} $\nu_s(\text{C=O})$ at 1577 cm^{-1} $\nu(\text{C-H})$ at 2936 and 3004 cm^{-1}	Jones et al. 1955 Jones et al. 1954 Kakihana et al. 1982	$\nu(\text{CH}_3)$ at 1360 cm^{-1} $\nu(\text{C-H})$ at 2717, 2829, 2935 cm^{-1}	Frost et al. 2000 Wang et al. 2005
Sucrose	$\nu(\text{C-C})$ at 935 cm^{-1} $\nu(\text{C-O})$ at 1054, 1128 cm^{-1} $\delta(\text{C-O-H})$ at 1408 cm^{-1} $\nu(\text{CH}_2)$ at 2916 cm^{-1} $\nu(\text{O-H})$ at 3356 cm^{-1}	Brizuela et al. 2012 Or et al. 2018	$\nu(\text{CH}_2)$ at 836 cm^{-1} $\nu(\text{C-O})$ at 1132 cm^{-1} $\nu(\text{CH}_2)$ at 1339 cm^{-1} $\delta(\text{CH}_2)$ at 1462 cm^{-1} $\nu(\text{C-H})$ at 2910 cm^{-1} $\nu(\text{O-H})$ at 3345 cm^{-1}	Mathlouthi et al. 1980 Brizuela et al. 2012
Sodium dodecyl sulfate	$\nu_{as}(\text{ROSO}_3^-)$ at 1221, 1249 cm^{-1} $\delta(\text{CH}_2)$ at 1469 cm^{-1} $\nu(\text{CH})$ at 2885, 2921, 2955 cm^{-1} $\nu(\text{O-H})$ at 3471 cm^{-1}	Sperline et al. 1992 Gao et al. 2010	$\nu(\text{ROSO}_3^-)$ at 1086 cm^{-1} $\nu(\text{C-C})$ at 1270 cm^{-1} $\delta(\text{C-C})$ at 1441 cm^{-1} $\nu(\text{C-H})$ at 2727, 2846, 2878 cm^{-1}	Picquart et al. 1986 Ault et al. 2013
Ammonium oxalate	$\nu(\text{C-O})$ at 1302, 1439 cm^{-1} $\nu(\text{C=O})$ at 1719 cm^{-1} $\nu(\text{N-H})$ at 3000 cm^{-1} $\nu(\text{O-H})$ at 3196 cm^{-1}	Frost et al. 2003	$\nu(\text{C-C})$ at 875 cm^{-1} $\nu(\text{C-O})$ at 1452, 1476 cm^{-1} $\nu(\text{N-H})$ at 3029 cm^{-1}	Hibben et al. 1935 Frost et al. 2003

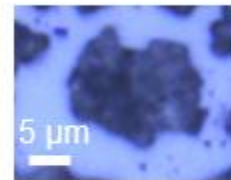
Ammonium Nitrate



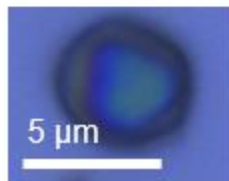
Sucrose



Ammonium Oxalate



Sodium Acetate



SDS

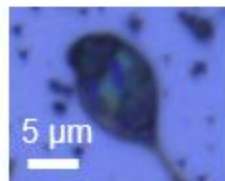


Figure E.3. Optical images of each particle analyzed in Figure 6.3. All particles had an aerodynamic diameter <400 nm before spreading onto the silicon substrate.

References

1. Pöschl, U., Atmospheric aerosols: composition, transformation, climate and health effects. *Angew. Chem. Int. Ed.* **2005**, *44*, 7520 – 7540.
2. Seinfeld, J. H.; Pandis, S. N., *Atmospheric chemistry and physics: from air pollution to climate change*. John Wiley & Sons: 2016.
3. Ault, A.; Axson, J., Atmospheric aerosol chemistry: spectroscopic and microscopic advances. *Anal. Chem.* **2017**, *89*, 430-452.
4. Slade, J. H.; Vanreken, T. M.; Mwaniki, G. R.; Bertman, S.; Stirm, B.; Shepson, P. B., Aerosol production from the surface of the Great Lakes. *Geophys. Res. Lett.* **2010**, *37*, L18807.
5. Axson, J. L.; May, N. W.; Colon-Bernal, I. D.; Pratt, K. A.; Ault, A. P., Lake spray aerosol: a chemical signature from individual ambient particles. *Environ. Sci. Tech.* **2016**, *50*, 9835–9845.
6. Prather, K. A.; Hatch, C. D.; Grassian, V. H., Analysis of atmospheric aerosols. *Annu. Rev. Anal. Chem.* **2008**, *1*, 485-514.
7. Hinds, W. C., *Aerosol technology: Properties, behavior, and measurement of airborne particles*. 2 ed.; John Wiley & Sons: New York, 1999.
8. Kwamena, N. O. A., Buajarn, J., Reid, J. P., Equilibrium morphology of mixed organic/inorganic/aqueous aerosol droplets: investigating the effect of relative humidity and surfactants. *J. Phys. Chem. A* **2010**, *114*, 5787–5795.
9. Andreae, M. O.; Rosenfeld, D., Aerosol–cloud–precipitation interactions. Part 1. The nature and sources of cloud-active aerosols. *Earth Sci. Rev.* **2008**, *89*, 13-41.
10. Stocker, T. F.; Qin, D., *Climate change 2013: The physical science basis. Working group I contribution to the fifth assessment report of the intergovernmental panel on climate change*. Cambridge University Press: Cambridge, UK and New York, NY, USA, 2013.
11. Pope, C. A.; Dockery, D. W., Health effects of fine particulate air pollution: Lines that connect. *J. Air Waste Manage.* **2006**, *56*, (6), 709-742.
12. Shiraiwa, M.; Ueda, K.; Pozzer, A.; Lammel, G.; Kampf, C. J.; Fushimi, A.; Enami, S.; Arangio, A. M.; Frohlich-Nowoisky, J.; Fujitani, Y.; Furuyama, A.; Lakey, P. S. J.; Lelieveld, J.; Lucas, K.; Morino, Y.; Pöschl, U.; Takahama, S.; Takami, A.; Tong, H.; Weber, B.; Yoshino, A.; Sato, K., Aerosol Health Effects from Molecular to Global Scales. *Environ. Sci. Technol.* **2017**.
13. Riemer, N., Ault, A. P., West, M., Craig, R. L., Curtis, J. H., Aerosol mixing state: measurements, modeling, and impacts. *Rev. Geophys.* **2019**, *57*, 187-249.
14. Fierce, L.; Bond, T. C.; Bauer, S. E.; Mena, F.; Riemer, N., Black carbon absorption at the global scale is affected by particle-scale diversity in composition. *Nat. Commun.* **2016**, *7*, 8.
15. Zhang, Y.; Chen, Y.; Lambe, A. T.; Olson, N. E.; Lei, Z.; Craig, R. L.; Zhang, Z.; Gold, A.; Onasch, T. B.; Jayne, J. T.; Worsnop, D. R.; Gaston, C. J.; Thornton, J. A.; Vizuete, W.; Ault, A. P.; Surratt, J. D., Effect of the aerosol-phase state on secondary organic aerosol formation from

the reactive uptake of isoprene-derived epoxydiols (IEPOX). *Environ. Sci. Technol. Lett.* **2018**, *5*, 167-174.

16. Zhang, Y.; Chen, Y.; Lei, Z.; Olson, N. E.; Riva, M.; Koss, A. R.; Zhang, Z.; Gold, A.; Jayne, J. T.; Worsnop, D. R.; Onasch, T. B.; Kroll, J. H.; Turpin, B. J.; Ault, A. P.; Surratt, J. D., Joint impacts of acidity and viscosity on the formation of secondary organic aerosol from isoprene epoxydiols (IEPOX) in phase separated particles. *ACS Earth Space Chem.* **2019**, *3*, (12), 2646-2658.

17. Moore, M. J. K.; Furutani, H.; Roberts, G. C.; Moffet, R. C.; Gilles, M. K.; Palenik, B.; Prather, K. A., Effect of organic compounds on cloud condensation nuclei (CCN) activity of sea spray aerosol produced by bubble bursting. *Atmos. Environ.* **2011**, *45*, (39), 7462-7469.

18. Moffet, R. C.; Prather, K. A., In-situ measurements of the mixing state and optical properties of soot with implications for radiative forcing estimates. *Proc. Natl. Acad. Sci. U. S. A.* **2009**, *106*, (29), 11872-11877.

19. Zhang, Q.; Thompson, J. E., Effect of particle mixing morphology on aerosol scattering and absorption: A discrete dipole modeling study. *Geo. Res. J.* **2014**, *3*, 9-18.

20. Bondy, A. L.; Bonanno, D.; Moffet, R. C.; Wang, B.; Laskin, A.; Ault, A. P., The diverse chemical mixing state of aerosol particles in the southeastern United States. *Atmos. Chem. Phys.* **2018**, *18*, (16), 12595-12612.

21. Axson, J. L. S.; Hongru; Bondy, Amy L.; Landry, Christopher C.; Welz, Jason; Creamean, Jessie M.; Ault, Andrew P., Transported mineral dust deposition case study at a hydrologically sensitive mountain site: size and composition shifts in ambient aerosol and snowpack. *Aerosol Air Qual. Res.* **2016**, *16*, (3), 555-567.

22. Kirpes, R. M.; Bondy, A. L.; Bonanno, D.; Moffet, R. C.; Wang, B.; Laskin, A.; Ault, A. P.; Pratt, K. A., Secondary sulfate is internally mixed with sea spray aerosol and organic aerosol in the winter Arctic. *Atmos. Chem. Phys.* **2018**, *18*, (6), 3937-3949.

23. Laskin, A.; Cowin, J. P.; Iedema, M. J., Analysis of individual environmental particles using modern methods of electron microscopy and X-ray microanalysis. *J. Electron Spectros.* **2006**, *150*, 260-274.

24. Patterson, J. P.; Collins, D. B.; Michaud, J. M.; Axson, J. L.; Sultana, C. M.; Moser, T.; Dommer, A. C.; Conner, J.; Grassian, V. H.; Stokes, M. D.; Deane, G. B.; Evans, J. E.; Burkart, M. D.; Prather, K. A.; Gianneschi, N. C., Sea spray aerosol structure and composition using cryogenic transmission electron microscopy. *ACS Cent. Sci.* **2016**, *2*, 40-47.

25. Laskin, A.; Gilles, M. K.; Knopf, D. A.; Wang, B.; China, S., Progress in the analysis of complex atmospheric particles. *Annu Rev Anal Chem* **2016**, *9*, 117-143.

26. Riva, M.; Chen, Y.; Zhang, Y.; Lei, Z.; Olson, N.; Boyer, H. C.; Narayan, S.; Yee, L. D.; Green, H.; Cui, T.; Zhang, Z.; Baumann, K. D.; Fort, M.; Edgerton, E. S.; Budisulistiorini, S.; Rose, C. A.; Ribeiro, I.; e Oliveira, R. L.; Santos, E.; Szopa, S.; Machado, C.; Zhao, Y.; Alves, E.; de Sa, S.; Hu, W.; Knipping, E.; Shaw, S.; Duvoisin Junior, S.; Souza, R. A. F. d.; Palm, B. B.; Jimenez, J. L.; Glasius, M.; Goldstein, A. H.; Pye, H. O. T.; Gold, A.; Turpin, B. J.; Vizuete, W.; Martin, S. T.; Thornton, J.; Dutcher, C. S.; Ault, A. P.; Surratt, J. D., Increasing isoprene epoxydiol-to-inorganic sulfate aerosol (IEPOX:SulfInorg) ratio results in extensive conversion of inorganic sulfate to organosulfur forms: implications for aerosol physicochemical properties. *Environ. Sci. Technol.* **2019**, *53*, (15), 8682-8694.

27. May, N. W.; Gunsch, M. J.; Olson, N. E.; Bondy, A. L.; Kirpes, R. M.; Bertman, S. B.; China, S.; Laskin, A.; Hopke, P. K.; Ault, A. P.; Pratt, K. A., Unexpected contributions of sea spray and lake spray aerosol to inland particulate matter. *Environ. Sci. Technol. Lett.* **2018**, *5*, 405-412.
28. Willis, R. D., Blanchard, F. T., Conner, T. L. , Guidelines for the application of SEM/EDX analytical techniques to particulate matter samples. *National Exposure Research Laboratory Report, Office of Research and Development* **2002**.
29. Shen, H.; Peters, T. M.; Casuccio, G. S.; Lersch, T. L.; West, R. R.; Kumar, A.; Kumar, N.; Ault, A. P., Elevated concentrations of lead in particulate matter on the neighborhood-scale in Delhi, India as determined by single particle analysis. *Environ. Sci. Technol.* **2016**, *50*, (10), 4961-4970.
30. Anderson, B. J.; Musicant, D. R.; Ritz, A. M.; Ault, A.; Gross, D.; Yuen, M.; Gälli, M., User-friendly clustering for atmospheric data analysis. *Carleton College, Northfield, MN, USA* **2005**.
31. Jain, A. K., Data clustering: 50 years beyond K-means. *Pattern Recognit. Lett.* **2010**, *31*, (8), 651-666.
32. Likas, A., Vlassis, N., Verbeek, J. J. , The global k-means clustering algorithm. *Pattern Recognit.* **2003**, *36*, 451-461.
33. Craig, R. L.; Nandy, L.; Axson, J. L.; Dutcher, C. S.; Ault, A. P., Spectroscopic determination of aerosol pH from acid-base equilibria in inorganic, organic, and mixed systems. *J. Phys. Chem. A* **2017**, *121*, (30), 5690-5699.
34. Olson, N. E.; Lei, Z.; Craig, R. L.; Zhang, Y.; Chen, Y.; Lambe, A. T.; Zhang, Z.; Gold, A.; Surratt, J. D.; Ault, A. P., Reactive uptake of isoprene epoxydiols increases the viscosity of the core of phase-separated aerosol particles. *ACS Earth Space Chem.* **2019**, *3*, 1402-1414.
35. Rindelaub, J. D.; Craig, R. L.; Nandy, L.; Bondy, A. L.; Dutcher, C. S.; Shepson, P. B.; Ault, A. P., Direct measurement of pH in individual particles via Raman microspectroscopy and variation in acidity with relative humidity. *J. Phys. Chem. A* **2016**, *120*, (6), 911-917.
36. Ault, A. P.; Zhao, D.; Ebben, C. J.; Tauber, M. J.; Geiger, F. M.; Prather, K. A.; Grassian, V. H., Raman microspectroscopy and vibrational sum frequency generation spectroscopy as probes of the bulk and surface compositions of size-resolved sea spray aerosol particles. *Phys. Chem. Chem. Phys.* **2013**, *15*, (17), 6206-6214.
37. Kirpes, R. M.; Bonanno, D.; May, N. W.; Fraund, M.; Barget, A. J.; Moffet, R. C.; Ault, A. P.; Pratt, K. A., Wintertime Arctic sea spray aerosol composition controlled by sea ice lead microbiology. *ACS Cen Sci* **2019**, *5*, 1760–1767.
38. Ault, A. P.; Guasco, T. L.; Baltrusaitis, J.; Ryder, O. S.; Trueblood, J. V.; Collins, D. B.; Ruppel, M. J.; Cuadra-Rodriguez, L. A.; Prather, K. A.; Grassian, V. H., Heterogeneous reactivity of nitric acid with nascent sea spray aerosol: large differences observed between and within individual particles. *J. Phys. Chem. Lett.* **2014**, *5*, (15), 2493-2500.
39. Riva, M.; Budisulistiorini, S. H.; Chen, Y.; Zhang, Z.; D'Ambro, E. L.; Zhang, X.; Gold, A.; Turpin, B. J.; Thornton, J. A.; Canagaratna, M. R.; Surratt, J. D., Chemical characterization of secondary organic aerosol from oxidation of isoprene hydroxyhydroperoxides. *Environ. Sci. Tech.* **2016**, *50*, (18), 9889-9899.
40. Surratt, J. D., Gomez-Gonzalez, Y., Chan, Arthur W. H., Vermeylen, Reinhilde. Shahgholi, Mona. Kleindienst, Tadeusz E., Edney, Edward O., Offenber, John H., Lewandowski, Michael.

- Jaoui, Mohammed. Maenhaut, Willy. Claeys, Magda. Flagan, Richard C., Seinfeld, John H., Organosulfate formation in biogenic secondary organic aerosol *J. Phys. Chem. A* **2008**, *112*, 8345–8378.
41. Hettiyadura, A. P. S.; Al-Naiema, I. M.; Hughes, D. D.; Fang, T.; Stone, E. A., Organosulfates in Atlanta, Georgia: Anthropogenic influences on biogenic secondary organic aerosol formation. *Atmospheric Chemistry and Physics Discussions* **2018**, 1-27.
42. Bondy, A. L.; Craig, R. L.; Zhang, Z.; Gold, A.; Surratt, J. D.; Ault, A. P., Isoprene-derived organosulfates: vibrational mode analysis by Raman spectroscopy, acidity-dependent spectral modes, and observation in individual atmospheric particles. *J. Phys. Chem. A* **2018**, *122*, (1), 303-315.
43. Craig, R. L.; Bondy, A. L.; Ault, A. P., Surface enhanced Raman spectroscopy enables observations of previously undetectable secondary organic aerosol components at the individual particle level. *Anal. Chem.* **2015**, *87*, (15), 7510-7514.
44. Laskina, O.; Morris, H. S.; Grandquist, J. R.; Qin, Z.; Stone, E. A.; Tivanski, A. V.; Grassian, V. H., Size matters in the water uptake and hygroscopic growth of atmospherically relevant multicomponent aerosol particles. *J. Phys. Chem. A* **2015**, *119*, (19), 4489-4497.
45. Craig, R. L.; Bondy, A. L.; Ault, A. P., Computer-controlled Raman microspectroscopy (CC-Raman): A method for the rapid characterization of individual atmospheric aerosol particles. *Aerosol. Sci. Technol.* **2017**, *51*, 1099–1112.
46. Tirella, P. S.; Craig, R. L.; Tubbs, D. B.; Olson, N. E.; Lei, Z.; Ault, A. P., Extending surface enhanced Raman spectroscopy (SERS) of atmospheric aerosol particles to the accumulation mode (150-800 nm). *Environ. Sci.: Processes Impacts* **2018**, *20*, 1570-1580.
47. Ofner, J.; Deckert-Gaudig, T.; Kamilli, K. A.; Held, A.; Lohninger, H.; Deckert, V.; Lendl, B., Tip-enhanced Raman spectroscopy of atmospherically relevant aerosol nanoparticles. *Anal. Chem.* **2016**, *88*, (19), 9766-9772.
48. Doughty, D. C.; Hill, S. C., Raman spectra of atmospheric particles measured in Maryland, USA over 22.5 h using an automated aerosol Raman spectrometer. *J. Quant. Spectrosc. Radiat. Transf.* **2020**, *244*.
49. Doughty, D. C.; Hill, S. C., Automated aerosol Raman spectrometer for semi-continuous sampling of atmospheric aerosol. *J. Quant. Spectrosc. Radiat. Transf.* **2017**, *188*, 103-117.
50. Bondy, A. L.; Kirpes, R. M.; Merzel, R. L.; Pratt, K. A.; Banaszak Holl, M. M.; Ault, A. P., Atomic force microscopy-infrared spectroscopy of individual atmospheric aerosol particles: subdiffraction limit vibrational spectroscopy and morphological analysis. *Anal. Chem.* **2017**, *89*, 8594-8598.
51. Lei, Z.; Bliesner, S. E.; Mattson, C. N.; Cooke, M. E.; Olson, N. E.; Chibwe, K.; Albert, J. N. L.; Ault, A. P., Aerosol acidity sensing via polymer degradation. *Anal. Chem.* **2020**, *92*, (9), 6502-6511.
52. Or, V. W.; Estillore, A. D.; Tivanski, A. V.; Grassian, V. H., Lab on a tip: atomic force microscopy - photothermal infrared spectroscopy of atmospherically relevant organic/inorganic aerosol particles in the nanometer to micrometer size range. *Analyst* **2018**, *143*, 2765-2774.
53. Dazzi, A.; Prater, C. B.; Hu, Q.; Chase, D. B.; Rabolt, J. F.; Marcott, C., AFM-IR: Combining atomic force microscopy and infrared spectroscopy for nanoscale chemical characterization *Appl. Spectrosc.* **2012**, *66*, (12), 1365-1384.

54. Dazzi, A., Prazeres, R., Glotin, F., Ortega, J. M., Local infrared microspectroscopy with subwavelength spatial resolution with an atomic force microscope tip used as a photothermal sensor. *Opt. Lett.* **2005**, *30*, (18), 2388-2390.
55. Dazzi, A.; Prater, C. B., AFM-IR: Technology and applications in nanoscale infrared spectroscopy and chemical imaging. *Chem. Rev.* **2016**, *117*, 5146–5173.
56. Morris, H. S.; Estillore, A. D.; Laskina, O.; Grassian, V. H.; Tivanski, A. V., Quantifying the hygroscopic growth of individual submicrometer particles with atomic force microscopy. *Anal. Chem.* **2016**, *88*, (7), 3647-54.
57. Olson, N. E.; Xiao, Y.; Lei, Z.; Ault, A. P., Simultaneous optical photothermal infrared (O-PTIR) and Raman spectroscopy of submicrometer atmospheric particles. *Anal Chem* **2020**, *92*, (14), 9932-9939.
58. Hale, R. C.; Seeley, M. E.; La Guardia, M. J.; Mai, L.; Zeng, E. Y., A global perspective on microplastics. *J. Geophys. Res. Oceans* **2020**, *125*, (1).
59. Klementieva, O.; Sandt, C.; Martinsson, I.; Kansiz, M.; Gouras, G. K.; Borondics, F., Super-resolution infrared imaging of polymorphic amyloid aggregates directly in neurons. *Adv. Sci.* **2020**.
60. Li, X.; Zhang, D.; Bai, Y.; Wang, W.; Liang, J.; Cheng, J. X., Fingerprinting a living cell by Raman integrated mid-infrared photothermal microscopy. *Anal Chem* **2019**, *91*, (16), 10750-10756.
61. Li, Z., Kuno, M., Hartland, G., Super-resolution mid-infrared imaging using photothermal microscopy. In *Conference on Lasers and Electro-Optics*, Optical Society of America: San Jose, California, United States, 2016; Vol. ATu3J.7.
62. Zhang, D., Li, C., Zhang, C., Slipchenko, M. N., Eakins, G., Cheng, J. X., Depth-resolved mid-infrared photothermal imaging of living cells and organisms with submicrometer spatial resolution. *Sci. Adv.* **2016**, *2*, (9), e1600521.
63. Li, C.; Zhang, D.; Slipchenko, M. N.; Cheng, J. X., Mid-infrared photothermal imaging of active pharmaceutical ingredients at submicrometer spatial resolution. *Anal Chem* **2017**, *89*, (9), 4863-4867.
64. Druy, M. A.; Furstenberg, R.; Crocombe, R. A.; Kendziora, C. A.; Papantonakis, M. R.; Nguyen, V.; McGill, R. A., *Chemical imaging using infrared photothermal microspectroscopy*. 2012.
65. Pöschl, U., Atmospheric aerosols: Composition, transformation, climate and health effects. *Atmos. Chem.* **2005**, *44*, 7520 – 7540.
66. Knopf, D. A.; Alpert, P. A.; Wang, B., The role of organic aerosol in atmospheric ice nucleation: a review. *ACS Earth Space Chem.* **2018**, *2*, (3), 168-202.
67. Ault, A.; Axson, J., Atmospheric aerosol chemistry: spectroscopic and microscopic advances. *Anal. Chem.* **2016**, *89*, 430-452.
68. Riemer, N., Ault, A. P., West, M., Craig, R. L., Curtis, J. H., Aerosol mixing state: measurements, modeling, and impacts. *Review of Geophysics* **2019**, *57*, 1-63.
69. Saukko, E.; Lambe, A. T.; Massoli, P.; Koop, T.; Wright, J. P.; Croasdale, D. R.; Pedernera, D. A.; Onasch, T. B.; Laaksonen, A.; Davidovits, P.; Worsnop, D. R.; Virtanen, A., Humidity-dependent phase state of SOA particles from biogenic and anthropogenic precursors. *Atmospheric Chemistry and Physics* **2012**, *12*, (16), 7517-7529.

70. Zhang, Y.; Sanchez, M. S.; Douet, C.; Wang, Y.; Bateman, A. P.; Gong, Z.; Kuwata, M.; Renbaum-Wolff, L.; Sato, B. B.; Liu, P. F.; Bertram, A. K.; Geiger, F. M.; Martin, S. T., Changing shapes and implied viscosities of suspended submicron particles. *Atmospheric Chemistry and Physics* **2015**, *15*, (14), 7819-7829.
71. You, Y.; Smith, M. L.; Song, M.; Martin, S. T.; Bertram, A. K., Liquid-liquid phase separation in atmospherically relevant particles consisting of organic species and inorganic salts. *Int. Rev. Phys. Chem.* **2014**, *33*, (1), 43-77.
72. You, Y.; Renbaum-Wolff, L.; Bertram, A. K., Liquid-liquid phase separation in particles containing organics mixed with ammonium sulfate, ammonium bisulfate, ammonium nitrate or sodium chloride. *Atmos. Chem. Phys.* **2013**, *13*, (23), 11723-11734.
73. Altaf, M. B.; Freedman, M. A., Effect of drying rate on aerosol particle morphology. *J. Phys. Chem. Lett.* **2017**, *8*, 3613-3618.
74. Freedman, M. A., Phase separation in organic aerosol. *Chem. Soc. Rev.* **2017**, *46*, 7694-7705.
75. Freedman, M. B., Baustian, K. J., Wise, M. E., Tolbert, M. A., Characterizing the morphology of organic aerosols at ambient temperature and pressure. *Anal. Chem.* **2010**, *82*, 7965-7972.
76. Slade, J. H.; Ault, A. P.; Bui, A. T.; Ditto, J. C.; Lei, Z.; Bondy, A. L.; Olson, N. E.; Cook, R. D.; Desrochers, S. J.; Harvey, R. M.; Erickson, M. H.; Wallace, H. W.; Alvarez, S. L.; Flynn, J. H.; Boor, B. E.; Petrucci, G. A.; Gentner, D. R.; Griffin, R. J.; Shepson, P. B., Bouncer particles at night: biogenic secondary organic aerosol chemistry and sulfate drive diel variations in the aerosol phase in a mixed forest. *Environ. Sci. Technol.* **2019**, *53*, 4977-4987.
77. You, Y.; Renbaum-Wolff, L.; Carreras-Sospedra, M.; Hanna, S. J.; Hiranuma, N.; Kamal, S.; Smith, M. L.; Zhang, X.; Weber, R. J.; Shilling, J. E.; Dabdub, D.; Martin, S. T.; Bertram, A. K., Images reveal that atmospheric particles can undergo liquid-liquid phase separations. *Proc. Natl. Acad. Sci. U. S. A.* **2012**, *109*, (33), 13188-13193.
78. Bondy, A. L.; Bonanno, D.; Moffet, R. C.; Wang, B.; Laskin, A.; Ault, A. P., The diverse chemical mixing state of aerosol particles in the southeastern United States. *Atmos. Chem. Phys.* **2018**, *18*, (16), 12595-12612.
79. Carlton, A. G., Wiedinmyer, C., Kroll, J. H., A review of Secondary Organic Aerosol (SOA) formation from isoprene. *Atmospheric Chemistry and Physics* **2009**, *9*, 4987-5005.
80. Guenther, A., Karl, T., Harley, P., Wiedinmyer, C., Palmer, P. I., Geron, C., Estimates of global terrestrial isoprene emissions using MEGAN (Model of Emissions of Gases and Aerosols from Nature). *Atmospheric Chemistry and Physics* **2006**, *6*, 3181-3210.
81. Renbaum-Wolff, L.; Grayson, J. W.; Bateman, A. P.; Kuwata, M.; Sellier, M.; Murray, B. J.; Shilling, J. E.; Martin, S. T.; Bertram, A. K., Viscosity of alpha-pinene secondary organic material and implications for particle growth and reactivity. *Proc. Natl. Acad. Sci. U. S. A.* **2013**, *110*, (20), 8014-8019.
82. Beauregard, D., *Locating and estimating air emissions from sources of toluene*. Office of Air Quality Planning and Standards, United States Environmental Protection Agency, EPA: Research Triangle Park, NC, 1994.
83. Hallquist, M., Wenger, J. C., Baltensperger, U., Rudich, Y., Simpson, D., Claeys, M., Dommen, J., Donahue, N. M., George, C., Goldstein, A. H., Hamilton, J. F., Herrmann, H., Hoffmann, T., Iinuma, Y., Jang, M., Jenkin, M. E., Jimenez, J. L., Kiendler-Scharr, A.,

- Maenhaut, W., McFiggans, G., Mentel, Th. F.; Monod, A., Prevot, A. S. H., Seinfeld, J. H., Surratt, J. D., Szmigielski, R., Wildt, J., The formation, properties, and impacts of secondary organic aerosol: current and emerging issues. *Atmospheric Chemistry and Physics* **2009**, *9*, 5155–5236.
84. Zhang, H., Lindsay D. Yee, Ben H. Lee, Michael P. Curtis, David R.; Worton, G. I.-V., John H. Offenberg, Michael Lewandowski, Tadeusz; E. Kleindienst, M. R. B., Amara L. Holder, William A. Lonneman, Kenneth S.; Docherty, M. J., Havala O. T. Pye, Weiwei Hu, Douglas A. Day, Pedro; Campuzano-Jost, J. L. J., Hongyu Guo, Rodney J. Weber, Joost de Gouw, Abigail R. Koss, Eric S. Edgerton, William Brune, Claudia Mohr, Felipe D. Lopez-; Hilfiker, A. L., Nathan M. Kreisberg, Steve R. Spielman, Susanne V. Hering, Kevin; R. Wilson, J. A. T., Allen H. Goldstein, Monoterpenes are the largest source of summertime organic aerosol in the Southeastern United States. *Proc. Natl. Acad. Sci. U. S. A.* **2018**, *115*, 2038-2043.
85. Guenther, A. B.; Jiang, X.; Heald, C. L.; Sakulyanontvittaya, T.; Duhl, T.; Emmons, L. K.; Wang, X., The Model of Emissions of Gases and Aerosols from Nature version 2.1 (MEGAN2.1): an extended and updated framework for modeling biogenic emissions. *Geosci. Mod. Devel.* **2012**, *5*, (6), 1471-1492.
86. Bates, K. H.; Crouse, J. D.; St Clair, J. M.; Bennett, N. B.; Nguyen, T. B.; Seinfeld, J. H.; Stoltz, B. M.; Wennberg, P. O., Gas phase production and loss of isoprene epoxydiols. *J Phys Chem A.* **2014**, *118*, (7), 1237-1246.
87. Paulot, F.; Crouse, J. D.; Kjaergaard, H. G.; Kurten, A.; St Clair, J. M.; Seinfeld, J. H.; Wennberg, P. O., Unexpected epoxide formation in the gas-phase photooxidation of isoprene. *Science* **2009**, *325*, (5941), 730-733.
88. Riva, M.; Budisulistiorini, S. H.; Zhang, Z.; Gold, A.; Thornton, J. A.; Turpin, B. J.; Surratt, J. D., Multiphase reactivity of gaseous hydroperoxide oligomers produced from isoprene ozonolysis in the presence of acidified aerosols. *Atmos. Env.* **2017**, *152*, 314-322.
89. Gaston, C. J.; Riedel, T. P.; Zhang, Z.; Gold, A.; Surratt, J. D.; Thornton, J. A., Reactive uptake of an isoprene-derived epoxydiol to submicron aerosol particles. *Environ. Sci. Technol.* **2014**, *48*, (19), 11178-11186.
90. Riedel, T. P.; Lin, Y.-H.; Budisulistiorini, S. H.; Gaston, C. J.; Thornton, J. A.; Zhang, Z.; Vizuete, W.; Gold, A.; Surratt, J. D., Heterogeneous reactions of isoprene-derived epoxides: reaction probabilities and molar secondary organic aerosol yield estimates. *Environ. Sci. Technol. Lett.* **2015**, *2*, (2), 38-42.
91. Jang, M., Czoschke, N. M., Lee, S., Kamens, R. M., Heterogeneous atmospheric aerosol production by acid-catalyzed particle-phase reactions. *Science* **2002**, *298*, 814-817.
92. Czoschke, N. M., Jang, M., Kamens, R. M., Effect of acidic seed on biogenic secondary organic aerosol growth. *Atmos. Env.* **2003**, *37*, (30), 4287-4299.
93. Budisulistiorini, S. H.; Baumann, K.; Edgerton, E. S.; Bairai, S. T.; Mueller, S.; Shaw, S. L.; Knipping, E. M.; Gold, A.; Surratt, J. D., Seasonal characterization of submicron aerosol chemical composition and organic aerosol sources in the southeastern United States: Atlanta, Georgia, and Look Rock, Tennessee. *Atmospheric Chemistry and Physics* **2016**, *16*, (8), 5171-5189.
94. Hu, W. W.; Campuzano-Jost, P.; Palm, B. B.; Day, D. A.; Ortega, A. M.; Hayes, P. L.; Krechmer, J. E.; Chen, Q.; Kuwata, M.; Liu, Y. J.; de Sá, S. S.; McKinney, K.; Martin, S. T.; Hu, M.; Budisulistiorini, S. H.; Riva, M.; Surratt, J. D.; St. Clair, J. M.; Isaacman-Van Wertz, G.; Yee,

- L. D.; Goldstein, A. H.; Carbone, S.; Brito, J.; Artaxo, P.; de Gouw, J. A.; Koss, A.; Wisthaler, A.; Mikoviny, T.; Karl, T.; Kaser, L.; Jud, W.; Hansel, A.; Docherty, K. S.; Alexander, M. L.; Robinson, N. H.; Coe, H.; Allan, J. D.; Canagaratna, M. R.; Paulot, F.; Jimenez, J. L., Characterization of a real-time tracer for isoprene epoxydiols-derived secondary organic aerosol (IEPOX-SOA) from aerosol mass spectrometer measurements. *Atmospheric Chemistry and Physics* **2015**, *15*, (20), 11807-11833.
95. Fuzzi, S., Andreae, M. O., Huebert, B. J., Kulmala, M., Bond, T. C., Boy, M., Doherty, S. J., Guenther, A., Kanakidou, M., Kawamura, K., Kerminen, V. M., Lohmann, U., Russell, L.M., Poschl, U., Critical assessment of the current state of scientific knowledge, terminology, and research needs concerning the role of organic aerosols in the atmosphere, climate, and global change. *Atmospheric Chemistry and Physics* **2006**, *6*, 2017–2038.
96. Reid, J. P.; Dennis-Smith, B. J.; Kwamena, N. O.; Miles, R. E.; Hanford, K. L.; Homer, C. J., The morphology of aerosol particles consisting of hydrophobic and hydrophilic phases: hydrocarbons, alcohols and fatty acids as the hydrophobic component. *Phys. Chem. Chem. Phys.* **2011**, *13*, (34), 15559-15572.
97. Erdakos, G. B.; Chang, E. I.; Pankow, J. F.; Seinfeld, J. H., Prediction of activity coefficients in liquid aerosol particles containing organic compounds, dissolved inorganic salts, and water—Part 3: Organic compounds, water, and ionic constituents by consideration of short-, mid-, and long-range effects using X-UNIFAC.3. *Atmos. Environ.* **2006**, *40*, (33), 6437-6452.
98. Riva, M.; Bell, D. M.; Hansen, A. M.; Drozd, G. T.; Zhang, Z.; Gold, A.; Imre, D.; Surratt, J. D.; Glasius, M.; Zelenyuk, A., Effect of organic coatings, humidity and aerosol acidity on multiphase chemistry of isoprene epoxydiols. *Environ. Sci. Technol.* **2016**, *50*, (11), 5580-5588.
99. Shiraiwa, M.; Zuend, A.; Bertram, A. K.; Seinfeld, J. H., Gas-particle partitioning of atmospheric aerosols: interplay of physical state, non-ideal mixing and morphology. *Phys. Chem. Chem. Phys.* **2013**, *15*, (27), 11441-11453.
100. Renbaum-Wolff, L.; Song, M.; Marcolli, C.; Zhang, Y.; Liu, P. F.; Grayson, J. W.; Geiger, F. M.; Martin, S. T.; Bertram, A. K., Observations and implications of liquid-liquid phase separation at high relative humidities in secondary organic material produced by a-pinene ozonolysis without inorganic salts. *Atmospheric Chemistry and Physics* **2016**, *16*, (12), 7969-7979.
101. Chang, E. I.; Pankow, J. F., Prediction of activity coefficients in liquid aerosol particles containing organic compounds, dissolved inorganic salts, and water—Part 2: Consideration of phase separation effects by an X-UNIFAC model. *Atmos. Environ.* **2006**, *40*, (33), 6422-6436.
102. Zuend, A.; Seinfeld, J. H., Modeling the gas-particle partitioning of secondary organic aerosol: the importance of liquid-liquid phase separation. *Atmospheric Chemistry and Physics* **2012**, *12*, (9), 3857-3882.
103. Brunamonti, S., Krieger, U. K., Marcolli, C., Peter, T., Redistribution of black carbon in aerosol particles undergoing liquid-liquid phase separation. *Geophys. Res. Lett.* **2015**, *42*, 2532–2539.
104. Lienhard, D. M.; Huisman, A. J.; Krieger, U. K.; Rudich, Y.; Marcolli, C.; Luo, B. P.; Bones, D. L.; Reid, J. P.; Lambe, A. T.; Canagaratna, M. R.; Davidovits, P.; Onasch, T. B.; Worsnop, D. R.; Steimer, S. S.; Koop, T.; Peter, T., Viscous organic aerosol particles in the upper troposphere: diffusivity-controlled water uptake and ice nucleation? *Atmospheric Chemistry and Physics* **2015**, *15*, (23), 13599-13613.

105. Virtanen, A.; Joutsensaari, J.; Koop, T.; Kannosto, J.; Yli-Pirila, P.; Leskinen, J.; Makela, J. M.; Holopainen, J. K.; Poschl, U.; Kulmala, M.; Worsnop, D. R.; Laaksonen, A., An amorphous solid state of biogenic secondary organic aerosol particles. *Nature* **2010**, *467*, (7317), 824-827.
106. Pajunoja, A.; Malila, J.; Hao, L.; Joutsensaari, J.; Lehtinen, K. E. J.; Virtanen, A., Estimating the viscosity range of SOA particles based on their coalescence time. *Aerosol. Sci. Technol.* **2013**, *48*, (2), i-iv.
107. Surratt, J. D.; Chan, A. W.; Eddingsaas, N. C.; Chan, M.; Loza, C. L.; Kwan, A. J.; Hersey, S. P.; Flagan, R. C.; Wennberg, P. O.; Seinfeld, J. H., Reactive intermediates revealed in secondary organic aerosol formation from isoprene. *Proc. Natl. Acad. Sci. U. S. A.* **2010**, *107*, (15), 6640-6645.
108. Budisulistiorini, S. H.; Nenes, A.; Carlton, A. M. G.; Surratt, J. D.; McNeill, V. F.; Pye, H. O. T., Simulating aqueous-phase isoprene-epoxydiol (IEPOX) secondary organic aerosol production during the 2013 Southern Oxidant and Aerosol Study (SOAS). *Environ. Sci. Technol.* **2016**, *51*, 5026-5034.
109. Surratt, J. D.; Murphy, S. M.; Kroll, J. H.; Ng, N. L.; Hildebrandt, L.; Sorooshian, A.; Szmigielski, R.; Vermeylen, R.; Maenhaut, W.; Claeys, M.; Flagan, R. C.; Seinfeld, J. H., Chemical composition of secondary organic aerosol formed from the photooxidation of isoprene. *J. Phys. Chem. A* **2006**, *110*, (31), 9665-9690.
110. Lin, Y. H.; Zhang, Z.; Docherty, K. S.; Zhang, H.; Budisulistiorini, S. H.; Rubitschun, C. L.; Shaw, S. L.; Knipping, E. M.; Edgerton, E. S.; Kleindienst, T. E.; Gold, A.; Surratt, J. D., Isoprene epoxydiols as precursors to secondary organic aerosol formation: acid-catalyzed reactive uptake studies with authentic compounds. *Environ. Sci. Technol.* **2012**, *46*, (1), 250-258.
111. Lin, Y. H.; Budisulistiorini, S. H.; Chu, K.; Siejack, R. A.; Zhang, H.; Riva, M.; Zhang, Z.; Gold, A.; Kautzman, K. E.; Surratt, J. D., Light-absorbing oligomer formation in secondary organic aerosol from reactive uptake of isoprene epoxydiols. *Environ. Sci. Technol.* **2014**, *48*, (20), 12012-12021.
112. Hosny, N. A.; Fitzgerald, C.; Tong, C.; Kalberer, M.; Kuimova, M. K.; Pope, F. D., Fluorescent lifetime imaging of atmospheric aerosols: a direct probe of aerosol viscosity. *Faraday Discuss.* **2013**, *165*, 343.
113. Shiraiwa, M.; Li, Y.; Tsimpidi, A. P.; Karydis, V. A.; Berkemeier, T.; Pandis, S. N.; Lelieveld, J.; Koop, T.; Poschl, U., Global distribution of particle phase state in atmospheric secondary organic aerosols. *Nature Comm.* **2017**, *8*, 15002.
114. Booth, A. M.; Murphy, B.; Riipinen, I.; Percival, C. J.; Topping, D. O., Connecting bulk viscosity measurements to kinetic limitations on attaining equilibrium for a model aerosol composition. *Environ. Sci. Technol.* **2014**, *48*, (16), 9298-9305.
115. Berkemeier, T.; Shiraiwa, M.; Pöschl, U.; Koop, T., Competition between water uptake and ice nucleation by glassy organic aerosol particles. *Atmospheric Chemistry and Physics* **2014**, *14*, (22), 12513-12531.
116. Shrestha, M.; Zhang, Y.; Upshur, M. A.; Liu, P.; Blair, S. L.; Wang, H. F.; Nizkorodov, S. A.; Thomson, R. J.; Martin, S. T.; Geiger, F. M., On surface order and disorder of alpha-pinene-derived secondary organic material. *J. Phys. Chem. A* **2014**, *119*, (19), 4609-4617.
117. Veghte, D. P.; Altaf, M. B.; Freedman, M. A., Size dependence of the structure of organic aerosol. *J. Am. Chem. Soc.* **2013**, *135*, (43), 16046-16049.

118. Gorkowski, K.; Donahue, N. M.; Sullivan, R. C., Emulsified and liquid-liquid phase separated states of alpha-pinene secondary organic aerosol determined using aerosol optical tweezers. *Environ. Sci. Technol.* **2017**, *51*, 12154-12163.
119. Guo, H.; Xu, L.; Bougiatioti, A.; Cerully, K. M.; Capps, S. L.; Hite, J. R.; Carlton, A. G.; Lee, S. H.; Bergin, M. H.; Ng, N. L.; Nenes, A.; Weber, R. J., Fine-particle water and pH in the southeastern United States. *Atmospheric Chemistry and Physics* **2015**, *15*, (9), 5211-5228.
120. Pajunoja, A.; Lambe, A. T.; Hakala, J.; Rastak, N.; Cummings, M. J.; Brogan, J. F.; Hao, L.; Paramonov, M.; Hong, J.; Prisle, N. L.; Malila, J.; Romakkaniemi, S.; Lehtinen, K. E. J.; Laaksonen, A.; Kulmala, M.; Massoli, P.; Onasch, T. B.; Donahue, N. M.; Riipinen, I.; Davidovits, P.; Worsnop, D. R.; Petäjä, T.; Virtanen, A., Adsorptive uptake of water by semisolid secondary organic aerosols. *Geophys. Res. Lett.* **2015**, *42*, (8), 3063-3068.
121. Bertram, A. K.; Martin, S. T.; Hanna, S. J.; Smith, M. L.; Bodsworth, A.; Chen, Q.; Kuwata, M.; Liu, A.; You, Y.; Zorn, S. R., Predicting the relative humidities of liquid-liquid phase separation, efflorescence, and deliquescence of mixed particles of ammonium sulfate, organic material, and water using the organic-to-sulfate mass ratio of the particle and the oxygen-to-carbon elemental ratio of the organic component. *Atmospheric Chemistry and Physics* **2011**, *11*, (21), 10995-11006.
122. Ciobanu, V. G.; Marcolli, C.; Krieger, U. K.; Weers, U.; Peter, T., Liquid-liquid phase separation in mixed organic/inorganic aerosol particles. *The journal of physical chemistry. A* **2009**, *113*, (41), 10966-10978.
123. Song, M.; Liu, P.; Martin, S. T.; Bertram, A. K., Liquid-liquid phase separation in particles containing secondary organic material free of inorganic salts. *Atmos. Chem. Phys.* **2017**, *17*, (18), 11261-11271.
124. Lehtipalo, K.; Sipilä, M.; Junninen, H.; Ehn, M.; Berndt, T.; Kajos, M. K.; Worsnop, D. R.; Petäjä, T.; Kulmala, M., Observations of nano-CN in the nocturnal boreal forest. *Aerosol. Sci. Technol.* **2011**, *45*, (4), 499-509.
125. Prisle, N. L.; Engelhart, G. J.; Bilde, M.; Donahue, N. M., Humidity influence on gas-particle phase partitioning of α -pinene + O₃ secondary organic aerosol. *Geophys. Res. Lett.* **2010**, *37*, (1), L01802.
126. Vaden, T. D.; Song, C.; Zaveri, R. A.; Imre, D.; Zelenyuk, A., Morphology of mixed primary and secondary organic particles and the adsorption of spectator organic gases during aerosol formation. *Proc. Natl. Acad. Sci. U. S. A.* **2010**, *107*, (15), 6658-6663.
127. Smith, M. L.; Bertram, A. K.; Martin, S. T., Deliquescence, efflorescence, and phase miscibility of mixed particles of ammonium sulfate and isoprene-derived secondary organic material. *Atmos. Chem. Phys.* **2012**, *12*, (20), 9613-9628.
128. Smith, M. L.; Kuwata, M.; Martin, S. T., Secondary organic material produced by the dark ozonolysis of α -pinene minimally affects the deliquescence and efflorescence of ammonium sulfate. *Aerosol Sci. Technol.* **2011**, *45*, (2), 244-261.
129. Song, M.; Liu, P. F.; Hanna, S. J.; Zaveri, R. A.; Potter, K.; You, Y.; Martin, S. T.; Bertram, A. K., Relative humidity-dependent viscosity of secondary organic material from toluene photo-oxidation and possible implications for organic particulate matter over megacities. *Atmospheric Chemistry and Physics* **2016**, *16*, (14), 8817-8830.
130. Craig, R. L.; Peterson, P. K.; Nandy, L.; Lei, Z.; Hossain, M. A.; Camarena, S.; Dodson, R. A.; Cook, R. D.; Dutcher, C. S.; Ault, A. P., Direct determination of aerosol pH: size-resolved

measurements of submicrometer and supermicrometer aqueous particles. *Anal. Chem.* **2018**, *90*, (19), 11232-11239.

131. Imre, D. G.; Xu, J.; Tang, I. N.; McGraw, R., Ammonium bisulfate/water equilibrium and metastability phase diagrams. *J. Phys. Chem. A* **1997**, *101*, 4191-4195.

132. Lambe, A. T.; Ahern, A. T.; Williams, L. R.; Slowik, J. G.; Wong, J. P. S.; Abbatt, J. P. D.; Brune, W. H.; Ng, N. L.; Wright, J. P.; Croasdale, D. R.; Worsnop, D. R.; Davidovits, P.; Onasch, T. B., Characterization of aerosol photooxidation flow reactors: heterogeneous oxidation, secondary organic aerosol formation and cloud condensation nuclei activity measurements. *Atmos. Meas. Tech.* **2011**, *4*, (3), 445-461.

133. Bruns, E. A.; El Haddad, I.; Keller, A.; Klein, F.; Kumar, N. K.; Pieber, S. M.; Corbin, J. C.; Slowik, J. G.; Brune, W. H.; Baltensperger, U.; Prévôt, A. S. H., Inter-comparison of laboratory smog chamber and flow reactor systems on organic aerosol yield and composition. *Atmos. Meas. Tech.* **2015**, *8*, (6), 2315-2332.

134. Lambe, A. T.; Chhabra, P. S.; Onasch, T. B.; Brune, W. H.; Hunter, J. F.; Kroll, J. H.; Cummings, M. J.; Brogan, J. F.; Parmar, Y.; Worsnop, D. R.; Kolb, C. E.; Davidovits, P., Effect of oxidant concentration, exposure time, and seed particles on secondary organic aerosol chemical composition and yield. *Atmos. Chem. Phys.* **2015**, *15*, (6), 3063-3075.

135. Pieber, S. M.; Kumar, N. K.; Klein, F.; Comte, P.; Bhattu, D.; Dommen, J.; Bruns, E. A.; Kılıç, D.; El Haddad, I.; Keller, A.; Czerwinski, J.; Heeb, N.; Baltensperger, U.; Slowik, J. G.; Prévôt, A. S. H., Gas-phase composition and secondary organic aerosol formation from standard and particle filter-retrofitted gasoline direct injection vehicles investigated in a batch and flow reactor. *Atmos. Chem. Phys.* **2018**, *18*, (13), 9929-9954.

136. Shrestha, M.; Zhang, Y.; Ebben, C. J.; Martin, S. T.; Geiger, F. M., Vibrational sum frequency generation spectroscopy of secondary organic material produced by condensational growth from alpha-pinene ozonolysis. *J. Phys. Chem. A* **2013**, *117*, (35), 8427-8436.

137. Zanca, N.; Lambe, A. T.; Massoli, P.; Paglione, M.; Croasdale, D. R.; Parmar, Y.; Tagliavini, E.; Gilardoni, S.; Decesari, S., Characterizing source fingerprints and ageing processes in laboratory-generated secondary organic aerosols using proton-nuclear magnetic resonance (1H-NMR) analysis and HPLC HULIS determination. *Atmos. Chem. Phys.* **2017**, *17*, (17), 10405-10421.

138. Lambe, A.; Massoli, P.; Zhang, X.; Canagaratna, M.; Nowak, J.; Daube, C.; Yan, C.; Nie, W.; Onasch, T.; Jayne, J.; Kolb, C.; Davidovits, P.; Worsnop, D.; Brune, W., Controlled nitric oxide production via O(1D) + N2O reactions for use in oxidation flow reactor studies. *Atmos. Meas. Tech.* **2017**, *10*, (6), 2283-2298.

139. Palm, B. B.; Campuzano-Jost, P.; Ortega, A. M.; Day, D. A.; Kaser, L.; Jud, W.; Karl, T.; Hansel, A.; Hunter, J. F.; Cross, E. S.; Kroll, J. H.; Peng, Z.; Brune, W. H.; Jimenez, J. L., In situ secondary organic aerosol formation from ambient pine forest air using an oxidation flow reactor. *Atmos. Chem. Phys.* **2016**, *16*, (5), 2943-2970.

140. Tkacik, D. S.; Lambe, A. T.; Jathar, S.; Li, X.; Presto, A. A.; Zhao, Y.; Blake, D.; Meinardi, S.; Jayne, J. T.; Croteau, P. L.; Robinson, A. L., Secondary organic aerosol formation from in-use motor vehicle emissions using a potential aerosol mass reactor. *Environ Sci Technol* **2014**, *48*, (19), 11235-11242.

141. Bahreini, R.; Middlebrook, A. M.; Brock, C. A.; de Gouw, J. A.; McKeen, S. A.; Williams, L. R.; Daumit, K. E.; Lambe, A. T.; Massoli, P.; Canagaratna, M. R.; Ahmadov,

- R., Carrasquillo, A. J., Cross, E. S., Ervens, B., Holloway, J. S., Hunter, J. F., Onasch, T. B., Pollack, I. B., Roberts, J. M., Ryerson, T. B., Warneke, C., Davidovits, P., Worsnop, D. R., Kroll, J. H., Mass spectral analysis of organic aerosol formed downwind of the Deepwater Horizon oil spill: field studies and laboratory confirmation. *Environ. Sci. Technol.* **2012**, *46*, 8025–8034.
142. Ortega, A. M.; Hayes, P. L.; Peng, Z.; Palm, B. B.; Hu, W.; Day, D. A.; Li, R.; Cubison, M. J.; Brune, W. H.; Graus, M.; Warneke, C.; Gilman, J. B.; Kuster, W. C.; de Gouw, J.; Gutiérrez-Montes, C.; Jimenez, J. L., Real-time measurements of secondary organic aerosol formation and aging from ambient air in an oxidation flow reactor in the Los Angeles area. *Atmos. Chem. Phys.* **2016**, *16*, (11), 7411-7433.
143. Zhang, Z.; Lin, Y. H.; Zhang, H.; Surratt, J. D.; Ball, L. M.; Gold, A., Technical Note: Synthesis of isoprene atmospheric oxidation products: isomeric epoxydiols and the rearrangement products <i>cis</i>- and <i>trans</i>-3-methyl-3,4-dihydroxytetrahydrofuran. *Atmospheric Chemistry and Physics* **2012**, *12*, (18), 8529-8535.
144. Midgley, P. A.; Weyland, M.; Thomas, J. M.; Johnson, B. F. G., Z-Contrast tomography: a technique in three-dimensional nanostructural analysis based on Rutherford scattering. *Chem. Comm.* **2001**, (10), 907-908.
145. DeCarlo, P. F.; Slowik, J. G.; Worsnop, D. R.; Davidovits, P.; Jimenez, J. L., Particle morphology and density characterization by combined mobility and aerodynamic diameter measurements. part 1: theory. *Aerosol. Sci. Technol.* **2004**, *38*, (12), 1185-1205.
146. DeRieux, W.-S. W.; Li, Y.; Lin, P.; Laskin, J.; Laskin, A.; Bertram, A. K.; Nizkorodov, S. A.; Shiraiwa, M., Predicting the glass transition temperature and viscosity of secondary organic material using molecular composition. *Atmospheric Chemistry and Physics* **2018**, *18*, (9), 6331-6351.
147. Koop, T.; Bookhold, J.; Shiraiwa, M.; Poschl, U., Glass transition and phase state of organic compounds: dependency on molecular properties and implications for secondary organic aerosols in the atmosphere. *Phys. Chem. Chem. Phys.* **2011**, *13*, (43), 19238–19255.
148. Shiraiwa, M., Ammann, M., Koop, T., Pöschl, U., Gas uptake and chemical aging of semisolid organic aerosol particles. *Proc. Natl. Acad. Sci. U. S. A.* **2011**, *103*, (27), 11003–11008.
149. Lee, H. D.; Kaluarachchi, C. P.; Hasenecz, E. S.; Zhu, J. Z.; Popa, E.; Stone, E. A.; Tivanski, A. V., Effect of dry or wet substrate deposition on the organic volume fraction of core-shell aerosol particles. *Atmos. Meas. Tech.* **2019**, *12*, (3), 2033-2042.
150. Liu, P.; Li, Y. J.; Wang, Y.; Bateman, A. P.; Zhang, Y.; Gong, Z.; Bertram, A. K.; Martin, S. T., Highly viscous states affect the browning of atmospheric organic particulate matter. *ACS Cent. Sci.* **2018**, *4*, (2), 207-215.
151. Fard, M. M.; Krieger, U. K.; Peter, T., Kinetic limitation to inorganic ion diffusivity and to coalescence of inorganic inclusions in viscous liquid-liquid phase-separated particles. *J. Phys. Chem. A* **2017**, *121*, 9284-9296.
152. Venkateswarlu, P., Bist, H. D., Jain, Y. S., Laser excited Raman spectrum of ammonium sulfate single crystal. *J. Raman Spectrosc.* **1975**, *3*, 143-151.
153. Jentzsch, P. V.; Kampe, B.; Ciobota, V.; Rosch, P.; Popp, J., Inorganic salts in atmospheric particulate matter: Raman spectroscopy as an analytical tool. *Spectrochim. Acta A Molec. Biomolec. Spectrosc.* **2013**, *115*, 697-708.
154. Sobanska, S.; Hwang, H.; Choel, M.; Jung, H. J.; Eom, H. J.; Kim, H.; Barbillat, J.; Ro, C. U., Investigation of the chemical mixing state of individual Asian dust particles by the combined

- use of electron probe X-ray microanalysis and Raman microspectrometry. *Anal. Chem.* **2012**, *84*, (7), 3145–3154.
155. Zhou, Q.; Pang, S. F.; Wang, Y.; Ma, J. B.; Zhang, Y. H., Confocal Raman studies of the evolution of the physical state of mixed phthalic acid/ammonium sulfate aerosol droplets and the effect of substrates. *J. Phys. Chem. B* **2014**, *118*, (23), 6198–6205.
156. Hatch, L. E.; Creamean, J. M.; Ault, A. P.; Surratt, J. D.; Chan, M. N.; Seinfeld, J. H.; Edgerton, E. S.; Su, Y.; Prather, K. A., Measurements of isoprene-derived organosulfates in ambient aerosols by aerosol time-of-flight mass spectrometry - part 1: single particle atmospheric observations in Atlanta. *Environ. Sci. Technol.* **2011**, *45*, (12), 5105–5111.
157. Hatch, L. E.; Creamean, J. M.; Ault, A. P.; Surratt, J. D.; Chan, M. N.; Seinfeld, J. H.; Edgerton, E. S.; Su, Y.; Prather, K. A., Measurements of isoprene-derived organosulfates in ambient aerosols by aerosol time-of-flight mass spectrometry-part 2: temporal variability and formation mechanisms. *Environ. Sci. Technol.* **2011**, *45*, (20), 8648-8655.
158. Weber, R. J., Guo, H., Russell, A. G., Nenes, A., High aerosol acidity despite declining sulfate concentrations over the past 15 years. *Nat. Geosci. Lett.* **2016**, *9*, 282-286.
159. Riva, M.; Chen, Y.; Zhang, Y.; Lei, Z.; Olson, N.; Boyer, H. C.; Narayan, S.; Yee, L. D.; Green, H.; Cui, T.; Zhang, Z.; Baumann, K. D.; Fort, M.; Edgerton, E. S.; Budisulistiorini, S.; Rose, C. A.; Ribeiro, I.; e Oliveira, R. L.; Santos, E.; Szopa, S.; Machado, C.; Zhao, Y.; Alves, E.; de Sa, S.; Hu, W.; Knipping, E.; Shaw, S.; Duvoisin Junior, S.; Souza, R. A. F. d.; Palm, B. B.; Jimenez, J. L.; Glasius, M.; Goldstein, A. H.; Pye, H. O. T.; Gold, A.; Turpin, B. J.; Vizuete, W.; Martin, S. T.; Thornton, J.; Dutcher, C. S.; Ault, A. P.; Surratt, J. D., Increasing isoprene epoxydiol-to-inorganic sulfate aerosol (IEPOX:Sulfinorg) ratio results in extensive conversion of inorganic sulfate to organosulfur forms: implications for aerosol physicochemical properties. *Environ. Sci. Technol.* **2019**, *Just accepted*.
160. Pye, H. O.; Pinder, R. W.; Piletic, I. R.; Xie, Y.; Capps, S. L.; Lin, Y. H.; Surratt, J. D.; Zhang, Z.; Gold, A.; Luecken, D. J.; Hutzell, W. T.; Jaoui, M.; Offenberg, J. H.; Kleindienst, T. E.; Lewandowski, M.; Edney, E. O., Epoxide pathways improve model predictions of isoprene markers and reveal key role of acidity in aerosol formation. *Environ. Sci. Technol.* **2013**, *47*, (19), 11056–11064.
161. Schmedding, R.; Ma, M.; Zhang, Y.; Farrell, S.; Pye, H. O. T.; Chen, Y.; Wang, C.-t.; Rasool, Q. Z.; Budisulistiorini, S. H.; Ault, A. P.; Surratt, J. D.; Vizuete, W., α -Pinene-derived organic coatings on acidic sulfate aerosol impacts secondary organic aerosol formation from isoprene in a box model. *Atmos. Environ.* **2019**, *Just accepted*.
162. Silvern, R. F.; Jacob, D. J.; Kim, P. S.; Marais, E. A.; Turner, J. R.; Campuzano-Jost, P.; Jimenez, J. L., Inconsistency of ammonium–sulfate aerosol ratios with thermodynamic models in the eastern US: a possible role of organic aerosol. *Atmos. Chem. Phys.* **2017**, *17*, (8), 5107-5118.
163. Lewis, E. R., Schwartz, S. E., *Sea salt aerosol production: Mechanisms, methods, measurements, and models - A critical review*. American Geophysical Union: Washington D. C., 2004; Vol. 152.
164. May, N. W.; Axson, J. L.; Watson, A.; Pratt, K. A.; Ault, A. P., Lake spray aerosol generation: a method for producing representative particles from freshwater wave breaking. *Atmos. Meas. Tech.* **2016**, *9*, 4311–4325.

165. Doubrawa, P.; Barthelmie, R. J.; Pryor, S. C.; Hasager, C. B.; Badger, M.; Karagali, I., Satellite winds as a tool for offshore wind resource assessment: the Great Lakes wind atlas. *Remote Sens. Environ.* **2015**, *168*, 349-359.
166. Monahan, E. C., Fresh water whitecaps. *J. Atmos. Sci.* **1969**, *26*, 1026-1029.
167. Chung, S. H.; Basarab, B. M.; Vanreken, T. M., Regional impacts of ultrafine particle emissions from the surface of the Great Lakes. *Atmospheric Chemistry and Physics* **2011**, *11*, 12601–12615.
168. May, N. W.; Olson, N. E.; Panas, M.; Axson, J. L.; Tirella, P. S.; Kirpes, R. M.; Craig, R. L.; Gunsch, M. J.; China, S.; Laskin, A.; Ault, A. P.; Pratt, K. A., Aerosol emissions from Great Lakes harmful algal blooms. *Environ. Sci. Technol.* **2017**, *52*, 397–405.
169. Hjelmfelt, M. R., Numerical study of the influence of environmental conditions on lake-effect snowstorms over Lake Michigan. *Mon. Weather Rev.* **1989**, *118*, 138-150.
170. Wang, J.; Bai, X.; Hu, H.; Clites, A.; Colton, M.; Lofgren, B., Temporal and spatial variability of Great Lakes ice cover, 1973–2010*. *J. Clim.* **2012**, *25*, (4), 1318-1329.
171. Desai, A. R., Austin, J. A., Bennington, V., McKinley, G. A., Stronger winds over a large lake in response to weakening air-to-lake temperature gradient. *Nat. Geosci. Lett.* **2009**, *2*, 855-858.
172. Novakov, T., Penner, J. E., Large contribution of organic aerosols to cloud-condensation-nuclei concentrations. *Nat. Lett.* **1993**, *365*, 823-826.
173. Pierce, J. R., Adams, P. J., Efficiency of cloud condensation nuclei formation from ultrafine particles. *Atmos. Chem. Phys* **2007**, *7*, 1367-1379.
174. Farmer, D. K.; Cappa, C. D.; Kreidenweis, S. M., Atmospheric processes and their controlling influence on cloud condensation nuclei activity. *Chem. Rev.* **2015**, *115*, (10), 4199-4217.
175. Szyrmer, W., Zawadzki, I., Biogenic and anthropogenic sources of ice-forming nuclei: A review. *Bull. Amer. Meteor. Soc.* **1997**, *78*, (2), 209-228.
176. McFiggans, G., Artaxo, P., Baltensperger, U., Coe, H., Facchini, M. C., Feingold, G., Fuzzi, S., Gysel, M., Laaksonen, A., Lohmann, U., Mentel, T. F., Murphy, D. M., O'Dowd, C. D., Snider, J. R., Weingartner, E., The effect of physical and chemical aerosol properties on warm cloud droplet activation. *Atmos. Chem. Phys* **2006**, *6*, 2593-2649.
177. Levin, Z., Ganor, E., Gladstein, V., The effects of desert particles coated with sulfate on rain formation in the Eastern Mediterranean. *J. Appl. Meteorol.* **1996**, *35*, 1511-1523.
178. Pierce, J. R.; Evans, M. J.; Scott, C. E.; Andrea, S. D.; Farmer, D. K.; Swietlicki, E.; Spracklen, D. V., Weak global sensitivity of cloud condensation nuclei and the aerosol indirect effect to Criegee + SO₂ chemistry. *Atmos. Chem. Phys* **2013**, *13*, (6), 3163-3176.
179. Bates, T. S.; Huebert, B. J.; Gras, J. L.; Griffiths, F. B.; Durkee, P. A., International global atmospheric chemistry (IGAC) project's first aerosol characterization experiment (ACE 1): overview. *J. Geophys. Res.: Atmos.* **1998**, *103*, 16297-16318.
180. Bigg, E. K., Ice nucleus concentrations in remote areas. *J. Atmos. Sci.* **1973**, *30*, 1153-1157.
181. Bigg, E. K., Ice forming nuclei in the high Arctic. *Tellus* **2017**, *48B*, (2), 223-233.
182. Rogers, J. S., Stall, R. E., Burke, M. J., Low-temperature conditioning of the ice nucleation active bacterium, *Erwinia herbicola*. *Cryobiology* **1987**, *24*, 270-279.
183. Fletcher, N. H., Nucleation by crystalline particles. *J. Chem. Phys.* **1963**, *38*, 237-240.

184. Quinn, P. K., Bates, T. S., Coffman, D. J., Covert, D. S., Influence of particle size and chemistry on the cloud nucleating properties of aerosols *Atmos. Chem. Phys* **2008**, *8*, 1029-1042.
185. Huang, W. T. K.; Ickes, L.; Tegen, I.; Rinaldi, M.; Ceburnis, D.; Lohmann, U., Global relevance of marine organic aerosol as ice nucleating particles. *Atmospheric Chemistry and Physics* **2018**, *18*, (15), 11423-11445.
186. Brooks, S. D., Thornton, D. C. O., Marine aerosols and clouds. *Annu. Rev. Mar. Sci.* **2018**, *10*, 289–313.
187. Gaston, C.; Cahill, J.; Collins, D.; Suski, K.; Ge, J.; Barkley, A.; Prather, K., The cloud nucleating properties and mixing state of marine aerosols sampled along the Southern California coast. *Atmosphere* **2018**, *9*, (2), 52.
188. Vergara-Temprado, J.; Murray, B. J.; Wilson, T. W.; Sullivan, D.; Browse, J.; Pringle, K. J.; Ardon-Dryer, K.; Bertram, A. K.; Burrows, S. M.; Ceburnis, D.; DeMott, P. J.; Mason, R. H.; Dowd, C. D.; Rinaldi, M.; Carslaw, K. S., Contribution of feldspar and marine organic aerosols to global ice nucleating particle concentrations. *Atmospheric Chemistry and Physics* **2017**, *17*, (5), 3637-3658.
189. Wilson, T. W.; Ladino, L. A.; Alpert, P. A.; Breckels, M. N.; Brooks, I. M.; Browse, J.; Burrows, S. M.; Carslaw, K. S.; Huffman, J. A.; Judd, C.; Kilthau, W. P.; Mason, R. H.; McFiggans, G.; Miller, L. A.; Najera, J. J.; Polishchuk, E.; Rae, S.; Schiller, C. L.; Si, M.; Temprado, J. V.; Whale, T. F.; Wong, J. P.; Wurl, O.; Yakobi-Hancock, J. D.; Abbatt, J. P.; Aller, J. Y.; Bertram, A. K.; Knopf, D. A.; Murray, B. J., A marine biogenic source of atmospheric ice-nucleating particles. *Nature* **2015**, *525*, 234-238.
190. Ayers, G. P., Gras, J. L., Seasonal relationship between cloud condensation nuclei and aerosol methanesulfonate in marine air. *Nature* **1991**, *353*, 834-835.
191. Orellana, M. V., Matrai, P. A., Leck, C., Rauschenberg, C. D., Lee, A. M., Coz, E., Marine microgels as a source of cloud condensation nuclei in the high Arctic. *Proc Natl Acad Sci USA* **2011**, *108*, (33), 13612-13617.
192. Coggon, M. M.; Sorooshian, A.; Wang, Z.; Metcalf, A. R.; Frossard, A. A.; Lin, J. J.; Craven, J. S.; Nenes, A.; Jonsson, H. H.; Russell, L. M.; Flagan, R. C.; Seinfeld, J. H., Ship impacts on the marine atmosphere: insights into the contribution of shipping emissions to the properties of marine aerosol and clouds. *Atmos. Chem. Phys* **2012**, *12*, (18), 8439-8458.
193. DeMott, P. J.; Hill, T. C.; McCluskey, C. S.; Prather, K. A.; Collins, D. B.; Sullivan, R. C.; Ruppel, M. J.; Mason, R. H.; Irish, V. E.; Lee, T.; Hwang, C. Y.; Rhee, T. S.; Snider, J. R.; McMeeking, G. R.; Dhaniyala, S.; Lewis, E. R.; Wentzell, J. J.; Abbatt, J.; Lee, C.; Sultana, C. M.; Ault, A. P.; Axson, J. L.; Diaz Martinez, M.; Venero, I.; Santos-Figueroa, G.; Stokes, M. D.; Deane, G. B.; Mayol-Bracero, O. L.; Grassian, V. H.; Bertram, T. H.; Bertram, A. K.; Moffett, B. F.; Franc, G. D., Sea spray aerosol as a unique source of ice nucleating particles. *Proc. Natl. Acad. Sci. U. S. A.* **2016**, *113*, (21), 5797-5803.
194. Collins, D. B.; Ault, A. P.; Moffet, R. C.; Ruppel, M. J.; Cuadra-Rodriguez, L. A.; Guasco, T. L.; Corrigan, C. E.; Pedler, B. E.; Azam, F.; Aluwihare, L. I.; Bertram, T. H.; Roberts, G. C.; Grassian, V. H.; Prather, K. A., Impact of marine biogeochemistry on the chemical mixing state and cloud forming ability of nascent sea spray aerosol. *J. Geophys. Res. Atmos.* **2013**, *118*, (15), 8553-8565.

195. Pietsch, R. B.; Vinatzer, B. A.; Schmale, D. G., 3rd, Diversity and abundance of ice nucleating strains of *Pseudomonas syringae* in a freshwater lake in Virginia, USA. *Front. Microbiol.* **2017**, *8*, 318-329.
196. Knackstedt, K.; Moffett, B. F.; Hartmann, S.; Wex, H.; Hill, T. C. J.; Glasgo, E.; Reitz, L.; Augustin-Bauditz, S.; Beall, B.; Bullerjahn, G. S.; Frohlich-Nowoisky, J.; Grawe, S.; Lubitz, J.; Stratmann, F.; McKay, R. M., A terrestrial origin for abundant riverine nanoscale ice-nucleating particles. *Environ. Sci. Technol.* **2018**, *52*, 12358-12367.
197. Moffett, B.; Hill, T.; DeMott, P., Abundance of biological ice nucleating particles in the Mississippi and its major tributaries. *Atmosphere* **2018**, *9*, (8), 307.
198. Borduas-Dedekind, N.; Ossola, R.; David, R. O.; Boynton, L. S.; Weichlinger, V.; Kanji, Z. A.; McNeill, K., Photomineralization mechanism changes the ability of dissolved organic matter to activate cloud droplets and to nucleate ice crystals. *Atmos. Chem. Phys.* **2019**, *19*, 12397-12412.
199. Moffett, B. F., Fresh water ice nuclei. *Fund. Appl. Limnol.* **2016**, *188*, (1), 19-23.
200. Twohy, C. H.; Anderson, J. R., Droplet nuclei in non-precipitating clouds: composition and size matter. *Environ. Res. Lett.* **2008**, *3*, (4), 045002.
201. Hill, K. A.; Shepson, P. B.; Galbavy, E. S.; Anastasio, C.; Kourtev, P. S.; Konopka, A.; Stirm, B. H., Processing of atmospheric nitrogen by clouds above a forest environment. *J. Geophys. Res.* **2007**, *112*, D11301.
202. Chapra, S. C.; Dove, A.; Warren, G. J., Long-term trends of Great Lakes major ion chemistry. *J. Great Lakes Res.* **2012**, *38*, 550-560.
203. Gibson, E. R.; Hudson, P. K.; Grassian, V. H., Aerosol chemistry and climate: Laboratory studies of the carbonate component of mineral dust and its reaction products. *Geophys. Res. Lett.* **2006**, *33*, (13), L13811.
204. Sullivan, R. C., Moore, M. J. K., Petters, M. D., Kreidenweis, S. M., Roberts, G. C., Prather, K. A., Timescale for hygroscopic conversion of calcite mineral particles through heterogeneous reaction with nitric acid. *Phys. Chem. Chem. Phys.* **2009**, *11*, 7826-7837
205. Gard, E. E., Kleeman, M. J., Gross, D. S., Hughes, L. S., Allen, J. O., Morrical, B. D., Fergenson, D. P., Dienes, T., Galli, M. E., Johnson, R. J., Cass, G. R., Prather, K. A., Direct observation of heterogeneous chemistry in the atmosphere. *Science* **1998**, *279*, 1184-1187.
206. Bondy, A. L.; Wang, B.; Laskin, A.; Craig, R. L.; Nhliziyo, M. V.; Bertman, S. B.; Pratt, K. A.; Shepson, P. B.; Ault, A. P., Inland sea spray aerosol transport and incomplete chloride depletion: varying degrees of reactive processing observed during SOAS. *Environ. Sci. Technol.* **2017**, *51*, 9533-9542.
207. Ault, A. P.; Guasco, T. L.; Ryder, O. S.; Baltrusaitis, J.; Cuadra-Rodriguez, L. A.; Collins, D. B.; Ruppel, M. J.; Bertram, T. H.; Prather, K. A.; Grassian, V. H., Inside versus outside: Ion redistribution in nitric acid reacted sea spray aerosol particles as determined by single particle analysis. *J. Am. Chem. Soc.* **2013**, *135*, 14528-14531.
208. Kourtev, P. S.; Hill, K. A.; Shepson, P. B.; Konopka, A., Atmospheric cloud water contains a diverse bacterial community. *Atmos. Env.* **2011**, *45*, (30), 5399-5405.
209. Schmale, D. G., 3rd; Ault, A. P.; Saad, W.; Scott, D. T.; Westrick, J. A., Perspectives on harmful algal blooms (HABs) and the cyberbiosecurity of freshwater systems. *Front. Bioeng. Biotechnol.* **2019**, *7*, 128.
210. Prather, K. A.; Hatch, C. D.; Grassian, V. H., Analysis of atmospheric aerosols. *Annu. Rev. Anal. Chem.* **2008**, *1*, 485-514.

211. Boone, E. J.; Laskin, A.; Laskin, J.; Wirth, C.; Shepson, P. B.; Stirm, B. H.; Pratt, K. A., Aqueous processing of atmospheric organic particles in cloud water collected via aircraft sampling. *Environ. Sci. Technol.* **2015**, *49*, (14), 8523-8530.
212. Garman, K. E., Hill, K. A., Wyss, P., Carlsen, M., Zimmerman, J. R., Stirm, B. H., Carney, T. Q., Santini, R., Shepson, P. B., An airborne and wind tunnel evaluation of a wind turbulence measurement system for aircraft-based flux measurements. *J. Atmos. Ocean. Tech.* **2006**, *23*, 1696-1708.
213. Dai, C.; Wang, Q.; Kalogiros, J. A.; Lenschow, D. H.; Gao, Z.; Zhou, M., Determining boundary-layer height from aircraft measurements. *Boundary Layer Meteorol.* **2014**, *152*, (3), 277-302.
214. Salmon, O. E.; Welp, L. R.; Baldwin, M.; Hajny, K.; Stirm, B. H.; Shepson, P. B., Vertical profile observations of water vapor deuterium excess in the lower troposphere. *Atmos. Chem. Phys.* **2019**, *19*, 11525–11543.
215. Crosson, E. R., A cavity ring-down analyzer for measuring atmospheric levels of methane, carbon dioxide, and water vapor. *Appl. Phys. B* **2008**, *92*, (3), 403-408.
216. Karion, A.; Sweeney, C.; Wolter, S.; Newberger, T.; Chen, H.; Andrews, A.; Kofler, J.; Neff, D.; Tans, P., Long-term greenhouse gas measurements from aircraft. *Atmos. Meas. Tech.* **2013**, *6*, (3), 511-526.
217. Chen, H., Winderlich, J., Gerbig, C., Hofer, A., Rella, C. W., Crosson, E. R., Van Pelt, A. D., Steinbach, J., Kolle, O., Beck, V., Daube, B. C., Gottlieb, E. W., Chow, V. Y., Santoni, G. W., Wofsy, S. C., High-accuracy continuous airborne measurements of greenhouse gases (CO₂ and CH₄) using the cavity ring-down spectroscopy (CRDS) technique. *Atmos. Meas. Tech.* **2010**, *3*, 375–386.
218. Peterson, P. K.; Pöhler, D.; Sihler, H.; Zielcke, J.; General, S.; Frieß, U.; Platt, U.; Simpson, W. R.; Nghiem, S. V.; Shepson, P. B.; Stirm, B. H.; Dhaniyala, S.; Wagner, T.; Caulton, D. R.; Fuentes, J. D.; Pratt, K. A., Observations of bromine monoxide transport in the Arctic sustained on aerosol particles. *Atmospheric Chemistry and Physics* **2017**, *17*, (12), 7567-7579.
219. Laskina, O.; Morris, H. S.; Grandquist, J. R.; Estillore, A. D.; Stone, E. A.; Grassian, V. H.; Tivanski, A. V., Substrate-deposited sea spray aerosol particles: influence of analytical method, substrate, and storage conditions on particle size, phase, and morphology. *Environ. Sci. Technol.* **2015**, *49*, (22), 13447–13453.
220. Huebert, B. J., Vanbramer, S., Tschudy, K. L., Liquid cloudwater collection using modified Mohnen slotted rods. *J. Atmos. Chem.* **1988**, *6*, 251-263.
221. Donner, L. J., Boundary layer control on convective available potential energy: Implications for cumulus parameterization. *J. Geophys. Res.* **2003**, *108*, 4701.
222. Blanchard, D. O., Assessing the vertical distribution of convective available potential energy. *Weather Forecast.* **1998**, *13*, 870-877.
223. Ott, D. K.; Cyrs, W.; Peters, T. M., Passive measurement of coarse particulate matter. *J. Aerosol Sci.* **2008**, *39*, (2), 156-167.
224. Ault, A. P.; Williams, C. R.; White, A. B.; Neiman, P. J.; Creamean, J. M.; Gaston, C. J.; Ralph, F. M.; Prather, K. A., Detection of Asian dust in California orographic precipitation. *J. Geophys. Res.* **2011**, *116*, D16205.
225. Ault, A. P.; Peters, T. M.; Sawvel, E. J.; Casuccio, G. S.; Willis, R. D.; Norris, G. A.; Grassian, V. H., Single-particle SEM-EDX analysis of iron-containing coarse particulate matter in

an urban environment: sources and distribution of iron within Cleveland, Ohio. *Environ. Sci. Technol.* **2012**, *46*, (8), 4331–4339.

226. Gross, D. S.; Atlas, R.; Rzeszutarski, J.; Turetsky, E.; Christensen, J.; Benzaid, S.; Olson, J.; Smith, T.; Steinberg, L.; Sulman, J., Environmental chemistry through intelligent atmospheric data analysis. *Environ. Modell. Softw.* **2010**, *25*, (6), 760-769.

227. Rebotier, T. P.; Prather, K. A., Aerosol time-of-flight mass spectrometry data analysis: a benchmark of clustering algorithms. *Anal Chim Acta* **2007**, *585*, 38-54.

228. Kirpes, R. M.; Bondy, A. L.; Bonanno, D.; Moffet, R. C.; Wang, B.; Laskin, A.; Ault, A. P.; Pratt, K. A., Secondary sulfate is internally mixed with sea spray aerosol and organic aerosol in the winter Arctic. *Atmos. Chem. Phys* **2018**, *18*, (6), 3937-3949.

229. Hopkins, R. J.; Lewis, K.; Desyaterik, Y.; Wang, Z.; Tivanski, A. V.; Arnott, W. P.; Laskin, A.; Gilles, M. K., Correlations between optical, chemical and physical properties of biomass burn aerosols. *Geophys. Res. Lett.* **2007**, *34*, (18), L18806.

230. Gunsch, M. J.; Schmidt, S. A.; Gardner, D. J.; Bondy, A. L.; May, N. W.; Bertman, S. B.; Pratt, K. A.; Ault, A. P., Particle growth in an isoprene-rich forest: Influences of urban, wildfire, and biogenic air masses. *Atmos. Env.* **2018**, *178*, 255-264.

231. VanReken, T. M.; Mwaniki, G. R.; Wallace, H. W.; Pressley, S. N.; Erickson, M. H.; Jobson, B. T.; Lamb, B. K., Influence of air mass origin on aerosol properties at a remote Michigan forest site. *Atmos. Environ.* **2015**, *107*, 35-43.

232. Cahill, R. A., Geochemistry of recent Lake Michigan sediments. *Illinois State Geological Survey: Champaign, IL* **1981**.

233. Pilson, M. E. Q., An Introduction to the Chemistry of the Sea, 2nd ed. *Cambridge University Press: Cambridge, U.K.* **2013**.

234. Ault, A. P.; Moffet, R. C.; Baltrusaitis, J.; Collins, D. B.; Ruppel, M. J.; Cuadra-Rodriguez, L. A.; Zhao, D.; Guasco, T. L.; Ebben, C. J.; Geiger, F. M.; Bertram, T. H.; Prather, K. A.; Grassian, V. H., Size-dependent changes in sea spray aerosol composition and properties with different seawater conditions. *Environ. Sci. Tech.* **2013**, *47*, (11), 5603-5612.

235. Creamean, J. M.; Lee, C.; Hill, T. C.; Ault, A. P.; DeMott, P. J.; White, A. B.; Ralph, F. M.; Prather, K. A., Chemical properties of insoluble precipitation residue particles. *J. Aerosol Sci.* **2014**, *76*, 13-27.

236. Wurzler, S.; Reisin, T. G.; Levin, Z., Modification of mineral dust particles by cloud processing and subsequent effects on drop size distributions. *J. Geophys. Res. Atmos.* **2000**, *105*, (D4), 4501-4512.

237. Gunsch, M. J.; May, N. W.; Wen, M.; Bottenus, C. L. H.; Gardner, D. J.; VanReken, T. M.; Bertman, S. B.; Hopke, P. K.; Ault, A. P.; Pratt, K. A., Ubiquitous influence of wildfire emissions and secondary organic aerosol on summertime atmospheric aerosol in the forested Great Lakes region. *Atmospheric Chemistry and Physics* **2018**, *18*, (5), 3701-3715.

238. Axson, J. L.; Creamean, J. M.; Bondy, A. L.; Capracotta, S. S.; Warner, K. Y.; Ault, A. P., An in situ method for sizing insoluble residues in precipitation and other aqueous samples. *Aerosol. Sci. Technol.* **2014**, *49*, 24-34.

239. Creamean, J. M., Axson, J. L., Bondy, A. L., Craig, R. L., May, N. W., Shen, H., Weber, M. H., Pratt, K. A., Ault, A. P., Changes in precipitating snow chemistry with location and elevation in the California Sierra Nevada. *J. Geophys. Res. Atmos.* **2016**, *121*, 7296-7309.

240. Creamean, J. M.; Ault, A. P.; White, A. B.; Neiman, P. J.; Ralph, F. M.; Minnis, P.; Prather, K. A., Impact of interannual variations in sources of insoluble aerosol species on orographic precipitation over California's central Sierra Nevada. *Atmos. Chem. Phys.* **2015**, *15*, (11), 6535-6548.
241. Hindman II, E. E., Hobbs, P. V., Radke, L. F., Cloud condensation nucleus size distributions and their effects on cloud droplet size distributions. *J. Atmos. Sci.* **1977**, *34*, 951-956.
242. Hatch, C. D.; Gierlus, K. M.; Schuttlefield, J. D.; Grassian, V. H., Water adsorption and cloud condensation nuclei activity of calcite and calcite coated with model humic and fulvic acids. *Atmos. Environ.* **2008**, *42*, (22), 5672-5684.
243. Gierlus, K. M.; Laskina, O.; Abernathy, T. L.; Grassian, V. H., Laboratory study of the effect of oxalic acid on the cloud condensation nuclei activity of mineral dust aerosol. *Atmos. Environ.* **2012**, *46*, 125-130.
244. Roberts, P., Hallett, J., A laboratory study of the ice nucleating properties of some mineral particulates. *Q. J. Royal Meteorol. Soc.* **1968**, *94*, (399), 25-34.
245. Mason, B. J., Maybank, J., The fragmentation and electrification of freezing water drops. *Q. J. Royal Meteorol. Soc.* **1960**, *86*, (368), 176-185.
246. Sheesley, R. J., Schauer, J. J., Bean, E., Kenski, D., Trends in secondary organic aerosol at a remote site in Michigan's Upper Peninsula. *Environ. Sci. Technol.* **2004**, *38*, 6491-6500.
247. Creamean, J. M.; Ault, A. P.; White, A. B.; Neiman, P. J.; Ralph, F. M.; Minnis, P.; Prather, K. A., Impact of interannual variations in sources of insoluble aerosol species on orographic precipitation over California's central Sierra Nevada. *Atmos. Chem. Phys.* **2015**, *15*, (11), 6535-6548.
248. Carpenter, S. R., Caraco, N. F., Correll, D. L., Howarth, R. W., Sharpley, A. N., Smith, V. H., Nonpoint pollution of surface waters with phosphorus and nitrogen. *Ecol. Appl.* **1998**, *8*, (3), 559-568.
249. Backer, L. C.; Manassaram-Baptiste, D.; LePrell, R.; Bolton, B., Cyanobacteria and algae blooms: Review of health and environmental data from the Harmful Algal Bloom-Related Illness Surveillance System (HABISS) 2007-2011. *Toxins* **2015**, *7*, (4), 1048-1064.
250. Smith, V. H., Eutrophication of freshwater and coastal marine ecosystems. *Environ. Sci. & Pollut. Res.* **2003**, *10*, (2), 126-139.
251. Anderson, D. M., Gilbert, P. M., Burkholder, J. M., Harmful algal blooms and eutrophication: nutrient sources, composition, and consequences. *Estuaries* **2002**, *25*, (4), 704-726.
252. Paerl, H. W., Huisman, J., Blooms like it hot. *Science* **2008**, *320*, (5872), 57-58.
253. Paul, V. J., Global warming and cyanobacterial harmful algal blooms. In *Cyanobacterial Harmful Algal Blooms: State of the Science and Research Needs*, Hudnell, H. K., Ed. Springer New York: New York, NY, 2008; pp 239-257.
254. Walls, J. T.; Wyatt, K. H.; Doll, J. C.; Rubenstein, E. M.; Rober, A. R., Hot and toxic: Temperature regulates microcystin release from cyanobacteria. *Sci. Total Environ.* **2018**, *610-611*, 786-795.
255. O'Neil, J. M.; Davis, T. W.; Burford, M. A.; Gobler, C. J., The rise of harmful cyanobacteria blooms: The potential roles of eutrophication and climate change. *Harmful Algae* **2012**, *14*, 313-334.

256. Lurling, M.; Eshetu, F.; Faassen, E. J.; Kosten, S.; Huszar, V. L. M., Comparison of cyanobacterial and green algal growth rates at different temperatures. *Freshw. Biol.* **2013**, *58*, (3), 552-559.
257. Liu, X.; Lu, X.; Chen, Y., The effects of temperature and nutrient ratios on *Microcystis* blooms in Lake Taihu, China: An 11-year investigation. *Harmful Algae* **2011**, *10*, (3), 337-343.
258. Kosten, S.; Huszar, V. L. M.; Bécares, E.; Costa, L. S.; Donk, E.; Hansson, L. A.; Jeppesen, E.; Kruk, C.; Lacerot, G.; Mazzeo, N.; Meester, L.; Moss, B.; Lürling, M.; Nöges, T.; Romo, S.; Scheffer, M., Warmer climates boost cyanobacterial dominance in shallow lakes. *Global Change Biol.* **2012**, *18*, (1), 118-126.
259. Duan, H.; Ma, R.; Xu, X.; Kong, F.; Zhang, S.; Kong, W.; Hao, J.; Shang, L., Two-decade reconstruction of algal blooms in China's Lake Taihu. *Environ Sci Technol* **2009**, *43*, (10), 3522-3528.
260. Del Giudice, D.; Zhou, Y.; Sinha, E.; Michalak, A. M., Long-term phosphorus loading and springtime temperatures explain interannual variability of hypoxia in a large temperate lake. *Environ Sci Technol* **2018**, *52*, (4), 2046-2054.
261. Johnk, K. D.; Huisman, J. E. F.; Sharples, J.; Sommeijer, B. E. N.; Visser, P. M.; Stroom, J. M., Summer heatwaves promote blooms of harmful cyanobacteria. *Global Change Biol.* **2008**, *14*, (3), 495-512.
262. Carmichael, W. W.; Boyer, G. L., Health impacts from cyanobacteria harmful algae blooms: Implications for the North American Great Lakes. *Harmful Algae* **2016**, *54*, 194-212.
263. Steffen, M. M.; Davis, T. W.; McKay, R. M. L.; Bullerjahn, G. S.; Krausfeldt, L. E.; Stough, J. M. A.; Neitzey, M. L.; Gilbert, N. E.; Boyer, G. L.; Johengen, T. H.; Gossiaux, D. C.; Burtner, A. M.; Palladino, D.; Rowe, M. D.; Dick, G. J.; Meyer, K. A.; Levy, S.; Boone, B. E.; Stumpf, R. P.; Wynne, T. T.; Zimba, P. V.; Gutierrez, D.; Wilhelm, S. W., Ecophysiological examination of the Lake Erie microcystis bloom in 2014: Linkages between biology and the water supply shutdown of Toledo, OH. *Environ Sci Technol* **2017**, *51*, (12), 6745-6755.
264. Deneff, V. J., Cyanobacterial harmful algal blooms are a biological disturbance to western Lake Erie bacterial communities. *Environ. Microbiol.* **2016**, *19*, (3), 1149-1162.
265. Allen, J. I.; Smyth, T. J.; Siddorn, J. R.; Holt, M., How well can we forecast high biomass algal bloom events in a eutrophic coastal sea? *Harmful Algae* **2008**, *8*, (1), 70-76.
266. Downing, J. A.; Watson, S. B.; McCauley, E., Predicting cyanobacteria dominance in lakes. *Can. J. Fish. Aquat. Sci.* **2001**, *58*, (10), 1905-1908.
267. Wicks, R. J., Thiel, Pleter G. , Environmental factors affecting the production of peptide toxins in floating scums of the cyanobacterium *Microcystis aeruginosa* in a hypertrophic African reservoir. *Environ. Sci. Technol.* **1990**, *24*, 1413-1418.
268. Pitcher, G. C., Weeks, S. J., The variability and potential for prediction of harmful algal blooms in the Southern Benguela ecosystem. *Large Mar. Eco.* **2006**, *14*, 125-145.
269. Graham, J. L., Loftin, K. A., Meyer, M. T., Ziegler, A. C., Cyanotoxin mixtures and taste-and-odor compounds in cyanobacterial blooms from the Midwestern United States. *Environ. Sci. Technol.* **2010**, *44*, 7361-7368.
270. Chorus, I., Bartram, J., *Toxic cyanobacteria in water: A guide to their public health consequences, monitoring and management*. E & FN Spon: CRC Press, 1999.
271. Rineheart, K. L., Namikoshi, M., Choi, B. W., Structure and biosynthesis of toxins from blue-green algae (cyanobacteria). *J. Appl. Phycol.* **1994**, *6*, 159-176.

272. He, H.; Wu, S.; Wahome, P. G.; Bertin, M. J.; Pedone, A. C.; Beauchesne, K. R.; Moeller, P. D. R.; Carter, G. T., Microcystins containing doubly homologated tyrosine residues from a *Microcystis aeruginosa* bloom: Structures and cytotoxicity. *J Nat Prod* **2018**, *81*, (6), 1368-1375.
273. Yilmaz, M.; Foss, A. J.; Miles, C. O.; Ozen, M.; Demir, N.; Balci, M.; Beach, D. G., Comprehensive multi-technique approach reveals the high diversity of microcystins in field collections and an associated isolate of *Microcystis aeruginosa* from a Turkish lake. *Toxicon*. **2019**, *167*, 87-100.
274. Puddick, J.; Prinsep, M. R.; Wood, S. A.; Kaufononga, S. A.; Cary, S. C.; Hamilton, D. P., High levels of structural diversity observed in microcystins from *Microcystis CAWBG11* and characterization of six new microcystin congeners. *Mar Drugs* **2014**, *12*, (11), 5372-5395.
275. Carmichael, W., A world overview — One-hundred-twenty-seven years of research on toxic cyanobacteria — Where do we go from here? In *Cyanobacterial Harmful Algal Blooms: State of the Science and Research Needs*, Hudnell, H. K., Ed. Springer New York: New York, NY, 2008; pp 105-125.
276. Du, X.; Liu, H.; Yuan, L.; Wang, Y.; Ma, Y.; Wang, R.; Chen, X.; Losiewicz, M. D.; Guo, H.; Zhang, H., The diversity of cyanobacterial toxins on structural characterization, distribution and identification: a systematic review. *Toxins* **2019**, *11*, (9), 530.
277. Ward, C. J., Codd, G. A., Comparative toxicity of four microcystins of different hydrophobicities to the protozoan, *Tetrahymena pyriformis*. *J. Appl. Microbiol.* **1999**, *86*, 874-882.
278. Fischer, A.; Hoeger, S. J.; Stemmer, K.; Feurstein, D. J.; Knobeloch, D.; Nussler, A.; Dietrich, D. R., The role of organic anion transporting polypeptides (OATPs/SLCOs) in the toxicity of different microcystin congeners in vitro: a comparison of primary human hepatocytes and OATP-transfected HEK293 cells. *Toxicol Appl Pharmacol* **2010**, *245*, (1), 9-20.
279. Codd, G.; Bell, S.; Kaya, K.; Ward, C.; Beattie, K.; Metcalf, J., Cyanobacterial toxins, exposure routes and human health. *Eur. J. Phycol.* **1999**, *34*, (4), 405-415.
280. Fitzgeorge, R. B., Clark, S. A., Keevil, C. W., *Routes of intoxication*. Detection Methods for Cyanobacterial Toxins, 1994; p 69-74.
281. Benson, J. M.; Hutt, J. A.; Rein, K.; Boggs, S. E.; Barr, E. B.; Fleming, L. E., The toxicity of microcystin LR in mice following 7 days of inhalation exposure. *Toxicon*. **2005**, *45*, (6), 691-698.
282. Holden, J. P., Harmful algal blooms and hypoxia comprehensive research plan and action strategy: An interagency report In National Science and Technology Council Subcommittee on Ocean Science and Technology: 2016.
283. Quinn, P. K.; Collins, D. B.; Grassian, V. H.; Prather, K. A.; Bates, T. S., Chemistry and related properties of freshly emitted sea spray aerosol. *Chem. Rev.* **2015**, *115*, (10), 4383-4399.
284. Prather, K. A.; Bertram, T. H.; Grassian, V. H.; Deane, G. B.; Dale Stokes, M.; DeMott, P. J.; Aluwihare, L. I.; Palenik, B. P.; Azam, F.; Seinfeld, J. H.; Moffet, R. C.; Molina, M. J.; Cappa, C. D.; Geiger, F. M.; Roberts, G. C.; Russell, L. M.; Ault, A. P.; Baltusaitis, J.; Collins, D. B.; Corrigan, C. E.; Cuadra-Rodriguez, L. A.; Ebben, C. J.; Forestieri, S. D.; Guasco, T. L.; Hersey, S. P.; Kim, M. J.; Lambert, W. F.; Modini, R. L.; Mui, W.; Pedler, B. E.; Ruppel, M. J.; Ryder, O. S.; Schoepp, N. G.; Sullivan, R. C.; Zhao, D.; Thiemens, M. H., Bringing the ocean into the laboratory to probe the chemical complexity of sea spray aerosol. *Proc. Natl. Acad. Sci. U. S. A.* **2013**, *110*, 7550-7555.

285. Olson, N. E.; May, N. W.; Kirpes, R. M.; Watson, A. E.; Hajny, K. D.; Slade, J. H.; Shepson, P. B.; Stirm, B. H.; Pratt, K. A.; Ault, A. P., Lake spray aerosol incorporated into Great Lakes Clouds. *ACS Earth Space Chem.* **2019**, *3*, (12), 2765-2774.
286. Ebben, C. J.; Ault, A. P.; Ruppel, M. J.; Ryder, O. S.; Bertram, T. H.; Grassian, V. H.; Prather, K. A.; Geiger, F. M., Size-resolved sea spray aerosol particles studied by vibrational sum frequency generation. *J. Phys. Chem. A* **2013**, *117*, (30), 6589-6601.
287. Backer, L. C., Carmichael, W., Kirkpatrick, B., Williams, C., Irvin, M., Zhou, Y., Johnson, T. B., Nierenberg, K., Hill, V. R., Kieszak, S. M., Cheng, Y. S. *Recreational exposure to microcystins during a Microcystis aeruginosa bloom in Bear Lake, Michigan*; 2006.
288. Backer, L. C.; Carmichael, W.; Kirkpatrick, B.; Williams, C.; Irvin, M.; Zhou, Y.; Johnson, T. B.; Nierenberg, K.; Hill, V. R.; Kieszak, S. M.; Cheng, Y. S., Recreational exposure to low concentrations of microcystins during an algal bloom in a small lake. *Mar. Drugs* **2008**, *6*, (2), 389-406.
289. Backer, L. C.; McNeel, S. V.; Barber, T.; Kirkpatrick, B.; Williams, C.; Irvin, M.; Zhou, Y.; Johnson, T. B.; Nierenberg, K.; Aubel, M.; LePrell, R.; Chapman, A.; Foss, A.; Corum, S.; Hill, V. R.; Kieszak, S. M.; Cheng, Y. S., Recreational exposure to microcystins during algal blooms in two California lakes. *Toxicon.* **2010**, *55*, (5), 909-921.
290. Wood, S. A.; Dietrich, D. R., Quantitative assessment of aerosolized cyanobacterial toxins at two New Zealand lakes. *J. Environ. Monit.* **2011**, *13*, (6), 1617-1624.
291. Cheng, Y. S., Zhou, Y., Irvin, C. M., Barbara Kirkpatrick, B., Backer, L. C., Characterization of aerosols containing microcystin. *Mar. Drugs* **2007**, *5*, 136-150.
292. Rivasseau, C., Racaud, P., Deguin, A., Hennion, M. C., Evaluation of an ELISA kit for the monitoring of microcystins (cyanobacterial toxins) in water and algae environmental samples. *Environ. Sci. Technol.* **1999**, *33*, 1520-1527.
293. Metcalf, J. S., Beattie, K. A., Pflugmacher, S., Codd, G. A., Immuno-crossreactivity and toxicity assesment of conjugation products of the cyanobacterial toxin, microcystin-LR. *FEMS Microbiol. Lett.* **2000**, *189*, 155-158.
294. Bauer, S. E.; Ault, A.; Prather, K. A., Evaluation of aerosol mixing state classes in the GISS modelE-MATRIX climate model using single-particle mass spectrometry measurements. *J Geophys Res Atmos* **2013**, *118*, (17), 9834-9844.
295. Fitzgerald, E.; Ault, A. P.; Zauscher, M. D.; Mayol-Bracero, O. L.; Prather, K. A., Comparison of the mixing state of long-range transported Asian and African mineral dust. *Atmos. Env.* **2015**, *115*, 19-25.
296. Cheng, Y. S.; McDonald, J. D.; Kracko, D.; Irvin, C. M.; Zhou, Y.; Pierce, R. H.; Henry, M. S.; Bourdelais, A.; Naar, J.; Baden, D. G., Concentration and particle size of airborne toxic algae (brevetoxin) derived from ocean red tide events. *Environ. Sci. Technol.* **2005**, *39*, (10), 3443-3449.
297. Pierce, R. H., Red tide (*Ptychodiscus brevis*) toxin aerosols: a review. *Toxicon.* **1986**, *24*, 955-965.
298. Cheng, Y. S.; Villareal, T. A.; Zhou, Y.; Gao, J.; Pierce, R.; Naar, J.; Baden, D. G., Characterization of red tide aerosol on the Texas coast. *Harmful Algae* **2005**, *4*, 87-94.
299. Pierce, R. H.; Henry, M. S.; Blum, P. C.; Lyons, J.; Cheng, Y. S.; Yazzie, D.; Zhou, Y., Brevetoxin concentrations in marine aerosol: human exposure levels during a *Karenia brevis* harmful algal bloom. *Bull. Environ. Contam. Toxicol.* **2003**, *70*, (1), 161-165.

300. Kirkpatrick, B.; Fleming, L. E.; Bean, J. A.; Nierenberg, K.; Backer, L. C.; Cheng, Y. S.; Pierce, R.; Reich, A.; Naar, J.; Wanner, A.; Abraham, W. M.; Zhou, Y.; Hollenbeck, J.; Baden, D. G., Aerosolized red tide toxins (brevetoxins) and asthma: Continued health effects after 1 hour beach exposure. *Harmful Algae* **2011**, *10*, (2), 138-143.
301. Fleming, L. E.; Kirkpatrick, B.; Backer, L. C.; Bean, J. A.; Wanner, A.; Dalpra, D.; Tamer, R.; Zaias, J.; Cheng, Y. S.; Pierce, R.; Naar, J.; Abraham, W.; Clark, R.; Zhou, Y.; Henry, M. S.; Johnson, D.; Van De Bogart, G.; Bossart, G. D.; Harrington, M.; Baden, D. G., Initial evaluation of the effects of aerosolized Florida red tide toxins (brevetoxins) in persons with asthma. *Environ. Health Perspect.* **2005**, *113*, (5), 650-657.
302. Pilotto, L. S., Douglas, R. M., Burch M. D., Cameron S., Beers M., Rouch G. J., Robinson P., Kirk M., Cowie C. T., Hardiman S., Moore C., Attewell R. G., Health effects of exposure to cyanobacteria (blue-green algae) during recreational water-related activities. *Aust. NZ J. Public Health* **1997**, *21*, (6), 562-566.
303. Backer, L. C.; Fleming, L. E.; Rowan, A.; Cheng, Y. S.; Benson, J.; Pierce, R. H.; Zaias, J.; Bean, J. A.; Bossart, G. D.; Johnson, D.; Quimbo, R.; Baden, D. G., Recreational exposure to aerosolized brevetoxins during Florida red tide events. *Harmful Algae* **2003**, *2*, (1), 19-28.
304. Abraham, W. M.; Bourdelais, A. J.; Ahmed, A.; Serebriakov, I.; Baden, D. G., Effects of inhaled brevetoxins in allergic airways: toxin-allergen interactions and pharmacologic intervention. *Environ. Health Perspect.* **2005**, *113*, (5), 632-637.
305. Abraham, W. M.; Bourdelais, A. J.; Sabater, J. R.; Ahmed, A.; Lee, T. A.; Serebriakov, I.; Baden, D. G., Airway responses to aerosolized brevetoxins in an animal model of asthma. *Am. J. Respir. Crit. Care. Med.* **2005**, *171*, (1), 26-34.
306. Gambaro, A.; Barbaro, E.; Zangrando, R.; Barbante, C., Simultaneous quantification of microcystins and nodularin in aerosol samples using high-performance liquid chromatography/negative electrospray ionization tandem mass spectrometry. *Rapid Commun. Mass Spectrom.* **2012**, *26*, (12), 1497-1506.
307. Guasco, T. L.; Cuadra-Rodriguez, L. A.; Pedler, B. E.; Ault, A. P.; Collins, D. B.; Zhao, D.; Kim, M. J.; Ruppel, M. J.; Wilson, S. C.; Pomeroy, R. S.; Grassian, V. H.; Azam, F.; Bertram, T. H.; Prather, K. A., Transition metal associations with primary biological particles in sea spray aerosol generated in a wave channel. *Environ. Sci. Technol.* **2014**, *48*, (2), 1324-1333.
308. Blanchard, D. C.; Syzdek, L. D., Concentration of bacteria in jet drops from bursting bubbles. *J. Geophys. Res.* **1972**, *77*, (27), 5087-5099.
309. Wang, X.; Deane, G. B.; Moore, K. A.; Ryder, O. S.; Stokes, M. D.; Beall, C. M.; Collins, D. B.; Santander, M. V.; Burrows, S. M.; Sultana, C. M.; Prather, K. A., The role of jet and film drops in controlling the mixing state of submicron sea spray aerosol particles. *Proc. Natl. Acad. Sci. U. S. A.* **2017**, *114*, 6978-6983.
310. Baden, D. G., Brevetoxins: unique polyether dinoflagellate toxins. *FASEB J.* **1989**, *3*, (7), 1807-1817.
311. Baden, D. G., Mende, T. J., Szmant, A. M., Trainer, V. L., Edwards, R. A., Roszell, L. E., Brevetoxin binding: Molecular pharmacology versus immunoassay. *Toxicon.* **1988**, *26*, (1), 97-103.
312. Tsuji, K., Watanuki, T., Kondo, F., Watanabe, M. F., Suzuki, S., Nakazawa, H., Suzuki, M., Uchida, H., Harada, K. I., Stability of microcystins from cyanobacteria II- effect of UV light on decomposition and isomerization. *Toxicon.* **1995**, *33*, (12), 1619-1631.

313. Tsuji, K.; Naito, S.; Kondo, F.; Ishikawa, N.; Watanabe, M. F.; Suzuki, M.; Harada, K., Stability of microcystins from cyanobacteria: effect of light on decomposition and isomerization. *Environ. Sci. Technol.* **1994**, *28*, 173-177.
314. Marion, J. W.; Lee, J.; Wilkins, J. R., 3rd; Lemeshow, S.; Lee, C.; Waletzko, E. J.; Buckley, T. J., In vivo phycocyanin fluorescence as a potential rapid screening tool for predicting elevated microcystin concentrations at eutrophic lakes. *Environ Sci Technol* **2012**, *46*, (8), 4523-4531.
315. Birbeck, J. A.; Westrick, J. A.; O'Neill, G. M.; Spies, B.; Szlag, D. C., Comparative analysis of microcystin prevalence in Michigan lakes by online concentration LC/MS/MS and ELISA. *Toxins* **2019**, *11*, 13.
316. Pratt, K. A.; Mayer, J. E.; Holecek, J. C.; Moffet, R. C.; Sanchez, R. O.; Rebotier, T. P.; Furutani, H.; Gonin, M.; Fuhrer, K.; Su, Y.; Guazzotti, S.; Prather, K. A., Development and characterization of an aircraft aerosol time-of-flight mass spectrometer. *Anal. Chem.* **2009**, *81*, (40), 1792-1800.
317. Sultana, C. M.; Cornwell, G. C.; Rodriguez, P.; Prather, K. A., FATES: a flexible analysis toolkit for the exploration of single-particle mass spectrometer data. *Atmos. Meas. Tech.* **2017**, *10*, (4), 1323-1334.
318. Cahill, J. F.; Darlington, T. K.; Fitzgerald, C.; Schoepp, N. G.; Beld, J.; Burkart, M. D.; Prather, K. A., Online analysis of single cyanobacteria and algae cells under nitrogen-limited conditions using aerosol time-of-flight mass spectrometry. *Anal Chem* **2015**, *87*, (16), 8039-8046.
319. Pratt, K. A., DeMott, P. J., French, J. R., Wang, Z., Westphal, D. L., Heymsfield, A. J., Twohy, C. H., Prenni, A. J., Prather, K. A., In situ detection of biological particles in cloud ice-crystals. *Nat. Geosci.* **2009**, *2*, 398-401.
320. Sultana, C. M.; Al-Mashat, H.; Prather, K. A., Expanding single particle mass spectrometer analyses for the identification of microbe signatures in sea spray aerosol. *Anal. Chem.* **2017**, *89*, (19), 10162-10170.
321. Bergin, I. L.; Wilding, L. A.; Morishita, M.; Walacavage, K.; Ault, A. P.; Axson, J. L.; Stark, D. I.; Hashway, S. A.; Capracotta, S. S.; Leroueil, P. R.; Maynard, A. D.; Philbert, M. A., Effects of particle size and coating on toxicologic parameters, fecal elimination kinetics and tissue distribution of acutely ingested silver nanoparticles in a mouse model. *Nanotoxicology* **2016**, *10*, (3), 352-360.
322. Axson, J. L.; Stark, D. I.; Bondy, A. L.; Capracotta, S. S.; Maynard, A. D.; Philbert, M. A.; Bergin, I. L.; Ault, A. P., Rapid kinetics of size and pH-dependent dissolution and aggregation of silver nanoparticles in simulated gastric fluid. *J. Phys. Chem. A* **2015**, *119*, (35), 20632-20641.
323. Kramberger, P.; Ciringer, M.; Strancar, A.; Peterka, M., Evaluation of nanoparticle tracking analysis for total virus particle determination. *Viol. J.* **2012**, *9*, 265.
324. Malloy, A., Count, size and visualize nanoparticles. *Mater. Today* **2011**, *14*, (4), 170-173.
325. Halvorson, R. A.; Vikesland, P. J., Drop coating deposition Raman (DCDR) for microcystin-LR identification and quantitation. *Environ. Sci. Technol.* **2011**, *45*, (13), 5644-5651.
326. Daisey, J. M., McCaffrey, R. J., Gallagher, R. A., Polycyclic aromatic hydrocarbons and total extractable particulate organic matter in the Arctic Aerosol. *Atmos. Environ.* **1981**, *15*, (8), 1353-1363.
327. Li, W.; Shao, L., Mixing and water-soluble characteristics of particulate organic compounds in individual urban aerosol particles. *J. Geophys. Res.* **2010**, *115*, D02301.

328. Human health recreational ambient water quality criteria or swimming advisories for microcystins and cylindrospermopsin. In United States Environmental Protection Agency: Washington, D. C., 2016; Vol. 822-P-16-002.
329. 2015 Drinking water health advisories for two cyanobacterial toxins. In United States Environmental Protection Agency Office of Water: Washington, D. C., 2015; Vol. 820F15003.
330. Mazur-Marzec, H.; Meriluoto, J.; Plinski, M., The degradation of the cyanobacterial hepatotoxin nodularin (NOD) by UV radiation. *Chemosphere* **2006**, *65*, (8), 1388-1395.
331. Oehrle, S. A.; Southwell, B.; Westrick, J., Detection of various freshwater cyanobacterial toxins using ultra-performance liquid chromatography tandem mass spectrometry. *Toxicon*. **2010**, *55*, (5), 965-972.
332. Dai, M.; Xie, P.; Chen, J.; Liang, G.; Liu, Y.; Qiu, T., Quantitative determination of microcystins in rat plasma by LC-ESI tandem MS. *Chromatographia* **2008**, *68*, 811-815.
333. Allis, O., Dauphard, J., Hamilton, B., Shuilleabhain, A. N., Lehane, M., James, K. J., Furey, A., Liquid chromatography-tandem mass spectrometry application for the determination of extracellular hepatotoxins in Irish Lake and drinking waters. *Anal. Chem.* **2007**, *79*, 3436-3447.
334. Kubwabo, C.; Vais, N.; Benoit, F. M., Characterization of microcystins using in-source collision-induced dissociation. *Rapid Commun. Mass Spectrom.* **2005**, *19*, (5), 597-604.
335. Zhu, C., Gao, Y., Li, H., Meng, S., Li, L., Francisco, J. S., Zeng, X. C., Characterizing hydrophobicity of amino acid side chains in a protein environment via measuring contact angle of a water nanodroplet on planar peptide network. *Proc Natl Acad Sci USA* **2016**, *113*, (46), 12946-12951.
336. Rose, G. D., Wolfenden, R. , Hydrogen bonding, hydrophobicity, packing, and protein folding. *Annu. Rev. Biophys. Biomol. Struct.* **1993**, *22*, 381-415.
337. Kyte, J., Doolittle, R. F., A simple method for displaying the hydropathic character of a protein. *J. Mol. Biol.* **1982**, *157*, 105-132.
338. Biswas, K. M.; DeVido, D. R.; Dorsey, J. G., Evaluation of methods for measuring amino acid hydrophobicities and interactions. *J. Chromatogr. A.* **2003**, *1000*, 637-655.
339. Fuentes, E.; Coe, H.; Green, D.; McFiggans, G., On the impacts of phytoplankton-derived organic matter on the properties of the primary marine aerosol – Part 2: Composition, hygroscopicity and cloud condensation activity. *Atmos. Chem. Phys.* **2011**, *11*, (6), 2585-2602.
340. Cochran, R. E.; Laskina, O.; Jayarathne, T.; Laskin, A.; Laskin, J.; Lin, P.; Sultana, C.; Lee, C.; Moore, K. A.; Cappa, C. D.; Bertram, T. H.; Prather, K. A.; Grassian, V. H.; Stone, E. A., Analysis of organic anionic surfactants in fine and coarse fractions of freshly emitted sea spray aerosol. *Environ Sci Technol* **2016**, *50*, (5), 2477-2486.
341. Blanchard, D. C., The ejection of drops from the sea and their enrichment with bacteria and other materials: A review. *Estuaries* **1989**, *12*, (3), 127-137.
342. Aller, J. Y.; Kuznetsova, M. R.; Jahns, C. J.; Kemp, P. F., The sea surface microlayer as a source of viral and bacterial enrichment in marine aerosols. *J. Aerosol Sci.* **2005**, *36*, 801-812.
343. Jayarathne, T.; Sultana, C. M.; Lee, C.; Malfatti, F.; Cox, J. L.; Pendergraft, M. A.; Moore, K. A.; Azam, F.; Tivanski, A. V.; Cappa, C. D.; Bertram, T. H.; Grassian, V. H.; Prather, K. A.; Stone, E. A., Enrichment of saccharides and divalent cations in sea spray aerosol during two phytoplankton blooms. *Environ. Sci. Technol.* **2016**, *50*, 11511–11520.
344. McCord, J.; Lang, J. R.; Hill, D.; Strynar, M.; Chernoff, N., pH dependent octanol-water partitioning coefficients of microcystin congeners. *J Water Health* **2018**, *16*, (3), 340-345.

345. De Maagd, P. G., Hendriks, A. J., Seinen, W., Sijm, D. T., pH dependent hydrophobicity of the cyanobacteria in toxin microcystin-LR. *Wat. Res.* **1999**, *33*, (3), 667-680.
346. Chen, M.; Li, J.; Dai, X.; Sun, Y.; Chen, F., Effect of phosphorus and temperature on chlorophyll a contents and cell sizes of *Scenedesmus obliquus* and *Microcystis aeruginosa*. *Limnology* **2010**, *12*, (2), 187-192.
347. Bigg, E. K., Comparison of aerosol at four baseline atmospheric monitoring stations. *J. Appl. Meteorol.* **1980**, *19*, 521-533.
348. Andreae, M. O., Charlson, R. J., Bruynseels, F., Storms, H., Grieken, R. V., Maenhaut, W., Internal mixture of sea salt, silicates, and excess sulfate in marine aerosols. *Science* **1986**, *232*, 1620-1623.
349. Gobler, C. J., Sanudo-Wilhelmy, S. A., Effects of organic carbon, organic nitrogen, inorganic nutrients, and iron additions on the growth of phytoplankton and bacteria during a brown tide bloom. *Mar. Ecol. Prog. Ser.* **2001**, *209*, 19-34.
350. Goldman, J. C., Porcella, D. B., Middlebrooks, J. E., Toerien, D. F. *The effect of carbon on algal growth - Its relationship to eutrophication*; Utah Water Research Laboratory, 1971.
351. Ballah, M.; Bhojroo, V.; Neetoo, H., Assessment of the physico-chemical quality and extent of algal proliferation in water from an impounding reservoir prone to eutrophication. *J. Ecol. Environ.* **2019**, *43*, 5.
352. Russell, S. C.; Czerwieniec, G.; Lebrilla, C.; Tobias, H.; Fergenson, D. P.; Steele, P.; Pitesky, M.; Horn, J.; Srivastava, A.; Frank, M.; Gard, E. E., Toward understanding the ionization of biomarkers from micrometer particles by bio-aerosol mass spectrometry. *J. Am. Soc. Mass. Spectrom.* **2004**, *15*, (6), 900-909.
353. Facciponte, D. N.; Bough, M. W.; Seidler, D.; Carroll, J. L.; Ashare, A.; Andrew, A. S.; Tsongalis, G. J.; Vaickus, L. J.; Henegan, P. L.; Butt, T. H.; Stommel, E. W., Identifying aerosolized cyanobacteria in the human respiratory tract: A proposed mechanism for cyanotoxin-associated diseases. *Sci. Total Environ.* **2018**, *645*, 1003-1013.
354. Wisniewska, K.; Lewandowska, A. U.; Sliwinska-Wilczewska, S., The importance of cyanobacteria and microalgae present in aerosols to human health and the environment - Review study. *Environ. Int.* **2019**, *131*, 104964.
355. Olson, N. E.; Cooke, M. E.; Shi, J.; Birbeck, J. A.; Westrick, J. A.; Ault, A. P., Harmful algal bloom toxins in aerosol generated from inland lake water. *Environ Sci Technol* **2020**, *54*, (8), 4769-4780.
356. Hu, J.; Liu, J.; Zhu, Y.; Diaz-Perez, Z.; Sheridan, M.; Royer, H.; Leibensperger, R.; Maizel, D.; Brand, L.; Pependorf, K. J.; Gaston, C. J.; Zhai, R. G., Exposure to aerosolized algal toxins in South Florida increases short- and long-term health risk in *Drosophila* model of aging. *Toxins* **2020**, *12*, (12).
357. Schaefer, A. M.; Yrastorza, L.; Stockley, N.; Harvey, K.; Harris, N.; Grady, R.; Sullivan, J.; McFarland, M.; Reif, J. S., Exposure to microcystin among coastal residents during a cyanobacteria bloom in Florida. *Harmful Algae* **2020**, *92*, 101769.
358. Stewart, I.; Webb, P. M.; Schluter, P. J.; Fleming, L. E.; Burns, J. W., Jr.; Gantar, M.; Backer, L. C.; Shaw, G. R., Epidemiology of recreational exposure to freshwater cyanobacteria--an international prospective cohort study. *BMC public health* **2006**, *6*, 93.

359. Jang, M.; Berthold, D. E.; Yu, Z.; Silva-Sanchez, C.; Laughinghouse IV, H. D.; Denslow, N. D.; Han, S., Atmospheric progression of microcystin-LR from cyanobacterial aerosols. *Environ. Sci. Technol. Lett.* **2020**, *7*, (10), 740-745.
360. Wisniewska, K.; Sliwinska-Wilczewska, S.; Lewandowska, A.; Konik, M., The effect of abiotic factors on abundance and photosynthetic performance of airborne cyanobacteria and microalgae isolated from the Southern Baltic Sea region. *Cells* **2021**, *10*, (1).
361. Hoorman, J.; Hone, T.; Sudman, T.; Dirksen, T.; Iles, J.; Islam, K. R., Agricultural impacts on lake and stream water quality in Grand Lake St. Marys, Western Ohio. *Water Air Soil Pollut* **2008**, *193*, 309-322.
362. Filbrun, J. E.; Conroy, J. D.; Culver, D. A., Understanding seasonal phosphorus dynamics to guide effective management of shallow, hypereutrophic Grand Lake St. Marys, Ohio. *Lake Reservoir Manag* **2013**, *29*, (3), 165-178.
363. Steffen, M. M.; Zhu, Z.; McKay, R. M. L.; Wilhelm, S. W.; Bullerjahn, G. S., Taxonomic assessment of a toxic cyanobacteria shift in hypereutrophic Grand Lake St. Marys (Ohio, USA). *Harmful Algae* **2014**, *33*, 12-18.
364. Halvorson, R. A.; Leng, W.; Vikesland, P. J., Differentiation of microcystin, nodularin, and their component amino acids by drop-coating deposition Raman spectroscopy. *Anal Chem* **2011**, *83*, (24), 9273-9280.
365. Jones, L. H., Infrared spectra and structure of the crystalline sodium acetate complexes of U(VI), Np(VI), Pu(VI), and Am(VI). A comparison of metal-oxygen bond distance and bond force constant in this series. *J. Chem. Phys.* **1955**, *23*, (11), 2105-2107.
366. Jones, L. H.; McLaren, E., Infrared spectra of CH₃COONa and CD₃COONa and assignments of vibrational frequencies. *J. Chem. Phys.* **1954**, *22*, (11), 1796-1800.
367. Kakihana, M., Kotaka, M., Okamoto, M., Infrared spectra of ¹³C-substituted species of solid sodium acetate at 80 K. *J. Phys. Chem.* **1982**, *86*, (22), 4385-4387.
368. Frost, R. L., Jing, Y., Ding, Z., Raman and FTIR spectroscopy of natural oxalates: Implications for life on Mars. *Chinese Sci. Bull.* **2003**, *48*, (17), 1844-1852.
369. Mathlouthi, M., Luu, D. V., Laser-Raman spectra of D-glucose and sucrose in aqueous solution. *Carbohydr Res* **1980**, *81*, (2), 203-212.
370. Brizuela, A. B.; Bichara, L. C.; Romano, E.; Yurquina, A.; Locatelli, S.; Brandan, S. A., A complete characterization of the vibrational spectra of sucrose. *Carbohydr Res* **2012**, *361*, 212-218.
371. Frost, R. L., Klopogge, J. T., Raman spectroscopy of the acetates of sodium, potassium, and magnesium at liquid nitrogen temperature *J. Mol. Struct.* **2000**, *526*, 131-141.
372. Wang, L. Y., Zhang, Y. H., Zhao, L. J., Raman spectroscopic studies on single supersaturated droplets of sodium and magnesium acetate. *J. Phys. Chem. A* **2005**, *109*, 609-614.
373. Picquart, M.; Laborde, M., Raman Scattering in Aqueous Solutions of Sodium Dodecyl Sulfate. In *Surfactants in Solution: Volume 4*, Mittal, K. L.; Bothorel, P., Eds. Springer US: Boston, MA, 1986; pp 189-201.
374. Kirpes, R. M.; Rodriguez, B.; Kim, S.; China, S.; Laskin, A.; Park, K.; Jung, J.; Ault, A. P.; Pratt, K. A., Emerging investigator series: influence of marine emissions and atmospheric processing on individual particle composition of summertime Arctic aerosol over the Bering Strait and Chukchi Sea. *Environ Sci Process Impacts* **2020**, *22*, 1201-1213.

375. Onasch, T. B.; Siefert, R. L.; Brooks, S. D.; Prenni, A. J.; Murray, B.; Wilson, M. A.; Tolbert, M. A., Infrared spectroscopic study of the deliquescence and efflorescence of ammonium sulfate aerosol as a function of temperature. *J Geophys Res Atmos* **1999**, *104*, 21317-21326.
376. Hudson, P. K.; Murphy, D. M.; Cziczo, D. J.; Thomson, D. S.; de Gouw, J. A.; Warneke, C.; Holloway, J.; Jost, H.-J.; Hübler, G., Biomass-burning particle measurements: Characteristic composition and chemical processing. *J. Geophys. Res. Atmos.* **2004**, *109*, (D23), D23S27.
377. Wang, H.; Zhang, L.; Wang, D.; He, X., Experimental investigation on the wettability of respirable coal dust based on infrared spectroscopy and contact angle analysis. *Adv Powder Technol* **2017**, *28*, (12), 3130-3139.
378. Laskina, O.; Young, M. A.; Kleiber, P. D.; Grassian, V. H., Infrared extinction spectroscopy and micro-Raman spectroscopy of select components of mineral dust mixed with organic compounds. *J. Geophys. Res. Atmos.* **2013**, *118*, (12), 6593-6606.
379. Alali, H.; Gong, Z.; Videen, G.; Pan, Y.-L.; Muñoz, O.; Wang, C., Laser spectroscopic characterization of single extraterrestrial dust particles using optical trapping-cavity ringdown and Raman spectroscopy. *J Quant Spectrosc Radiat Transf.* **2020**, *255*.
380. Cain, J. P.; Gassman, P. L.; Wang, H.; Laskin, A., Micro-FTIR study of soot chemical composition—evidence of aliphatic hydrocarbons on nascent soot surfaces. *Phys. Chem. Chem. Phys.* **2010**, *12*, (20), 5206-5218.
381. Patel, M.; Azanza Ricardo, C. L.; Scardi, P.; Aswath, P. B., Morphology, structure and chemistry of extracted diesel soot—Part I: Transmission electron microscopy, Raman spectroscopy, X-ray photoelectron spectroscopy and synchrotron X-ray diffraction study. *Tribol. Int.* **2012**, *52*, 29-39.
382. Shaw, R. W., Paur, R. J., Composition of aerosol particles collected at rural sites in the Ohio River Valley. *Atmos. Environ.* **1983**, *17*, (10), 2031-2044.
383. Huntzicker, J. J.; Heyerdahl, E. K.; McDow, S. R.; Rau, J. A.; Griest, W. H.; MacDougall, C. S., Combustion as the principal source of carbonaceous aerosol in the Ohio River Valley. *J. Air Pollut. Control Assoc.* **1986**, *36*, (6), 705-709.
384. John, K.; Karnae, S.; Crist, K.; Kim, M.; Kulkarni, A., Analysis of trace elements and ions in ambient fine particulate matter at three elementary schools in Ohio. *J Air Waste Manag Assoc* **2007**, *57*, (4), 394-406.
385. Theoret, A., Sandorfy, C., Infrared spectra and crystalline phase transitions of ammonium nitrate. *Can. J. Chem.* **1964**, *42*, 57-62.
386. Rousseau, D. L., Miller, R. E., Leroi, G. E., Raman spectra of crystalline sodium nitrate. *J. Chem. Phys.* **1968**, *48*, (8), 3409.
387. Hand, V. L.; Capes, G.; Vaughan, D. J.; Formenti, P.; Haywood, J. M.; Coe, H., Evidence of internal mixing of African dust and biomass burning particles by individual particle analysis using electron beam techniques. *J Geophys Res* **2010**, *115*, (D13).
388. Bauer, S. E.; Ault, A.; Prather, K. A., Evaluation of aerosol mixing state classes in the GISS modelE-MATRIX climate model using single-particle mass spectrometry measurements. *J. Geophys. Res.: Atmos.* **2013**, *118*, (17), 9834-9844.
389. Dedoussi, I. C.; Eastham, S. D.; Monier, E.; Barrett, S. R. H., Premature mortality related to United States cross-state air pollution. *Nature* **2020**, *578*, (7794), 261-265.
390. Institute for Health Metrics and Evaluation - IHME, Global Burden of Disease Compare Data Visualization. In IHME, U. o. W., Ed. Seattle, WA:, 2016.

391. Eaves, L. A.; Smeester, L.; Hartwell, H. J.; Lin, Y.-H.; Arashiro, M.; Zhang, Z.; Gold, A.; Surratt, J. D.; Fry, R. C., Isoprene-derived Secondary Organic Aerosol Induces the Expression of micro RNAs (miRNAs) Associated with Inflammatory/Oxidative Stress Response in Lung Cells. *Chem. Res. Toxicol.* **2019**.
392. Laskin, A.; Iedema, M. J.; Cowin, J. P., Quantitative time-resolved monitoring of nitrate formation in sea salt particles using a CCSEM/EDX single particle analysis. *Environ. Sci. Technol.* **2002**, *36*, (23), 4948-4955.
393. O'Brien, R. E.; Wang, B.; Kelly, S. T.; Lundt, N.; You, Y.; Bertram, A. K.; Leone, S. R.; Laskin, A.; Gilles, M. K., Liquid-liquid phase separation in aerosol particles: imaging at the nanometer scale. *Environ Sci Technol* **2015**, *49*, (8), 4995-5002.
394. Takahama, S.; Johnson, A.; Russell, L. M., Quantification of carboxylic and carbonyl functional groups in organic aerosol infrared absorbance spectra. *Aerosol Sci. Technol.* **2013**, *47*, (3), 310-325.
395. Farmer, D.; Matsunaga, A.; Docherty, K.; Surratt, J.; Seinfeld, J.; Ziemann, P.; Jimenez, J., Response of an aerosol mass spectrometer to organonitrates and organosulfates and implications for atmospheric chemistry. *Proc. Natl. Acad. Sci. U. S. A.* **2010**, *107*, (15), 6670-6675.
396. Gen, M.; Chan, C. K., Electrospray surface-enhanced Raman spectroscopy (ES-SERS) for probing surface chemical compositions of atmospherically relevant particles. *Atmos. Chem. Phys.* **2017**, *17*, (22), 14025-14037.
397. Fu, Y.; Kuppe, C.; Valev, V. K.; Fu, H.; Zhang, L.; Chen, J., Surface-enhanced Raman spectroscopy: A facile and rapid method for the chemical component study of individual atmospheric aerosol. *Environ. Sci. Technol.* **2017**, *51*, (11), 6260-6267.
398. Wang, L.; Huang, D.; Chan, C. K.; Li, Y. J.; Xu, X. G., Nanoscale spectroscopic and mechanical characterization of individual aerosol particles using peak force infrared microscopy. *Chem. Commun.* **2017**, *53*, (53), 7397-7400.
399. Kurouski, D.; Dazzi, A.; Zenobi, R.; Centrone, A., Infrared and Raman chemical imaging and spectroscopy at the nanoscale. *Chem Soc Rev* **2020**, 10.1039/c8cs00916c.
400. Morsch, S.; Lyon, S. B.; Edmondson, S.; Gibbon, S. R., Reflectance in AFM-IR: Implications for interpretation and remote analysis of the buried interface. *Anal Chem* **2020**, 10.1021/acs.analchem.9b05793.
401. Dazzi, A.; Glotin, F.; Carminati, R., Theory of infrared nanospectroscopy by photothermal induced resonance. *J. Appl. Phys.* **2010**, *107*, 124519.
402. Mathurin, J.; Pancani, E.; Deniset-Besseau, A.; Kjoller, K.; Prater, C. B.; Gref, R.; Dazzi, A., How to unravel the chemical structure and component localization of individual drug-loaded polymeric nanoparticles by using tapping AFM-IR. *Analyst* **2018**, *143*, (24), 5940-5949.
403. Zhang, D.; Li, C.; Zhang, C.; Slipchenko, M. N.; Eakins, G.; Cheng, J.-X., Depth-resolved mid-infrared photothermal imaging of living cells and organisms with submicrometer spatial resolution. *Sci. Adv.* **2016**, *2*, (9), e1600521.
404. Busse, G., Photothermal transmission imaging and microscopy. *Optics Comm.* **1981**, *36*, (6), 441-443.
405. Wang, C. T.; Jiang, B.; Zhou, Y. W.; Jiang, T. W.; Liu, J. H.; Zhu, G. D.; Cai, W. B., Exploiting the surface-enhanced IR absorption effect in the photothermally induced resonance AFM-IR technique toward nanoscale chemical analysis. *Anal Chem* **2019**, *91*, (16), 10541-10548.

406. Wrobel, T. P.; Bhargava, R., Infrared spectroscopic imaging advances as an analytical technology for biomedical sciences. *Anal Chem* **2018**, *90*, (3), 1444-1463.
407. Nowak, D., Morrison, W., Wickramasinghe, H. K., Jahng, J., Potma, E., Wan, L., Ruiz, R., Albrecht, T. R., Schmidt, K., Frommer, J., Sanders, D. P., Park, S., Nanoscale chemical imaging by photoinduced force microscopy. *Sci. Adv.* **2016**, *2*, e1501571.
408. Jahng, J.; Fishman, D. A.; Park, S.; Nowak, D. B.; Morrison, W. A.; Wickramasinghe, H. K.; Potma, E. O., Linear and nonlinear optical spectroscopy at the nanoscale with photoinduced force microscopy. *Acc. Chem. Res.* **2015**, *48*, (10), 2671-2679.
409. Tumkur, T. U.; Yang, X.; Cerjan, B.; Halas, N. J.; Nordlander, P.; Thomann, I., Photoinduced force mapping of plasmonic nanostructures. *Nano. Lett.* **2016**, *16*, (12), 7942-7949.
410. Sobanska, S.; Falgayrac, G.; Rimetz-Planchon, J.; Perdrix, E.; Brémard, C.; Barbillat, J., Resolving the internal structure of individual atmospheric aerosol particle by the combination of Atomic Force Microscopy, ESEM–EDX, Raman and ToF–SIMS imaging. *Microchem. J.* **2014**, *114*, 89-98.
411. Marcott, C.; Kansiz, M.; Dillon, E.; Cook, D.; Mang, M. N.; Noda, I., Two-dimensional correlation analysis of highly spatially resolved simultaneous IR and Raman spectral imaging of bioplastics composite using optical photothermal Infrared and Raman spectroscopy. *J. Mol. Struct.* **2020**, *1210*.
412. Furstenberg, R.; Kendziora, C.; Papantonakis, M.; Nguyen, V.; McGill, R. A., *Chemical imaging using infrared photothermal microspectroscopy*. SPIE: 2012; Vol. 8374.
413. Gao, X.; Chorover, J., Adsorption of sodium dodecyl sulfate (SDS) at ZnSe and alpha-Fe₂O₃ surfaces: combining infrared spectroscopy and batch uptake studies. *J Colloid Interface Sci* **2010**, *348*, (1), 167-176.
414. Nakao, S.; Tang, P.; Tang, X.; Clark, C. H.; Qi, L.; Seo, E.; Asa-Awuku, A.; Cocker, D., Density and elemental ratios of secondary organic aerosol: Application of a density prediction method. *Atmos. Environ.* **2013**, *68*, 273-277.
415. Latimer, W. M., Schutz, P. W., Hicks, J. F. G., The heat capacity and entropy of calcium oxalate from 19 to 300* absolute. The entropy and free energy of oxalate ion. *J. Am. Chem. Soc.* **1993**, *55*, (3), 971-975.
416. Angell, C. A., Sichina, J. W., Oguni, M., Heat capacity of water at extremes of supercooling and superheating. *J. Phys. Chem.* **1982**, *86*, (6), 998-1002.
417. Zhou, S.-Q.; Ni, R., Measurement of the specific heat capacity of water-based Al₂O₃ nanofluid. *Appl. Phys. Lett.* **2008**, *92*, (9), 093123.
418. Clegg, S. L., Ho, S. S., Chan, C. K., Brimblecombe, P., Thermodynamic properties of aqueous (NH₄)₂SO₄ to high supersaturation as a function of temperature. *J. Chem. Eng. Data* **1995**, *40*, 1079-1090.
419. Stephenson, C. C., Bentz, D. R., Stevenson, D. A., The heat capacity of ammonium nitrate from 15 to 315 K. *J. Am. Chem. Soc.* **1955**, *77*, (8), 2161-2164.
420. Magoń, A.; Wurm, A.; Schick, C.; Pangloli, P.; Zivanovic, S.; Skotnicki, M.; Pyda, M., Heat capacity and transition behavior of sucrose by standard, fast scanning and temperature-modulated calorimetry. *Thermochim. Acta.* **2014**, *589*, 183-196.
421. Araki, N., Futamura, M., Makino, A., Shibata, H., Measurements of thermophysical properties of sodium acetate hydrate. *Int. J. Thermophys.* **1995**, *16*, (6), 1455-1466.

422. Bakshi, M. S., Crisantino, R., De Lisi, R., Milioto, S., Volume and heat capacity of sodium dodecyl sulfate-dodecyldimethylamine oxide mixed micelles. *J. Phys. Chem.* **1993**, *97*, 6914-6919.
423. Sengers, J. V.; Watson, J. T. R.; Basu, R. S.; Kamgar-Parsi, B.; Hendricks, R. C., Representative equations for the thermal conductivity of water substance. *J. Phys. Chem. Ref. Data* **1984**, *13*, (3), 893-933.
424. Zhang, M.; Che, Z.; Chen, J.; Zhao, H.; Yang, L.; Zhong, Z.; Lu, J., Experimental determination of thermal conductivity of water-agar gel at different concentrations and temperatures. *J. Chem. Eng. Data* **2011**, *56*, (4), 859-864.
425. Hale, G. M., Querry, M. R., Optical constants of water in the 200-nm to 200-um wavelength region. *Appl. Opt.* **1973**, *12*, (3), 555-563.
426. Earle, M. E., Pancescu, R. G., Cosic, B., Zasetsky, A. Y., Sloan, J. J., Temperature-dependent complex indices of refraction for crystalline (NH₄)₂SO₄. *J. Phys. Chem. A* **2006**, *110*, 13022-13028.
427. Jarzembski, M. A., Norman, M. L., Fuller, K. A., Srivastava, V., Cutten, D. R., Complex refractive index of ammonium nitrate in the 2–20nm spectral range. *Appl. Opt.* **2003**, *42*, (6), 922-930.
428. Deosarkar, S. D.; Mendkudle, M. S., Physicochemical properties and ion-solvent interactions in aqueous sodium, ammonium, and lead acetate solution. *Russ. J. Phys. Chem. A* **2014**, *88*, (9), 1527-1532.
429. Charles, D. F., Refractive indices of sucrose-water solutions in the range from 24 to 53% sucrose. *Anal. Chem.* **1965**, *37*, (3), 405-406.
430. Singh, R.; Chauhan, S.; Sharma, K., Surface tension, viscosity, and refractive index of sodium dodecyl sulfate (SDS) in aqueous solution containing polyethylene glycol (PEG), polyvinyl pyrrolidone (PVP), and their blends. *J. Chem. Eng. Data* **2017**, *62*, (7), 1955-1964.
431. Frej, H., Jakubczyk, M., Density, surface tension, and refractive index of aqueous ammonium oxalate solutions from 293 to 333 K. *J. Chem. Eng. Data* **1998**, *43*, 158-161.
432. Hibben, J. H., The Raman spectra of oxalic acid. *J. Chem. Phys.* **1935**, *3*, 675-679.